Airborne observations of turbulence and its influence on new particle formation in the atmospheric boundary layer

DISSERTATION

der Mathematisch-Naturwissenschaftlichen Fakultät
der Eberhard Karls Universität Tübingen
zur Erlangung des Grades eines
Doktors der Naturwissenschaften
(Dr. rer. nat.)

vorgelegt von
ANDREAS PLATIS
aus München

Tübingen
2016

Gedruckt mit Genehmigung der Mathematisch-Naturwissenschaftlichen Fakultät der
Eberhard Karls Universität Tübingen.

Tag der mündlichen Qualifikation: 2. Februar 2017

Dekan: Prof. Dr. Wolfgang Rosenstiel
1. Berichterstatter: Prof. Dr. Jens Bange
2. Berichterstatter: Prof. Dr. Stefan Emeis

Abstract

This thesis is a work in the field of atmospheric physics. It will illustrated by means of airborne measurements, how turbulence influences the formation of newly formed particles and how turbulence structures are modified by surface heterogeneity in the atmospheric boundary layer. The atmospheric boundary layer is the lowest part of the earth's atmosphere, which is in direct contact with the earth surface. In this layer turbulent fluctuations of moisture and temperature play an important role in aerosol research. A layer with enhanced temperature and humidity fluctuations lead to increased new particle formation. In a case study the boundary layer dynamics and its accompanied new particle formation event were investigated over a fairly homogeneous surface which yielded ideal conditions for the understanding of turbulent processes and its influence on new particle formation. However, natural landscapes rarely provide horizontal homogeneous conditions and have to be considered to be heterogeneous. The surface heterogeneity causes a more complex behaviour on the atmospheric boundary layer's flow as this is the case of homogeneous terrain. Therefore a second part of this thesis deals with the effects of surface heterogeneity (with several different surface types) on the ABL and its turbulence. Thus, one major aspect is, how the heterogeneous surface modify the kinematic expression of the turbulence (e.g vertical wind) and fluctuations of scalar quantities such as the temperature T and humidity q. In addition, these studies show that only second-order moments are adequate to describe the influence of surfaces heterogeneity. The second order moments use the quadratic terms of a sample e.g. structure function/parameter, variances and covariances (fluxes).

Zusammenfassung

Die vorliegende Arbeit ist im Bereich der Physik der Atmopshäre angesiedelt und behandelt fluggestützten Untersuchungen in der atmosphärischen Grenzschicht. Die Grenzschicht ist die unterste Schicht in der Atmosphäre und ist daher im ständigen Kontakt mit dem Boden. Es wird gezeigt wie Turbulenz in dieser Grenzschicht die Bildung von neuen Aerosolpartikeln beeinflusst und inwiefern die Bodenoberfläche Einfluss auf die Turbulenz nehmen kann. Für die Aersosolforschung, spielen in dieser Schicht turbulente Fluktuationen von Temperatur und Feuchte eine wichtige Rolle. Diese erhöhten Fluktuationen können zu einem Anstieg in der Partikelbildung führen. In einer Fallstudie wird im Rahmen dieser Doktorarbeit genau dieser Zusammenhang zwischen Turbulenz und Partikelneubildung erforscht. Dabei finden die Flugmessungen über einem homogenen Gebiet statt, welches ideale Bedingungen schafft um die turbulenten Prozesse im Bezug auf die Neubildung zu untersuchen. Natürliche Landschaften sind aber in der Regel nicht sehr homogen. Ein heterogener Untergrund wirkt sich viel komplexer auf die turbulente Strömung der Grenzschicht aus als ein homogener Boden. Daher wird in einem zweiten Teil der Arbeit der Einfluss von einem heterogenem Gelände (mit verschieden Bodentypen) auf die Turbulenz und deren Strukturen in der atmosphärischen Grenzschicht untersucht. Es wird gezeigt wie der heterogene Untergrund Einfluss auf die kinematischen Eigenschaften der Turbulenz (z.B vertikaler Wind) und wie auf die Skalaren Größen wie Temperatur und Feuchte nimmt. Es stellt sich dabei heraus, dass sich nur die statistischen Momente zweiter Ordnung eignen um den heterogenen Bodeneinfluss zu Beschreiben. Diese Momente sind zum Beispiel die Struktur Funktion sowie Varianz und Kovarianz.

Danksagung

Ich möchte mich bei allen Leuten bedanken, welche mich während meiner Zeit als Doktorand in Tübingen unterstützt haben und beim Anfertigen dieser Arbeit. Insbesondere möchte ich mich bedanken bei:

- Meinem Doktorvater Jens Bange bedanken, der mir diese wunderbare Möglichkeit im Rahmen des DFG Aerosolprojekts gegeben hat, diese Promotion in seiner Arbeitsgruppe durchzuführen. Jens unterstützte mich jederzeit tatkräftigt und ermöglichte mir viele Kontakte um mit Gleichgesinnten in Verbindung zu treten.

- Barbara Altstädter, Astrid Lampert, Birgit Wehner und Markus Hermann, mit denen ich zusammen in dem DFG Aerosolprojekt arbeiten durfte. Die Zusammenarbeit ermöglichte uns neue Erkenntnisse in der Aerosolforschung zu gewinnen aber auch eine für mich unvergessliche Zeit mit euch auf den zahlreichen Kampagnen und Projektreffen.

- Ein ganz großes Dankeschön geht an meine Arbeitsgruppe. Ich hätte es nicht für möglich gehalten in so einer entspannten aber auch produktiven Atmosphäre arbeiten zu dürfen. Jederzeit habe ich von euch Unterstützung erhalten. Aber auch außerhlab der Arbeitszeit bei Afterwork Bieren, Sport, Kino, Grillfesten habt ihr mir eine angenehme Zeit in Tübingen bereitet. Großes Merci an Norman Wildmann, Torsten Auerswald, Asmae El-Bahlouli, Milad Kiaee, Daniel Martinez Villagrasa, Bastian Paas, Uwe Putze, Alexander Rautenberg und David-James Tupman.

- Den Zahlreiche Studenten, die mich währen den Messkampagnen, Datenauswertung, Fliegerreparieren, Sicherheitpiloten beim UAV Fliegen und Entwicklung von neuen Messsyteme und vieles vieles mehr geholfen haben. Vielen Dank Marvin, Felix, Claudio, Niels, Leonie, Moritz, Dina, Max, Henrik, Markus und Philipp, Bernhard.

- Den Kollegen neben den schon oben genannten, die mir mit gutem Rat jederzeit zur Seite standen und mich mit inspirierenden Gesprächen auf neue Ideen und Lösungen gebracht haben. Danke Frank Beyrich, Wolfram Birmilli, Annette Junginger, Markus Ebner, Tatiana Miranda, Stefan Emeis und Aline van den Kroonenberg.

- Meiner Familie, die mich jederzeit ermuntert und unterstützt hat.

- Meine Freunden, die mir eine wunderbare Zeit auch neben meiner Promotion ermöglichten mit Klettern, Partys, Besen, Colle, Stochern, WG-Leben, Tennis, Beachen, Mountainbiken, Fliegen und vielem mehr.

Contents

Chapter 1

List of Publications

This thesis is presented as an integrated accumulation of three peer-reviewed publications. All three manuscripts have been or will be published soon in peer-reviewed journals.

1.1 Peer-reviewed publications, first author

I **Platis A**, Altstädter B, Wehner B, Wildmann N, Lampert A, Hermann M, Birmili W, Bange J (2016) An observational case study on the influence of atmospheric boundary-layer dynamics on new particle formation, Boundary-Layer Meteorology 158(1):67–92

II **Platis A**, Martínez-Villagrasa D., Beyrich F., Bange, J. (2016) Analysis of the influence of a lake on the lower convective boundary layer from airborne observations, Meteorologische Zeitschrift Schweizerbart Science Publishers, 2016

III **Platis A**, Martínez-Villagrasa D., Tupman D., Beyrich F., Bange, J. (2016) Observations of the temperature and humidity structure parameter over heterogeneous terrain by airborne measurements during the LITFASS 2003 campaign, Boundary-Layer Meteorology *under review*

1.2 Peer-reviewed publications, co-author

- Altstädter B, **Platis** A, Wehner B, Scholtz A, Wildmann N, Hermann M, Käthner R, Baars H, Bange J, Lampert A (2015) ALADINA–an unmanned research aircraft for observing vertical and horizontal distributions of ultrafine particles within the atmospheric boundary layer. Atmospheric Measurement Techniques 8(4):1627–1639

- Braam M, Beyrich F, Bange J, **Platis A**, Martin S, Maronga B, Moene AF (2015) On the discrepancy in simultaneous observations of the structure parameter of temperature using scintillometers and unmanned aircraft. Boundary-Layer Meteorology pp 1–27

- Altstädter B, Lampert A, Scholtz A, Bange J, **Platis A**, Hermann M, Wehner B (2013) Aerosol variability observed with rpas. ISPRS-International Archives of the Photogrammetry, Remote Sensing and Spatial Information Sciences 1(2):1–4

- Emeis, S.; Siedersleben, S.; Lampert, A.; **Platis, A.**; Bange, J.; Djath, B.; Schulz-Stellenfleth, J. Neumann, T. Exploring the wakes of large offshore wind farms Journal of Physics: Conference Series, 2016, 753, 092014

1.3 Conference contributions

- **Platis, Andreas**; Altstädter, Barbara; Wehner, Birgit; Wildmann, Norman; Lampert, Astrid; Hermann, Markus; Bange, Jens, Airborne Measured New Particle Formation Event in the Atmospheric Boundary Layer EGU General Assembly 2015, 12-17 April, 2015 in Vienna, Austria. id.3663,
  URL `http://meetingorganizer.copernicus.org/EGU2015/EGU2015-3663.pdf`

- **Platis, Andreas**; Martinez, Daniel; Bange, Jens Airborne-Measured Spatially-Averaged Temperature and Moisture Turbulent Structure Parameters Over a Heterogeneous Surface, In EGU General Assembly 2014, 27 April - 2 May, 2014 in Vienna, Austria, id.10401,
  URL `http://meetingorganizer.copernicus.org/EGU2014/EGU2014-10401.pdf`

- **Platis, Andreas**, D. Martinez, J. Bange Airborne-Measured Spatially-Averaged Temperature and Moisture Turbulent Structure Parameters Over a Heterogeneous Surface, In 21st Symposium on Boundary Layers and Turbulence, Leeds, UK, 09 - 13 June 2014,
  URL `https://ams.confex.com/ams/21BLT/webprogram/Paper247654.html`

- **Platis, Andreas**, Norman Wildmann, Dr. Shridar Ravi , Prof. Dr. Jens Bange Current state of wind-vector measurement with 5-hole probes aboard the research UAVs of the University of Tübingen, In ISARRA 2013, Palma de Mallorca, Spain, 18 – 20 February 2013,
  URL: `http://www.uibcongres.org/congresos/ponencia.en`

- **Platis, Andreas**, D. Martinez, J. Bange Airborne-Measured Spatially-Averaged Temperature and Moisture Turbulent Structure Parameters Over a Heterogeneous Surface, In ISARRA 2014, Odense, Denmark, 26 - 28 May 2014,
  URL `isarra.org/ISARRA2014_abstracts/ISARRA_2014_presentation_Platis.pdf`

- **Platis, Andreas**; Altstädter, Barbara; Wehner, Birgit; Wildmann, Norman; Lampert, Astrid; Hermann, Markus; Bange, Jens, Case study of a new particle formation event in the atmospheric boundary layer measured by unmanned aerial systems, In ISARRA 2015, University of Oklahoma, Norman Oklahoma, USA, - May 20 to 22, 2015,
  URL `http://www.isarra.org/page26.html`

- **Platis, Andreas**; Altstädter, Barbara; Wehner, Birgit; Wildmann, Norman; Lampert, Astrid; Hermann, Markus; Bange, Jens, Airborne Measured New Particle Formation Event in the Atmospheric Boundary Layer, In ISARRA 2016 on May 23 to 25 in Toulouse, France,
  URL `www.meteo.fr/cic/meetings/2016/isarra/abstracts.pdf`

- **Platis, Andreas**; Altstädter, Barbara; Wehner, Birgit; Wildmann, Norman; Lampert, Astrid; Hermann, Markus; Bange, Jens, An airborne case study on the influence of atmospheric boundary layer dynamics on the new particle formation, In 15th EMS Annual Meeting and 12th European Conference on Applications of Meteorology (ECAM), 07-11 September 2015, Sofia, Bulgaria,
  URL meetingorganizer.copernicus.org/EMS2015/EMS2015-125.pdf

- **Platis, Andreas**, N. Wildmann,,J. Bange: Ein „Remotely Piloted Air System“ (RPAS) als ergänzendes Messinstrument zur Standortevaluation am Beispiel des Projekts Lidar Complex, In 3. Fachtagung Energiemeteorologie, 4. – 6. Juni 2013 in Grainau, Germany,
  URL www.dlr.de/eoc/Portaldata/60/Resources/dokumente/1_clu

Chapter 2

Introduction

With every breath we take, we inhale approximately 7 or 8 litres of air each minute or 11,000 liters per day. Even if the air looks clear, we inhale tens of millions of solid particles and liquid droplets called aerosols. They drift in Earth's atmosphere and despite their small size, which can be less than the width of the smallest viruses, they have major impacts on our health and on our climate. Aerosols are suspensions of liquid, solid, or mixed particles with highly variable chemical composition and size distribution (Putaud et al., 2010). Aerosol particles range in size from 0.01 micrometer to several tens of micrometres in diameter. Their variability in chemical composition is due to the numerous sources and varying formation mechanisms (Figure 2.1). Aerosol particles are either emitted directly to the atmosphere (primary aerosols) or produced in the atmosphere from precursor gases (secondary aerosols).

Primary aerosols consist of both inorganic and organic components. They enter the atmosphere from many different natural and anthropogenic (human activity–related) sources (Andreae and Rosenfeld, 2008; Després et al., 2012). For example, nature generates sulfate aerosols from volcanoes, salt aerosols from sea spray, dust aerosols from desert areas, and carbonaceous aerosols formed from volatile organic compounds emitted by plants.

Secondary aerosol particles are produced in the atmosphere from precursor gases by condensation of vapours on pre-existing particles or by nucleation of new particles. These partilces are small; they range in size from a few nanometres up to 1 μm and have lifetimes of days to weeks. Secondary aerosols consist of mixtures of compounds; the main components are sulphate, nitrate, and organic carbon. The majority precursor gases are emitted from fossil fuel combustion, but fires and biogenic emissions of volatile organic compounds (VOCs) are also important.

Aerosols play an important role in the global climate balance, and therefore they are important in climate change. Natural variations of aerosols, especially due to episodic large eruptions of volcanoes, such as Mt. Pinatubo in 1991, are recognized as a significant climate forcing (Self et al., 1993; Parker et al., 1996), that is, a factor that alters the Earth's radiation balance and thus tends to cause a global temperature change. In addition, there are several ways in which humans are altering atmospheric aerosols, not only near the ground (e.g. industrial emissions) but as high as the lower stratosphere (where they are continuously emitted by aircraft), and thus affecting climate (e.g. through contrails) Charlson et al. (1992). Aerosols force climate in two ways (Hansen et al., 1997):

- **direct radiative forcing:** All atmospheric aerosols scatter incoming solar radiation. A few aerosol types can even absorb solar radiation. Aerosols that mainly scatter solar radiation have a cooling effect, by enhancing the total reflected solar radiation

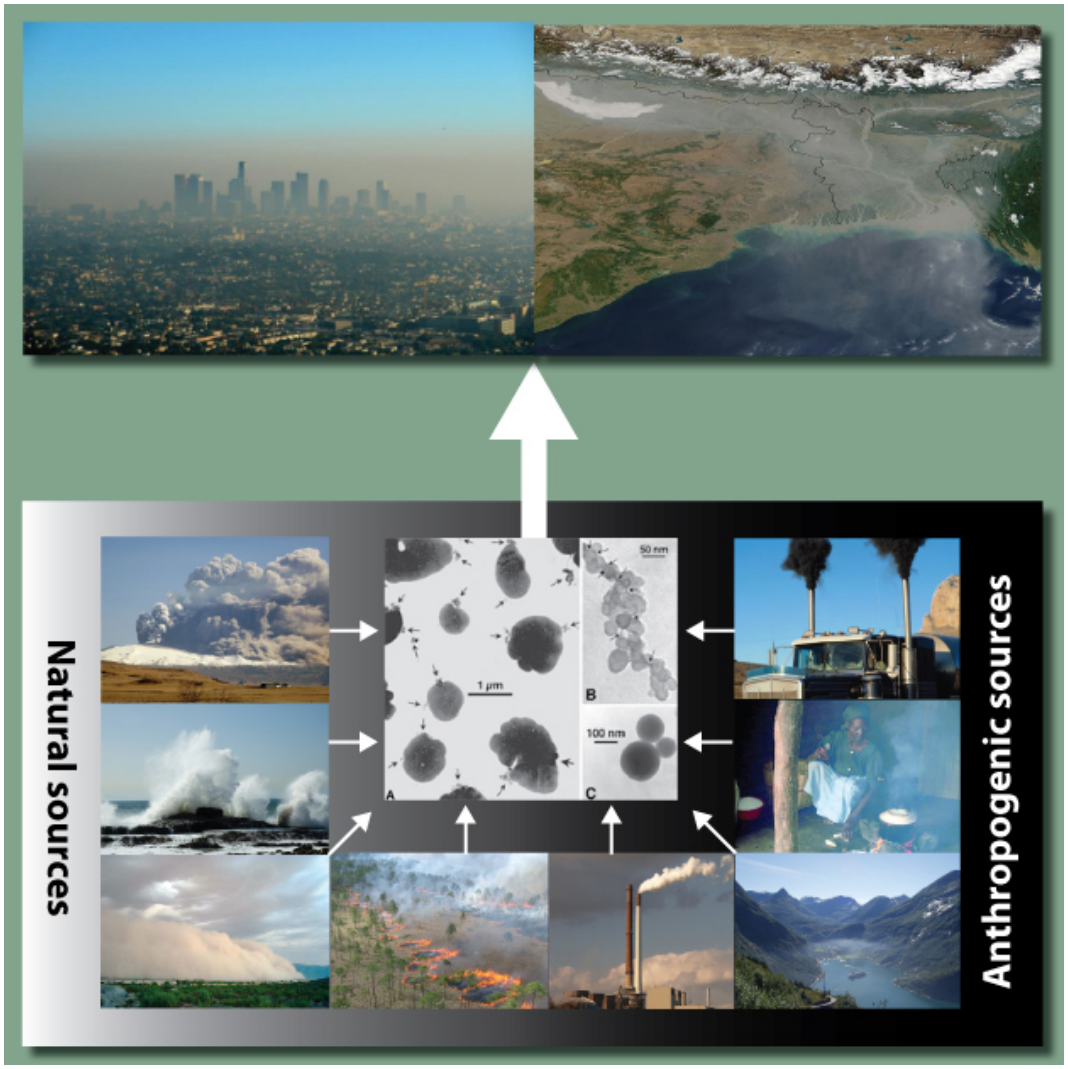

Figure 2.1: Top: local and large scale air pollution. Bottom: Sources include (counter-clockwise) volcanic eruptions (producing volcanic ash and sulphate), sea spray (sea salt and sulphate aerosols), desert storms (mineral dust), savannah biomass burning (black carbon (BC) and organic carbon (OC)), coal power plants (fossil fuel BC and OC, sulphate, nitrate), ships (BC, OC, sulphates, nitrate), cooking (domestic BC and OC), road transport (sulphate, BC, VOCs yielding OC). Centre: Electron microscope images of (A) sulphates, (B) soot, (C) fly ash, a product of coal combustion. Adapted from Myhre et al. (2013).

from the Earth (Lohmann and Feichter, 2005). Especially particles in the size range of about 0.1 to 1.0 µm (which are called accumulation mode) interact with solar and terrestrial radiation and have a direct impact on the radiation budget (IPCC, 2007) and thus on the Earth's climate.

- **indirect radiative forcing**: Aerosols interact with clouds and precipitation in many ways, acting either as cloud condensation nuclei (CCN) or as absorbing particles, redistributing solar energy as thermal energy inside cloud layers (Kerminen et al., 2005). The aerosol-cloud feedbacks remain the largest source of uncertainty in climate sensitivity estimates IPCC, 2007).

In contrast to aerosols, greenhouse gases have a well-understood effect on the global radiative balance and surface temperatures. Their concentration has little variability (except water vapour and ozone), and their long-term trends are well-known Taylor and Penner (1994). Therefore, there is high confidence in the greenhouse gas component of the anticipated climate change during the next few decades. Climate forcings due to aerosols are not determined well, especially the indirect radiative forcing. Thus, aerosols are one of the greatest sources of uncertainty in interpretation of climate change of the past century and in projection of future climate change (Ayers et al., 1997).

One aspect of the unknown quantification is the above listed second effect, that aerosol particles also serve as cloud condensation nuclei (CCN). These hygroscopic atmospheric particles (diameter 100 - 200 nm) provide a surface for the condensation of water vapour, enabling the formation of clouds, in a saturated environment and also modify cloud properties (indirect aerosol effect, (Kerminen et al., 2005)). Clouds with smaller, more numerous droplets have a larger surface area and therefore reflect up to 30 percent more sunlight (Kerminen et al., 2005). Further, the smaller water droplets in the cloud fall more slowly, thereby prolonging the lifespan of the cloud and strengthening its cooling effect. This indirect effect is believed to be changing rainfall patterns in populated regions worldwide.

The most powerful way to increase the CCN population is by nucleation of new particles (ultrafine particles ≈2-10 nm) and growth of these to CCN size (≈100 nm). CCN availability was observed to vary by an order of magnitude during new particle formation (NPF) events (Wiedensohler et al., 2009). A main production mechanism is the binary nucleation of sulfuric acid and water to stable molecular clusters (see Fig. 2.2). This nucleation of aerosol particles from gaseous precursors is a major source of new particle number concentration in the earth's atmosphere and occurs very often in the atmospheric boundary layer (ABL). Current research is dedicated to elucidate additional species involved in particle nucleation and growth.

However, many of the critical factors influencing the nucleation process are poorly known; see for example (Hoppel et al., 1994). Turbulence and mixing of air masses with different temperature and humidity properties have been discussed as possible processes, which could lead to favourable conditions for NPF by e.g. local, short-term supersaturation of precursor gases (Bigg, 1997; Nilsson et al., 2001). For example, Easter and Peters (1994) or Pirjola et al. (2000) found that turbulent fluctuations could enhance predicted nucleation rates, while Nilsson and Kulmala (1998) revealed nucleation enhancement due to the effect of mixing across a temperature and humidity gradient. For instance, in their discussion of the nucleation process Easter and Peters (1994) showed that because of the sensitivity of binary nucleation rates to changes in temperature and relative humidity (RH), small fluctuations in these quantities due to turbulence or mixing processes could lead to nucleation rates considerably higher than those expected from the mean temperature and RH. Bigg

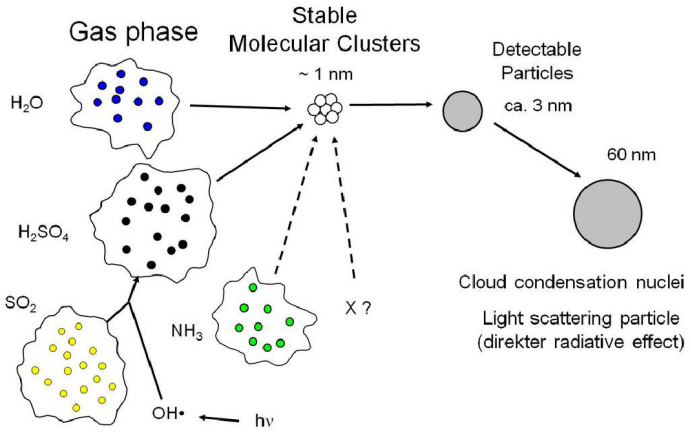

Figure 2.2: Processes involved in atmospheric new particle formation and growing of stable cluster to CCN Source: (W. Birmili/TROPOS) `https://www.tropos.de/fileadmin/_processed_/csm_nucleation_schematic_7184bbfc6f.jpg`

(1997) suggested that NPF results from "very sudden but sporadic mixing of limited horizontal and vertical extent between adjacent layers having strong thermal stability, the upper of which is both warmer and drier than the lower. Temperature and relative humidity differences need to be such that mixing will temporarily cause an increase in nucleation rate sufficient to bridge the gap between the existing supersaturation of the binary mixture and that required for homogeneous nucleation of new particles." In addition, Easter and Peters (1994) found by numerical simulations that humidity and temperature fluctuations can enhance nucleation and increase nucleation rates if the humidity and temperature fluctuations are anti-correlated, however this has never been validated by measurements in the ABL.

In experiments, Siebert et al. (2004) described NPF, due to effective mixing of high fluctuations in the temperature and water vapour in the SATURN ('Strahlung, vertikaler Austausch, Turbulenz und Partikel-Neubildung'; radiation, vertical exchange, turbulence and NPF) experiment. Hellmuth (2006) predicted the highest likelihood for nucleation near the top of the mixed layer, mainly due to thermodynamic reasons by numerical simulations. Further, NPF was observed to be correlated with increasing turbulence in the residual layer by Wehner et al. (2010) with the measurement system called Airborne Cloud Turbulence Observation System (ACTOS). Also Stratmann et al. (2003) investigated particle burst events in the residual layer and mixed layer with ACTOS, as well as Siebert et al. (2007). They also proposed NPF caused among others by a nocturnal low-level jets. This layer is often characterised by strong turbulence due to shear flows.

Consequently, knowledge about the occurrence and behaviour of atmospheric turbulence in the ABL is very important to investigate NPF. The turbulent flow in the atmosphere is complex and depends on various variables such as various gases, gas density, pressure, volume, moisture, land surface characteristics, solar input and temperature. These variables are governed by several forces and relationships such as gravity, gas laws, radiation laws, and fundamental forces (e.g. gravity, friction). All these variables are connected. In other words, all the gas is on the Earth's surface and every gas molecule has neighbouring gas molecules and through enough connections, every gas molecule has the ability to interact with another gas molecule given enough time.

Due to this chaotic-like and apparently complex behaviour, scientist developed theories, hypotheses and statistical techniques to be able to study atmospheric turbulence. In order to

improve understanding and validate theories and hypotheses, which might have been postulated decades before, experimental data and proper statistical tools are necessary. However, the ABL has a large vertical extent from the Earth's surface up to usually 1000-2000 m and a horizontal extend over various surface types. Thus we can not rely only on single point ground-based measurements (Kohsiek et al., 2002; Meijninger et al., 2002). An advantageous and expedient instrument to observe the ABL's horizontal and vertical variability are airborne platforms, not only to measure and validate turbulence, but to combine the turbulence measurements with observations of aerosols such as NPF.

The following thesis will illustrated by means of three published studies with airborne measurements, how turbulence influences the formation of newly formed particles (Platis et al., 2016a) and how turbulence structures are modified by surface heterogeneity in the ABL (Platis et al., 2016b, 2017). The three studies illustrate that one very powerful method to describe turbulence are second-order statistical moments. Second order use the quadratic terms of a sample e.g. structure function/parameter, variances and co-variances (such as fluxes). The first study shows that turbulent fluctuations of moisture and temperature in the ABL dynamics play an important role in Aerosol research. A layer with enhanced temperature and humidity fluctuations may lead to increased new particle formation. In this case study the ABL dynamics and its accompanied NPF event were investigated over a fairly homogeneous surface which yielded ideal conditions for the understanding of turbulent processes and its influence on NPF. However, natural landscapes rarely provide horizontal homogeneous conditions and have to be considered to be heterogeneous. Therefore the second and third study investigates the effects of surface heterogeneity (with several different surface types) on the ABL and its turbulence. The surface heterogeneity causes a more complex behaviour on the ABL's flow as this is the case in the first study. Thus, one major aspect of these two studies are, how the heterogeneous surface modify the kinematic expression of the turbulence (e.g vertical wind) and fluctuations of scalar quantities such as the temperature T and humidity q. In addition, these studies show that only second-order moments are adequate to describe the influence of surfaces heterogeneity. The three studies use airborne platforms as a tool to collect the experimental data in the ABL.

The following introduction gives an brief overview about what turbulence is, the ABL's nature, the concrete research fields (which are the convective boundary layer over heterogeneous surface and new particle formation in the ABL), a brief explanation about second order statistics, and the used airborne platforms. The introduction provides the reader the essential background in order to understand the three published studies.

2.1 Atmospheric Turbulence

Studying turbulence in the ABL implies the challenge of analysing the turbulent flow. Werner Heisenberg once said:

> "Before I die, I hope that someone will explain quantum mechanics to me.
> After I die, I hope that God will explain turbulence to me. But I wouldn't want
> to embarrass God by asking him"

In practical terms that means the equations of the turbulent fluid motion cannot be solved analytically. The difficulty stems from their nonlinearity. Nevertheless there are certain predictions which can be made based on a variety of physical arguments. This is important because the natural state of the ABL is dominated by turbulence. That turbulent state is the cause for the vertical transport of moisture, heat, momentum, and pollutants in the ABL.

Turbulence is commonly understood as numerous, three-dimensional rotating eddies moving irregularly with the mean horizontal air flow. Within the ABL turbulence is produced in two ways: (i) friction of the wind with obstacles near the surface (shear production, mechanical turbulence) or (ii) by density differences between air parcels (buoyancy production, convective turbulence).

Observations show that there is a broad spectrum of eddy sizes, which led Richardson (1922) to introduce the concept of energy cascades: The largest eddies, which are created by instabilities in the mean flow, are themselves subject to inertial instabilities. They will break-up (i.e. energy is progressively transferred from large eddies to smaller ones) or evolve into yet smaller vortices. Thus, there is a continual cascade of energy from large scale down to small. For the atmospheric turbulence this is reflected by the energy spectrum. The spectrum (see Fig. 2.3) is divided into the range of production, the inertial range, and the dissipation range. In the atmosphere the instability of the mean flow, which produces the largest eddies with highest energy values, is due to the above mentioned buoyancy and shear. This turbulent kinetic energy e is transferred from the large scales (low wave numbers) towards smaller scales (high wave numbers). This range of the energy spectrum is characterised by the -5/3 slope, the Kolmogorov law of locally isotropic turbulence. Kinetic energy is dissipating into heat at the small-eddy end of the spectrum (Petersen and Renfrew, 2009).

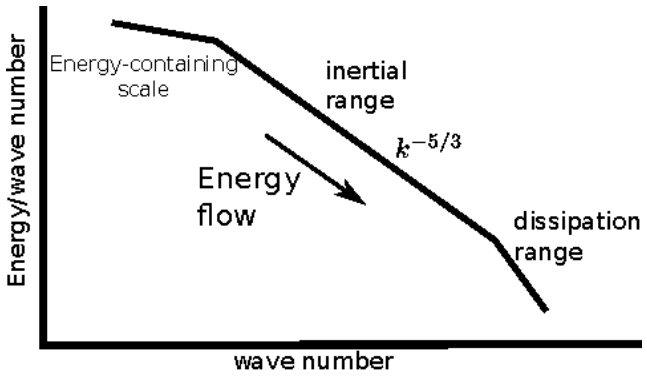

Figure 2.3: Schematic illustration of the power spectrum of ABL turbulence with logarithmic axis adapted from Größ et al. (2015)

2.1.1 Statistical Moments

The mathematical way to describe turbulence in a flow and its structure is by statistical moments. Moments are statistical measures which characterise signal properties. In the following a brief overview of the statistical moments are given.

Lower-order statistics refer to functions which use zeroth, first, and second powers of a sample. These are constant, linear, and quadratic terms (zeroth, first, and second powers), which are used for example in the arithmetic mean, and variance. The third and higher moments, are used in the skewness and kurtosis and are often called higher-order statistics. Due to the higher powers, higher-order statistics are significantly less robust than lower-order statistics. Mathematically speaking, a moment is just a geometric series of type

$$(a_1^s + a_2^s + ... + a_n^s)/n \tag{2.1}$$

where s describes the s-th moment and n is the numbers of values. When this set of values has a sufficiently strong central tendency, that is, a tendency to cluster around some partic-

ular value, then it may be useful to characterise the set by a few numbers that are related to its moments, the sums of integer powers of the values. Best known is the mean of the values $a_1^s ... a_N^s$ with $s = 1$,

$$\overline{a} = \frac{1}{N} \cdot \sum_{i=1}^{N} a_i \tag{2.2}$$

which is used to refer to one measure of the central tendency (first order momentum). After having identified a distribution's central value, one could characterises its "dispersion" or "variability" around that value now. Most common is the variance,

$$\mathrm{Var}(a_1 ... a_N) = \frac{1}{N-1} \cdot \sum_{i=1}^{N} (a_i - \overline{a})^2 = \overline{a'^2} \tag{2.3}$$

or its square root, the standard deviation,

$$\sigma(a_1 ... a_N) = \sqrt{\frac{1}{N-1} \cdot \sum_{i=1}^{N} (a_i - \overline{a})^2} \tag{2.4}$$

As the mean depends on the first moment of the data, so do the variance and standard deviation depend on the second moment($s = 2$). A very important turbulence quantification in the ABL research which uses the second order momentum is the turbulent kinetic energy. It is the mean kinetic energy per unit mass associated with eddies in the turbulent flow. Using the variance of the three wind components (u,v,w) one could calculate turbulent kinetic energy e which was already mentioned in Sect. 2.1 and is defined mathematically as:

$$e = \frac{1}{2} \left(\overline{u'^2} + \overline{v'^2} + \overline{w'^2} \right) \tag{2.5}$$

The variance is a special case of the covariance, where $a = b$ and is defined for the discrete case by

$$\overline{a'b'} = \frac{1}{N} \sum_{i=1}^{N} a'b' \tag{2.6}$$

The co-variance indicates the degree of common relationship between the two variables a and b (Stull, 1988). For example, $a = T$ which is the air temperature and $b = w$ the vertical wind velocity, respectively. On a hot summer day over land, the warmer than averaged air will rise (positive T' and positive w'), and the cooler than averaged air (negative T' and negative w') will sink. Thus, the product $w'T'$ will be positive on the average, indicating that w and T vary together. This co-variance $\overline{w'T'}$, which is also called the turbulent flux of sensible heat, is indeed found to be positive throughout 80% of CBL. In this thesis statistical moments are used to describe the turbulence structure and processes and how the heterogeneous surface modify the turbulent flow in the ABL. As shown later by the studies 3.2 and 3.3 only second-order moments are adequate to describe the influence of surfaces heterogeneity.

2.1.2 Structure Parameter

An additional statistic which can be calculated from second order moments to view common variation in a time series is the structure function. It is also an alternative to Fourier power spectra with the advantage of not using a Fourier transformations to calculate the covariance function and thus avoid systematic errors due to improper data windowing. Fourier

transformations apply to infinite-duration periodic data set (Stull, 1988). However, in our data set (but as well in the whole boundary layer meteorology) nothing is periodic for infinite time or infinite distance. The flight legs we analyse are always limited in distance. Thus data has to be conditioned by detrending, despiking filtering and bell tapering to satisfy requirements of Fourier transformations, but this modification always causes error or biases. Therefore the structure function $D_a(r)$ is used in this study, which is a measure of auto-correlation in a flow as a function of eddy size and uses differences rather than the product of two different points or a Fourier transformation. It was defined by Tatarskii (1971):

$$D_a(r) = \frac{1}{N-n} \sum_{i=1}^{N-n} [a(x_i) - a(x_i + r)]^2 \tag{2.7}$$

for a certain data record a, where x is the spatial coordinate, the number of data points in the record is denoted by N, where $r = r(n)$ is the spatial displacement (lag) that corresponds to the eddy size, and n is the number of data points associated with the lag r. $D_a(r)$ is of the order of all of the energy in eddies of size r or less (Davidson, 2004). The dominant contribution will come from the eddies of size r since these are the most energetic, assuming that larger eddies transport more energy. In order to show the close relation between structure function and turbulent kinetic energy for isotropic turbulence, the structure function $D_V(r)$ is calculated for the wind speed V. $D_V(r)$ can also be calculated by the variance σ_V and the auto-correlation function ρ_V

$$D_V(r) = 2\sigma_V^2 [1 - \rho_V(r)]. \tag{2.8}$$

For large r in the order of the integral length scale I the auto-correlation function becomes small:

$$\rho_V \xrightarrow{r \to I} 0, \text{ leading to } D_V \xrightarrow{r \to I} 2\sigma_V^2. \tag{2.9}$$

For isotropic turbulence ($\sigma_u = \sigma_v = \sigma_w = \sigma_V$, where u, v, w are the wind-speed components in the x, y, z direction, respectively) the turbulent kinetic energy e is

$$e = \frac{1}{2} \left(\sigma_u^2 + \sigma_v^2 + \sigma_w^2 \right) = \frac{3}{2} \sigma_V^2 \tag{2.10}$$

and thus according to Eq. 2.9,

$$D_V \xrightarrow{r \to I} \frac{4}{3} e, \tag{2.11}$$

where e is of all eddies of size r or less. In the inertial sub-range $D_V(r)$ depends only on the dissipation rate ε, r and Kolmogorov's constant $\beta = 2$ (Kolmogorov, 1941)

$$D_V(r) = \beta \, \varepsilon^{2/3} \, r^{2/3} = C_V^2 \, r^{2/3}, \tag{2.12}$$

with the structure parameter C_V^2 for the wind speed V

$$C_V^2 = D_V(r) \, r^{-2/3} \tag{2.13}$$

which is a proportionality factor in the 2/3-law expression (Kolmogorov, 1941) for the structure function. The relation of Eq. 2.13 can be only applied within the inertial sub-range of locally homogeneous and isotropic turbulence (Wyngaard et al., 1971). The structure parameter is calculated from in situ data using the structure function. By knowing the structure parameter C_V^2, the dissipation rate ε can be calculated from airborne measurements.

Besides the kinematic expression of the turbulence such as the dissipation rate and the turbulent kinetic energy, fluctuations of scalar quantities such as the temperature T and

humidity q are equally important to characterise the turbulence state of the atmosphere. The combination of (2.8) and (2.13) shows that an increase of the temperature variance σ_T results in an increase of the calculated C_T^2. C_q^2 and C_T^2 are obtained by using Eq. 2.13 with q and T instead of the wind speed V.

Often the question arises, what the timescale of one flight track is, in order to be able to understand if flights are fast enough such that the e.g. variance or structure parameter measurements can be considered as instantaneous snapshots. The airborne platforms we used in this study (see in Sect. 2.4) usually fly between 20-40 m s^{-1}, the flight tracks have a length of 1-10 km, resulting in times scales of a few minutes only. Within this time scale, Taylor's hypothesis of frozen turbulence (Wyngaard and Clifford, 1977) is fulfilled. Therefore, the turbulence measurement can be considered as coincidental.

2.2 Atmospheric boundary layer

All analysed data presented in this thesis were measured within or directly above the ABL. The ABL is the link between the Earth's surface, where most exchange of energy, matter and momentum takes place, and the free atmosphere. This part of the atmosphere can be defined as the layer affected by the surface at a timescale of one hour or below (e.g. Stull, 1988). Its typical vertical extension is from several hundreds of metres to a few kilometres. The corresponding exchange between the surface and the atmosphere strongly depends on the stratification of the boundary layer. Therefore detailed information on the vertical and horizontal ABL structure, especially with respect to temperature, humidity and wind and their turbulent fluctuations, is crucial to understanding the related exchange processes.

In general, there are three basic states of the boundary layer:

- the stable boundary layer (also called nocturnal boundary layer), which is found to occur at night due to longwave outgoing radiation,
- the neutral boundary layer, which occurs, for instance, in overcast conditions and high background winds (Garratt, 1994), or above nocturnal stable boundary layers
- the convective boundary layer (CBL), also called mixed layer, which is characterised by strong narrow updrafts of warm air due to surface forcings and cooler broader but weaker downdrafts.

Under a high pressure system and during day time usually a CBL is developed. This boundary layer can be divided into three well-defined idealised layers that occur over land surfaces (Fig 2.4). The lowest few centimetres of the surface layer is called the microlayer, where turbulence is absent and molecular transport dominates. The bottom 10% of the boundary layer is called the surface layer. It is the region, where turbulent fluxes and stress vary by less than 10% of their magnitude (Stull, 1988). The mixed layer is located above the surface layer. It is characterised by turbulence, which tends to mix heat, moisture and momentum vertically. Thus, constant vertical gradients of these three scalars are present in that layer. During daytime the ABL over land is dominated by strong turbulence, which is usually convectively driven, but there is also turbulence production by wind-shear (Garratt, 1994). The source of convective turbulence production in the absence of clouds is the heating of the surface by solar radiations. That surface warming causes a heat transfer from the surface layer into the mixed layer. In case of clouds atop the boundary layer, radiative cooling can also produce turbulence.

In the diurnal cycle, the boundary layer is growing by entrainment at the interface between the mixed layer and the free atmosphere atop. The maximum depth of a boundary layer is usually found to be in the late afternoon. The entrainment layer is the stably stratified capping zone and can be regarded as the transition zone to the free atmosphere. Rising thermals are able to penetrate into the entrainment zone and free atmosphere despite the stable conditions. Corresponding downdrafts are leading to entrainment of warmer air and dry air from the free atmosphere into the boundary layer as well as momentum transport. These up- and downdrafts cause high temperature and humidity fluctuations in that layer. The entrainment processes and the heating of the mixed layer lead to a continuous expansion of the convective boundary layer (CBL) during daytime.

All these layers are displayed together with the near-neutral so-called residual layer in Fig.2.4. The residual layer is the residuum of a mixed layer, which remains during night time, when the surface forcing and turbulent motions have vanished. It has immediate consequences for the boundary layer during daytime. It can rapidly merge into a CBL as soon as nocturnal inversions have vanished because it exhibits neutral stratification and well-mixed properties (Stull, 1988).

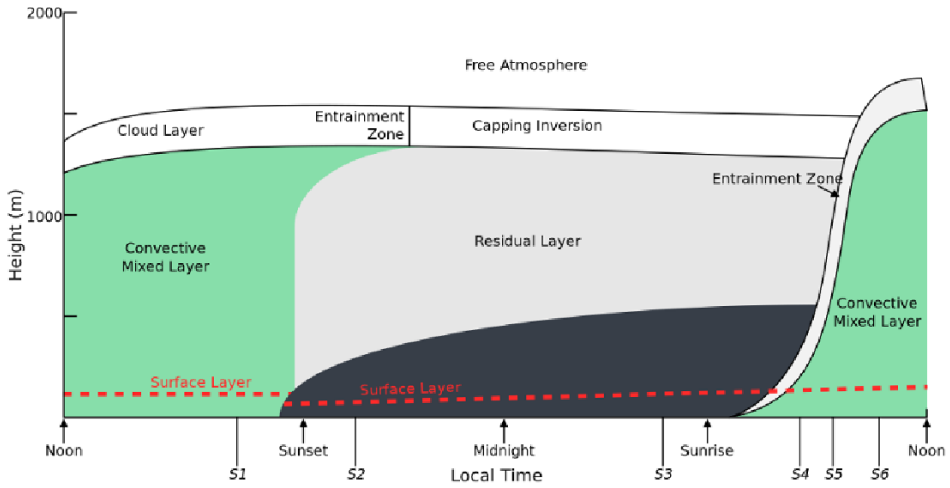

Figure 2.4: Diagram of the atmospheric boundary layer (Stull, 1988)

2.3 The ABL over heterogeneous terrain

Natural landscapes rarely provide horizontal homogeneous conditions and have to be considered to be heterogeneous. A high spatial variability in land use, vegetation, soil texture and wetness and cloud cover (leading to local variability of incoming shortwave radiation at the surface) are very common than homogeneous conditions (Letzel and Raasch, 2003) on the Earth's surface and my modify the turbulent flow in the ABL in addition.

Land surface heterogeneities can be divided into topographical and thermal heterogeneities. The former are caused by orography (such as mountains, valley, etc.), the latter by vegetation/artificial (like forest, lakes, cities etc.) elements and have been intensely investigated, e.g. heat-island by cities, local wind systems, orographic precipitation.

Heterogeneities usually cause horizontal differences in surface properties such as moisture, temperature, momentum and therefore lead to differences of the turbulent sensible and latent heat fluxes into the boundary layer. Their effect on the ABL, especially in case of

realistic heterogeneities, is still an open question. Experimental data and results are rare. Even the effect of sharp land-water discontinuities by a lake are not well understood (Mahrt, 2000). Flows over surface discontinuities can develop, for example local internal boundary layers (IBL) downstream, when the change of surface properties is sharp enough or the size of the surface heterogeneity is large. This situation may be enhanced when the change of surface properties is not sharp or is of small amplitude (Mahrt, 2000). Panofsky et al. (1982) and Højstrup (1982) already demonstrated that the variance spectra of the horizontal wind components in an IBL were influenced by upstream conditions. However, on smaller scales like an intermediate-size lake (only a few kilometres width) a well defined surface discontinuity is not necessarily transferred into the flow since the boundary layer may adjust without the formation of a new IBL. This situation may be enhanced when the change of surface properties is not sharp or is of small amplitude (Mahrt, 2000). An adjusting boundary flow is characterised by horizontal changes of some of the higher moments but does not exhibit significant horizontal variation of the mean variables (Mahrt, 1996). Such boundary-layer adjustments are probably common for smaller surface heterogeneity scales, like the intermediate-sized lake in our study, but have received little attention so far.

Further, the size of surface heterogeneities play an important role. When the value of the heterogeneity length scale is small, with respect to the size of boundary-layer eddies, the effect of this heterogeneity gets rapidly blended in the atmosphere by turbulent mixing and spatial variability. This is expressed by the concept of the blending height. The blending-height theory addresses the decreasing influence of surface heterogeneity with height, identifying a scaling depth where this influence progressively vanishes. Different formulations of the blending height z_{blend} have been discussed in the literature (Mahrt, 2000; Raupach and Finnigan, 1995; Wood and Mason, 1991), but there is no consensus in literature, especially depending on which forcings are more relevant. Therefore, a small heterogeneity length scale does not affect turbulent fluxes above a certain height close to the surface. This level is usually referred to as by the blending height, which should be considered a scaling depth rather than an exact level where the influence of surface heterogeneity suddenly vanishes (Mahrt, 2000).

In this thesis two aspects of the influence of heterogeneous terrain on the ABL were investigated. In a first study the effect of sharp land-water discontinuities by a lake on the convective boundary layer was explored, as already mentioned in Sect. 2. The specific objectives of the study (presented in Sect. 3.2) are to identify and describe the influence of a lake of intermediate-scale on the turbulent structure in the surface layer of a CBL, observed by airborne measurements and depict the limitations of such measurements, in regard to the statistical significance. The second aspect is the determination of the key parameters that contribute to the observed spatial changes over lake and land. The lake influence is only observable in variance, but not on all parameters and hardly on first order statistic. Furthermore we discuss vertical and horizontal propagation of the lake influence, with respect to published theoretical blending-height studies, e.g. from Raupach and Finnigan (1995); Mahrt (1996, 2000); Wood and Mason (1991).

The second study (in Sect. 3.3) investigates the effects of surface heterogeneity on the (second order statistic) structure parameter. In addition to the study above, several different surface types besides the lake are analysed by using the structure parameter as a statistical second order moment tool. Knowledge about the behaviour of the structure parameter over heterogeneous terrain is necessary in order to determine the reliability of scintillometers measurements. Scintillometers are a common measurement method for turbulence. They have the advantage of being able to measure path-integrated surface fluxes over large scale heterogeneous surfaces. Hence, compared to local point measurements, scintillome-

ters enable surface flux measurements over combined surface types patches like farmland, water and forest which are usually found over natural landscapes. Scintillometers determine the electromagnetic reflectivities, which are proportional to C_n^2, the structure parameter of the refractive index n (Thomson et al., 1978). Turbulent fluctuations of n are caused by fluctuations in temperature T and humidity Q. This implies that the refractive index structure parameter C_n^2 can be expressed in terms of the structure parameters of temperature C_T^2 (temperature fluctuation) and humidity C_Q^2 (humidity fluctuation) and the cross structure parameter C_{QT} (Wyngaard et al., 1978; van den Kroonenberg et al., 2012):

$$C_n^2 = a^2 C_T^2 + 2ab\, C_{QT} + b^2 C_Q^2\,, \tag{2.14}$$

where a and b depend on the wavelength of the radiation, and on mean atmospheric conditions such as pressure, humidity, and temperature. Consequently it is important to study the behaviour of the structure parameter over different surface types, because measurements of turbulent surface fluxes of sensible and latent heat are critical for a better understanding of the regional and global energy (Beyrich et al., 2012; Li et al., 2012) and may also be important for the understanding of ABL dynamics regarding NPF over heterogeneous terrain.

2.4 Airborne measurements in the ABL

Today instrumented aircraft are able to measure in-situ physical parameters in the atmosphere such as air pressure, temperature, humidity, wind and turbulence, gas and aerosol particle concentrations, aerosol and cloud particle size distributions and chemical composition, radiative properties and electric fields. The thermodynamic quantities of static air pressure, air temperature, water vapour density, and the 3D wind vector are the very basics of any meteorological measurements and in general required for further measurements of, e.g. aerosols and particles. The measurement of the turbulent fluctuations of the basic thermodynamic quantities requires special methods and probes. These have to be very accurate, sensitive and fast responding.

There are, however, problems inherent to the benefits of airborne measurement platforms. Sampling the atmosphere while flying through it causes severe perturbations. The properties of the atmosphere are modified by the airflow around the aircraft and within the instruments (Wendisch and Brenguier, 2013). Correction of this bias requires careful calibration of the instrument and post processing. Moreover, measurements of (turbulent) wind vectors require a precise geographical reference. For that the three–axis accelerations and rotations need to carefully be accounted for in the processing of such vector sampling. For many years, research aircraft were relying only on very expensive inertial systems, but the emergence of the Global Positioning System (GPS) constellation that provides accurate positioning at low frequencies (less than 1 Hz) and the development of miniaturised inertial systems that provide accurate accelerations and rotations at high frequencies (up to 100 Hz) have significantly improved the situation. Inexpensive systems now enable many research groups an easy access to airborne measurements of turbulent fluctuations (Wendisch and Brenguier, 2013). A further improvement for airborne atmospheric research, due to cheaper and miniaturised inertial systems, is the use of unmanned aerial systems (UAS) as an airborne measurement platform.

UAS, also called remotely piloted aircraft systems, offer many advantages as research platforms and have become increasingly important in the last decade. They can fly at various different places in the the atmosphere and do not rely on a single location like ground-based

instrument. Not only the miniaturisation of the inertial measurements system, but also other electronic components such as sensors or autopilot, allows the use of small and inexpensive UAS. The aircraft are in general small model aircraft. They fly automatically with low cruising speed at constant heights and predefined way points in order to derive accurate and comparable measurements of atmospheric parameters. Further advantages of these small unmanned research aircraft are minimal logistical requirements (e.g. no airport necessary), potentially lower costs compared to manned aircraft and high flexibility during mission flights. Further, they give the possibility to investigate atmospheric parameters at small scales and low altitudes and the potential for application in regions that are too dangerous for manned aircraft.

Another big advantage of UAS for turbulence measurements compared to manned aircraft is the decreased disturbance of the airflow by the aircraft, due to the smaller wingspan and wing load, which leads to smaller upwash (Crawford et al., 1996) and the reduced overall size, which decreases the disturbance of turbulence measurements according to Wyngaard (1985).A different way to reduce flow distortion, is to separate the measurement platform from the carrier platform. An example is the Helipod. It is an autonomously operating sensor package attached to a 15 m rope below a helicopter of almost any type. At a mission speed of 40 m s^{-1} the Helipod is outside the down-wash area of the helicopter's rotor blades in order to sample the unspoiled atmosphere.

For UAS-based research, measurements of atmospheric aerosol particles became one area of particular interest (Altstädter et al., 2015, 2013; Bates et al., 2013).. Recent years have seen limited campaigns with manned aircraft (e.g. ISDAC, McFarquhar et al. (2011); ARCTAS, Jacob et al. (2010)) to better understand the vertical and horizontal variability of aerosol particles, since aerosol have a big impact on the Earth's climate. While such campaigns can provide substantial insight and have the unique ability to deploy a variety of instruments to the same location, the cost of such efforts is unsustainable for routine observing. UAS can play a central role in decreasing the cost associated with making aerosol measurements in the ABL.

In this study three measurement platforms were used to probe the lower atmosphere. Two UAS platforms with aerosol payloads were used to investigate aerosol number concentrations and distribution in the ABL and boundary-layer dynamics in order to investigate a NPF. These two UAS are called MASC (Multi-purpose Airborne Sensor Carrier) and ALADINA (Application of Light-weight Aircraft for Detecting IN situ Aerosol) and are operated by the University of Tübingen and TU Braunschweig respectively. The third platform is called Helipod and used to measure thermodynamic quantities in the ABL, in order to observe the influence of surface heterogeneity on the ABL. The three systems will be described briefly:

2.4.1 Helipod

The Helipod is an an autonomously operating measurement system (Fig. 2.5) designed for boundary-layer field experiments. The is sensor package attached to a 15 m rope below a helicopter of almost any type. The Helipod is equipped with its own power supply, onboard computer and data storage, and carries a sensor equipment for in-situ measurements of humidity, air-, surface-temperature and the atmospheric wind vector, at 100 Hz sampling rate. The resolution of the fast resistance temperature sensor is high (much better than 0.1 Kelvin) and about 30 Hz, which is fast enough to resolve turbulent temperature fluctuations (Bange and Roth, 1999). Hence, it is suited for small-scale turbulence measurements and for calculating the turbulent fluxes using the eddy co-variance method. The surface tempera-

Figure 2.5: Helipod measurement system

ture is measured by an infrared temperature sensor simultaneously with the thermodynamic measurements. At a mission speed of 40 m s^{-1} the Helipod is outside the down-wash area of the helicopter's rotor blades. More details can be found in Bange et al. (2002) and Bange and Roth (1999).

2.4.2 MASC

One of the tow used UAV in this thesis is the MASC. It is a small model aircraft, which is operated by the group of Environmental Physics at the University of Tübingen (Fig. 2.6). The wingspan is between 2.5 and 3 metres with a total weight of 5–7 kg, depending on the battery and payload. MASC is powered by an electrical pusher engine and is able to fly up to 90 min at a typical cruising speed of 25 m s^{-1} with full battery load.

The aircraft is controlled by the research on-board computer system (ROCS) autopilot, developed at the Institute for Flight Mechanics and Control Stuttgart which allows the aircraft to fly pre-defined flight paths at a controlled altitude and airspeed. Due to a very precise height control by the autopilot, typically with a precision of ± 2 m, MASC enables high precision wind and turbulence measurement. To perform measurements of thermodynamic scalars and turbulence, the system is equipped with a five-hole probe system, a fine-wire platinum resistance thermometer and a thermocouple for fast response temperature measurements, a capacitive humidity sensor, a barometric pressure transducer, and an inertial measurement unit with GPS receiver. The method to calculate the three-dimensional wind vector from the airflow vector and the inertial measurements of the UAS is presented in van den Kroonenberg et al. (2008). The wind and temperature measurements achieve a frequency resolution of 10–20 Hz (Wildmann et al., 2014b). Humidity measurements after post-processing are able to resolve turbulence up to 3 Hz (Wildmann et al., 2014a) .

MASC is equipped with the on-board data acquisition system called AMOC. It offers the possibility of data storage and real-time data transfer by a telemetry downlink during the flight of each data channels. The standard sensor system of MASC is extended with the aerosol sensor CLASP within the framework of this thesis. A detailed outlook is given in Sect. 5

Figure 2.6: Left panel: UAS of type MASC (Multi-Purpose Airborne Sensor Carrier) operated by University of Tübingen. Right panel: UAS of type ALADINA (Application of Light-weight Aircraft for Detecting In situ Aerosol) operated by the University of Braunschweig.

2.4.3 ALADINA

In the framework of the DFG funded project LA 2907/5-1, BA 1988/14-1, WI 1449/22-1, which was part of this PhD study, the new state of the art aerosol measuring device ALADINA was developed on the basis of the Carolo P360. It was equipped with a newly developed miniaturised meteorological and aerosol payload to measure the particle size distribution and particle number concentrations. The same meteorological payload and on-board computer were used as already implemented for the UAS of type MASC. More details can be found in Altstädter et al. (2015).

The automatically ALADINA, Fig. 2.6) belongs to the family of unmanned "Carolo P360" aircraft. It was developed at ILR Technical University of Braunschweig, and has a maximum take-off weight of 20 kg, with a wingspan of 3.6 m and a typical cruising speed of 25 m/s. ALADINA is able to carry 3 kg scientific payload.

In order to stay below the weight limit for the payload, commercially available instruments were chosen and modified with respect to space, weight and measurement properties Fig. 2.7. Two Condensation Particle Counters, CPCs, (model 3007, TSI Inc.) with different lower threshold diameters were implemented in ALADINA. With both CPCs we are able to measure the total particle number concentration of ultrafine particles N_{5-10} in the diameter range from 5 to 10 nm.

Further the measurement speed of the CPCs was improved, in order to investigate the connection between the aerosol particle concentration and atmospheric turbulence. Therefore the aerosol volume flow of the CPCs was increased from originally 0.1 l min^{-1} to 0.16 l min^{-1}. Thus, the response time of the new set-up is now surprisingly fast, with $<$1.3 s for the $t_{10\%-90\%}$ time.

Particles larger 0.3 µm are measured using a Met One Optical Particle Counter (OPC), model GT-526, Met One. This OPC counts particles in 6 size bins from 0.3 to 10.0 µm. The aerosol sensors are mounted in the sensor compartment of ALADINA (Fig. 2.7) in addition to the same meteorological sensor and on-board data acquisition as used in MASC (Section 2.4.2). Due to real-time data transfer it is possible to identify layers of enhanced aerosol concentration and temperature inversions during the flight at the ground station and to adapt the flight mission accordingly.

Figure 2.7: ALADINA payload: a) 1 five-hole probe, 2 temperature sensor (Thermocouple) and humidity sensor P14 Rapid, 3 aerosol inlet, 4 fast temperature sensor (Fine wire platinum resistance thermometer), 5 GPS antenna, 6 telemetry antenna; b) 7 first CPC 8 second CPC 9 OPC. Source: (Altstädter et al., 2015)

Chapter 3

Results

This section gives a brief overview and summary of the most important results which are described and explained in more detail in the attached peer-reviewed publications in Sect. 3.1 - 3.3.

3.1 Publication I - An observational case study on the influence of atmospheric boundary-layer dynamics on new particle formation

This study is about an experimental case study of a NPF connected to turbulence, which occurred during the morning transition of the atmospheric boundary layer (ABL) on 3 April 2014, in Melpitz, Eastern Germany. The event was characterised with high spatial resolution by unmanned aerial systems (UAS) and ground-based instruments. The observations represent, to the authors' knowledge, the first depiction of a NPF event with respect to the airborne characterisation of the morning transition from a shallow convective boundary layer below a strong capping inversion layer to a mixed boundary layer with high temporal and spatial resolution of thermodynamic fluctuations by second order statistics, and N_{5-10} particle number concentrations.

Eleven vertical profiles of number concentrations of ultrafine particles in the diameter range from 5 to 10 nm N_{5-10} spanning a 140 min time period could be analysed for the present study, thus demonstrating the complete time evolution of the NPF event and second order statistics of turbulent fluctuations, as opposed to only measuring during isolated periods as done in earlier studies like Wehner et al. (2010) , Wehner et al. (2007) and Siebert et al. (2007).

The airborne observations showed the start (at 0937 UTC) of a NPF event with enhanced concentrations N_{5-10} at around 500 m above ground within the inversion as displayed in Fig. 3.1. During the next half an hour number concentration of freshly nucleated particles increased 3.2 in this layer. Strong gradients of mean temperature ΔT and mixing ratio Δq as well as increased fluctuations of T and q were measured only in the inversion. Second order statistics show high values in the NPF layer. The temperature structure parameter C_T^2 was up to 15 times higher in the inversion layer compared to the remaining parts of the vertical profile while C_q^2 was up to 5 times higher in the inversion layer, indicating strong temperature and humidity fluctuations. Likewise, profiles of the standard deviation of temperature (σ_T) and humidity (σ_q) show comparably high values in the inversion layer. There are distinct hints that enhanced nucleation rates are connected with an anti-correlation

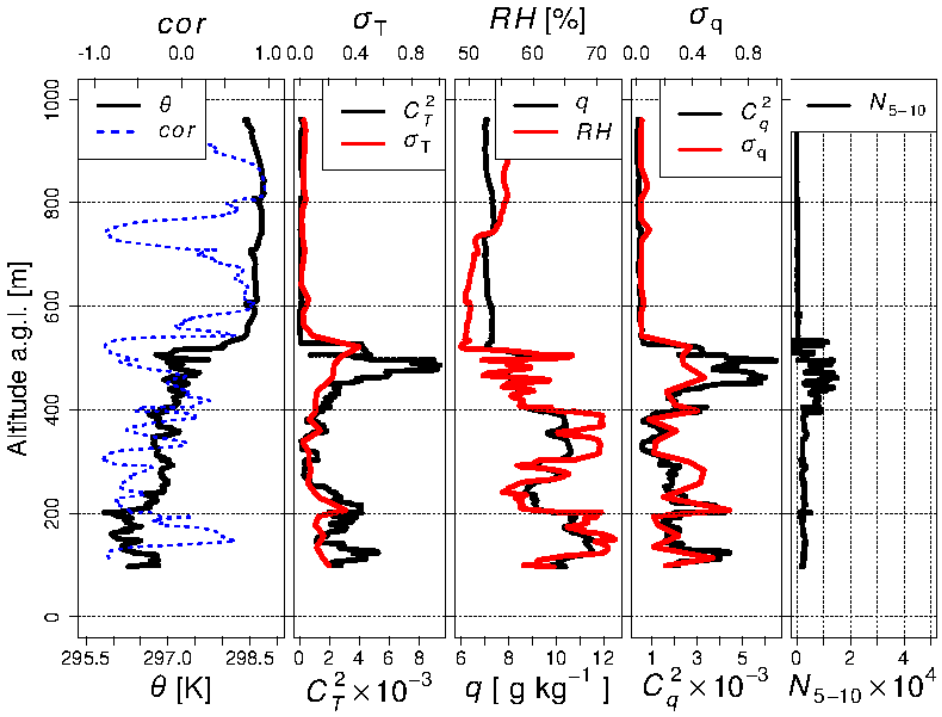

Figure 3.1: Vertical profiles of ALADINA flight at 0833 UTC on 3 April 2014. From left to right. **1**: Potential temperature θ (black). Blue dotted line shows the correlation coefficient (cor) between temperature and humidity **2**: C_T^2 (black) and temperature variance σ_T (red). Units are $[\mathrm{K^2\,m^{-2/3}}]$ for C_T^2 and [K] for σ_T. **3**: Mixing ratio q (black) and relative humidity RH (red). **4**: C_q^2 (black) and humidity variance σ_Q (red). Units are $[\mathrm{g^2kg^{-2}\,m^{-2/3}}]$ for C_T^2 and $[\mathrm{g\,kg^{-1}}]$ for σ_q. **5**: Difference of N_{5-10} between CPC1 - CPC2 = N_{5-10}. Number concentration of N_{5-10} is per $\mathrm{cm^3}$.

between humidity and temperature fluctuations as proposed by Easter and Peters (1994). NPF was observed in layers with strong anti-correlation between those two parameters.

The airborne in-situ observations suggest that turbulence plays an important role in NPF: High turbulent fluctuations of temperature and humidity create the conditions for supersaturation of precursor gases due to non-linear mixing (Nilsson et al., 2001; Bigg, 1997). The analysis supports the hypothesis that NPF was possibly initiated by the thermodynamics and turbulent fluctuations within the inversion layer, where high temperature and humidity fluctuations where observed as shown in Fig. 3.1 and 3.2. In addition observations show that the kinematic expression of the turbulence such as turbulent kinetic energy and dissipation rate ε did not play an important role in the formation of new particles since they were very low in this layer (see Fig. 3.3). The dissipation rate decreases with height due to the inversion and no local maximum of ε is detected. The stable stratified thermal inversion has a damping influence on the production of turbulent kinetic energy, which means decreasing dissipation due to the turbulent energy cascade (Caughey and Palmer, 1979).

Simultaneously to the airborne observations ground based measurements we performed in Melpitz. Particle measurements with a Neutral cluster and Air Ion Spectrometer (NAIS) at ground level showed a rapid simultaneous increase of N_{5-10} and the precursor gas SO_2 a few minutes after breakthrough of the shallow CBL, where the enhanced number concentrations of N_{5-10} were found.

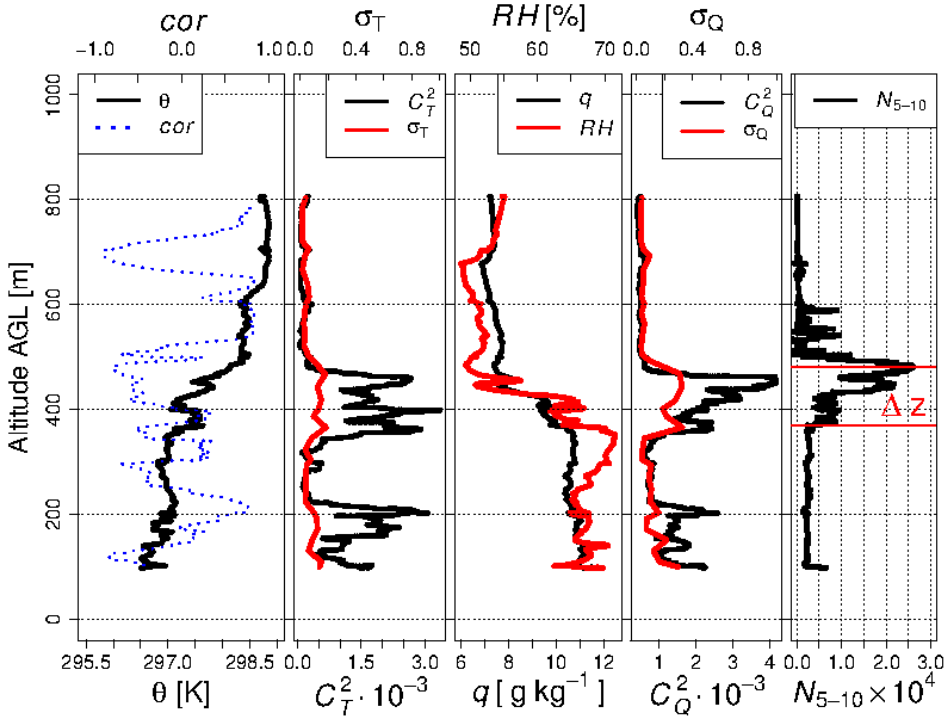

Figure 3.2: Vertical profiles of ALADINA flight at 0833 UTC on 3 April 2014. Explanation same as in Fig. 3.1

With regard to the estimation of turbulent mixing and dissipation rates, it is very likely that these particles observed at the ground were formed locally at higher altitudes and mixed downwards, similar to findings of Wehner et al. (2010). After breakthrough of the shallow CBL, NPF was detected near the ground, as essential precursor gases for NPF like SO_2 were mixed downward from the inversion. No vertical measurements of potential precursor gases are available for the campaign. Moreover, with the breakthrough of the shallow CBL, the sink for condensing material is reduced as a result of vertical mixing with air from aloft. This air contains less Aitken mode particles and therefore can foster the formation of new particles and subsequent growth. It is worth noting that model simulations of particle formation in a convective boundary layer tend to predict the highest likelihood for nucleation near the top of the mixed layer (entrainment zone), mainly for thermodynamic reasons (e.g. Hellmuth, 2006).

These results might have consequences for the interpretation of earlier published observations of NPF events particularly such observations, where data was recorded only at ground level. In the morning, stable thermal stratification may trap enhanced concentrations of nucleation mode particles at higher altitudes. Once daytime convection initiates, turbulence mixes the boundary layer, and the vertical profile of nucleation mode particles becomes more homogeneous. The ground-based observations without the airborne in-situ measurements may result in a misinterpretation or inexplicability of location and processes causing the increase in nucleation mode particles. We assume that the inversion layer is responsible for creating favourable thermodynamic conditions with enhanced temperature and humidity fluctuation for a NPF event. Similar spatial/temporal dynamic of the ABL in combination with NPF could be confirmed in a recent study by Hovorka et al. (2016).

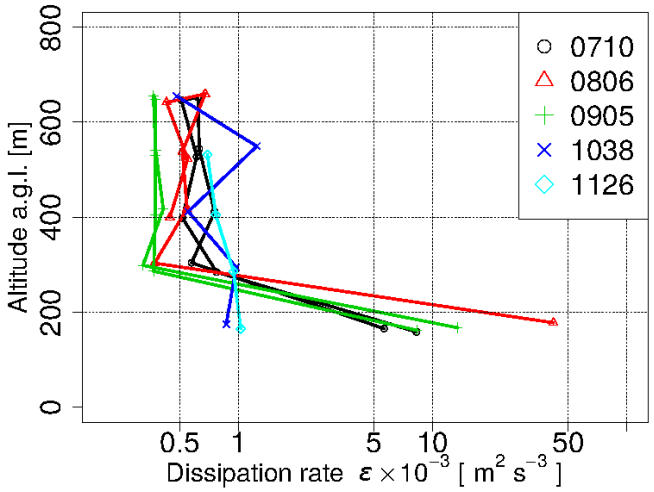

Figure 3.3: Logarithmic plot of energy dissipation rates ε versus height during morning transition for all 5 MASC flights between 0710 and 1126 UTC. The first three flights (green, red and black) consist each of an ascent and descent, the last two (blue and turquoise) only of an ascent.

3.2 Publication II - Analysis of the influence of a lake on the lower convective boundary layer from airborne observations

With regard to turbulence as an important factor for NPF the influence of natural heterogeneous landscapes on the ABL and its turbulent flow is investigated. The influence of an intermediate-scale lake on airborne measurements taken below 100 m has been analysed for 34 flight legs flown during two consecutive field campaigns in the summer of 2002 and 2003. The spatial variability for mean quantities is not very significant. Although there are some hints that our analysed data indicate a cooling over the lake at 100 m above ground and that we can distinguish between a drier atmosphere over the lake compared to the more moister air over forest. The second order moment related to potential temperature (σ_θ) exhibit a clear decrease in the vicinity of the lake for the lowest flight leg at 70-80 m above ground level (see Figure 3.5). Most likely, the lack of thermals above a cool surface favours such a drop for theses parameters and their random variability. Second-order moments of humidity and vertical wind, however, are not suited to identify the underlying lake, at least in our study. At higher elevated flight legs (170 m and 280 m) the influence of the lake was not detectable by our airborne observations. However, the lack of iterative passes of one flight during same environmental conditions reduces the statistical significance, due to a sampling error in the same order as the measurement value. Only one flight of the selected dataset, which contained consecutive passes along the same leg and hence a low sampling error, showed that the observed variances of σ_θ are reduced significantly over the lake. These results allow us to consider the drops of σ_θ produced at the vicinity of the lake as qualitative indicators of the lake influence to the atmosphere at the observed level, even though with just single passes.

Several length scales of surface heterogeneity were calculated, following previous studies of Mahrt (2000) and Bange et al. (2006). These scales consider different parameters

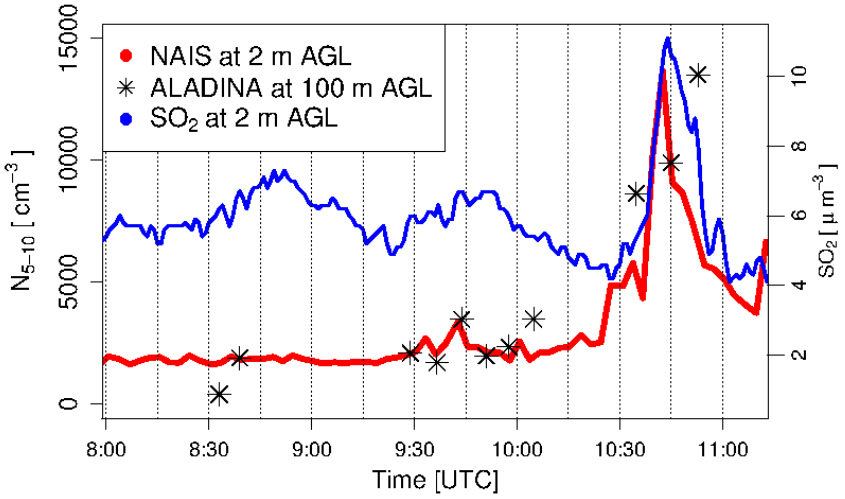

Figure 3.4: Upper plot shows the evolution of integrated particle number concentrations for $N_{5-10}\,\mathrm{cm}^{-3}$ with a 3 min average measured by NAIS (red) at 2 m a.g.l. in Melpitz on 3 April 2014 between 0800 UTC and 1130 UTC. Black stars indicate the number concentrations for $N_{5-10}\,\mathrm{cm}^{-3}$ measured by ALADINA. The ALADINA number concentrations measurement is a 10 s average during the ascent or descent of a vertical profile around 100 m a.g.l. . SO_2 (blue) measured by a gas concentration unit.

depending on the stability conditions of the flow. Only the scale that considers the variance of vertical velocity or a velocity scale was compatible with our observations. Probably the variety of buoyancy conditions in our dataset (which includes days with a weak surface heat flux and strong winds together with days with strong convection) requires a stability parameter able to describe the vertical mixing induced by both wind shear and thermal heating in order to fit to all conditions during our flight experiment. In addition, the application of a convective scale for those cases where the boundary-layer depth was known, indicates that the 2 km wide lake could affect the lower CBL for wind speeds below 4 m s^{-1}. Unfortunately, the lack of iterative passes at higher altitudes precludes the capacity to confirm these results in the current work.

Finally, the downstream propagation of the lake influence has been addressed by calculating the cross-correlation function between the surface radiative temperature and the variance of potential temperature for the entire leg. Although a clear relationship between the spatial lag of the maximum correlation and the horizontal advective speed could only be identified for 8 out of 32 cases, this relation indicates promising results when it is applied solely to the lake influence.

3.3 Publication III - Observations of the temperature and humidity structure parameter over heterogeneous terrain by airborne measurements during the LITFASS 2003 campaign

The turbulent structure parameters for temperature C_T^2 and humidity C_Q^2 and their cross-structure parameter C_{QT} were investigated by using Helipod flight data collected in the CBL. The data used in this study is a part of the same data set as used in the previous study (Section

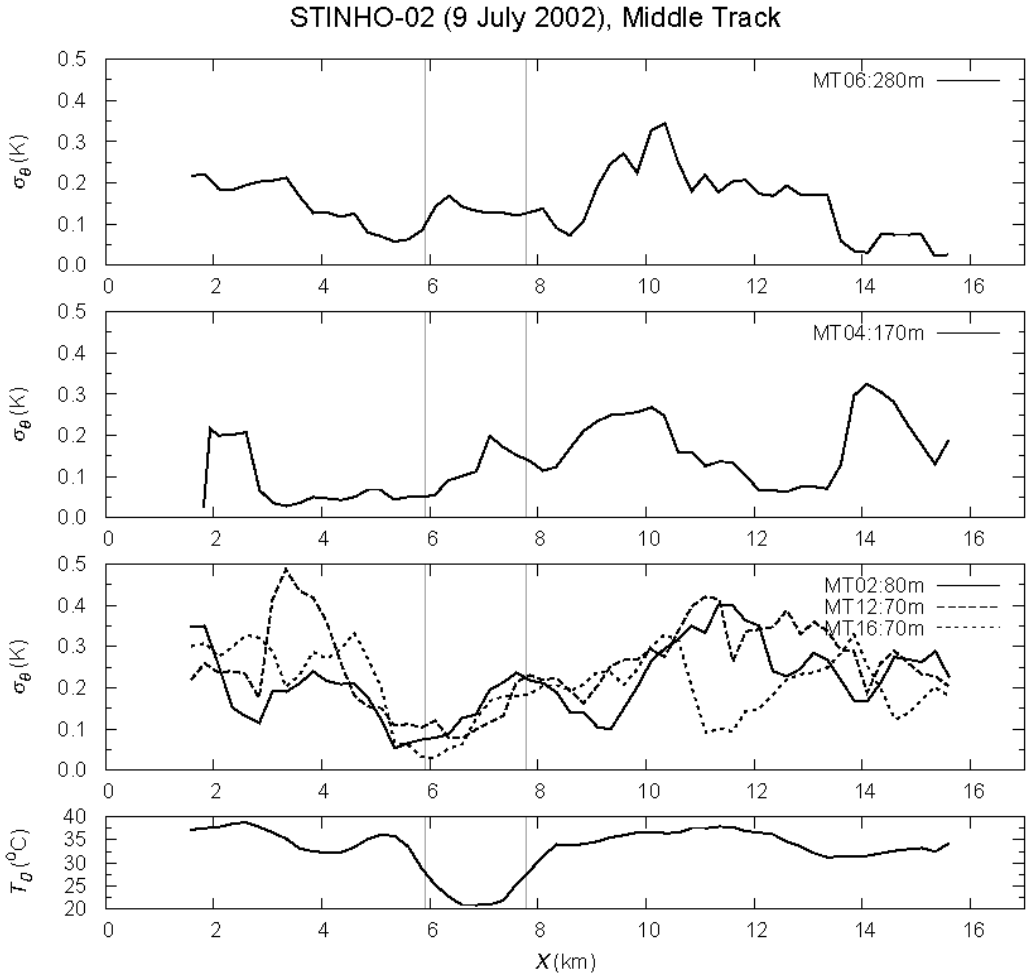

Figure 3.5: Standard deviation of potential temperature for each middle track (MT) leg at 280 m (MT06), at 170 m (MT04) and below 100 m (MT02, MT12, MT16) of STI09 flight. Data are computed for a window of 1 km width, sequentially marched through the leg by increments of 250 m. Lower panel shows the corresponding distribution of the surface temperature measured during the flight leg (MT02). Wind direction is from the south-east. That means wind is blowing parallel to the flight direction (from the right side to the left side in the panel). Average wind speed is between 5.5 and 7.1 m s^{-1}.

3.2). The LITFASS-2003 campaign measured these parameters on flights of up to 20 km length over heterogeneous terrain and close to the ground. This is normally not feasible with a common manned aircraft or unmanned air vehicles due to restrictions on legal permissions. The close-to-ground flights obtained data in CBL surface layer over heterogeneous surfaces of different types including forest, lakes and farmland. Two types of flight pattern were used to observe the behaviour of the structure parameter over heterogeneous surface.

The homogeneous Flights (HOM) were used to calculate the structure parameter over the entire flight leg, in order to derive a structure parameter value characterising one surface type. This method allows a classification of all three structure parameters for each surface type. In order to compute spatially resolved series of the structure parameter, heterogeneous (HET) Flights were analysed with a track over a mixed surface and including different

surface types.

According to the method of van den Kroonenberg et al. (2012), the spatial series of C_Q^2, C_T^2 and C_{QT} were obtained from calculating $D_Q(r)$, $D_T(r)$ and $D_{QT}(r)$ within a moving window with length $W = 600$ m. This window was defined for each data point i of the humidity (temperature) spatial series, with i as the centre point. By moving this window, the local structure parameters, $C_Q^2(i)$, $C_T^2(i)$ and $C_{QT}(i)$ were calculated. The resulting resolution by moving the window is a structure parameter every 0.4 m (equivalent to a 100 Hz sampling rate at 40 m s^{-1} typical ground speed), which were calculated from humidity and temperature data over the distance W.

Braam et al. (2013) noted that variability of structure parameter due to surface heterogeneity has to be constant in time in contrast to the local variability. Thus, the variability with time was reduced by averaging the spatial series of the dimension-less structure parameter A_Q, A_T and A_{QT} over all flights.

Variability of C_T^2 along the flight legs was detected (see Fig. 3.6) by using both flight strategies, and was explained by the strong surface fluxes variability caused by the different types of surface vegetation.

There is a strong indication that C_T^2 measured at about 100 m above ground is influenced by surface heterogeneity even for smaller surface length scales around 2 km, although C_T^2 variability is also attributed to random turbulence. We could classify C_T^2 according to each surface type. The highest values of C_T^2 were found over forest patches. Lower values were found over the lake and moderate values over farmland. Hence, C_T^2 measured at about 100 m above ground is associated with surface heterogeneity and confirms findings from van den Kroonenberg et al. (2012). In general, values over forest were one order larger than over farmland and two orders larger than over the lake.

To our knowledge this is the first study investigating a variability of C_{QT} and C_Q^2 over heterogeneous terrain experimentally. The C_Q^2 and C_{QT} behave very similar, but exhibit a more complex behaviour than C_T^2. Our data suggest that C_Q^2 is decoupled from the surface flux even at low levels which is ascribed to the entrainment of dry air at the top of the boundary, except for the sharp water-land discontinuity. A significant difference between C_Q^2 over lake and land is calculated (by the Welch's Test) with a 99% significance level, despite the high fluctuation in C_Q^2. A 50% lower mean C_Q^2 is observed over the lake. It is possible that this sharp change in surface sensible heat fluxes from positive to negative values over the lake might have caused the reduced values of C_Q^2 at around 100 m height during convective conditions, despite the strong and dominant effect by entrainment.

However, a disparity is observed between HOM and HET flights for C_Q^2. HOM and HET flights show a clear footprint of the lake in C_T^2, but only HET flights show the lake footprint in C_Q^2. As supported by many other studies (e.g. Roth and Oke, 1995; Sempreviva and Højstrup, 1998; Albertson and Parlange, 1999) there is a different behaviour of the passive scalar (water vapour) compared to the active (temperature). Over heterogeneous landscape, water vapour flux and sensible heat flux have different source regions (Kustas and Albertson, 2003). Bertoldi et al. (2013) could show by LES and aircraft observation that the footprint of water vapour has a larger distance from the flight track than sensible heat. Hence, C_T^2 at aircraft altitude appears to be in phase with the surface, whereas the footprint of C_Q^2 at the observation height is no longer over the lake, but over the surrounding land which is further away.

Since the Helipod proved the reliability to measure C_T^2, C_{QT} and C_Q^2, we were able to calculate temperature-humidity correlation coefficient R_{QT}. It is often assumed that temperature and humidity fluctuations are perfectly correlated (either positive or negative) which

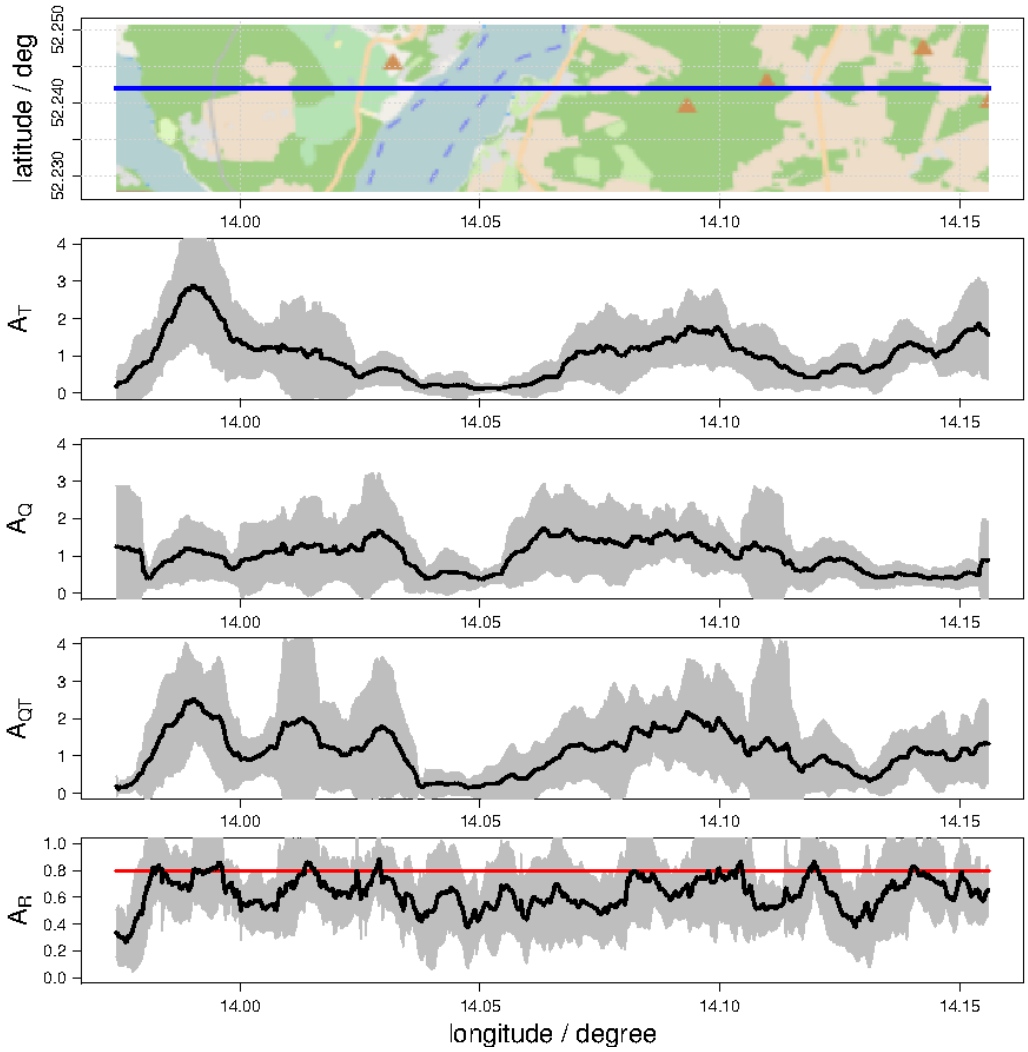

Figure 3.6: Spatial Series averaged over 8 flights for leg WE08. At the top the map is plotted with the flight track (blue line) for one of the 8 flights. The coordinates of all other flight tracks differ only marginally. Below is the averaged normalised spatial series A_T , A_Q, A_{QT}, of the structure parameters and A_R. The grey area represents the standard deviation of the averaged normalised structure parameter for each data point i. Bottom plot: The black line shows the average of temperature-humidity correlation coefficient R_{QT} over 8 flights. The red line shows $R_{QT} = 0.8$ as proposed by Fairall et al. (1980).

implies that $R_{QT} = \pm 1$ (e.g. Andreas, 1989; Hill, 1997; Meijninger et al., 2002; Beyrich et al., 2005). In fact, this assumption is theoretically demanded for a flow that strictly obeys Monin-Obukhov similarity theory (MOST) (Hill, 1989), implying that MOST is valid for C_T^2 and C_Q^2. R_{QT} was in the range between 0.4 and 1.0 along the flight track over heterogeneous terrain similar to findings from Beyrich et al. (2005); Fairall et al. (1980). Combining all flights, R_{QT} was in average approximately 0.7. Assigning the R_{QT} variability to underlying surface types was not possible, however there was indication that values with the underlying lake were lower. The results show R_{QT} is less than unity for most of our measurements, in contrast to the assumption of unity in Monin-Obukhov similarity theory, but violation of MOST is small as long as $R_{QT} > 0.7$ (Meijninger et al., 2006). These observations agree

well with LES studies from Li et al. (2012); Maronga (2014). A dissimilarity between the transport of heat and moisture ($R_{QT} \neq 1$) is caused by significant entrainment, because C_Q^2 does not follow MOST any more.

Chapter 4

Discussion

Within this thesis, research on the NPF in the ABL and its turbulent flow with regard to the heterogeneous surface influence has been described. The presented studies demonstrate the benefit of the tool of airborne in-situ measurements and the analysis of second order moments to describe turbulent processes and the behaviour of the ABL dynamics.

A turbulent layer in the ABL responsible for triggering a NPF event could be recognised by the use of second order moments. These moments, such as the structure parameter and variances were able to identify this layer with high temperature and humidity fluctuations. These turbulent fluctuations are assumed to create favourable thermodynamic conditions for a NPF event, whereas observations show that the kinematic expression of the turbulence such as the dissipation rate ε and the turbulent kinetic energy has only a minor role. These results make turbulent fluctuations of temperature and humidity an important ingredient for NPF. The event was measured over a fairly homogeneous surface which yielded ideal conditions for the understanding of turbulent processes and its influence on NPF. However, natural landscapes rarely provide horizontal homogeneous conditions and have to be considered to be heterogeneous. Thus, the influence of the surface heterogeneity on temperature and humidity fluctuations was investigated in two further studies. The second order moment of temperature (here used as the structure parameter C_T^2 as an indication for high temperature fluctuation) is an adequate and suitable instrument to describe the underlying surface. Variability of C_T^2 along the flight legs at about 80 m above the ground over heterogeneous surface was detected and could be explained by the strong surface fluxes variability caused by the different types of surface vegetation. Especially over a lake the surface influence on the ABL is apparent. The second order moment related to potential temperature (σ_θ) exhibit a clear decrease in the vicinity of the lake. In contrast, first order moment do not detect a significant signal of the underlying surface. As a result second order moments enable to observe a signal of a lake foot print in the ABL at least for the lowest flight legs at around 80 m above the ground. However, not all second-order moments exhibit a signal of the lake foot print. Second order moments of humidity (C_Q^2, σ_m) and kinematic turbulence expression (e.g. vertical wind), are not suited to identify the underlying lake by airborne measurements, at least in our study.

Naturally, as shown by the studies, the airborne in-situ measurements however have their limitations. The length of flight legs must be sufficiently long to be able to include all contributing eddies in order to obtain accurate second order moments measurements. Model simulations of the boundary layer like LES (Maronga et al., 2014; Sühring and Raasch, 2013) suggest that measured turbulent quantities require sufficient temporal averaging and an adequate ratio of path length in order to decrease the statistical uncertainty due to ran-

domly distributed convection. Consequently, when performing measurement flights, many iterative flight passes are necessary in order to obtain sufficient statistics and thus a low measurement error. This, however, was not always feasible when flying with the Helipod, due to its limited flight time because of expensive operational costs when dealing with this airborne platform. More favourable regarding operational costs were the UAS. The costs are much lower, but compared to the manned aircraft (such as Helipod) the length of UAS flight legs is very limited due to CAA laws. Flights out of sight of a safety pilot are not allowed at the moment, at least in Germany and the U.S, which restricts the flight leg to 1-2 kilometres distance. This length was not always sufficient long to include all contributing eddies in the studies, causing a relatively high systematic statistical uncertainty in the second order statistics (Mann and Lenschow, 1994; Lenschow et al., 1994). This uncertainty can be only reduced by averaging over all the passes for a given flight for each window which requires even more iterative passes along the same leg.

In the future a further development of the UAS's autopilot control system is necessary to fulfill requirements by the CAA in order to perform flights out of sight of safety aircraft pilots. Furthermore, improvement of flight duration by long endurance batteries is necessary to achieve a continuous operation of UAS. At the moment, with the common UAS such as MASC or ALADINA one measurement flight duration is in the order of 30-60 minutes. The turn over time between landing and the next take-off is approximately 30 minutes, resulting in observation gaps. Moreover flight operation with UAS and Helipod are restricted to the time between sunrise and sunset, at least in Europe and in the USA. However, observations of boundary-layer phenomena like low level jets occur usually only at night time.

Nevertheless there are many advantages that justify airborne observations. Only in-situ measurements are a direct observation of the atmosphere, rather than a model simulation obtained during different atmospheric conditions, representing a single ideal case and situation. Further, remote sensing instruments are often limited by their time and spatial resolution, therefore not allowing dissolving turbulence. As shown elaborately in Sect. 3.1, it might be necessary to have airborne observations in order not to misinterpret location and processes. Airborne in-situ measurements down to a few metres above ground are possible with UAS. In remote areas, UAS are a flexible measurement tool, requiring only small infrastructure. UAS can provide additional meteorological data, especially over regions which are potentially dangerous or have restricted airspace, such as volcanoes, nuclear power plants or chemical factories. The costs of operating a UAS is relatively low, which enables small research groups to also use these systems.

Another possibility to enhance the measurements from UAS is to operate multiple aircraft simultaneously. Two independent MASC, as well as MASC in combination with other UAS, have already been deployed in experiments (Platis et al., 2016a). A further technical possibility is a coordinated swarm flight of multiple UAV, this has yet to be implemented for the autopilot of the UAS. Airborne observations at multiple altitudes and locations allow measurements of instantaneous vertical profiles or fluxes and extends the limited measurements in space and time, which achieves more statistically significant results.

Chapter 5

Future Perspectives

In the future a further improvement of the aerosol in situ measurement system is planned. With ALADINA a state of the art aerosol measurement device is now available in combination with a high resolution meteorological turbulence measurement system (Sect. 2.4.2). ALADINA proofed the reliability to be able to measure ultrafine particles in the atmospheric boundary layer. However, the time resolution of the ALADINA on-board aerosol measurement system (1 Hz) compared to the high frequent meteorological measurements (10-30 Hz) is still very low. In addition ALADINA is a very large and heavy UAS in the 25 kg weight range compared to the light aircraft MASC. Thus, MASC is equipped with a newly developed aerosol on-board instrumentation, which enables aerosol research with very light UAS and high frequency aerosol measurements in order to measure aerosol fluxes. Since MASC is a light but also a much smaller and lighter aircraft compared to ALADINA a miniaturised optical particle counter has to be implemented. Currently, MASC is equipped therefore with an aerosol sensor called CLASP in addition to the thermodynamic-turbulence sensor unit. CLASP is an very small an high frequent optical particle counter (OPC) and was developed by the University of Leeds. Norris et al. (2012) and Hill et al. (2008) successfully applied the OPC, called Compact Lightweight Aerosol Spectrometer Probe (CLASP), in two studies over the Atlantic ocean and were even able to calculated turbulent aerosol fluxes.

CLASP enables measurements of particle concentrations with a sampling frequency of 10 Hz. The advantage of CLASP is its robust, compact and lightweight construction that enabled integration into a very light and small UAS such as MASC (Fig. 5.1). This sensor is able to measure aerosol concentrations in 16 user-defined channels for particles with diameters in the range from 0.24 to 18.5 µ m at a sampling frequency of 10 Hz. First test flights were performed as part of the field experiment MelCol.

The MASC including CLASP is now able to measure aerosol concentrations and even aerosol fluxes. The general shape of the aerosol size spectra measured with CLASP is comparable to spectra that are shown in literature (for example Sproson et al. (2013)). However, no quantitative investigation is possible at the moment. During a preliminary campaign, measurement inaccuracies between a twin scanning mobility particle sizer (TSMPS) at the ground and close to ground flights with the airborne CLASP was found. The comparison to the TSMPS data showed large differences to both sensor systems. The concentration of the TSMPS was in the order of one or two magnitudes higher than the measured concentration with CLASP. More flights and further investigations are necessary to analyse the characteristics of CLASP and will be done in the nearest future.

Besides ultrafine particles and their growth to CCN, also other aerosol particles may serve as CCN. Prior studies suggest that primary biological material such as pollen could

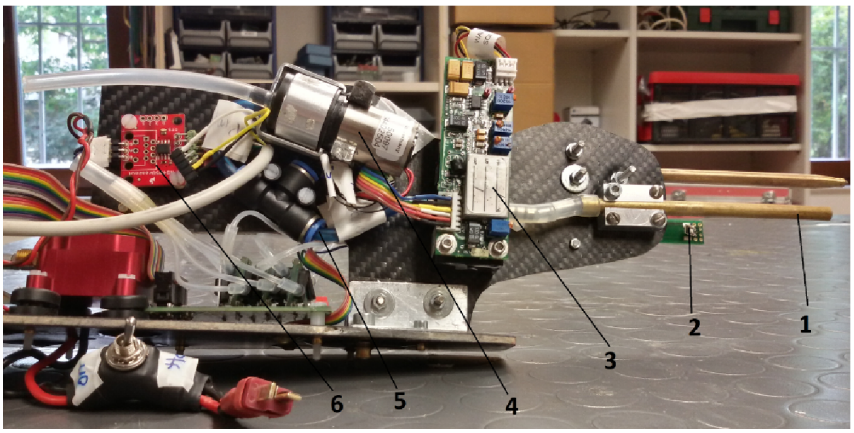

Figure 5.1: CLASP mounted on the MASC sensor board. CLASP's inlet tube (1), humidity sensor mounted on circuit board (2), scatter cell (3), pump (4), CLASP's flow sensor (5) and RS485-UART converter chip (6).

alter cloud properties (Sun and Ariya, 2006; Pope, 2010), and high ambient concentrations of biological particles are linked to rainfall events (Huffman et al., 2013). Laboratory measurements indicate that whole pollen grains have the ability to act as CCN (Pope, 2010) and ice nuclei (Von Blohn et al., 2005) Pollen are released from terrestrial vegetation in large quantities to transmit the male genetic material for reproduction. Aerobiology studies indicate that pollen with sizes ranging from 20 to 45 µ m (Linder, 2000) can be transported up to 100- 1000 km (Schueler and Schlünzen, 2006) and have been observed both in the atmospheric boundary layer and free troposphere (Noh et al., 2013). Consequently it is indispensable to study the type of aerosol particle as well. Furthermore pollen dispersion plays an important role for example in the allergy/hay fever forecast, the distribution of trangenic germination, infection of crops by fungus spores, etc. However, pollen a much larger than the typical measurement range of optical particle counters such as operated in ALADINA or CLASP. Therefore a new technique is developed at the at the University of Tübingen to further improve aerosol research. Particles are sampled with special pollen filters and a specially developed pollen trap on board a multi copter. After the measurement flight, these samples will then be analysed with a newly developed flow cam, which works automatically. This flow cam is able to detect the type of pollen and estimate the number concentration of pollen per volume. Thus, an automatically working accurate estimate can be achieved not only of the number concentration and size distribution, but also an exact type and classification of pollen .

Bibliography

Albertson JD, Parlange MB (1999) Natural integration of scalar fluxes from complex terrain. Advances in Water Resources 23(3):239–252

Altstädter B, Lampert A, Scholtz A, Bange J, Platis A, Hermann M, Wehner B (2013) Aerosol variability observed with rpas. ISPRS-International Archives of the Photogrammetry, Remote Sensing and Spatial Information Sciences 1(2):1–4

Altstädter B, Platis A, Wehner B, Scholtz A, Wildmann N, Hermann M, Käthner R, Baars H, Bange J, Lampert A (2015) Aladina–an unmanned research aircraft for observing vertical and horizontal distributions of ultrafine particles within the atmospheric boundary layer. Atmospheric Measurement Techniques 8(4):1627–1639

Andreae M, Rosenfeld D (2008) Aerosol–cloud–precipitation interactions. part 1. the nature and sources of cloud-active aerosols. Earth-Science Reviews 89(1):13–41

Andreas EL (1989) Two-wavelength method of measuring path-averaged turbulent surface heat fluxes. Journal of Atmospheric and Oceanic Technology 6(2):280–292

Ayers G, Cainey J, Gillett R, Ivey J (1997) Atmospheric sulphur and cloud condensation nuclei in marine air in the southern hemisphere. Philosophical Transactions of the Royal Society of London B: Biological Sciences 352(1350):203–211

Bange J, Roth R (1999) Helicopter-borne flux measurements in the nocturnal boundary layer over land - a case study. Boundary-Layer Meteorol 92:295–325

Bange J, Beyrich F, Engelbart DAM (2002) Airborne measurements of turbulent fluxes during LITFASS-98: A case study about method and significance. Theor Appl Climatol 73:35–51

Bange J, Spieß T, Herold M, Beyrich F, Hennemuth B (2006) Turbulent fluxes from helipod flights above quasi-homogeneous patches within the LITFASS area. Bound-Layer Meteor

Bates T, Quinn P, Johnson J, Corless A, Brechtel F, Stalin S, Meinig C, Burkhart J (2013) Measurements of atmospheric aerosol vertical distributions above svalbard, norway using unmanned aerial systems (uas). Atmospheric Measurement Techniques Discussions 6(2):2483–2499

Bertoldi G, Kustas WP, Albertson JD (2013) Evaluating source area contributions from aircraft flux measurements over heterogeneous land using large-eddy simulation. Boundary-layer meteorology 147(2):261–279

Beyrich F, Kouznetsov RD, Leps JP, Lüdi A, Meijninger WM, Weisensee U (2005) Structure parameters for temperature and humidity from simultaneous eddy-covariance and scintillometer measurements. Meteorologische Zeitschrift 14(5):641–649

Beyrich F, Bange J, Hartogensis OK, Raasch S, Braam M, van Dinther D, Gräf D, van Kesteren B, van den Kroonenberg AC, Maronga B, et al. (2012) Towards a validation of scintillometer measurements: the litfass-2009 experiment. Boundary-layer meteorology 144(1):83–112

Bigg E (1997) A mechanism for the formation of new particles in the atmosphere. Atmos Res 43(2):129–137

Braam M, Moene AF, Beyrich F (2013) Variability of the structure parameters of temperature and humidity observed in the atmospheric surface layer under unstable conditions. Boundary-Layer Meteorology pp 1–24

Caughey S, Palmer S (1979) Some aspects of turbulence structure through the depth of the convective boundary layer. Q J R Meteorol Soc 105(446):811–827

Charlson RJ, Schwartz S, et al. (1992) Climate forcing by anthropogenic aerosols. Science 255(5043):423

Crawford TL, Dobosy RJ, Dumas EJ (1996) Aircraft wind measurement considering lift-induced upwash. Bound-Layer Meteor 80:79–94

Davidson PA (2004) Turbulence: an introduction for scientists and engineers, 235 pp. Oxford University Press

Després VR, Huffman JA, Burrows SM, Hoose C, Safatov AS, Buryak G, Fröhlich-Nowoisky J, Elbert W, Andreae MO, Pöschl U, et al. (2012) Primary biological aerosol particles in the atmosphere: a review. Tellus B 64

Easter RC, Peters LK (1994) Binary homogeneous nucleation: Temperature and relative humidity fluctuations, nonlinearity, and aspects of new particle production in the atmosphere. J Appl Meteorol 33(7):775–784

Fairall C, Schacher G, Davidson K (1980) Measurements of the humidity structure function parameters, c q 2and c tq, over the ocean. Boundary-Layer Meteorology 19(1):81–92

Garratt JR (1994) Review: the atmospheric boundary layer. Earth-Science Reviews 37(1-2):89–134

Größ J, Birmili W, Hamed A, Sonntag A, Wiedensohler A, Spindler G, Maninnen HE, Nieminen T, Kulmala M, Hõrrak U, Plass-Dülmer C (2015) Evolution of gaseous precursors and meteorological parameters during new particle formation events in the central european boundary layer. Atmos Chem Phys Discuss 15(2):2305–2353, DOI 10.5194/acpd-15-2305-2015, URL `http://www.atmos-chem-phys-discuss.net/15/2305/2015/`

Hansen J, Sato M, Lacis A, Ruedy R (1997) The missing climate forcing. Philosophical Transactions of the Royal Society of London B: Biological Sciences 352(1350):231–240

Hellmuth O (2006) Columnar modelling of nucleation burst evolution in the convective boundary layer–first results from a feasibility study Part I: Modelling approach. Atmos Chem Phys 6(12):4175–4214

Hill MK, Brooks BJ, Norris SJ, Smith MH, Brooks IM, De Leeuw G (2008) A compact lightweight aerosol spectrometer probe (clasp). Journal of Atmospheric and Oceanic Technology 25(11):1996–2006

Hill RJ (1989) Implications of monin-obukhov similarity theory for scalar quantities. Journal of the Atmospheric Sciences 46(14):2236–2244

Hill RJ (1997) Algorithms for obtaining atmospheric surface-layer fluxes from scintillation measurements. J Atmos Oceanic Technol 14:456–467

Højstrup J (1982) Velocity spectra in the unstable planetary boundary layer. J Atmos Sci 39:2239–2248

Hoppel W, Frick G, Fitzgerald J, Larson R (1994) Marine boundary layer measurements of new particle formation and the effects nonprecipitating clouds have on aerosol size distribution. Journal of Geophysical Research: Atmospheres 99(D7):14,443–14,459

Hovorka J, Leoni C, Dočekalová V, Ondráček J, Zíková N (2016) Aerosol distribution in the planetary boundary layer aloft a residential area. In: IOP Conference Series: Earth and Environmental Science, IOP Publishing, vol 44, p 052017

Huffman JA, Prenni A, DeMott P, Pöhlker C, Mason R, Robinson N, Fröhlich-Nowoisky J, Tobo Y, Després V, Garcia E, et al. (2013) High concentrations of biological aerosol particles and ice nuclei during and after rain. Atmos Chem Phys 13(13):6151–6164

Jacob DJ, Crawford J, Maring H, Clarke A, Dibb JE, Emmons L, Ferrare R, Hostetler C, Russell P, Singh H, et al. (2010) The arctic research of the composition of the troposphere from aircraft and satellites (arctas) mission: design, execution, and first results. Atmospheric Chemistry and Physics 10(11):5191–5212

Kerminen VM, Lihavainen H, Komppula M, Viisanen Y, Kulmala M (2005) Direct observational evidence linking atmospheric aerosol formation and cloud droplet activation. Geophysical research letters 32(14)

Kohsiek W, Meijninger W, Moene A, Heusinkveld B, Hartogensis O, Hillen W, De Bruin H (2002) An extra large aperture scintillometer for long range applications. Boundary-layer meteorology 105(1):119–127

Kolmogorov A (1941) Local structure of turbulence in an incompressible fluid for very large Reynolds numbers. Dokl Akad Nauk SSSR 30:299–303

van den Kroonenberg A, Martin S, Beyrich F, Bange J (2012) Spatially-averaged temperature structure parameter over a heterogeneous surface measured by an unmanned aerial vehicle. Boundary-Layer Meteorol 142(1):55–77

van den Kroonenberg AC, Martin T, Buschmann M, Bange J, Vörsmann P (2008) Measuring the wind vector using the autonomous mini aerial vehicle m^2av. J Atmos Oceanic Technol 25(11):1969–1982

Kustas WP, Albertson JD (2003) Effects of surface temperature contrast on land-atmosphere exchange: A case study from monsoon 90. Water Resources Research 39(6)

Lenschow D, Mann J, Kristensen L (1994) How long is long enough when measuring fluxes and other turbulence statistics? Journal of Atmospheric and Oceanic Technology 11(3):661–673

Letzel MO, Raasch S (2003) Large eddy simulation of thermally induced oscillations in the convective boundary layer. Journal of the atmospheric sciences 60(18):2328–2341

Li D, Bou-Zeid E, De Bruin HA (2012) Monin–obukhov similarity functions for the structure parameters of temperature and humidity. Boundary-layer meteorology 145(1):45–67

Linder H (2000) Pollen morphology and wind pollination in angiosperms. Pollen and Spores: Morphology and Biology pp 73–88

Lohmann U, Feichter J (2005) Global indirect aerosol effects: a review. Atmospheric Chemistry and Physics 5(3):715–737

Mahrt L (1996) The bulk aerodynamic formulation over heterogeneous surfaces. Bound-Layer Meteor 78:87–119

Mahrt L (2000) Surface heterogeneity and vertical structure of the boundary layer. Bound-Layer Meteor 96:33–62

Mann J, Lenschow DH (1994) Errors in airborne flux measurements. Journal of Geophysical Research: Atmospheres (1984–2012) 99(D7):14,519–14,526

Maronga B (2014) Monin–obukhov similarity functions for the structure parameters of temperature and humidity in the unstable surface layer: Results from high-resolution large-eddy simulations. Journal of the Atmospheric Sciences 71(2):716–733

Maronga B, Hartogensis OK, Raasch S, Beyrich F (2014) The effect of surface heterogeneity on the structure parameters of temperature and specific humidity: a large-eddy simulation case study for the litfass-2003 experiment. Boundary-Layer Meteorology 153(3):441–470

McFarquhar GM, Ghan S, Verlinde J, Korolev A, Strapp JW, Schmid B, Tomlinson JM, Wolde M, Brooks SD, Cziczo D, et al. (2011) Indirect and semi-direct aerosol campaign: The impact of arctic aerosols on clouds. Bulletin of the American Meteorological Society 92(2):183

Meijninger WML, Hartogensis OK, Kohsiek W, Hoedjes JCB, Zuurbier RM, de Bruin HAR (2002) Determination of area-averaged sensible heat fluxes with a large aperture scintillometer over a heterogeneous surface – Flevoland field experiment. Bound-Layer Meteor 105:37–62

Meijninger WML, Beyrich F, Lüdi A, Kohsiek W, de Bruin HAR (2006) Scintillometer-based turbulent fluxes of sensible and latent heat over a heterogeneous land surface – a contribution to LITFASS-2003. Bound-Layer Meteor 121:89–110

Myhre G, Myhre C, Samset B, Storelvmo T (2013) Aerosols and their relation to global climate and climate sensitivity. Nature Education Knowledge 4(7)

Nilsson E, Rannik Ü, Kulmala M, Buzorius G, O'dowd C (2001) Effects of continental boundary layer evolution, convection, turbulence and entrainment, on aerosol formation. Tellus B 53(4):441–461

Nilsson ED, Kulmala M (1998) The potential for atmospheric mixing processes to enhance the binary nucleation rate. J Geophys Res Atmos 103(D1):1381–1389

Noh Y, Lee H, Mueller D, Lee K, Shin D, Shin S, Choi T, Choi Y, Kim K (2013) Investigation of the diurnal pattern of the vertical distribution of pollen in the lower troposphere using lidar. Atmospheric Chemistry and Physics 13(15):7619–7629

Norris SJ, Brooks IM, Hill MK, Brooks BJ, Smith MH, Sproson DA (2012) Eddy covariance measurements of the sea spray aerosol flux over the open ocean. Journal of Geophysical Research: Atmospheres 117(D7)

Panofsky H, Larko D, Lipschutz R, Stone G, Bradley E, Bowen AJ, Højstrup J (1982) Spectra of velocity components over complex terrain. Quarterly Journal of the Royal Meteorological Society 108(455):215–230

Parker D, Wilson H, Jones PD, Christy J, Folland CK (1996) The impact of mount pinatubo on world-wide temperatures. International Journal of Climatology 16(5):487–497

Petersen G, Renfrew I (2009) Aircraft-based observations of air–sea fluxes over denmark strait and the irminger sea during high wind speed conditions. Quarterly Journal of the Royal Meteorological Society 135(645):2030–2045

Pirjola L, O'Dowd CD, Brooks IM, Kulmala M (2000) Can new particle formation occur in the clean marine boundary layer? J Geophys Res Atmos 105(D21):26,531–26,546

Platis A, Altstädter B, Wehner B, Wildmann N, Lampert A, Hermann M, Birmili W, Bange J (2016a) An observational case study on the influence of atmospheric boundary-layer dynamics on new particle formation. Boundary-Layer Meteorology 158(1):67–92

Platis A, Martinez-Villagrasa D, Beyrich F, Bange J (2016b) Analysis of the influence of a lake on the lower convective boundary layer from airborne observations. Meteorologische Zeitschrift pp –, DOI 10.1127/metz/2016/0802, URL `http://dx.doi.org/10.1127/metz/2016/0802`

Platis A, Martinez-Villagrasa D, Beyrich F, Bange J (2017) Observations of the temperature and humidity structure parameter over heterogeneous terrain by airborne measurements during the litfass 2003 campaign. Boundary-Layer Meteorology Under reviewe

Pope F (2010) Pollen grains are efficient cloud condensation nuclei. Environmental Research Letters 5(4):044,015

Putaud JP, Van Dingenen R, Alastuey A, Bauer H, Birmili W, Cyrys J, Flentje H, Fuzzi S, Gehrig R, Hansson HC, et al. (2010) A european aerosol phenomenology–3: Physical and chemical characteristics of particulate matter from 60 rural, urban, and kerbside sites across europe. Atmospheric Environment 44(10):1308–1320

Raupach RR, Finnigan JJ (1995) Scale issues in boundary-layer meteorology: surface energy balances in heterogeneous terrain. Hydro Proc 9:589–612

Richardson LF (1922) Weather prediction by numerical process. Cambridge University Press

Roth M, Oke TR (1995) Relative efficiencies of turbulent transfer of heat, mass, and momentum over a patchy urban surface. Journal of the Atmospheric Sciences 52(11):1863–1874

Schueler S, Schlünzen KH (2006) Modeling of oak pollen dispersal on the landscape level with a mesoscale atmospheric model. Environmental Modeling & Assessment 11(3):179–194

Self S, Zhao JX, Holasek RE, Torres RC, King AJ (1993) The atmospheric impact of the 1991 mount pinatubo eruption

Sempreviva AM, Højstrup J (1998) Transport of temperature and humidity variance and covariance in the marine surface layer. Boundary-Layer Meteorology 87(2):233–253

Siebert H, Stratmann F, Wehner B (2004) First observations of increased ultrafine particle number concentrations near the inversion of a continental planetary boundary layer and its relation to ground-based measurements. Geophys Res Lett 31(9)

Siebert H, Wehner B, Hellmuth O, Stratmann F, Boy M, Kulmala M (2007) New-particle formation in connection with a nocturnal low-level jet: Observations and modeling results. Geophys Res Lett 34(16):DOI: 10.1029/2007GL029,891

Sproson D, Brooks I, Norris S (2013) The effect of hygroscopicity on eddy covariance estimates of sea-spray aerosol fluxes: a comparison of high-rate and bulk correction methods. Atmospheric Measurement Techniques 6(2):323–335

Stratmann F, Siebert H, Spindler G, Wehner B, Althausen D, Heintzenberg J, Hellmuth O, Rinke R, Schmieder U, Seidel C, et al. (2003) New-particle formation events in a continental boundary layer: First results from the saturn experiment. Atmospheric Chemistry and Physics 3(5):1445–1459

Stull R (1988) An Introduction to Boundary Layer Meteorology. Kluwer Academic Publisher, Dordrecht

Sühring M, Raasch S (2013) Heterogeneity-induced heat-flux patterns in the convective boundary layer: can they be detected from observations and is there a blending height?—a large-eddy simulation study for the litfass-2003 experiment. Boundary-Layer Meteorology 148(2):309–331

Sun J, Ariya PA (2006) Atmospheric organic and bio-aerosols as cloud condensation nuclei (ccn): A review. Atmospheric Environment 40(5):795–820

Tatarskii VI (1971) The effects of the turbulent atmosphere on wave propagation. Jerusalem: Israel Program for Scientific Translations p 472 pp

Taylor K, Penner JE (1994) Response of the climate system to atmospheric aerosols and greenhouse gases

Thomson D, Coulter R, Warhaft Z (1978) Simultaneous measurements of turbulence in the lower atmosphere using sodar and aircraft. Journal of Applied Meteorology 17:723–734

Von Blohn N, Mitra SK, Diehl K, Borrmann S (2005) The ice nucleating ability of pollen: Part iii: New laboratory studies in immersion and contact freezing modes including more pollen types. Atmospheric Research 78(3):182–189

Wehner B, Siebert H, Stratmann F, Tuch T, Wiedensohler A, Petäjä T, Dal Maso M, Kulmala M (2007) Horizontal homogeneity and vertical extent of new particle formation events. Tellus B 59(3):362–371

Wehner B, Siebert H, Ansmann A, Ditas F, Seifert P, Stratmann F, Wiedensohler A, Apituley A, Shaw R, Manninen H, Kulmala M (2010) Observations of turbulence-induced new particle formation in the residual layer. Atmos Chem Phys 10(9):4319–4330

Wendisch M, Brenguier JL (2013) Airborne measurements for environmental research: methods and instruments. John Wiley & Sons

Wiedensohler A, Cheng Y, Nowak A, Wehner B, Achtert P, Berghof M, Birmili W, Wu Z, Hu M, Zhu T, Takegawa N, Kita K, Kondo Y, Lou S, Hofzumahaus A, Holland F, Wahner A, Gunthe S, Rose D, Su H, Pöschl U (2009) Rapid aerosol particle growth and increase of cloud condensation nucleus activity by secondary aerosol formation and condensation: A case study for regional air pollution in northeastern China. J Geophys Res Atmos 114(D2)

Wildmann N, Kaufmann F, Bange J (2014a) An inverse-modelling approach for frequency response correction of capacitive humidity sensors in abl research with small remotely piloted aircraft (rpa). Atmospheric Measurement Techniques 7(9):3059–3069

Wildmann N, Ravi S, Bange J (2014b) Towards higher accuracy and better frequency response with standard multi-hole probes in turbulence measurement with remotely piloted aircraft (rpa). Atmos Meas Tech 7(4):1027–1041

Wood N, Mason P (1991) The influence of stability on effective roughness lengths for momentum and heat transfer. Q J R Meteorol Soc 117:1025–1056

Wyngaard J, Clifford S (1977) Taylor's hypothesis and high-frequency turbulence spectra. Journal of the Atmospheric Sciences 34(6):922–929

Wyngaard JC (1985) Structure of the planetary boundary layer and implications for its modeling. Journal of climate and applied meteorology 24(11):1131–1142

Wyngaard JC, Izumi Y, Collins SA (1971) Behavior of the refractive-index-structure parameter near the ground. J Opt Soc Am 61:1646–1650

Wyngaard JC, Pennell WT, Lenschow DH, LeMone MA (1978) The temperature-humidity covariance budget in the convectice boundary layer. J Atmos Sci 35:47–58

Appendix A

Peer-reviewed first-author publications

A.1 An Observational Case Study on the Influence of Atmospheric Boundary-Layer Dynamics on New Particle Formation - Publication I

Boundary-Layer Meteorol
DOI 10.1007/s10546-015-0084-y

ARTICLE

An Observational Case Study on the Influence of Atmospheric Boundary-Layer Dynamics on New Particle Formation

Andreas Platis[1] · Barbara Altstädter[3] · Birgit Wehner[2] · Norman Wildmann[1] · Astrid Lampert[3] · Markus Hermann[2] · Wolfram Birmili[2] · Jens Bange[1]

Received: 26 January 2015 / Accepted: 31 August 2015

Abstract We analyze the influence of atmospheric boundary-layer development on new particle formation (NPF) during the morning transition. Continuous in-situ measurements of vertical profiles of temperature, humidity and aerosol number concentrations were quasi-continously measured near Melpitz, Germany, by unmanned aerial systems to investigate the potential connection between NPF and boundary-layer dynamics in the context of turbulence, temperature and humidity fluctuations. On 3 April 2014 high number concentrations of nucleation mode particles up to 6.0×10^4 cm^{-3} were observed in an inversion layer located about 450 m above ground level. The inversion layer exhibited a spatial temperature structure parameter C_T^2 15 times higher and a spatial humidity structure parameter C_q^2 5 times higher than in the remaining part of the vertical profile. The study provides hints that the inversion layer is responsible for creating favorable thermodynamic conditions for a NPF event. In addition, this layer showed a strong anti-correlation of humidity and temperature fluctuations. Using estimates of the turbulent mixing and dissipation rates, it is concluded that the downward transport of particles by convective mixing was also the reason of the sudden increase of nucleation mode particles measured on ground. This work supports the hypothesis that many of the NPF events that are frequently observed near the ground may, in fact, originate at elevated altitude, with newly formed particles subsequently being mixed down to the ground.

Keywords Nucleation mode particles · Morning transition · New particle formation · Temperature and humidity structure parameter · Unmanned aerial system

✉ Andreas Platis
andreas.platis@uni-tuebingen.de

1 Zentrum für Angewandte Geowissenschaften, Universität Tübingen, Hölderlinstr. 12, 72074 Tübingen, Germany

2 Leibniz-Institut für Troposphärenforschung e.V. (TROPOS), Permoserstraße 15, 04318 Leipzig, Germany

3 Technische Universität Braunschweig, Institut für Flugführung Institute of Flight Guidance, Hermann-Blenk-Str. 27, 38108 Braunschweig, Germany

Published online: 19 September 2015

1 Introduction

Atmospheric aerosol particles influence the atmospheric radiation budget and thus the Earth's climate through the backscatter of solar light back to space (Ramanathan et al. 2001a; Barbaro et al. 2014) and by absorbing solar radiation. Further, they have an indirect aerosol climate effect, e.g. by the presence of cloud condensation nuclei (CCN). These nuclei modify cloud properties, thus have an influence on determining the cloud lifetime and albedo (Rosenfeld 2000; Ramanathan et al. 2001b). The size of airborne particles varies between 0.001 and 10 μm diameter (Seinfeld and Pandis 2012) and it is thus helpful to classify these particles into particle modes to cover this wide range. We use the term "nucleation mode particles" to refer to particles in the nucleation mode (diameter 5–10 nm) denoted N_{5-10} particles hereafter. Due to subsequent growth, particles can reach the lower Aitken mode (diameter 10–30 nm) and Aitken mode (diameter 30–100 nm). Larger particles belong to the accumulation mode (diameter 0.1–1 μm) and the coarse mode (diameter >1 μm) (e.g. Nojgaard et al. 2012; Kannosto et al. 2008). The number concentration of N_{5-10} particles is an indicator for recent new particle formation (NPF), because this size range was found to show a clear increase during NPF events without significant influence of anthropogenically emitted particles (Wehner et al. 2007). A powerful way to increase the CCN population is by nucleation of new particles and growth of these particles to CCN size (∼100 nm). CCN availability was observed to vary by an order of magnitude during NPF events (Wiedensohler et al. 2009).

New particle formation has been observed at various sites and altitudes of the atmosphere (e.g. Wiedensohler et al. 1996; Weber and Friedlander 1997; Kulmala et al. 2004; Jaatinen et al. 2009). The formation rate of 3 nm particles in the atmospheric boundary layer (ABL) varies over three orders of magnitude from 0.01 to 10 cm^{-3} s^{-1} (Kulmala et al. 2004). Various nucleation mechanisms are suggested to form nucleation mode particles. A detailed discussion of different NPF scenarios in combination with ABL dynamics is given by Bigg (1997) and Nilsson et al. (2001). Nucleation requires sufficient amounts of precursor gases (Kulmala et al. 2004). The most studied and best understood atmospheric nucleation mechanisms are binary homogeneous nucleation by H_2SO_4 and H_2O (Kulmala et al. 2004) and ternary nucleation by H_2O, NH_3 and H_2SO_4 (Korhonen et al. 1999). Several nucleation studies have considered the effect of enhanced radiation on photochemistry (e.g. enhanced OH radical production leading to enhanced H_2SO_4 production) associated with sunny days (O'Dowd et al. 1999). Nojgaard et al. (2012) correlated nucleation mode particles positively with O_3, which indicates that photochemistry plays a key role for most of the nucleation mode particles. Incoming solar radiation is not only an important factor in producing particle precursors gases, it is also the most important energy source for turbulence and convection in the ABL. Newly formed particles themselves have only a small influence on the direct radiation forcing (compared to larger particles as mentioned by Barbaro et al. 2014), because they are much smaller than the wavelengths of solar radiation. It was also found that meteorological processes could enhance the nucleation probability under conditions where the mean precursor concentrations were insufficient to trigger nucleation.

Knowledge of the influence of ABL development and turbulent mixing on NPF is however still poor. Turbulence and mixing of air masses with different temperature and humidity properties have been discussed as possible processes, which could lead to favorable conditions for NPF by e.g. local, short-term supersaturation of precursor gases (Bigg 1997; Nilsson et al. 2001). For example, Easter and Peters (1994) or Pirjola et al. (2000) found that turbulent fluctuations could enhance predicted nucleation rates, while Nilsson and Kulmala (1998) revealed nucleation enhancement due to the effect of mixing across a temperature and

humidity gradient (e.g. over a capping inversion). Nilsson et al. (2001) showed fluctuations of temperature and humidity occurring in the entrainment layer and during convection as contributing factor for nucleation. Bigg (1997) suggested that NPF results from "very sudden but sporadic mixing of limited horizontal and vertical extent between adjacent layers having strong thermal stability, the upper of which is both warmer and drier than the lower. Temperature and relative humidity differences need to be such that mixing will temporarily cause an increase in nucleation rate sufficient to bridge the gap between the existing supersaturation of the binary mixture and that required for homogeneous nucleation of new particles." In addition, Easter and Peters (1994) found by numerical simulations that humidity and temperature fluctuations can enhance nucleation and increase nucleation rates if the humidity and temperature fluctuations are anti-correlated, however this has never been validated by measurements in the ABL. A characteristic quantity for the intensity of turbulent temperature and humidity fluctuations in the ABL is the structure parameter. Wyngaard and LeMone (1980) observed a strong, entrainment-induced peak in structure parameter of temperature C_T^2 and humidity C_q^2 in the inversion layer, consequently the inversion layer is known for strong temperature and humidity fluctuations. In experiments, Siebert et al. (2004) described NPF in the thermal inversion layer, due to effective mixing of high fluctuations in the potential temperature and water vapour density in the SATURN ('Strahlung, vertikaler Austausch, Turbulenz und Partikel–Neubildung'; radiation, vertical exchange, turbulence and NPF) experiment. Hellmuth (2006) predicted the highest likelihood for nucleation near the top of the mixed layer, mainly due to thermodynamic reasons by numerical simulations. Further, NPF was observed to be correlated with increasing turbulence in the residual layer by Wehner et al. (2010) with the measurement system called Airborne Cloud Turbulence Observation System (ACTOS). Also Stratmann et al. (2003) investigated particle burst events in the residual layer and mixed layer with ACTOS, as well as Siebert et al. (2007). They also proposed NPF caused among others by a nocturnal low-level jets. This layer is often characterized by strong turbulence due to shear flows. Crumeyrolle et al. (2010) observed that the vertical extension of NPF events seem to coincide exactly with the top of the turbulent convective ABL.

This study contributes to a better understanding of NPF in the ABL, especially which role ABL dynamics, like turbulent fluctuations of temperature and humidity, play in NPF. However, all these possible processes have not been proven by continuous in-situ measurements of the ABL vertical profile. In general, data concerning this topic are sparse as the majority of available NPF measurements were performed at ground. Therefore, no direct conclusions about the influence of ABL dynamics on NPF could be given. Further, the altitude of nucleation events cannot be assigned by ground-based measurements only. Thus, a measurement campaign was conducted in April 2014 with the two unmanned aerial systems (UAS) called Application of Light-weight Aircraft for Detecting In-situ Aerosol (ALADINA) and Multi-purpose Airborne Sensor Carrier (MASC) supported by ground measurements in Melpitz, Eastern Germany, to provide in-situ observations of the vertical variability of NPF and meteorological parameters.

With ALADINA, information about the vertical distribution of newly formed aerosol particles and turbulence can be obtained (Altstädter et al. 2015). With MASC complementary information about turbulence within the ABL and a three-dimensional picture of atmospheric processes and thermodynamic quantities are received (Wildmann et al. 2014a). The systems can be used very flexible with minimal logistic efforts and potentially lower costs compared to manned aircraft. Further, UAS enable flying close to the ground surface, which is not possible with manned aircraft due to safety reasons. Further a continuous monitoring of the ABL processes to close the spatial gap of data in the ABL between ground-based instruments,

lidar column measurements; and measurements at higher altitudes is easier by UAS than by large manned aircraft (Altstädter et al. 2015). Manned aircraft have been investigating the large scale variability of the particle concentration along air-mass trajectories (O'Dowd et al. 2009). With ALADINA the lack of detailed measurements of the small-scale vertical and horizontal variability can be filled. This measurement data might be of importance for the implementation of NPF in models (Boy et al. 2006).

In Sect. 2, the structure parameter theory is described, in Sect. 3 the experiment, applied measurement systems and methodology are described, namely the airframes ALADINA and MASC. In Sect. 4, the case study of the NPF event is presented and discussed in Sect. 5. Finally, a summary and conclusions are presented in Sect. 6.

2 Methods

2.1 Turbulence Statistics

In order to understand NPF in a turbulent flow a short introduction to the theory and statistics of turbulence is provided. The turbulence structure can be described with the structure function. It is a measure of auto-correlation in a flow as a function of eddy size. It is also an alternative to Fourier power spectra with the advantage of not using a Fourier transformations to calculate the covariance function and thus avoid systematic errors due to improper data windowing. For the wind speed V we used the following equation to calculate the structure function $D_V(r)$, which was defined by Tatarskii (1971),

$$D_V(r) = \frac{1}{N-n} \sum_{i=1}^{N-n} [V(x_i) - V(x_i + r)]^2 \tag{1}$$

for a certain data record V, where x is the spatial coordinate, the number of data points in the record is denoted by N, where $r = r(n)$ is the spatial displacement (lag) that corresponds to the eddy size, and n is the number of data points associated with the lag r. $D_V(r)$ is of the order of all of the energy in eddies of size r or less (Davidson 2004). The dominant contributions come from the eddies of size r since these are the most energetic, assuming that larger eddies transport more energy. In order to show the close relation between structure function and turbulent kinetic energy (TKE), for isotropic turbulence the structure function can also be calculated by the variance σ_V and the autocorrelation function ρ_V

$$D_V(r) = 2\sigma_V^2 \left[1 - \rho_V(r)\right]. \tag{2}$$

For large r in the order of the integral length scale I (see below) the auto-correlation function becomes small,

$$\rho_V \xrightarrow{r \to I} 0, \quad \text{leading to} \quad D_V \xrightarrow{r \to I} 2\sigma_V^2. \tag{3}$$

For isotropic turbulence ($\sigma_u = \sigma_v = \sigma_w = \sigma_V$, where u, v, w are the wind-speed components in the x, y, z direction, respectively) the TKE e is

$$e = \frac{1}{2}\left(\sigma_u^2 + \sigma_v^2 + \sigma_w^2\right) = \frac{3}{2}\sigma_V^2 \tag{4}$$

and thus according to Eq. 3,

$$D_V \xrightarrow{r \to I} \frac{4}{3}e, \tag{5}$$

where e is the turbulent kinetic energy of all eddies of size r or less. In the inertial subrange $D_V(r)$ depends only on the dissipation rate ε, r and Kolmogorov's constant $\beta = 2$ (Kolmogorov 1941)

$$D_V(r) = \beta\, \varepsilon^{2/3}\, r^{2/3} = C_V^2\, r^{2/3}, \tag{6}$$

with the structure parameter C_V^2 for the wind speed V

$$C_V^2 = D_V(r)\, r^{-2/3} \tag{7}$$

which is a proportionality factor in the 2/3-law expression (Kolmogorov 1941) for the structure function. The relation of Eq. 7 can be only applied within the inertial subrange of locally homogeneous and isotropic turbulence (Wyngaard et al. 1971). The structure parameter is calculated from in-situ data using the structure function. By knowing the structure parameter C_V^2, the dissipation rate ε can be calculated from airborne measurements.

The unmanned aircraft performed several vertical profiles during the morning with straight climbing- or descending-legs in east-west and west-east directions to measure the wind speed V. Accurate measurements of the turbulent wind vector with the five-hole probe are only possible when flying straight legs (Wildmann et al. 2014b). To achieve this, the autopilot system must control the aircraft. The autopilot system of ALADINA was not always in control during ascents or descents, so only vertical profiles measured by MASC aircraft were used to determine ε, since man-controlled ALADINA flights were not straight enough. C_V^2 is estimated from a moving window along the vertical profiles with a time interval length of 10 s (1000 data points). Results of vertical profiles of the energy dissipation rate will be presented and discussed in Sect. 4.2.

Besides the dissipation rate also temperature T and humidity q fluctuations are important to characterize the turbulent structure. Turbulent fluctuations of q and T provide indications in which layers of the ABL favorable meteorological conditions for NPF are expected. The combination of (2) and (7) shows that an increase of the temperature variance σ_T results in an increase of the calculated C_T^2. C_q^2 and C_T^2 are obtained by using Eq. 7 with q and T instead of the wind speed V. Therefore the spatial structure parameters of humidity C_q^2 and temperature C_T^2 are calculated along the vertical profiles according to the method of van den Kroonenberg et al. (2012). The standard deviations of both quantities are calculated as an additional measure of turbulence (Wyngaard et al. 1971) and are then compared with the N_{5-10} number concentrations.

The structure parameters C_T^2 and C_q^2 (for temperature and water vapour mixing ratio, respectively) were calculated from the in-situ flight data as follows: theoretically, in a $D_q(r) \times r^{-2/3}$ versus r diagram, assuming infinitely fast humidity sensors, the inertial subrange would be displayed as a horizontal plateau at C_q^2 (for diagrams, see van den Kroonenberg et al. 2012). Thus these kinds of diagrams are a direct method to calculate the structure parameters. The lower limit of inertial subrange (the inner or Taylor microscale λ, at the boundary to dissipation, see Westin et al. 1994) is in the order of of 1 mm. The outer (integral) length scale I, as a measure of the size of the eddies which contain most of the turbulent energy, is usually in the order of a few hundred metres. Turbulence is produced at scales larger than I and decays at the transition to the dissipation range represented by λ.

In practice, due to limited sensor response, the smallest scales could not be resolved by our temperature and humidity sensors. Instead, the measured part of the inertial subrange ends at the smallest resolved scales $r_{\min}$. Due to the sufficient length of horizontal flight legs, the transition to the production range (which is in the order but larger than I) is covered by the measurements in this analysis. In a $D_q(r) \times r^{-2/3}$ versus r diagram the transition

to the production range, i.e. the end of the inertial subrange, can be identified as the end of the horizontal plateau at length scale $r_P > I$. It depends, among others, on the thermal stratification, the boundary-layer height and the nearest stably stratified layer (Lumley and Panofsky 1964). The structure function's precise upper limit r_P is therefore complex to predict. After analysis of the flight data set, for all flights an upper limit r_{max} was defined, which was always within the inertial subrange, i.e. $r_P > I \gtrsim r_{max}$. The structure parameters were then calculated within the limits r_{min}, r_{max}. This method assures that only inertial-subrange data was used for the calculations and that the calculated structure parameters do not depend on r_{min}, r_{max}, but their statistical uncertainty (accuracy) does.

The integral length scale I_q of mixing ratio q varied between 34 and 110 m for all considered flights. Hence, for C_q^2 we found the section between $r_{min} = 4.0$ m and $r_{max} = 30$ m to be part of the inertial subrange for all flights. The structure parameters C_T^2 for temperature T and C_V^2 for wind speed V were calculated in a similar way, the inertial length scale I_T was found to be between 28 and 160 m, therefore the upper limit was set to $r_{max} = 25$ m. For the wind speed the lower limit was found to be $r_{min} = 25$ m and $r_{max} = 34$ m.

To indicate the variation of temperature, humidity and wind-speed fluctuations along the vertical profiles, a vertically-resolved structure parameter is required. Hence, $D_q(r)$, $D_T(r)$ and $D_V(r)$, respectively, were calculated within a moving data window along the vertical profiles. To ensure a statistical uncertainty below 10 % (see van den Kroonenberg et al. 2012), the width of the data window was at least 1000 data points, which corresponds to a vertical span of 30 m (corresponding to a data sampling rate of 100 Hz times a climb rate of 3 m s^{-1}).

2.2 Field Site and Flight Strategy

The NPF measurement campaign was conducted at the field research station of the Leibniz Institute for Tropospheric Research (TROPOS). The site near the village of Melpitz is located 41 km north-east of Leipzig, Germany. The site is on a flat meadow and surrounded by agricultural land (Spindler et al. 2013). The grass surface is suitable for UAS take-off and landing. Air masses are influenced by urban and agricultural emissions due to the proximity to Leipzig and due to its surrounding of grass, crop land and woods. No obstacles or larger sources of pollution lie within the immediate vicinity of the station. Several ground-based instruments are used in Melpitz for long-term observations of meteorological parameters, gas concentrations (O_3, NO, NO_2 and SO_2) and atmospheric aerosols (Wehner et al. 2010). Aerosol number concentrations are determined by a twin differential mobility particle sizer (TDMPS) (Wiedensohler et al. 2012) in the range between 3 nm and 10 µm with a time resolution of 10 min. A Neutral cluster and Air Ion Spectrometer (NAIS) is capable of measuring mobility distributions of sub-3 nm neutral and charged aerosol particles and clusters (Kulmala et al. 2007) in the mobility diameter range of 0.8–40 nm. The instrument is described in more detail by Manninen et al. (2009), Größ et al. (2015). Scans are performed every 3 min and offer the possibility to observe the temporal size development of atmospheric aerosol particles at the ground. Previous studies demonstrate the station's great potential for detecting formation mechanisms of nucleation mode particles (Wehner et al. 2007; Siebert et al. 2004). Long-term measurements for two years (July 2003 to June 2005) by Jaatinen et al. (2009) show nucleation events at this field site and implied that 26 % of all measurement days contain NPF events.

During the field campaign, combined flights with the two research aircraft ALADINA and MASC were performed in addition to continuous ground-based measurements, as described in Sect. 2.2. The flight strategy was vertical profiling with both aircrafts in order to catch the development of the ABL and to observe the vertical distribution of aerosol particles. During the campaign from 2–7 April 2014, 38 flights with both UAS were performed. This study

will focus on 11 flights performed on 3 April from 0621 UTC in the early morning until 1226 UTC.

2.3 Unmanned Aerial Systems: ALADINA and MASC

ALADINA was designed for the study of small-scale horizontal and vertical distribution and variability of aerosol particles in the size range of 5 nm to 10 μm. Complementary to ground-based monitoring instruments, it provides in-situ measurements of aerosol and meteorological properties at variable altitudes up to 1000 m. The aircraft is of type Carolo P360 developed at the Institute of Aerospace Systems at the Technische Universität Braunschweig. It has a wingspan of 3.6 m and a maximum take-off weight of 25 kg. A large payload bay allows to carry aerosol measurement instruments (see Sect. 2.4). ALADINA can be operated automatically by the autopilot system called Research Onboard Computing System (ROCS). ROCS is provided by the Institute of Flight Mechanics and Control of the University Stuttgart (Wildmann et al. 2014a). The autopilot controls a constant airspeed of 28 $\pm$1 m s^{-1} and constant altitude with a precision of $\pm$2 m. More details on ALADINA can be found in Altstädter et al. (2015).

A meteorological sensor package mounted at the front of the aircraft was designed and integrated by the Environmental Physics Group of the Eberhard-Karls University of Tübingen (EKUT). In order to perform measurements of thermodynamic scalars and turbulence, the system is equipped with a five-hole probe system (Wildmann et al. 2014b), fast response temperature sensors (for more informations see Wildmann et al. 2013) a capacitive humidity sensor, a barometric pressure transducer, and an inertial measurement unit (IMU) with GPS receiver. The wind and temperature measurements achieve a frequency resolution of 100–20 Hz. A relative humidity sensor of type P14 Rapid by Innovative Sensor Technologies (IST) is used as a small and light-weight solution to measure the water vapour content of the air. The sensor has a specified response time of 1.5 s.

For additional information about turbulence within the ABL and to obtain a three-dimensional picture of atmospheric processes, the second unmanned research aircraft MASC (Multi-purpose Airborne Sensor Carrier) was operated at the same time as ALADINA. MASC was developed at the EKUT and carries the same meteorological sensors used on ALADINA, but no aerosol payload. The electrically powered motor-glider has a take-off weight of 5–7 kg and a wingspan between 2.6 and 3.4 m, depending on battery and payload. MASC is also controlled by autopilot ROCS with a cruising speed of 25 m s^{-1}.

2.4 Aerosol Measurements on ALADINA

The aerosol instrumentation, which is carried by ALADINA, consists of three particle counters: One optical particle counter (model GT-526, Met One Instruments Inc.) and two condensation particle counters (model 3007, TSI Inc.) Before integration into ALADINA, the particle counters were reduced in size and mass and then calibrated at the laboratory at TROPOS. The optical particle counter is capable of measuring the particle number concentrations in the range 0.3–10 μm particle diameter, sectioned into six particle size channels. The condensation particle counters determine total particle number concentrations with different lower threshold diameters. The first condensation particle counters (CPC1) measures the number concentrations of particles with diameters between 5 nm and 2 μm (N_5) and the second (CPC2) the number of particles in the range between 10 and 2 μm (N_{10}). Nucleation mode particle number concentrations are then derived from the difference of the count rates of the two condensation particle counters ($N_5 - N_{10} = N_{5-10}$). The time resolution of condensation

particle counters is 1.3 s and the uncertainty of the measured number concentrations is ±15 %. Further explanations of the sensors and ALADINA are given in Altstädter et al. (2015). Note that the lower detection limit of CPC1 has been changed from originally 6 nm since this publication. The lower detection limit of the condensation particle counters can be adjusted by changing the temperature difference in the devices. For this campaign the limit was set to 5 nm.

3 Results

3.1 Synoptic Situation

On 3 April 2014, the weather situation was dominated by an anticyclone over central and eastern Europe and a cyclone over the Atlantic Ocean. This resulted in a south-west wind direction with advection of warm sub-tropical air from Sahara to eastern Germany. In order to investigate the origin of the airmass, backward trajectories were calculated using the NOAA "On-line Transport and Dispersion Model" HYSPLIT (Draxler and Rolph 2003). Figure 1 shows trajectories arriving at Melpitz on 3 April 0600 UTC in different heights: 500, 1000, and 1500 m. The trajectories indicate that the airmasses over Melpitz spent the past 48 hours over southern Europe with an origin of the 1000 m airmass over North Africa. Due to the high pressure system over Central Europe, no rain was observed along the trajectories. Further, the ground wind speed was very low, around 1–2 m s^{-1} until 1300 UTC with variable wind direction (Fig. 2). Thus, advection of air can be neglected near the surface.

3.2 ABL Evolution

Air temperatures at the ground ranged from 11 °C in the early morning to 22 °C in the afternoon. Due to almost cloud-free conditions during night, an undisturbed boundary-layer development (e.g. Barbaro et al. 2014) was observed throughout the morning with a surface inversion of $\Delta T = 10$ K. Figure 2 reveals an almost unimpeded solar irradiance on 3 April morning measured by the ground-based sun-radiometer in Melpitz. Only around 0800 UTC and during the afternoon between 1400 and 1700 UTC solar radiation was damped due to cloud cover.

The temperature evolution of the ABL is shown in Fig. 3. Eleven vertical profiles of potential temperature θ are measured with the two UAS from 0621 UTC to 1207 UTC. The morning transition starts with a strong inversion, starting from the surface up to 200 m above ground level (a.g.l.) in the morning at 0624 UTC. With solar radiation heating up the near-surface air, a shallow CBL develops below the strong, stably stratified layer, i.e. the base of the inversion is lifted up to 190 m a.g.l. until 0904 UTC. At 0958 UTC the base of the inversion is lifted up to 500 m a.g.l. and the top of inversion is located now at 600 m a.g.l., indicating the beginning of the convective breakthrough. Between 0958 UTC and 1037 UTC then, the shallow CBL breaks trough the inversion and reaches the neutrally stratified residual layer. Afterwards, the boundary-layer top is above the maximum flight altitude of 1000 m, thus was not observed anymore. A detailed view of the stratification of the boundary layer in terms of temperature profiles compared to nucleation mode particles (N_{5-10}) number concentrations is presented in the following section.

3.3 NPF Event

Figure 4 shows selected vertical profiles of aerosol number concentrations during the boundary-layer morning transition measured with ALADINA on 3 April from 0833 UTC

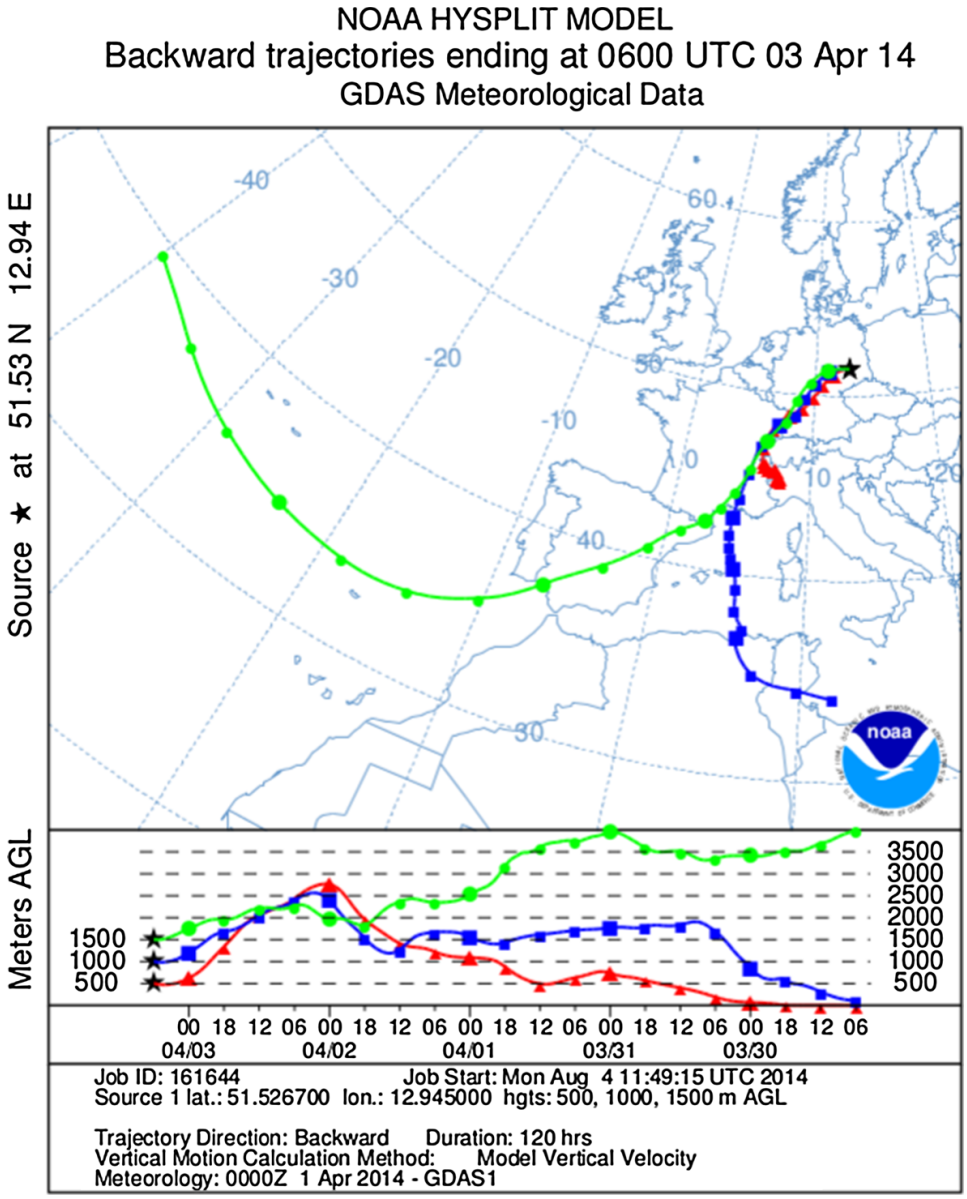

Fig. 1 120 h-backward trajectories arriving on 3 April 2014 at 0600 UTC, at heights of 500, 1000, and 1500 m above ground level (a.g.l.) over Melpitz, calculated by HYSPLIT model

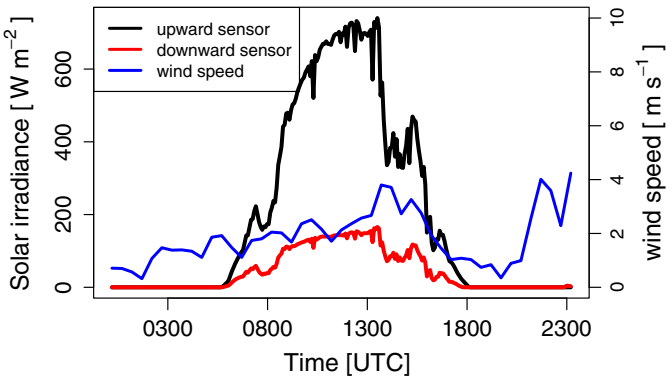

Fig. 2 Solar irradiance measured by two pyranometers at surface on 3 April 2014 at Melpitz research station. Solar irradiance is received in the spectral range from 300 to 2800 nm and the whole hemisphere (180 degrees field of view) looking upward (*black*) and downward (*red*). The wind speed at 2-m height is shown by the *blue line*

until 1053 UTC. The black line presents number concentrations N_5 measured by CPC1, the red line N_{10} by CPC2. In the first profiles at 0833 and 0839 UTC almost no difference between CPC1 and CPC2 is measured and some spots of N_{5-10} below 400 m, respectively.

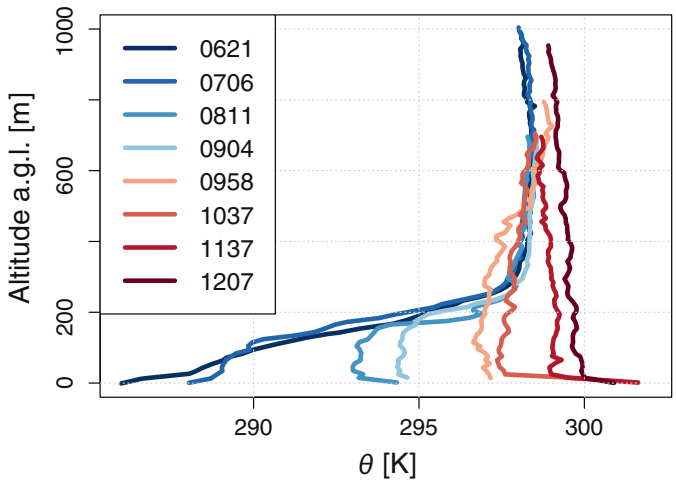

Fig. 3 Temperature evolution of the ABL on 3 April 2014. Potential temperature θ is plotted from 8 (out of 11 due to clarity) vertical profiles between 0624 and 1207 UTC measured by MASC and ALADINA

However, in a layer between 410 m and 500 m a.g.l. an increase in the total aerosol number concentration is seen for larger particles with diameter 10 nm -2µm, indicating pre-existing aerosol. In the profiles at 0929 UTC, N_{5-10} are observed considerably in a layer between 400 and 570 m for the first time during that day. A hypothesis is that NPF has started recently in that layer where enhanced N_{5-10} is observed. Until 0958 UTC, the number concentrations increase to a maximum of $N_{5-10} \approx 2.5 \times 10^4\,\mathrm{cm}^{-3}$. Thereby, further NPF is necessary to explain the increase of N_{5-10} in that layer between 400 - 570 m a.g.l., although the layer height and thickness vary slightly.

At 1004 UTC, the N_{5-10} particles are spread downwards into the shallow CBL. In that moment of the downward transport of N_{5-10} particles, the maximum concentration decreases to $N_{5-10} \approx 1.8 \times 10^4\ \mathrm{cm}^{-3}$ as the layer peters out due to the downward mixing. Afterwards, between 1045 and 1053 UTC, the concentrations begin to rise again up to $N_{5-10} \approx 6.0 \times 10^4\ \mathrm{cm}^{-3}$ in the mixed layer. Thus, obviously NPF was continued or even enhanced during the mixing process and afterwards. For a better understanding of the evolution of NPF, temperature and humidity stratification are presented in combination with the number concentrations of N_{5-10} (Figs. 5, 6, 7, 8 and 9).

Vertical profiles including potential temperature (θ), mixing ratio (q), relative humidity (RH), structure parameters (C_T^2, C_q^2), standard deviation of temperature and humidity (σ_T, σ_q) and nucleation mode particle number concentrations (N_{5-10}) measured by the condensation particle counters are shown in Fig. 5, where almost no N_{5-10} particles can be identified at 0833 UTC as mentioned in the previous paragraph. A shallow CBL up to 190 m a.g.l. is observed; thermally driven convection has started. Above there is a thermal inversion ($\partial_z\theta > 0$), with a temperature difference of $\Delta T = 5$ K up to 200 m a.g.l. . Above the inversion, the convective layer has a higher absolute and relative humidity, due to evaporation from the surface. Evaporation started after sunrise, because of surface heating by solar radiation. The inversion's layer humidity gradient has a difference of mixing ratio $\Delta q = 3\,\mathrm{g\,kg}^{-1}$ and difference of relative humidity $\Delta RH = 40$ %. At 0937 UTC (Fig. 6) the shallow CBL grows up to 500 m a.g.l. with $\theta = 297$ K, followed by an inversion with $\Delta T = 2$ K and a change of humidity of $\Delta q = 2\,\mathrm{g\,kg}^{-1}$. NPF is now observed with particle number concentrations up to $N_{5-10} \approx 1.6 \times 10^4\ \mathrm{cm}^{-3}$, located between 400 and 570 m a.g.l. . 20 min later (Fig. 7) at 0958 UTC the inversion which is still at around 500 m weakens further, however the maximum N_{5-10} increases to $\approx 2.5 \times 10^4\ \mathrm{cm}^{-3}$.

The next vertical profile (Fig. 8), measured at 1004 UTC, shows the breakthrough of the shallow CBL through the inversion layer into the residual layer. The temperature profile still

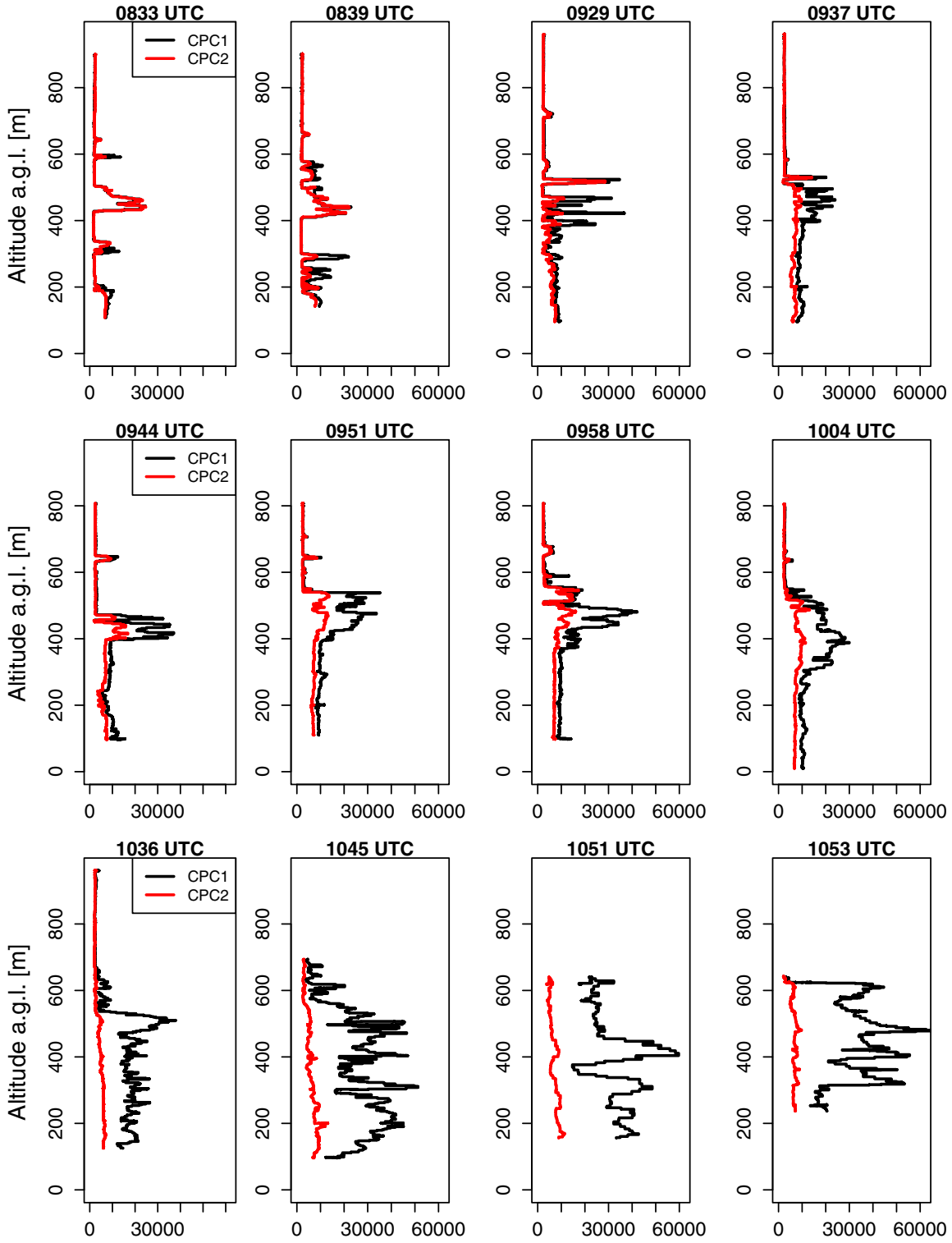

Fig. 4 Selected vertical profiles of particle number concentrations versus height of all measured ALADINA profiles from 3 flights on 3 April 2014 during the morning transition. CPC1 (N_{10}) is represented with a *black line*, CPC2 (N_5) is *red*. The difference between CPC1 and CPC2 is the N_{5-10} particle number concentrations. The x-axis represents the number concentration per cm^3

indicates a weak inversion of 0.5 K at 500 m. N_{5-10} particles are spread downwards into the convective layer towards the ground. 30 min later, at 1036 UTC, significant concentrations in N_{5-10} are detected throughout the whole boundary layer from surface up to 670 m a.g.l. (Fig. 4) with the maximum concentrations still at the height of the former inversion layer.

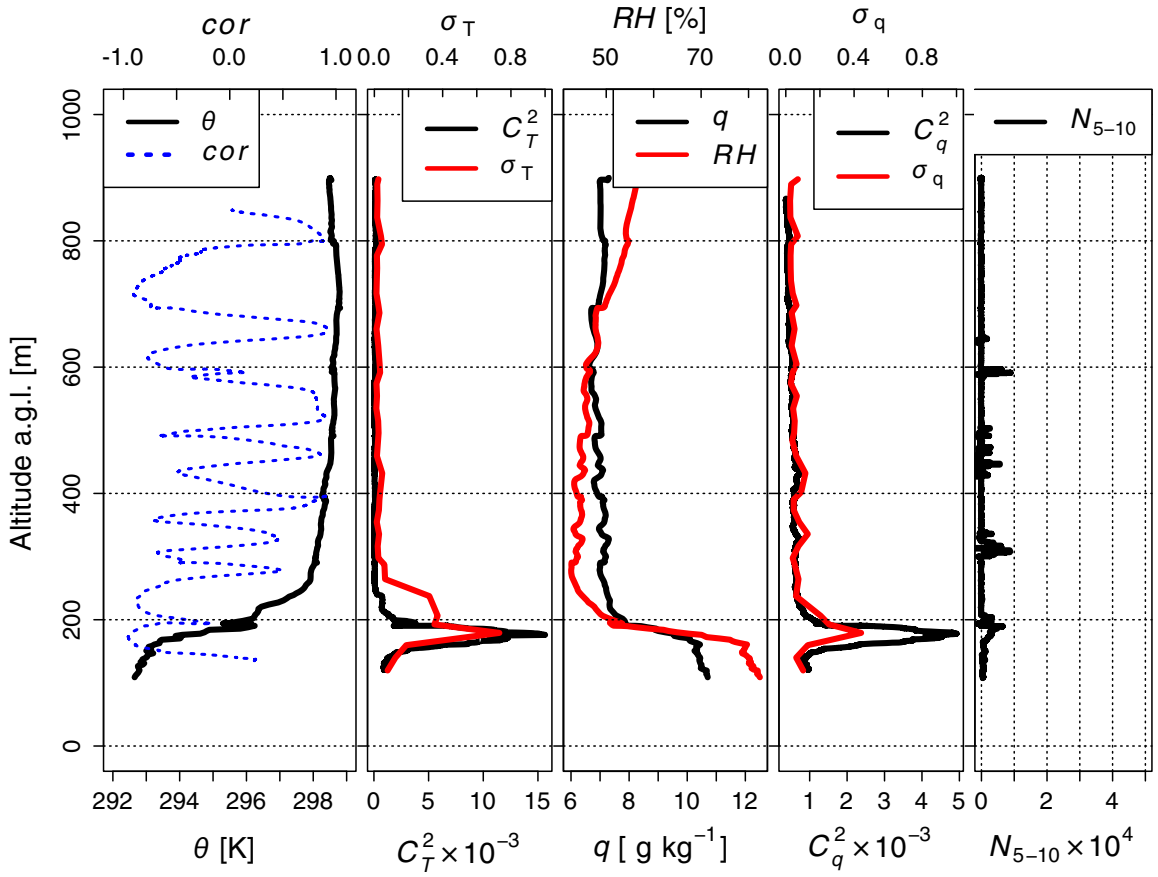

Fig. 5 Vertical profiles of ALADINA flight at 0833 UTC on 3 April 2014. From *left* to *right*. *1* Potential temperature θ (*black*). *Blue dotted line* shows the correlation coefficient (cor) between temperature and humidity. *2* C_T^2 (*black*) and temperature variance σ_T (*red*). Units are [$K^2\,m^{-2/3}$] for C_T^2 and [K] for σ_T. *3* Mixing ratio q (*black*) and relative humidity RH (*red*). *4* C_q^2 (*black*) and humidity variance σ_Q (*red*). Units are [$g^2kg^{-2}\,m^{-2/3}$] for C_T^2 and [$g\,kg^{-1}$] for σ_q. *5* Difference of N_{5-10} between CPC1 - CPC2 = N_{5-10}. Number concentration of N_{5-10} is per cm^3. (Phase 1, see Sect. 4 for explanation)

Now, the inversion disappears and a mixed layer is formed. During the next profiles, starting at 1036 UTC (Fig. 4) and at 1045 UTC (Fig. 9), the number concentrations of N_{5-10} in the mixed layer increase and reach the maximum measured value of $N_{5-10} \approx 6.0 \times 10^4$ cm^{-3} at 1053 UTC (Fig. 4). However, there is a strong vertical and temporal variation of the maximum number concentrations in the mixed layer.

The profiles of C_T^2, σ_T and C_q^2, σ_q versus height are presented in Figs. 5, 6, 7, 8 and 9. Structure parameter profiles at 0833 and 0937 UTC indicate a C_T^2 value more than 15 times higher, C_q^2 is up to five times higher, in the inversion layer than in the remaining part of the vertical profiles. Likewise, profiles of σ_T and σ_q show comparably large values in the inversion layer. The associated turbulent temperature and humidity fluctuations are caused by coherent (convective) structures, that have enough kinetic energy to travel from the heated surface far enough aloft to hit into the residuals of the nocturnal inversion and cause entrainment. Profiles after the breakthrough of the shallow CBL of C_T^2, C_q^2, σ_T and σ_q are shown at 1045 UTC in Fig. 9, which are similar to all the remaining observed profiles afterwards. Both C_T^2 and C_q^2 are varying along the profile with increasing maximum value towards the surface.

Figure 10 shows ε for five different flights versus height during the morning transition of the ABL from 0710 - 1126 UTC on 3 April 2014. The first three flights consist each of one

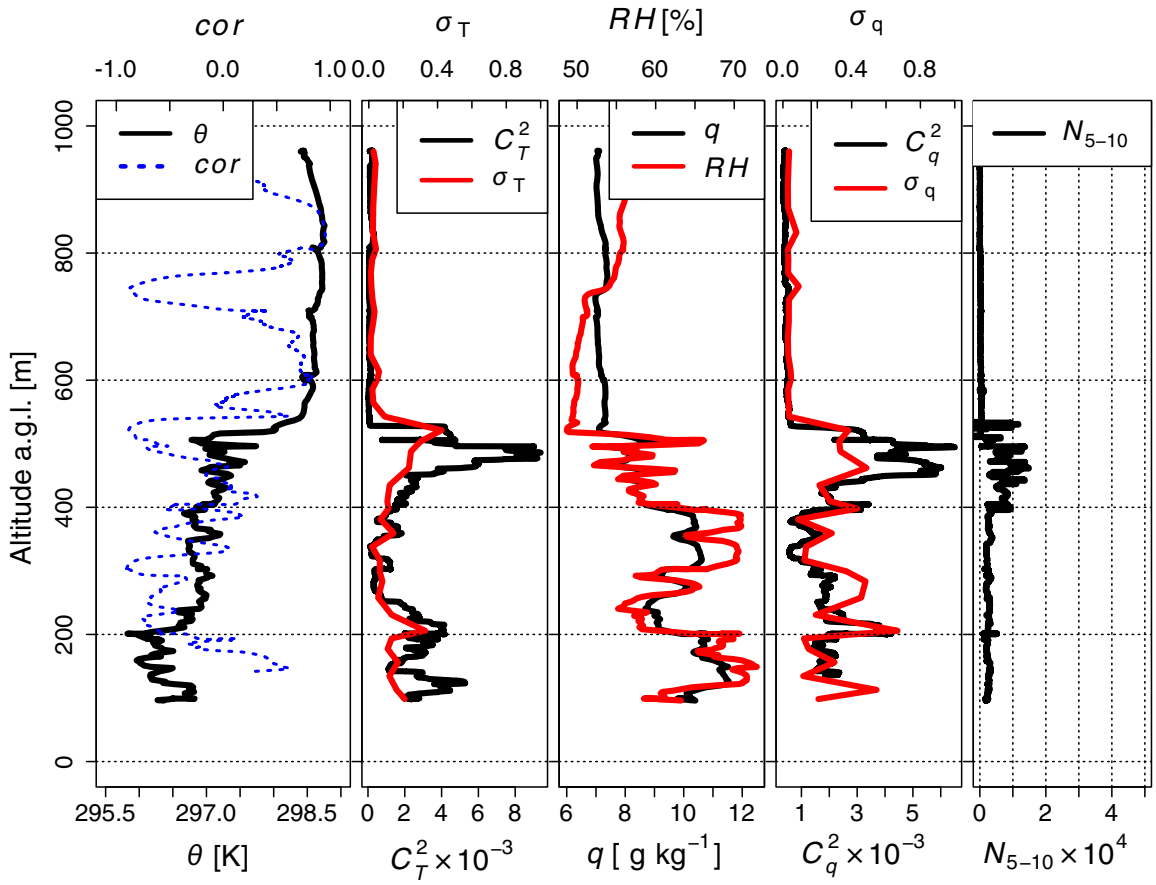

Fig. 6 Vertical profiles of ALADINA flight at 0937 UTC on 3 April 2014. Explanation same as in Fig. 5. (Phase 2)

ascent and one descent, the last two only of an ascent due to a different flight strategy. The first six profiles between 0710 and 0905 UTC have the maximum ε at the lowest height at about 170 m a.g.l. with values in the order between 10^{-2} and 10^{-1} m^2 s^{-3}, similar to the results presented in Caughey and Palmer (1979) for the surface layer. The dissipation rate decreases with height due to the inversion and no local maximum of ε is detected. The stable stratified thermal inversion has a damping influence on the production of TKE, which means decreasing dissipation due to the turbulent energy cascade (Caughey and Palmer 1979). After the breakthrough of the shallow CBL, ε is in the order of 10^{-3} m^2 s^{-3} in the mixed layer, similar to findings from Caughey and Palmer (1979).

3.4 Ground-Level Observations

The dataset is completed by simultaneous ground-level measurements, which include particle number size distributions at high diameter resolution as well as potential gas phase precursors. A striking feature in the ground-level particle number concentrations between 5 and 10 nm, obtained by the NAIS instrument (Fig. 11), is the rapid increase up to $N_{5-10} \approx 1.4 \times 10^4$ cm^{-3}, between 1025 and 1045 UTC. This coincides exactly with the time when the spread of N_{5-10} particles downwards to the surface was observed with ALADINA. It is worth to mention that the N_{5-10} number concentrations measured by ALADINA at 100 m above ground agree quantitatively with the ground-level values even though different instrumentation was used. Note that for Fig. 11 the ALADINA number concentrations measurement is a 10 s average (NAIS 3 min average) at around 100 m a.g.l. and the ground

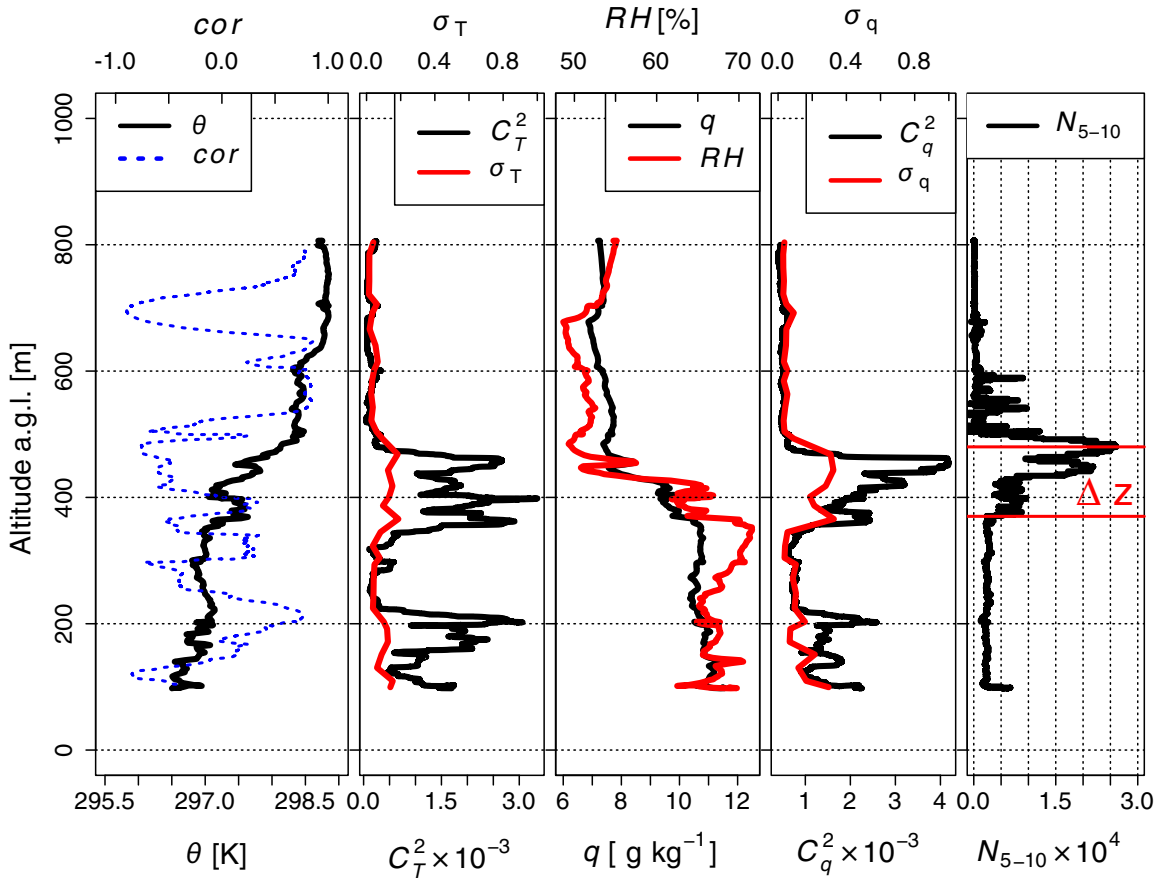

Fig. 7 Vertical profiles of ALADINA flight at 0958 UTC on 3 April 2014. Explanation same as in Fig. 5. In the plot for N_{5-10}, the two *red lines* mark the height difference (Δz) between 380 and 490 m a.g.l. within the number concentrations increase from background value to its maximum. (Phase 2)

measurement took place in 2 m a.g.l. . The results from ALADINA measurements at 100 m a.g.l. are still in a good agreement with ground-based measurements, since the ABL between ground and 100 m a.g.l. was always convectively driven well-mixed during ALADINA flights. In addition, the quality-assured ground-based measurements prove the reliability of N_{5-10} measurements by ALADINA.

It is an essential feature of our observation that the peak in ground-level N_{5-10} was accompanied by a similarly steep increase in SO_2. Importantly, both peaks rise at the very same time, around 1025 UTC. Our interpretation is that both peaks originate from downmixing of air from aloft, since there are no relevant local sources of SO_2 around Melpitz at the time of the observations (spring time). If this holds true, the enhancement of SO_2 in that layer from aloft might provide a (partial) explanation for the NPF event because SO_2 is, through hydroxyl radical oxidation to sulphuric acid, a known precursor for the formation of new atmospheric particles (Sipilä et al. 2010) (Table 1).

The ground-based NO and NOx values at Melpitz are shown in Table 1. With the downmixing of NPF at 1000 UTC, NO and NO_x both decrease. NO_x levels off at around 10 $\mu g\,m^{-3}$ at noon, and NO, which can be taken as an indicator of fresh emissions, such as from traffic, decreases rapidly down to levels below 1 $\mu g\,m^{-3}$ after 1000 UTC as well. For comparison, NO at the roadside in Dresden: 30–50 $\mu g\ m^{-3}$, urban background: 5–15 $\mu g\ m^{-3}$ (Birmili et al. 2013). This is between one and two orders of magnitude higher than what was observed in Melpitz on 3 April 2014. This does not rule out anthropogenic influence entirely, but it appears very unlikely.

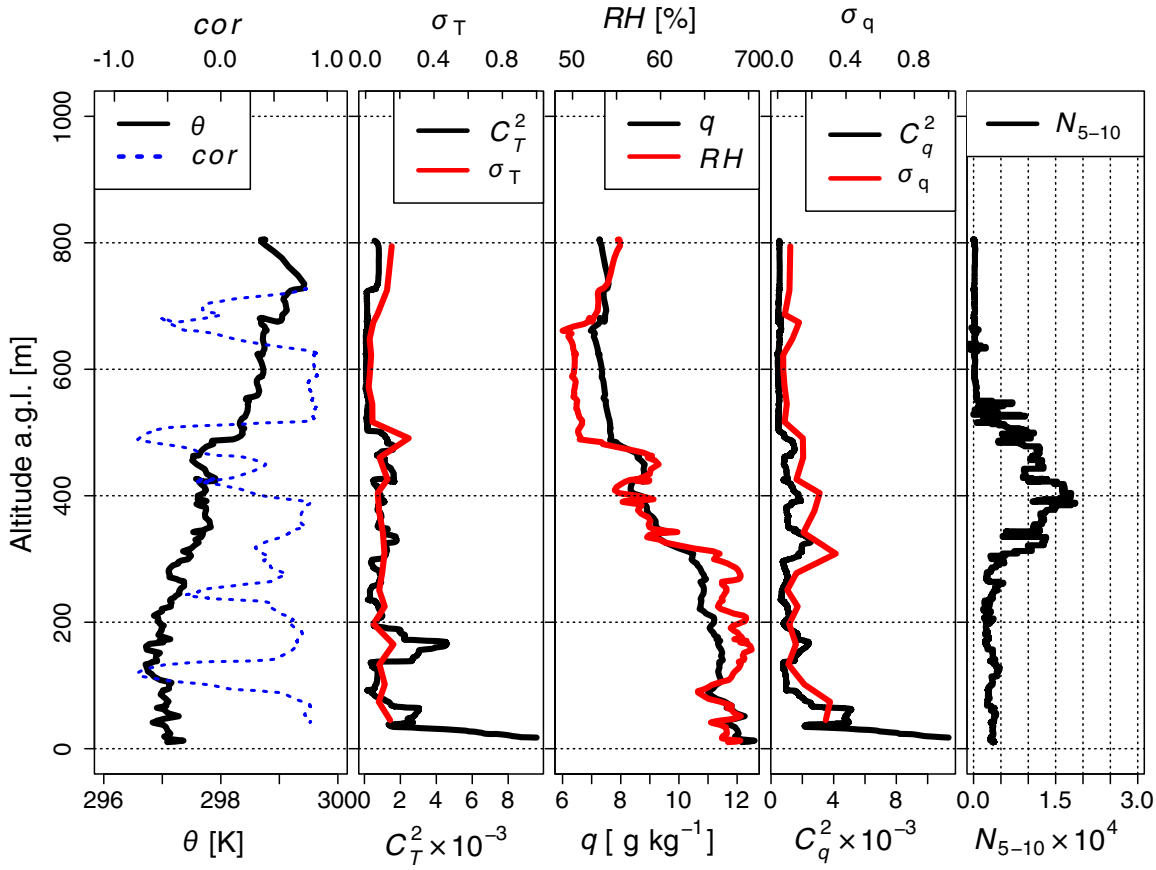

Fig. 8 Vertical profiles of ALADINA flight at 1004 UTC on 3 April 2014. Explanation same as in Fig. 5. (Phase 3)

The TDMPS indicates a rapid growth of number size distributions of $N_{5-10} \approx 0.1 \times 10^4\,\mathrm{cm}^{-3}$ to $N_{5-10} > 1.0 \times 10^4\,\mathrm{cm}^{-3}$ (Fig. 12) during the time period from 1025 to 1045 UTC. Prior to that, no considerable number concentrations of N_{5-10} were measured. However, both ground-based measurements show the appearance of N_{5-10} after the break of the inversion with subsequent growth, indicated with a black dashed line over the whole day, although the subsequent growth seems to be interrupted in the afternoon between 1400 and 1600 UTC, caused by cloud cover (Fig. 2). Before breakthrough of the shallow CBL, Aitken mode aerosol number concentrations with diameters between 40 nm and 100 nm are very high (dN/dlog $D_p \approx 5000\,\mathrm{cm}^{-3}$). This pre-existing particle population acts as a sink for condensable vapours existing in the atmosphere, as well as for the freshly formed particles and is called a condensation sink (CS). The condensation sink describes the loss rate (in molecules s^{-1}) of vapour to the aerosol phase existing in the atmosphere. When particle concentrations are high, the sink can be the limiting factor in the formation of new particles. All the vapour then condenses onto pre-existing particles instead of forming new ones (Wehner et al. 2007). The condensation sink is high and almost constant before the breakthrough and decreases after the increase of N_{5-10} particles at the ground (see Fig. 11).

4 Discussion

According to many previous studies on NPF events, solar radiation is an important prerequisite, because these events are thought to be driven by photochemical processes. For example,

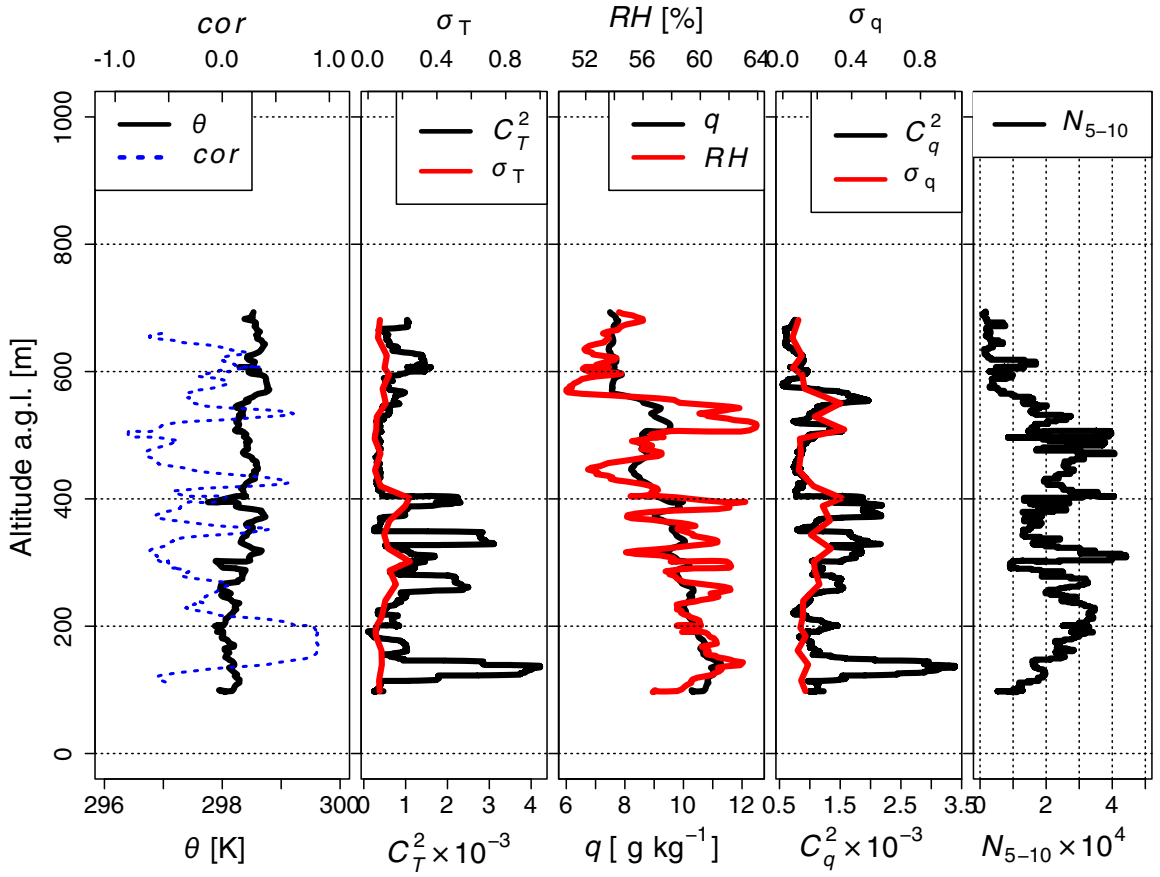

Fig. 9 Vertical profiles of ALADINA flight at 1045 UTC on 3 April 2014. Explanation same as in Fig. 5. (Phase 4)

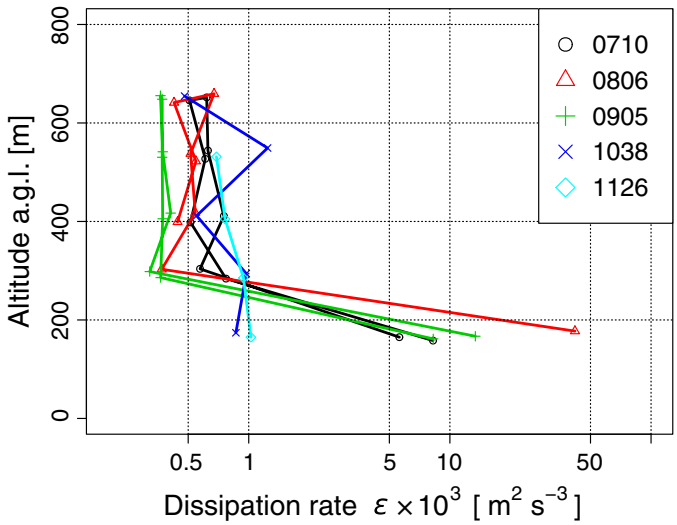

Fig. 10 Logarithmic plot of energy dissipation rates ε versus height during morning transition for all 5 MASC flights between 0710 and 1126 UTC. The first three flights (*green*, *red* and *black*) consist each of an ascent and descent, the last two (*blue* and *turquoise*) only of an ascent

regional-scale NPF events are typically observed only during daytime and on days with low cloud cover (Nilsson et al. 2001). According to Sect. 3.2, solar irradiation was only fractionally disturbed by clouds on 3 April 2014. In analogy to previous field studies in Melpitz (Birmili and Wiedensohler 2000; Größ et al. 2015), we assume solar radiation as the main factor controlling the occurrence of this NPF event, due to enhanced OH radical production leading to enhanced precursor gases production and also the most important energy source for turbulence and convection in the boundary layer.

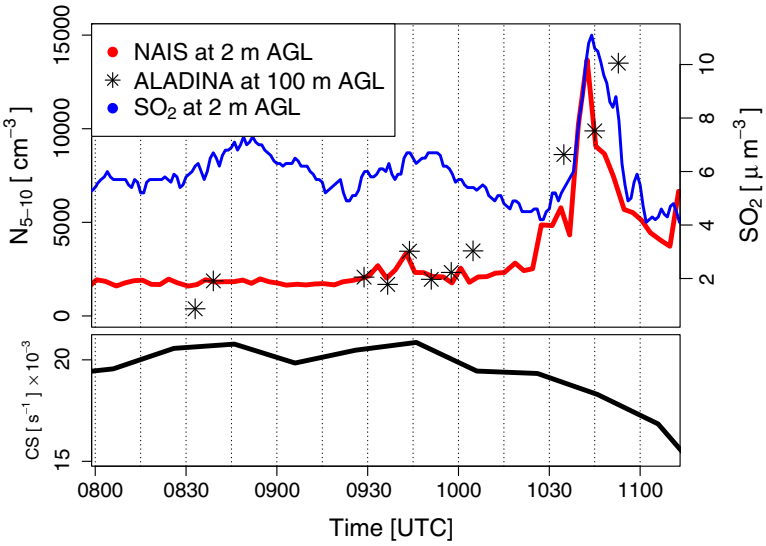

Fig. 11 *Upper plot* shows the evolution of integrated particle number concentrations for $N_{5-10}\,\mathrm{cm}^{-3}$ with a 3 min average measured by NAIS (*red*) at 2 m a.g.l. in Melpitz on 3 April 2014 between 0800 UTC and 1130 UTC. *Black stars* indicate the number concentrations for $N_{5-10}\,\mathrm{cm}^{-3}$ measured by ALADINA. The ALADINA number concentrations measurement is a 10-s average during the ascent or descent of a vertical profile around 100 m a.g.l. SO_2 (*blue*) measured by a gas concentration unit. The *bottom plot* shows the condensation sink (CS)

Table 1 Ground-based measurements of NO and NO_x in Melpitz on 3 April 2014, between 0500 and 1400 UTC

Time (UTC)	NO ($\mu g\,m^{-3}$)	NO_x ($\mu g\,m^{-3}$)
0500–0600	13.0	40.5
0700–0800	3.6	20.3
0900–1000	2.7	17.4
1000–1100	1.6	13.5
1100–1200	0.86	9.9
1200–1300	0.56	9.9
1300–1400	0.80	9.3

Values are 1-h means

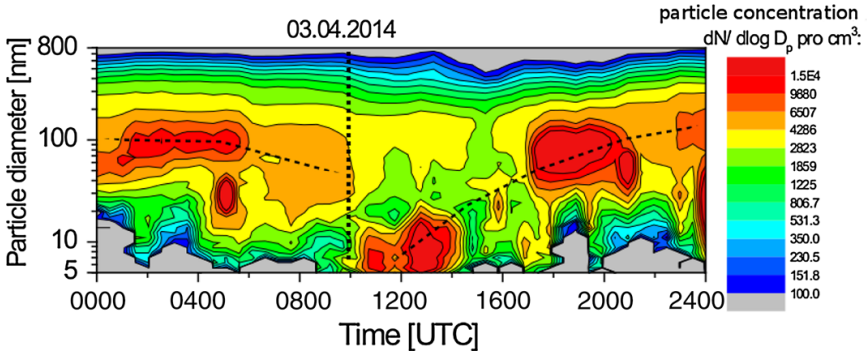

Fig. 12 Evolution of number size distributions measured by TDMPS (10-min average) at 2 m a.g.l. in Melpitz on 3 April 2014. The *colours* represent particle number concentration divided by the total number concentration, *grey* represents relatively low concentrations and *red* means high concentrations. *Vertical black dashed line* marks the moment when the shallow CBL breaks through the inversion. The *curved dashed line* presents roughly the maximum of number concentration for a size class

Further, there was a large radiative cooling at the surface during the night from 2 to 3 April 2014, due to clear-sky conditions. Thus a strong inversion developed at night, as shown in Sect. 3.2. The observations suggest that NPF occurred about one hour prior to the break-up of the near-surface inversion, most likely in the interface between the shallow convection and inversion, where entrainment can be assumed (see Bange et al. 2007). Due to the chronology of meteorological events, NPF near the ground was not measured at that time. We hypothesize that the start of NPF from 3 April 2014 is controlled among others by the thermodynamics of the inversion in this case study. As supposed by Nilsson and Kulmala (1998), the meteorological processes could trigger or enhance nucleation under conditions where the mean precursor concentrations were insufficient to provoke nucleation. On the basis of the observations, we can subdivide the NPF event into four chronological phases, dealing with different processes:

- **Phase 1:** Vertical profiles from 0833 - 0839 UTC (Fig. 5) show only small variation with almost no freshly nucleated particles.
- **Phase 2:** At 0929 UTC the start of a NPF event is observed, indicated by particles smaller than 10 nm (N_{5-10} particles). However, the event is only observed in the inversion layer not at the ground. It is a conspicuous observation that significant turbulent fluctuations of temperature and humidity occurred in the same layer (Figs. 6 and 7).
- **Phase 3:** At the end of phase 2 around 1004 UTC (Fig. 8), the shallow CBL breaks through the inversion and the freshly nucleated particles are spread downwards. Ground-level observations show a rapid rise of N_{5-10} particles and concentration of SO_2 increases at 1025 UTC (Fig. 11) as well as a decrease of CS.
- **Phase 4:** After 1036 UTC (Fig. 9), N_{5-10} particles are spread throughout the whole mixed layer.

4.1 Freshly Formed Particles Before the NPF Event (Phase 1)

In the first profiles at 0833 UTC no N_{5-10} is measured. At 0839 UTC some small spots of N_{5-10} appear in the zone between 200 and 300 m a.g.l. Our interpretation of this incident is that minor particle formation apparently happened in some spots in the zone between 200 and 300 m as well, before the main NPF event. At 0833 UTC, the inversion is just below this zone (Fig. 5), with a clear trend for convection to increase the mixed layer height further aloft. At 0833 UTC, no such new particles could be seen in the 200–300 m zone, but they are there at 0839 UTC, on ALADINA's downward flight. This would imply that the particles in that zone would have formed within the few minutes between 0833 UTC and 0839 UTC. At 0929 UTC, the concentration gradients in the 200–300 m zone seem to have leveled off to around 0.8×10^4 cm^{-3}, which is clearly higher than the initial background concentrations in that zone at 0833 UTC. Another option, which we cannot entirely rule out is the existence of certain horizontal inhomogeneities, possibly leading to the advection of particles between 0833 UTC and 0839 UTC.

4.2 Turbulent Fluctuations Related to the Start of NPF Event (Phase 2)

The atmospheric conditions are described in the layer where the NPF was initiated for phase 2. For all observed profiles during the morning transition before the breakthrough of the shallow CBL, the maximum of the structure parameter and standard deviation are always located within the inversion layer, where NPF started. Wyngaard and LeMone (1980) showed similar results with strong entrainment-induced peaks in structure parameter levels near the top of the mixed layer: C_T^2 values (that means turbulent temperature fluctuations) generated

by entrainment near the top of the boundary layer are as much as 100 times greater than those generated there by the surface fluxes. It should be noted that Wyngaard and LeMone (1980) and van den Kroonenberg et al. (2012) observed an exponential $-4/3$ decrease with height of the structure parameters in the well-mixed layer. This is not seen in our data, because we obtained measurements in a shallow CBL.

No maximum in the dissipation rate ε is detected in the inversion layer. Consequently, fewer wind fluctuations are observed in the inversion but large fluctuations of temperature and humidity, because of entrainment processes of overshooting thermals from shallow CBL into the stable stratified inversion layer. Similar observations were done during the SAT-URN experiment (Siebert et al. 2004), who observed likewise NPF in a layer with turbulent fluctuations.

It is an instrumental observation that the only layer in the vertical profile with significantly enhanced concentrations of N_{5-10} was observed in the inversion and was accompanied by the strong turbulent fluctuations expressed by $C_T^2, \sigma_T, C_q^2, \sigma_q$. Hence, a direct conclusion is that in this study NPF starts in the layer where maximum humidity and temperature fluctuations are measured and the maximum gradients of temperature and humidity are located before the breakthrough of the inversion layer by the shallow CBL. The measurements of our case study are consistent with the favorable conditions described by Easter and Peters (1994) and Nilsson and Kulmala (1998), who proposed NPF in the inversion layer due to high thermodynamic fluctuations and high gradients of temperature and humidity. Consequently, turbulence and non-linear mixing of thermodynamic variables could lead to favorable conditions (e.g. supersaturation of precursor gases) for NPF as assumed by Nilsson et al. (2001). Furthermore it backups the hypothesis from Bigg (1997), who suggested that in a strong stable stratified thermal layer NPF results from very sudden, but sporadic mixing of air.

A numerical study by Easter and Peters (1994) suggested that binary nucleation rates may increase by a factor up to 70 if humidity and temperature fluctuations are anti-correlated. Hence, a spatial correlation coefficient (cor) is plotted along the vertical profiles in Fig. 5, 6, 7, 8 and 9 (blue dotted line) with values between -1 for fully anti-correlated and $+1$ for fully correlated. When NPF occurs in the inversion at $\approx$500 m a.g.l. (explained in Sect. 3.3), indicated by enhanced number concentrations of N_{5-10}, likewise a strong anti-correlation (correlation coefficient $= -0.9$) is found in this layer (Figs. 6 and 7). At 1045 UTC (Fig. 9), after NPF is spread throughout the whole boundary layer the strongest anti-correlation is observed for the strongest N_{5-10} signal at 500 and 330 m. Note that the correlation is wiggly. RH and mixing ratio vary due to turbulence, which we assume to cause this wiggly behaviour of the correlation coefficient. In Figs. 6 and 7 an abrupt rise of 5–10 % RH is measured at 700 m a.g.l. Here, the anti-correlation is related to the increase of RH, since mixing ratio is increasing and temperature is decreasing with height. There are distinct hints that the hypothesis of enhanced nucleation rates in the case of an anti-correlation of humidity and temperature fluctuations is valid in the ABL. Whenever NPF is observed, a strong anti-correlation of humidity and temperature fluctuations can be assigned in this layer, although anti-correlation is also noticed in other regions, where no NPF is observed.

In this work, NPF was found to be associated with strong thermodynamic fluctuations in the same layer. Although we do not have the necessary in-situ data to prove the fluctuations being the unique reason for NPF (in particular, precursor gas concentrations in the upper layer are missing), we observe certain parallels with the hypothesis forwarded by Nilsson et al. (2001). In any case, sufficient precursor gases must be available. Unfortunately, we do not have such information for the inversion layer, but a rapid increase of SO_2 was observed, at the same time as the swift increase of N_{5-10} at the ground at 1025 UTC. It appears reasonable

that SO_2 and N_{5-10} particles are mixed downwards simultaneously from aloft, and that the precursor gas was situated already aloft in the inversion layer.

4.3 Downward Transport of Newly Formed Particles (Phase 3)

After the breakthrough of the shallow CBL, we consider whether the observed abrupt ground-level increase of N_{5-10} and SO_2 could be explained by the downward transport of newly formed particles from near the inversion (e.g. Nilsson et al. 2001).

At 1004 UTC, thermal convection reached the layer with NPF between 400 and 570 m (see Fig. 8) and started to transport N_{5-10} particles downwards. Hence, a broader layer with N_{5-10} is now observed between 250 and 570 m. Therefore, an explanation is that those particles observed during the morning flights in the inversion were mixed downwards and caused the strong and abrupt rise of N_{5-10} particles at the ground.

From the present data, it is not possible to determine the exact age of the small particles, but assuming a typical growth rate in the order of a few nm per hour (Kulmala et al. 2004), makes a nucleation process plausible as much as one hour prior to the observation of elevated N_{5-10}. However, the time increment of N_{5-10} increases to a local maximum at the ground in less than 60 min at 1045 UTC (see Fig. 11). In order to examine, if the increase of N_{5-10} at the ground can be explained by downward transport, two first order methods derived from Wehner et al. (2010) and Siebert et al. (2004) are performed: First, we assume that the mean energy dissipation rate shallow CBL by MASC (Fig. 10) during the profile at 1038 UTC ($\overline{\varepsilon} \approx 1 \times 10^{-3}$ m^2 s^{-3}), is approximately the same at around 1004 UTC when N_{5-10} particles started to spread downwards. $\overline{\varepsilon}$ is the mean value of all measured ε between 200 m and 600 m a.g.l. . Further, assuming the same $\overline{\varepsilon}$ for the height $z \approx 500$ m, the time scale τ_{mix} can be estimated which is needed to mix down the particles from z to ground level by

$$\tau_{\mathrm{mix}} \approx \left(\frac{z^2}{\overline{\varepsilon}}\right)^{\frac{1}{3}} \approx 630 \text{ s} \approx 10 \text{ min}. \tag{8}$$

Because of this short time scale the swift increase of N_{5-10}, observed by NAIS, can be explained by taking into account only vertical mixing of the particles, measured earlier by ALADINA in the inversion.

The second method to reinforce if the observed ground-level increase of N_{5-10} can be explained by taking into account only downward transport of newly formed particles, considers the vertical turbulent mixing (Siebert et al. 2004). The temporal evolution of the particle number concentration N (the indices for the size ranges are omitted) in the mixed layer, can be described as

$$\partial_t \overline{N} = -\partial_z \overline{w'N'} = \mathrm{K}\, \partial_z^2 \overline{N}, \tag{9}$$

where K is the turbulent exchange coefficient and $\overline{w'N'}$ is the mean vertical turbulent flux of N, which is approximated by the gradient approach also known as "K-Theory" (Berkowicz and Prahm 1979) with

$$\overline{w'N'} = \mathrm{K}\, \partial_z \overline{N}\ . \tag{10}$$

The formulation of Hanna (1968) can be used to derive the turbulent exchange coefficient, assuming that K is similar for momentum and particle concentrations. K is determined by the properties of the vertical velocity spectrum, in particular the standard deviation of the vertical wind σ_w and the wavenumber peak k_m, which represents the inverse of the typical length scale for the dominant eddies,

$$K = 0.085\,\sigma_w\,k_m^{-1}. \tag{11}$$

From the wind data of the MASC flight at 1004 UTC, $\sigma_w = 0.3$ and $k_m^{-1} = 230$ m is calculated, resulting in $K = 5.8\ \mathrm{m^2\ s^{-1}}$. Equation 9 can be approximated to

$$\frac{\Delta\,\overline{N}}{\Delta t} = \frac{\mathrm{K}}{(\Delta z)^2}\Delta\overline{N}, \tag{12}$$

with the complete method explained in detail in Siebert et al. (2004). In Eq. 12 the height difference is $\Delta z \approx 110$ m. This is the height difference between 380 m and 490 m a.g.l., marked with two red lines in Fig. 7. Within these heights, N_{5-10} increases distinctly from background number concentrations ($N_{5-10}^{\mathrm{Back}} \approx 0.2 \times 10^4\ \mathrm{cm^{-3}}$) to a maximum of $N_{5-10} \approx 2.6 \times 10^4\ \mathrm{cm^{-3}}$. The increase of N_{5-10} is $\Delta\overline{N} \approx 2.4 \times 10^4\ \mathrm{cm^{-3}}$. With $K = 5.8\ \mathrm{m^2\ s^{-1}}$, Eq. 12 yields a temporal change of particle number concentrations $\Delta\overline{N}/\Delta t \approx 11.6\ \mathrm{cm^{-3}s^{-1}}$. The transport of these particles down to ground level is rapid, about 10 min, as estimated in Eq. 8, after particles are mixed into the convective layer.

From ground-based measurements (Figs. 11 and 12), particles increase rapidly from background particle number concentrations at the ground $N_{5-10}^{\mathrm{Back}} \approx 0.2 \times 10^4\ \mathrm{cm^{-3}}$ to a local maximum value of $N_{5-10} \approx 1.4 \times 10^4\ \mathrm{cm^{-3}}$ between 1025 and 1045 UTC ($\Delta t = 1200$ s). Hence, the change of particle number concentrations ($\Delta\overline{N}/\Delta t \approx 10.0\ \mathrm{cm^{-3}s^{-1}}$) is the same as derived from ALADINA data ($\Delta\overline{N}/\Delta t \approx 11.6\ \mathrm{cm^{-3}s^{-1}}$) within the measurement uncertainty range of 15 %.

This leads to the conclusion that the burst of N_{5-10} at the ground level occurring between 1025 and 1045 UTC can be explained due to the vertical downward transport of newly formed particles at the inversion. No other source is needed for a reasonable explanation. An abrupt increase of SO_2 and a change of CS with N_{5-10} were observed simultaneously at the ground, but there there was no or very little horizontal advection of air near to the ground. A conclusive mechanism explaining the prompt increase, is that the precursor gas SO_2 and less CS were situated in the inversion layer before as well. As air is mixed down from the inversion layer precursor gas and less CS were carried with it. At the ground CS is almost constant and does not show a clear decrease just before the increase of N_{5-10}. This fact supports the interpretation of the NPF aloft and the downward transport of these freshly formed particles.

Further, the low concentrations of NO and NO_x (Table 1) do not rule out anthropogenic influence entirely, but it appears very unlikely to be the main responsible factor for the new particles observed between 1000 UTC and 1400 UTC when the atmosphere was perfectly mixed. The downward-mixing theory is also supported by the study of a four-year analysis of NPF events of ground-based aerosol observations in Melpitz by Größ et al. (2015). These authors noted a statistical correlation of NPF events near the ground with enhanced SO_2 concentrations, which were apparently entrained from aloft. The results from our work might thus provide a key to the explanation of these frequently occurring NPF events.

The airborne measurements and ground-based observations, together with the two first-order assumptions of vertical particle transport, support the hypothesis made by Nilsson et al. (2001) and Siebert et al. (2004), that NPF results due to effective mixing in the inversion layer.

4.4 Progress and Development of the NPF After Downward Spreading (Phase 4)

Between 1045 and 1053 UTC (see Fig. 4) NPF was continued or even enhanced during the mixing process and afterwards throughout the whole mixed layer. At 1053 UTC, the number concentrations of N_{5-10} in the mixed layer reached the maximum measured value

of $N_{5-10} \approx 6.0 \times 10^4\,\mathrm{cm}^{-3}$. Thus, additional new particles were formed within the whole mixed layer. Interestingly, this high concentration ($N_{5-10} \approx 6.0 \times 10^4\,\mathrm{cm}^{-3}$), measured by ALADINA in the middle part of the well mixed layer between 1045 and 1053 UTC, was never observed at the ground stations. For this particular NPF event the maximum concentration were assumed to be lower at the ground, because the particles were initially created at higher altitudes. With the process of downward spreading they peter out vertically then.

From the present observations it can be concluded that N_{5-10} particles measured by the ground-based instruments were advected downwards from the inversion. But after the break of the thermal inversion and the down-mixing, the process of NPF itself is assumed to spread downwards additionally. When this occurs, the whole mixed layer becomes favorable for forming new particles. This could explain why N_{5-10} is higher in profiles after 1045 UTC (Fig. 4) than the maximum number concentrations measured in the inversion layer before. A direct relation between large structure parameter and increased NPF can not be identified anymore. In the convective state of the boundary layer, turbulence is caused by convection. These dynamic convective eddies cause turbulent fluctuations of temperature and humidity as they travel through the mixed-layer. That is why temperature and humidity fluctuations are not located anymore in distinct layer but throughout the whole boundary layer such as NPF. It should be stressed again, that the high thermodynamic fluctuations in the inversion layer before were just assumed to be the trigger for the start of the NPF event.

It is very likely, as mentioned before, that sufficient precursor gases, besides turbulence caused by convection, are available throughout the whole mixed layer for NPF with the breakthrough of the shallow CBL. Moreover, the decrease of condensation sink (CS) can support the formation of new particles near the ground as mentioned in Sect. 3.3 (Fig. 11). The pre-existing particle population (e.g. Aitken Mode particles and large particles) acts as a sink for condensable vapours present in the atmosphere, as well as for the newly formed particles. CPC2 which measures particle sizes between 10 nm and 2 µm (N_{10}) indicates number concentrations of $\approx 8 \times 10^3\,\mathrm{cm}^{-3}$ for the lowest flight altitude at 100 m for all measured profiles until 1004 UTC (Fig. 4). In contrast, above the inversion CPC2 measures 75 % less N_{10} from which can be deduced that air aloft the inversion contains a smaller pre-existing particle population.

Hence, the decrease of condensation sink is a result of vertical mixing with air containing less pre-existing particles like Aitken Mode concentrations from aloft (see also Wehner et al. 2007). The TDMPS data (Fig. 12) shows this process too. During morning hours, the maximum concentration occurs in the Aitken mode ranging between 40 to 100 nm at ground level. At 1000 UTC this mode disappears, due to the break-up of the nocturnal inversion and subsequent dilution with air also from free atmosphere with relatively low Aitken mode number concentrations. This process was observed similarly in previous studies like Wehner et al. (2007), too. Therefore with the mixing from air above, the sink for condensing material is reduced and NPF and subsequent growth can be encouraged in addition at the ground now.

5 Conclusion

This paper presents an experimental case study of a NPF event, which occurred during the morning transition of the atmospheric boundary layer (ABL) on 3 April 2014, in Melpitz, eastern Germany. The event was characterized with high spatial resolution by unmanned aerial systems (UAS) and ground-based instruments. The observations represent, to our knowledge, the first characterization of a NPF event with respect to the airborne characterization of the

morning transition from a shallow convective boundary layer below a strong capping inversion layer to a mixed boundary layer with high temporal and spatial resolution of thermodynamic fluctuations, turbulence and N_{5-10} particle number concentrations.

Eleven vertical profiles of N_{5-10} number concentrations spanning a 140-min time period could be analyzed for the present study, thus demonstrating the complete time evolution of the NPF event, as opposed to only measuring during isolated periods as done in earlier studies like Wehner et al. (2010), Wehner et al. (2007), Siebert et al. (2007). The airborne observations showed the start of a NPF event with enhanced concentrations of N_{5-10} at around 400–500 m above ground within the inversion. Strong gradients of mean temperature ΔT and mixing ratio Δq as well as increased fluctuations of T and q were measured only in the inversion. The temperature structure parameter C_T^2 was up to 15 times higher in the inversion layer compared to the remaining parts of the vertical profile while C_q^2 was up to five times higher in the inversion layer, indicating strong temperature and humidity fluctuations. Likewise, profiles of the standard deviation of temperature (σ_T) and humidity (σ_q) show comparably high values in the inversion layer. There are distinct hints that enhanced nucleation rates are connected with an anti-correlation between humidity and temperature fluctuations as proposed by Easter and Peters (1994). NPF was observed in layers with strong anti-correlation of humidity and temperature fluctuations.

The airborne in-situ observations suggest that turbulence plays an important role in NPF: High turbulent fluctuations of temperature and humidity create the conditions for supersaturation of precursor gases due to non-linear mixing (Nilsson et al. 2001; Bigg 1997). The analysis supports the hypothesis that NPF was possibly initiated by the thermodynamics and turbulent fluctuations within the inversion layer.

Particle measurements with NAIS and TDMPS at ground level showed a rapid simultaneous increase of N_{5-10} and the precursor gas SO_2 a few minutes after breakthrough of the shallow CBL, where the enhanced number concentrations of N_{5-10} were found. With regard to the estimation of turbulent mixing and dissipation rates, it is very likely that these particles observed at the ground were formed locally at higher altitudes and mixed downwards, similar to findings of Wehner et al. (2010). Although in that study, NPF occurred in the residual layer.

After breakthrough of the shallow CBL, NPF was detected near the ground, as essential precursor gases for NPF like SO_2 were mixed downward from the inversion. No vertical measurements of potential precursor gases are available for the campaign. Moreover, with the breakthrough of the shallow CBL, the sink for condensing material is reduced as a result of vertical mixing with air from aloft. This air contains less Aitken mode particles and therefore can foster the formation of new particles and subsequent growth. It is worth to note that model simulations of particle formation in a convective boundary layer tend to predict the highest likelihood for nucleation near the top of the mixed layer (entrainment zone), mainly due to thermodynamic reasons (e.g. Hellmuth 2006).

These results might have consequences for the interpretation of earlier published observations of NPF events, particularly such observations, where data was recorded only at ground level. In the morning, stable thermal stratification may trap enhanced concentrations of nucleation mode particles at higher altitudes. Once daytime convection initiates, turbulence mixes the boundary layer, and the vertical profile of nucleation mode particles becomes more homogeneous. The ground-based observations without the airborne in-situ measurements may result in a misinterpretation or inexplicability of location and processes causing the increase in nucleation mode particles.

The present results of the vertical distribution of nucleation mode particles in the ABL and under which conditions NPF occurs with respect to the thermodynamic conditions provide valuable input for improving numeric models. In the future, it would be necessary to

have simultaneous, vertically resolved aerosol, chemical (precursor gases) and turbulence measurements within the boundary layer, in order to understand the nucleation process itself. For that, a campaign is planned in summer 2015 in Melpitz. Further, long term studies are necessary to compare favourable and non-favourable conditions for NPF events in inversions and near the ground.

Acknowledgments The authors thank the UAS pilots Lutz Bretschneider and Markus Auer for flying ALADINA and MASC safely over Melpitz. We thank Achim Grüner for technical support during preparing and conducting the campaigns in Melpitz. Thanks also to Johannes Größ for providing the NAIS-data from Melpitz. We thank Joe Smith and Ralf Käthner for the ground-crew support. This work is supported by the Deutsche Forschungsgemeinschaft (LA 2907/5-1, WI 1449/22-1, BA 1988/14-1).

References

Altstädter B, Platis A,Wehner B, Scholtz A,Wildmann N, Hermann M, Käthner R, Baars H, Bange J, Lampert A (2015)ALADINA: an unmanned research aircraft for observing vertical and horizontal distributions of ultrafine particles within the atmospheric boundary layer. Atmos Meas Tech 8(4):1627–1639. doi:10.5194/amt-8-1627-2015

Bange J, Spieß T, van den Kroonenberg AC (2007) Characteristics of the early-morning shallow convective boundary layer from helipod flights during STINHO-2. Theor Appl Climatol 90:113–126

Barbaro E, Arellano JVG, Ouwersloot HG, Schröter JS, Donovan DP, Krol MC (2014) Aerosols in the convective boundary layer: Shortwave radiation effects on the coupled land-atmosphere system. J Geophys Res Atmos 119(10):5845–5863

Berkowicz R, Prahm LP (1979) Generalization of K theory for turbulent diffusion. part I: Spectral turbulent diffusivity conceptpectral turbulent diffusivity concept. J Appl Meteorol 18(3):266–272

Bigg E (1997) A mechanism for the formation of new particles in the atmosphere. Atmos Res 43(2):129–137

Birmili W, Wiedensohler A (2000) New particle formation in the continental boundary layer: meteorological and gas phase parameter influence. Geophys Res Lett 27(20):3325–3328

Birmili W, Tomsche L, Sonntag A, Opelt C, Weinhold K, Nordmann S, Schmidt W (2013) Variability of aerosol particles in the urban atmosphere of Dresden (Germany): efects of spatial scale and particle size. Meteorol Z 22(2):195–211

Boy M, Hellmuth O, Korhonen H, Nilsson E, ReVelle D, Turnipseed A, Arnold F, Kulmala M (2006) MALTE-model to predict new aerosol formation in the lower troposphere. Atmos Chem Phys 6(12):4499–4517

Caughey S, Palmer S (1979) Some aspects of turbulence structure through the depth of the convective boundary layer. Q J R Meteorol Soc 105(446):811–827

Crumeyrolle S, Manninen H, Sellegri K, Roberts G, Gomes L, Kulmala M, Weigel R, Laj P, Schwarzenboeck A (2010) New particle formation events measured on board the ATR-42 aircraft during the EUCAARI campaign. Atmos Chem Phys 10(14):6721–6735

Davidson PA (2004) Turbulence: an introduction for scientists and engineers. Oxford University Press, Oxford 235 pp

Draxler R, Rolph G (2003) HYSPLIT (hybrid single-particle lagrangian integrated trajectory). NOAA Air Resources Laboratory, Silver Spring

Easter RC, Peters LK (1994) Binary homogeneous nucleation: temperature and relative humidity fluctuations, nonlinearity, and aspects of new particle production in the atmosphere. J Appl Meteorol 33(7):775–784

Größ J, Birmili W, Hamed A, Sonntag A, Wiedensohler A, Spindler G, Maninnen HE, Nieminen T, Kulmala M, Hõrrak U, Plass-Dülmer C (2015) Evolution of gaseous precursors and meteorological parameters during new particle formation events in the Central European boundary layer. Atmos Chem Phys Discuss 15(2):2305–2353. doi:10.5194/acpd-15-2305-2015, http://www.atmos-chem-phys-discuss.net/15/2305/2015/

Hanna SR (1968) A method of estimating vertical eddy transport in the planetary boundary layer using characteristics of the vertical velocity spectrum. J Atmos Sci 25(6):1026–1033

Hellmuth O (2006) Columnar modelling of nucleation burst evolution in the convective boundary layer-first results from a feasibility study Part I: Modelling approach. Atmos Chem Phys 6(12):4175–4214

Jaatinen A, Hamed A, Joutsensaari J, Mikkonen S, Birmili W, Wehner B, Spindler G, Wiedensohler A, Decesari S, Mircea M, Facchini MC, Junninen H, Kulmala M, Lehtined KEJ, Laaksonen A (2009) A comparison of new particle formation events in the boundary layer at three different sites in Europe. Boreal Environ Res 14:481–498

Kannosto J, Lemmetty M, Virtanen A, Mäkelä J, Keskinen J, Junninen H, Hussein T, Aalto P, Kulmala M (2008) Mode resolved density of atmospheric aerosol particles. Atmos Chem Phys Discuss 8(2):7263–7288

Kolmogorov A (1941) Local structure of turbulence in an incompressible fluid for very large Reynolds numbers. Dokl Akad Nauk SSSR 30:299–303

Korhonen P, Kulmala M, Laaksonen A, Viisanen Y, McGraw R, Seinfeld J (1999) Ternary nucleation of H_2SO_4, NH_3, and H_2O in the atmosphere. J Geophys Res Atmos 104(D21):26,349–26,353

Kulmala M, Vehkamäki H, Petäjä T, Dal Maso M, Lauri A, Kerminen VM, Birmili W, McMurry PH (2004) Formation and growth rates of ultrafine atmospheric particles: a review of observations. J Aerosol Sci 35(2):143–176

Kulmala M, Riipinen I, Sipilä M, Manninen HE, Petäjä T, Junninen H, Dal Maso M, Mordas G, Mirme A, Vana M, Hirsikko A, Laakso L, Harrison RM, Hanson I, Leung C, Lehtined KEJ, Kerminen VM (2007) Toward direct measurement of atmospheric nucleation. Science 318(5847):89–92

Lumley L, Panofsky H (1964) The structure of atmospheric turbulence. Wiley, New York 239 pp

Manninen HE, Petäjä T, Asmi E, Riipinen I, Nieminen T, Mikkilä J, Hõrrak U, Mirme A, Mirme S, Laakso L, Kerminen VM, Kulmala M (2009) Long-term field measurements of charged and neutral clusters using Neutral cluster and Air Ion Spectrometer (NAIS). Boreal Environ Res 14:591–605

Nilsson ED, Kulmala M (1998) The potential for atmospheric mixing processes to enhance the binary nucleation rate. J Geophys Res Atmos 103(D1):1381–1389

Nilsson E, Rannik Ü, Kulmala M, Buzorius G, O'dowd C (2001) Effects of continental boundary layer evolution, convection, turbulence and entrainment, on aerosol formation. Tellus B 53(4):441–461

Nojgaard JK, Nguyen QT, Glasius M, Sorensen LL (2012) Nucleation and Aitken mode atmospheric particles in relation to O_3 and NOX at semirural background in Denmark. Atmos Environ 49:275–283. doi:10.1016/j.atmosenv.2011.11.040

O'Dowd C, McFiggans G, Creasey DJ, Pirjola L, Hoell C, Smith MH, Allan BJ, Plane J, Heard DE, Lee JD, Pilling MJ, Kulmala M (1999) On the photochemical production of new particles in the coastal boundary layer. Geophys Res Lett 26(12):1707–1710

O'Dowd C, Yoon Y, Junkermann W, Aalto P, Kulmala M, Lihavainen H, Viisanen Y (2009) Airborne measurements of nucleation mode particles II: boreal forest nucleation events. Atmos Chem Phys 9(3):937–944

Pirjola L, O'Dowd CD, Brooks IM, Kulmala M (2000) Can new particle formation occur in the clean marine boundary layer? J Geophys Res Atmos 105(D21):26,531–26,546

Ramanathan V, Crutzen P, Kiehl J, Rosenfeld D (2001a) Aerosols, climate, and the hydrological cycle. Science 294(5549):2119–2124

Ramanathan V, Crutzen PJ, Lelieveld J, Mitra A, Althausen D, Anderson J, Andreae M, Cantrell W, Cass G, Chung C, Clarke AD, Coakley J, Collins W, Conant W, Dulac F, Heintzenberg J, Heymsfield A, Holben B, Howell S, Hudson J, Jayaraman A, Kiehl J, Krishnamurti T, Lubin D, McFarquhar G, Novakov T, Ogren J, Podgorny I, Prather K, Priestly K, Prospero J, Quinn P, Rajeev K, Rasch P, Rupert SRS, Satheesh S, Shaw G, Sheridan P, Valero F (2001b) Indian Ocean experiment: an integrated analysis of the climate forcing and effects of the great Indo-Asian haze. J Geophys Res 106(D22):28,371–28,398

Rosenfeld D (2000) Suppression of rain and snow by urban and industrial air pollution. Science 287(5459):1793–1796

Seinfeld JH, Pandis SN (2012) Atmospheric chemistry and physics: from air pollution to climate change. Wiley, New York

Siebert H, Stratmann F, Wehner B (2004) First observations of increased ultrafine particle number concentrations near the inversion of a continental planetary boundary layer and its relation to ground-based measurements. Geophys Res Lett 31(9):L09102

Siebert H, Wehner B, Hellmuth O, Stratmann F, Boy M, Kulmala M (2007) New-particle formation in connection with a nocturnal low-level jet: observations and modeling results. Geophys Res Lett. doi:10.1029/2007GL029,891

Sipilä M, Berndt T, Petäjä T, Brus D, Vanhanen J, Stratmann F, Patokoski J, Mauldin RL, Hyvärinen AP, Lihavainen H, Kulmala M (2010) The role of sulfuric acid in atmospheric nucleation. Science 327(5970):1243–1246

Spindler G, Grüner A, Müller K, Schlimper S, Herrmann H (2013) Long-term size-segregated particle (PM10, PM2.5, PM1) characterization study at Melpitz-influence of air mass inflow, weather conditions and season. J Atmos Chem 70(2):165–195

Stratmann F, Siebert H, Spindler G, Wehner B, Althausen D, Heintzenberg J, Hellmuth O, Rinke R, Schmieder U, Seidel C et al (2003) New-particle formation events in a continental boundary layer: first results from the SATURN experiment. Atmos Chem Phys 3(5):1445–1459

Tatarskii VI (1971) The effects of the turbulent atmosphere on wave propagation. Israel Program for Scientific Translations, Jerusalem: 472 pp

van den Kroonenberg A, Martin S, Beyrich F, Bange J (2012) Spatially-averaged temperature structure parameter over a heterogeneous surface measured by an unmanned aerial vehicle. Boundary-Layer Meteorol 142(1):55–77

Weber AP, Friedlander SK (1997) In situ determination of the activation energy for restructuring of nanometer aerosol agglomerates. J Aerosol Sci 28(2):179–192

Wehner B, Siebert H, Stratmann F, Tuch T, Wiedensohler A, Petäjä T, Dal Maso M, Kulmala M (2007) Horizontal homogeneity and vertical extent of new particle formation events. Tellus B 59(3):362–371

Wehner B, Siebert H, Ansmann A, Ditas F, Seifert P, Stratmann F, Wiedensohler A, Apituley A, Shaw R, Manninen H, Kulmala M (2010) Observations of turbulence-induced new particle formation in the residual layer. Atmos Chem Phys 10(9):4319–4330

Westin K, Boiko A, Klingmann B, Kozlov V, Alfredsson P (1994) Experiments in a boundary layer subjected to free stream turbulence. Part 1. Boundary layer structure and receptivity. J Fluid Mech 281:193–218

Wiedensohler A, Covert DS, Swietlicki E, Aalto P, Heintzenberg J, Leck C (1996) Occurrence of an ultrafine particle mode less than 20 nm in diameter in the marine boundary layer during Arctic summer and autumn. Tellus B 48(2):213–222

Wiedensohler A, Cheng Y, Nowak A, Wehner B, Achtert P, Berghof M, Birmili W, Wu Z, Hu M, Zhu T, Takegawa N, Kita K, Kondo Y, Lou S, Hofzumahaus A, Holland F, Wahner A, Gunthe S, Rose D, Su H, Pöschl U (2009) Rapid aerosol particle growth and increase of cloud condensation nucleus activity by secondary aerosol formation and condensation: a case study for regional air pollution in northeastern China. J Geophys Res Atmos 114(D2):D00G08

Wiedensohler A, Birmili W, Nowak A, Sonntag A, Weinhold K, Merkel M, Wehner B, Tuch T, Pfeifer S, Fiebig M, Fjäraa A, Asmi E, Sellegri K, Depuy R, Venzac H, Villani P, Laj P, Aalto P, Ogren J, Swietlicki E, Williams P, Roldin P, Quincey P, Hüglin C, Fierz-Schmidhauser R, Gysel M, Weingartner E, Riccobono F, Santos S, Grüning C, Faloon K, Beddows D, Harrison R, Monahan C, Jennings S, O'Dowd C, Marinoni A, Horn HG, Keck L, Jiang J, Scheckman J, McMurry PH, Deng Z, Zhao C, Moerman M, Henzing B, de Leeuw G, Löschau G, Bastian S (2012) Mobility particle size spectrometers: harmonization of technical standards and data structure to facilitate high quality long-term observations of atmospheric particle number size distributions. Atmos Meas Tech 5:657–685

Wildmann N, Mauz M, Bange J (2013) Two fast temperature sensors for probing of the atmospheric boundary layer using small remotely piloted aircraft (RPA). Atmos Meas Tech 6:2101–2113. doi:10.5194/amt-6-2101-2013

Wildmann N, Hofsäß M, Weimer F, Joos A, Bange J (2014a) MASC-a small remotely piloted aircraft (RPA) for wind energy research. Adv Sci Res 11(1):55–61

Wildmann N, Ravi S, Bange J (2014b) Towards higher accuracy and better frequency response with standard multi-hole probes in turbulence measurement with remotely piloted aircraft (RPA). Atmos Meas Tech 7(4):1027–1041

Wyngaard J, LeMone M (1980) Behavior of the refractive index structure parameter in the entraining convective boundary layer. J Atmos Sci 37(7):1573–1585

Wyngaard JC, Izumi Y, Collins SA (1971) Behavior of the refractive-index-structure parameter near the ground. J Opt Soc Am 61:1646–1650

A.2 Analysis of the influence of a lake on the lower convective boundary layer from airborne observations - Publication II

Meteorologische Zeitschrift, PrePub DOI 10.1127/metz/2016/0802

Boundary Layer Meteorology

Analysis of the influence of a lake on the lower convective boundary layer from airborne observations

Andreas Platis[1]*, Daniel Martinez-Villagrasa[2], Frank Beyrich[3] and Jens Bange[1]

[1]Zentrum für Angewandte Geowissenschaften, Universität Tübingen, Germany
[2]University of the Balearic Islands, Palma, Mallorca, Spain
[3]Deutscher Wetterdienst (DWD) Meteorologisches Observatorium Lindenberg, Germany

(Manuscript received April 22, 2016; in revised form August 30, 2016; accepted September 9, 2016)

Abstract

The influence of an intermediate-scale lake, with a dimension of approximately 2 km × 10 km, on a convective boundary layer has been analysed. Data were collected by the airborne platform Helipod during the STINHO 2002 and LITFASS 2003 campaigns in eastern Germany, during early summer months, when the lake was much colder than the surrounding surface. The objective was to assess which atmospheric parameters show influence from the lake by the airborne observations. While spatial variability for mean quantities is not significant at the observation height of 70 m and above, the second-order statistics related to potential temperature exhibit a clear decrease in the vicinity of the lake for measurements taken below 100 m above ground level. Second-order statistics of humidity and vertical wind velocity are not suited to identify the foot print of the lake in our study. Several length scales of surface heterogeneity were calculated following previous studies. Only the scale that considers vertical velocity is compatible with our airborne observations. In addition, the application of a convective scale indicates that the lake could affect the lower convective boundary layer above the lake and above the surrounding land downstream of the flow for low wind speeds (below 4 m s^{-1}). Finally, the downstream propagation of the lake influence has been addressed by calculating the cross-correlation function between the surface radiative temperature and the variance of potential temperature. A clear relationship between the spatial lag of the maximum correlation and the horizontal advectivon could be identified.

Keywords: Helipod, Lake, LITFASS 2003, Convective boundary layer, Surface heterogeneity influences, turbulence

1 Introduction

Local and regional climate and weather is affected by the interaction between the land and the atmospheric boundary layer (ABL) and depends highly on the surface characteristics, which may influence the spatial structure of the ABL. Natural landscapes are usually heterogeneous with different surface types like patches of farmland, water, villages, forests, etc., each with different heat, moisture and roughness characteristics. These specific features accompanied with different scales of surface heterogeneity (usually varying from meters to kilometers), generates different sizes and strengths of turbulent eddies which affect the overlying convective boundary layer (CBL). Therefore, the vertical extension of this influence depends on the characteristic horizontal scale of surface heterogeneity (L_{het}), the turbulence intensity, thermal stability and the horizontal advection of the boundary-layer flow (Mahrt, 1996). The horizontal variability of the turbulent structure may be influenced by both the length scale and amplitude of the surface heterogeneity (Mahrt, 2000).

A number of studies addressed the interaction between a heterogeneous surface and the ABL mostly by high-resolution large eddy simulation (LES) in the last 25 years (Hadfield et al., 1991; Hadfield et al., 1992; Avissar and Schmidt, 1998; Letzel and Raasch, 2003). They have found that the simulated CBL structure was strongly affected by the spatial variation of surface heat flux and that larger scales of landscape heterogeneity have more influence on the CBL. However, many studies have been performed with simplified surface conditions and only one dimensional heterogeneous heat flux fields.

Simulations with realistic surface data from field campaigns have been performed only recently as they demand high computational resources (Sühring and Raasch, 2013; Maronga and Raasch, 2013; Maronga et al., 2014; Huang and Margulis, 2009). Based on the LES results from two selected cases of the Lindenberg Inhomogeneous Terrain - Fluxes between Atmosphere and Surface: A long-term Study (LITFASS 2003) campaign with ground-based measured surface forcing data as an input for LES, Sühring and Raasch (2013) and Maronga and Raasch (2013) concluded that the influence of surface heterogeneity is present throughout the entire boundary layer for both sensible and latent heat fluxes during strong CBL conditions.

*Corresponding author: Andreas Platis, Zentrum für Angewandte Geowissenschaften, Universität Tübingen, Hölderlinstr. 12, 72074 Tübingen, Germany, e-mail: andreas.platis@uni-tuebingen.de

They did not detect any blending height (above which the influence of the surface heterogeneity vanishes) for convective conditions and L_{het} larger than the boundary-layer height z_i. In another LITFASS-2003 case study Maronga et al. (2014) showed by LES that local effects of surface heterogeneity remain prominent in the lower ABL. They could not give any proof for a blending height for the temperature structure parameter (a measure for temperature fluctuation similar to the temperature variance σ_θ), but for the LITFASS-2003 case study it seems that blending of the temperature structure parameter occur above several tens of metres above the ground. Furthermore, they conclude that the structure parameter for temperature is highly correlated with the surface sensible heat flux. However, structure parameter for humidity (describes the strength of humidity fluctuations) is decoupled from the latent surface flux even at low levels which is ascribed to the entrainment of dry air at the top of the boundary layer. Huang and Margulis (2009) discovered that potential temperature is more sensitive to surface heterogeneity than humidity. By using vertical profiles of temperature variance they could identify a thermal blending height in a CBL which was in good agreement to predictions from Wood and Mason (1991) and Mahrt (2000).

The blending height is viewed here as a scaling depth that describes the decrease of the influence of surface heterogeneity with height. A blending height is not a sharp boundary where the influence of surface heterogeneity suddenly and completely vanishes, but it describes a vertical scale at which the impact of surface heterogeneity decreases to some relatively small value. Different formulations of this height have been discussed in the literature, depending on which forcings are more relevant (for a complete review see Mahrt, 2000; Bange et al., 2006). The blending height can be reformulated in terms of internal boundary layers (IBL). An IBL grows to a maximum depth which is small compared to the upstream boundary-layer depth, and then encounters a new surface type and looses surface support (Mahrt, 2000). An IBL is expected if a clear change in the mean variables is identified.

Flow of marine air over a heated land surface is a classic example of the mesoscale internal boundary layer, see references in Garratt (1990). Another possible location where an IBL can form is above a lake. Unlike a large uniform open ocean the fetch above a lake is typically limited, which supports the development of a local IBL. Panofsky et al. (1982) and Højstrup (1982) already demonstrated that the variance spectra of the horizontal wind components in an IBL were influenced by upstream conditions. However, on smaller scales like an intermediate-size lake (only a few kilometres width) a well defined surface discontinuity is not necessarily transferred into the flow since the boundary layer may adjust without the formation of a new IBL. This situation may be enhanced when the change of surface properties is not sharp or is of small amplitude (Mahrt, 2000). An adjusting boundary flow is characterized by horizontal changes of some of the higher moments but does not exhibit significant horizontal variation of the mean variables. Such boundary-layer adjustments are probably common for smaller surface heterogeneity scales, like the intermediate-sized lake in our study, but have received little attention so far.

Comprehensive studies of the direct influence of a lake on the lower ABL are scarce. Sahlée et al. (2014) showed that the structure of the turbulence above the lake is influenced by the surroundings. Variance spectra of both horizontal velocity and scalars during both unstable and stable stratification displayed a low frequency peak. However, a lack of concurrent observations over the adjacent land, precluded any comparison of the spatial structure between land and lake. In a study from Samuelsson et al. (2010) the impact of lakes on the European climate was considered. A simulation where all lakes in the model domain are replaced by land surface is compared with a simulation including lakes. The numerical results stated that the lakes induce a warming on the European climate for all seasons. However the study does not show any direct impact on the boundary layer or the local flow. Based on airborne observations obtained during the Upper Spencer Gulf experiments in South Australia, Shao et al. (1991) and Shao and Hacker (1990) investigated the structure of turbulence in a coastal boundary layer, which is an extreme case of horizontal inhomogeneity. They showed that the boundary layer over this highly non-uniform surface is characterized by extensive variations in its thermal stratification and turbulence characteristics and that the behaviour of statistical parameters of second- and higher moments seemed to be determined mainly by local forcing. Bange et al. (2006) analysed airborne measurements from the LITFASS-2003 and Structure of the Turbulent transport over INHOmogeneous surfaces (STINHO-2) field campaigns to study the response of second-order statistics like turbulent flux profiles to a patchy landscape with different underlying surfaces like farmland, forest and a lake. The case studies showed that the sensible heat fluxes determined over the different sub-areas presented clearly different values at surface level and at 80 m. Especially, the vertical profiles over water surfaces produced its own vertical profile of sensible heat flux under weak-wind conditions, apparently unaffected by the surrounding forest and farmland.

Aforementioned works like Sühring and Raasch (2013) and Bange et al. (2006) show evidence that the lake has an influence on the vertical profile of latent and sensible heat fluxes above the lake. However, the authors did not find any scaling depth (as those by Mahrt, 2000; Strunin et al., 2004) that could successfully predict the conditions for a horizontal mixing state of the CBL. In addition, none of the scaling parameters analysed by e.g. Bange et al. (2006) and Sühring and Raasch (2013) were successful in predicting the vertical extension of the surface heterogeneity or explaining the spatial variability of latent heat fluxes. One possible explanation could be that too many different types

of surfaces, and hence heterogeneity scales, where involved in such analysis. Further Sühring and Raasch (2013) argued that those flights in Bange et al. (2006) that showed horizontal mixing had a poor statistical representation of the mean flux estimation from a single leg and thus, they are not suitable for such studies.

In the present study airborne measurements from LITFASS-2003 and STINHO-2 field campaigns (Beyrich et al., 2002; Beyrich and Mengelkamp, 2006) are analysed in order to evaluate if the influence of a lake on spatial structure of the convective boundary layer (CBL) is apparent. The lake is of intermediate size with a dimension of approximately $2\times10\,\mathrm{km}^2$ and called Scharmützelsee. It represents a surface heterogeneity with a well defined length scale (lake boundaries) and a sharp and strong change in surface conditions. This is because it has a colder and smoother surface and is surrounded by warmer and rougher terrain during the measurement period in late spring and early summer time. Additional flights from the field campaigns used in Bange et al. (2006) and Sühring and Raasch (2013) were analysed. We report comprehensive observations of the lake influence on the first and second order statistics like the variance of temperature and humidity by airborne measurements and depict the limitations of such measurements regarding the statistical significance. We determine the key parameters that contribute to the observed spatial changes over lake and land and show as well the lack of lake influence on certain parameters. Further, we try to characterize the horizontal shift of the lake influence. The study evaluates if an IBL can be observed for the LITFASS-2003 area and describes in more detail the downstream propagation of the lake-influenced boundary layer. We follow the suggestions and analysis of blending heights and IBL published by Raupach and Finnigan (1995); Mahrt (1996); Mahrt (2000); Wood and Mason (1991). The proposed minimum horizontal scale (L_{het} which is described by theses studies) of the surface heterogeneity that would influence the airborne measurements at observation level, is checked and compared with the current airborne data set.

Section 2 briefly describes the experimental dataset used in the present study. The main flow characteristics close to the surface over the lake-land discontinuity as well as an error discussion are addressed for a case study in Section 3, with an extension to the rest of selected cases. Section 4 assesses the length scales that describe the vertical extension of surface heterogeneity with the current dataset, while Section 5 studies the stream wise propagation of the heterogeneity influence. Finally, a conclusion is presented in Section 6.

2 Experiment

2.1 Dataset

The data analysed in this study were collected during two consecutive field campaigns in the summers of 2002 and 2003, that were part of the series of the LITFASS experiments. This program was initiated in 1995 in order to develop and test a strategy for the determination of the area-averaged turbulent fluxes over a heterogeneous landscape (see Beyrich et al. (2002) for more details). The STINHO-2 experiment took place between 24 June and 10 July, 2002, (Raabe et al., 2005), while the LITFASS-2003 campaign was carried out between 19 May and 17 June, 2003 (Beyrich and Mengelkamp, 2006).

Both campaigns were performed around the MOL-RAO (Meteorological Observatory Lindenberg – Richard-Aßmann Observatory) of the German Meteorological Service (Deutscher Wetterdienst, DWD) in the area of Brandenburg, Germany, 60 km south-east from Berlin. The experimental site is a $20 \times 20\,\mathrm{km}^2$ flat area with an elevation difference across the site of less than 100 m. The region consists of a coniferous forest in the western part (43 % of the area) and agricultural fields in the eastern part (31 %, mainly cereals). The whole area is covered by lakes and villages that add heterogeneity to the field. The lake Scharmützelsee has a dimension of approximately $2 \times 10\,\mathrm{km}^2$, and the long-axis is mainly oriented north-south.

The campaigns were part of the EVA_GRIPS (regional EVAporation at GRId/Pixel Scale over heterogeneous surfaces) and the VERTIKO (VERTIcal transport of energy and trace gases at anchor stations under Complex natural conditions) networks and provided a comprehensive data set on surface-atmosphere interaction processes at the mesoscale (Mengelkamp et al., 2006; Göckede et al., 2004). Measurements included the instrumentation equipment from the Falkenberg boundary-layer field site (GM Falkenberg) of DWD, a regional network of micro-meteorological stations, the 99-m meteorological tower and airborne measurements sampled by the helicopter-borne turbulence probe Helipod, among other ground-based remote sensing devices (see Raabe et al. (2005) and Beyrich and Mengelkamp (2006) for a complete overview).

The Helipod is a measurement system designed for boundary-layer field experiments. It is an autonomously operating sensor package attached to a 15 m rope below a helicopter of almost any type. The Helipod is equipped with its own power supply, on-board computer, data storage, navigation systems, radar altimeter and carries a sensor equipment for in-situ measurements of the atmospheric wind vector, humidity and air and surface temperatures at 100 Hz sampling rate. The resolution of the fast resistance temperature sensor is high (much better than 0.1 Kelvin) and about 30 Hz, which is fast enough to resolve turbulent temperature fluctuations (Bange and Roth, 1999). Hence, it is suited for small-scale turbulence measurements and for calculating the turbulent fluxes using the eddy covariance method. The surface temperature is measured by an infrared temperature sensor simultaneously with the thermodynamic measurements. At a mission speed of $40\,\mathrm{m\,s}^{-1}$ the Helipod is outside the down-wash area of the helicopter's

Table 1: List of selected flights. All flights took place in 2003 except STI09 which was in 2002. Ws is the wind speed. Local time is UTC + 2 hours. Times are the entire flight time.

Flight code	Date	Time (UTC)	Heights of legs (m)	Weather (Clouds)	Wind dir (°)	Ws ($m\,s^{-1}$)
IBL-lake						
STI09	09.07	1320–1500	70, 80, 90, 180, 280	2/8 Ci	150	6.0
LIT13	13.06	1312–1412	86, 472, 603, 742, 922	5/8 Ci	300	8.0
LIT14	14.06	0922–1020	86, 472, 603, 742, 922	7/8 Ci, 3/8 Cu	280	4.0
North box						
LIT24	24.05	1312–1405	100, 400, 700	4–6/8 Ci	141	6.3
LIT25	25.05	0929–1040	100, 400, 700	1/8 Ci	142	2.2
LIT07	07.06	0953–1050	100, 400, 700	1/8 Ci	151	3.3
E-W grids						
LIT28	28.05	1203–1307	100	3–4/8 Ci	28–54	5.0
LIT03	03.06	1122–1225	100	4/8 Ci	92–148	2.6
LIT04	04.06	1216–1321	100	3–6/8 Ci	125–159	5.0
LIT06	06.06	1132–1239	100	2/8 Ci	260–310	5.5
LIT10	10.06	0906–1010	100	5/8 Ci	113–175	3.0
LIT12	12.06	0923–1026	100	2–3/8 Ci	274–348	4.0
LIT13	13.06	0940–1041	100	3–2/8 Ci	300	4.3
LIT17	17.06	1235–1333	100	3/8 Cu 4/8 Ci	68–168	2.8

rotor blades. More details can be found in Bange et al. (2002) and Bange and Roth (1999).

More than 100 flight hours of Helipod data were compiled during these two field campaigns. A total of 14 flights that covered the lake-land transition were selected, 13 from the LITFASS-2003 experiment and an additional one from the STINHO-2 experiment (see Table 1). Basically, all flights included in this study had at least one leg crossing the lake in a west-east direction at about 100 m above ground level. In the following study all given heights are always with respect to the ground level.

All selected flights that contribute to our particular database were performed either in the morning or in the early afternoon in a convective regime, although with different wind conditions. Three types of flight patterns can be recognized from this data base, that will be referred as 'IBL-lake', 'North Box' and 'E-W grids' for the rest of the text (Figure 1b) and Table 1). There are three flights that crossed the lake approximately parallel to the mean wind direction during the flight (IBL-lake, see Figure 1a)), which was either southeasterly (STI09) or northwesterly (LIT13, LIT14). The rest of them contain legs in the west-east direction, crossing the lake at different heights over the same latitude (North Box) or over three different sections of the lake, from the southern edge to the middle part of the lake (E-W grids), see Figure 1.

2.2 Data analysis

We have analysed the spatial series and the second-order statistics for potential temperature θ, water vapor mixing ratio m and wind vector components. In order to study how the surface heterogeneity affects them and up to which height, it is necessary to determine a suitable horizontal length scale over which we compute the first- and second-order statistics within sub-legs (data windows) along a flight leg. As an example, the potential temperature variance is computed as

$$\sigma_\theta^2 = \frac{1}{N}\sum_{n=1}^{N}(\theta_n - \overline{\theta})^2 \qquad (2.1)$$

where N is the number of data points within the moving data window. The width of this window has to be small enough to resolve the surface heterogeneity along the leg, but large enough to cover the main scales that contribute to the turbulent fluctuations. van den Kroonenberg et al. (2012) defined (for a similar experiment at the same site) a minimum window width of twice the integral length scale to ensure that all turbulent scales within the inertial sub-range are included. Previous studies of our dataset show that the integral length scales of sensible and latent heat fluxes measured by the Helipod are smaller than 500 m (Bange et al., 2006). Thus, we have defined windows of 1-km width using unweighted means, sequentially shifted through the leg by increments of 250 m. In summary, for flux calculations, this value does not necessarily account for the largest eddies during strong convection conditions. However, 1-km width is a good compromise between the largest eddy scales within the surface layer and the detection of a possible lake influence. A similar strategy was followed by Mahrt (2000). For all these reasons, we believe that 1-km window is expected to capture almost all of the turbulent flux and its spatial variability. A more precise discussion on the sampling error is given in Section 3.2.

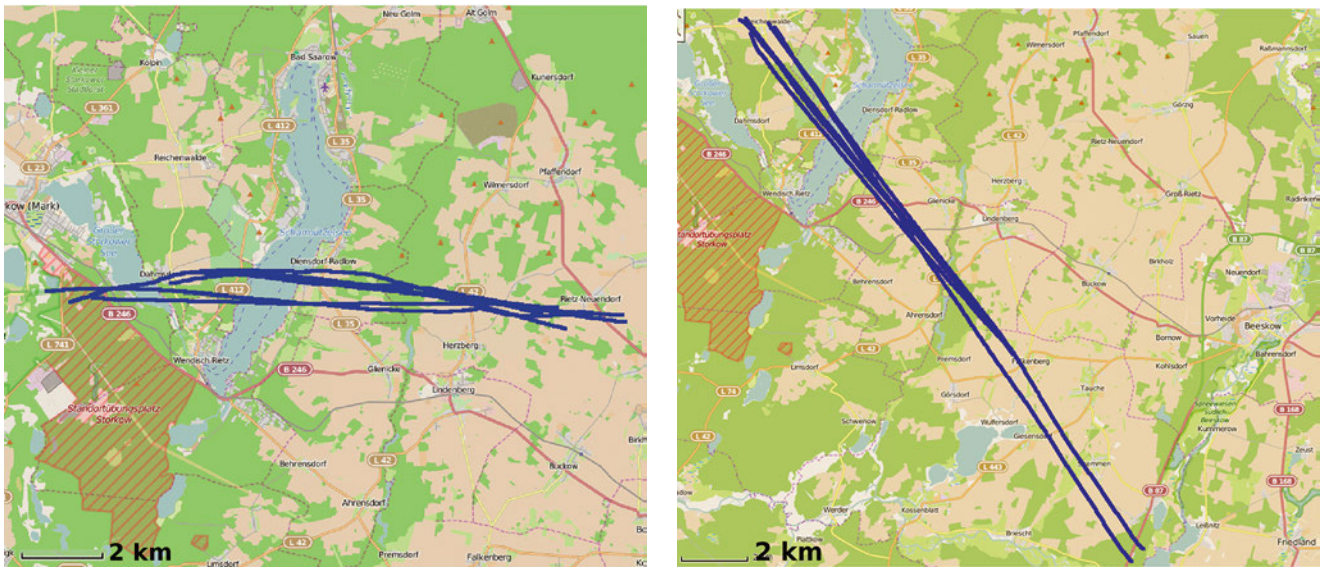

a) b)

Figure 1: Flight-tracks (blue lines) representative of those flights that cross the lake Scharmützelsee (a) following the mean wind (STI09, LIT13 and LIT14) or (b) in the east-west direction at different heights or over different sections of the lake (the rest of flights, see Tab. 1). Green areas refer to forest surfaces, blue to water and beige to farmland. Hatching areas indicate military zones. Source. Open Street Map. a) Flight-tracks of IBL-lake flights (STI09, LIT13, LIT14), b) Flight-tracks of LITFASS2003 flights (Northbox) and (E-W grids).

Table 2: Chronology of the legs performed during STI09 flight. Error in the Height column represents the standard deviation. Local time is UTC + 2 hours. Times report the analyzed flight period.

Time (UTC)	leg number (position)	Height (m)	θ average (K)	Wind dir (°)	Wind speed ($m\,s^{-1}$)	leg-parallel wind speed ($m\,s^{-1}$)
1327–1333	MT 02	83 ±17	303.5	143	6.3	6.3
1344–1352	MT 04	170 ±26	303.7	142	7.1	7.1
1402–1409	MT 06	282 ±28	303.9	145	6.6	6.6
1438–1444	MT 12	66 ±15	304.5	162	5.8	5.4
1500–1506	MT 16	68 ±12	304.7	162	5.5	5.1

3 Results

3.1 STINHO-2 Flight (STI09)

The flights chosen for the analysis of the land-water transition around lake Scharmützelsee (Table 1) were composed by straight and leveled paths (called legs) at different heights, ranging from 70 to 280 m. The distance of each single leg was between 7 and 16 km and covered different surface patches (forest, farmland, lake) along the leg. The main interest of this study is the impact of the lake. The influence of other patches, which are not in the vicinity of the lake, are not important. Those which are located close to the lake may influence the signal as well. However, the impact is very low since length scales of the other patches are much smaller than the lake width. Further, surface discontinuities, i.e. the change in surface forcing for the other patches is much lower than between land and water.

In order to study the influence of a surface discontinuity, it is appropriate to have a fine grid of legs closer to the surface. While all selected flights contain at least one leg below 100 m, only the STINHO-2 flight includes several legs within the first 100 m above ground. Therefore, this particular flight has been chosen for the initial study of the lake-land discontinuity influence on the CBL.

The flight performed on the 9th June 2002 (STI09) was composed of five legs crossing the lake over its middle part and are called middle track (MT) hereafter as shown in Figure 1a). These legs were performed between 40 to 280 m, following a direction approximately parallel to the mean wind. The sky was only slightly cloudy (2/8 Ci), with a mean wind speed of $6\,m\,s^{-1}$ from south-east direction (150°) at 100 m height. Table 2 shows the chronology of the legs of this flight. On that day, the CBL height z_i reached a value of 2100–2300 m, as derived from the wind profiler data (Beyrich and Mengelkamp, 2006).

Figure 2 shows the altitude variation along the five legs flown over the middle part of the lake. All legs contain significant changes in altitude, because the Helipod did not maintain a constant height above ground level. Since the three lowest legs overlap partially within a layer between 40 and 120 m, they will be analysed to-

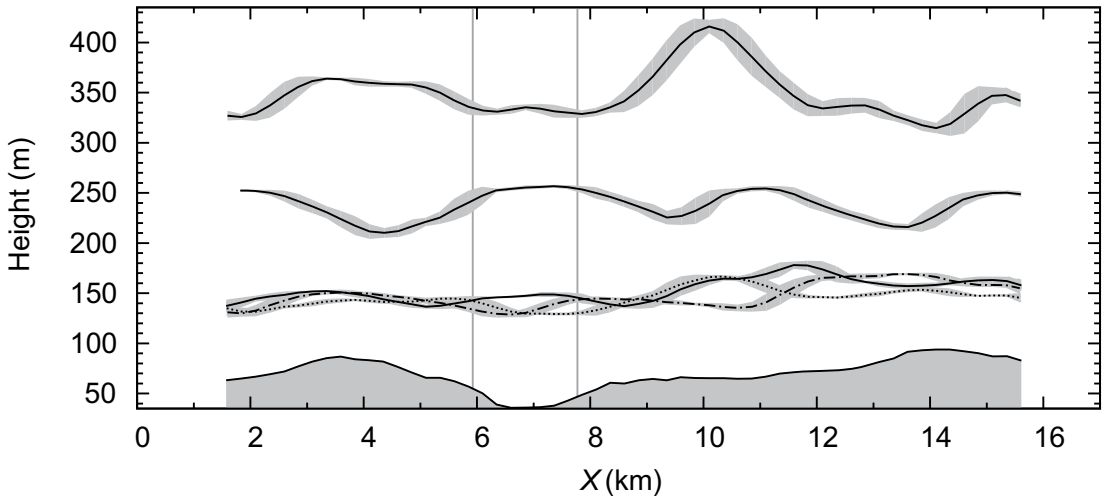

Figure 2: Averaged barometric heights along the five middle track (MT) legs performed during the STI09 flight. Shaded areas correspond to the standard deviation of the altitude along the 1-km window. Abscissa shows the distance along the leg, where X is the distance from an arbitrary point at the western edge of the flight paths. The lowest shaded area depicts the 1-km averaged topography. Vertical gray lines indicate lake boundaries.

gether to describe the flow characteristics close to the surface ($0.02z_i$–$0.05z_i$). The complete flight lasted more than one and a half hours in the early afternoon. Within this period, the air temperature increased approximately 1 K, mainly due to the diurnal cycle. This warming trend was also observed in data from the 99-m tower at the Falkenberg site (not shown). During these flights, moisture and wind vector for the mean flow did not show significant changes. This warming effect must be considered in the attempt to use the three legs performed below 100 m as different iterative measurements of the same layer. Further, we can assume that the CBL and the second-order statistical moments remain stationary. Indeed, during the 1.5 hour STI09 flight the radio sonde observations (not shown) show that the CBL grew from 1825 m (1052 UTC) to 2375 m (1637 UTC). Assuming a linear trend, that gives an evolution of 100 m hour^{-1} (150 m of growth for the entire flight). This change in the boundary-layer height can be ignored. Regarding the second-order moments, the surface fluxes close to the surface did not changing significantly during the flight time (Beyrich et al., 2006). Even if fluxes would change, we are only interested in the local differences of fluxes that are simultaneous. That is, the relation of local fluxes respect to their spatial averages for a given time. In this sense, the overall time evolution is not important.

3.2 Sampling Error

The second-order statistics like the standard deviation measurement itself are subject to errors. Flight legs that are not large enough compared to the largest energy-transporting eddies cause a systematic error since they lead to a systematic under- or overestimation of the turbulent flux or standard deviation (Grossmann et al., 1994). The sampling error can be estimated by the expression stated by Mann and Lenschow (1994) and Lenschow et al. (1994) representing the absolute systematic statistical uncertainty of the standard deviation σ_θ related to a single flight leg on which σ_θ was calculated:

$$\Delta\sigma_\theta = 2\frac{I_\theta}{P_l} \cdot \sigma_\theta \tag{3.1}$$

where I_θ is the integral length scale (see van den Kroonenberg et al., 2012) of θ and P_l the averaging length. Since I_θ is about 500 m during our flights and P_l about 1000 m (see Section 2.2), the sampling error becomes

$$\Delta\sigma_\theta \approx \sigma_\theta. \tag{3.2}$$

Furthermore, different measurements of finite duration or length under identical boundary conditions lead to different second-order statistics compared to the ensemble mean (Bange et al., 2013). Over land the standard deviation changes significantly over different passes as a consequence of turbulent elements. This is expressed by the random error. For σ_θ the random error $\sigma^2_{\sigma_\theta}$ is defined as the averaged squared differences between the ensemble and the actually measured standard deviation. Thus, σ_{σ_θ} can be interpreted as the standard deviation of σ_θ. An estimate is given by Lumley and Panofsky (1964); Lenschow and Stankov (1986) and is defined by:

$$\sigma^2_{\sigma_\theta} = 2\frac{I_{\sigma_\theta}}{P_l} \cdot \overline{(\sigma^2_\theta)'^2} \tag{3.3}$$

with

$$\overline{(\sigma^2_\theta)'^2} = \frac{1}{I-1}\sum_{i=1}^{I}(\sigma^2_\theta(i) - \sigma^2_\theta(\mathrm{leg}))^2 \tag{3.4}$$

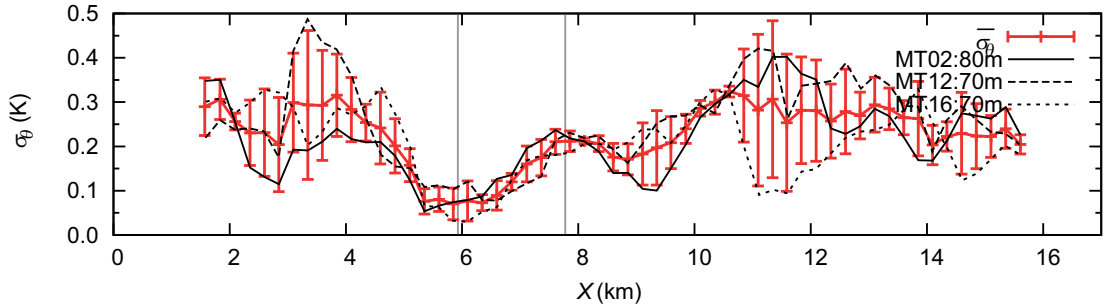

Figure 3: Standard deviation for σ_θ of the three passes at the lowest flight legs MT02, MT12, MT16. The red line indicates the average $\overline{\sigma_\theta}$ of the three legs. Error bars ζ_{σ_θ} mark the sampling error calculated after Eq. 3.6. Wind blows parallel to the flight direction (from the right side to the left side in the panel). Average wind speed is between 5.5 and 7.1 m s^{-1}. See Table 2 for more information.

where I is the number of (moving) data windows on one single flight leg. For instance on a 15 km long leg, I = 15,000/250 = 60 values for the variance (in Eq. 2.1) are calculated. σ_θ(leg) is the spatial average of the standard deviation of θ along the whole flight leg:

$$\sigma_\theta(\text{leg}) = \frac{1}{I}\sum_{i=1}^{I}\sigma_{\theta_i} \tag{3.5}$$

The total error of the measurement is the sum of σ_{σ_θ} and $\Delta\sigma_\theta$. Therefore, the uncertainty is in the same order of magnitude as σ_θ itself. The same also applies for the water vapor mixing ratio m. Generally, this influence can be reduced by averaging over all the passes for a given flight for each window. Unfortunately, this technique requires the performance of iterative passes along the same leg. In our dataset, the flights from the LITFASS-2003 campaign do not include more than one pass per leg, precluding the application of this technique. Only the selected STI09 flight includes three passes along the lowest leg. However, also the information of the LITFASS-2003 flights is qualitatively valuable and useful, especially when all flights are treated together as done in Section 3.5.

In Figure 3, σ_θ of the three lowest passes (MT02, MT12, MT16) of STI09 flight are shown. The average $\overline{\sigma_\theta}(i)$ over the number of passes P (in our case P = 3) is marked by the red line and its error bars for each (moving) window i along the flight leg. The error bars ζ_{σ_θ} are calculated by the statistical square average of the variation between σ_θ and $\overline{\sigma_\theta}$ for each (moving) window i along the flight leg:

$$\zeta^2_{\sigma_\theta}(i) = \frac{1}{P-1}\sum_{p=1}^{P}(\sigma_\theta(p,i) - \overline{\sigma_\theta}(i))^2 \tag{3.6}$$

The uncertainty ζ_{σ_θ} derived from measurements over the lake is significantly smaller than the observed drop in σ_θ over the lake, indicating that this drop is most likely related to the lake footprint. However, the following analysis has to be considered with caution. Even though the error is too high for a quantitative analysis, yet the lake remains qualitatively recognizable. A similar result is obtained for the standard deviation of the water vapor mixing ratio σ_m or the latent and sensible turbulent heat fluxes.

3.3 First-Order Statistics

Figure 4 shows the window average of potential temperature along the legs performed over the middle part of the lake. The warming trend of 1 K observed during the flight has been removed from the lowest three legs for better comparison. The window-averaged surface temperature, as measured from the lowest leg, has been also included. This variable reflects the presence of the lake, which is 15 K cooler than the surrounding area. Over land, lower surface temperatures allow the forest cover to be distinguished from farmland at both sides of the lake.

Considering the three lowest legs below 100 m, there are large variations of potential temperature over land. However, a cooling effect of approximately 0.5 K is observed over the lake, which is shifted downstream to the west between X = 5–6 km, since the prevailing wind direction is from the south-east. Note, that X is defined as the distance from an arbitrary point at the western edge of the flight paths. The standard deviation of potential temperature also decreases significantly over this part of the leg, as we will discuss later. This cooling effect related to the lake is hardly detected at 170 and 280 m (MT04 and MT06, respectively).

The average water vapor mixing ratio m (Figure 5) presents some variability along the legs that does not allow for clear detection of any lake influence. Over the forests at X = 4–5 km and 13–15 km a weak maximum of m is detected. Since the lake is partially surrounded by trees, with the large forest at the south of the lake, it is therefore possible to distinguish a drier atmosphere over the lake compared to the moister air over forest. The upper legs do not exhibit similar patterns. Strong convection plays a role on the variability of θ and m for the different passes as described in Mahrt (2000). However, the spatial organization and variability for both variables are not similar, indicating that m may be affected by other factors, e.g. such as entrainment, which is not directly related with surface patterns (Sühring

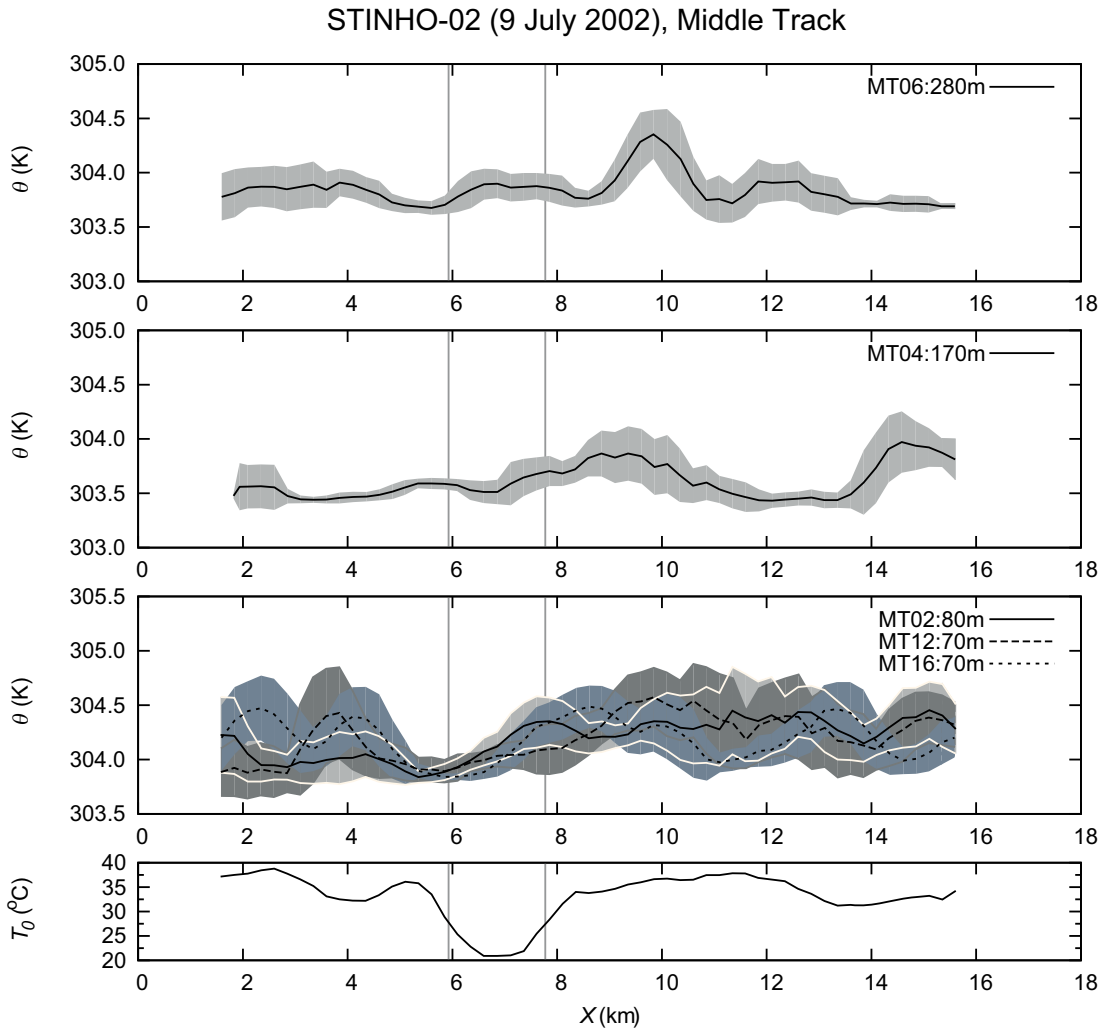

Figure 4: Averaged potential temperature (thick line) and standard deviation (shaded area) for each middle track (MT) leg at 280 m (MT06), at 170 m (MT04) and below 100 m (MT02, MT12, MT16) of STI09 flight. The time variability of the temperature is removed. Lower panel shows the corresponding distribution of the surface temperature measured during the flight leg (MT02). Abscissa and vertical grey lines as in Figure 2. Wind is blowing parallel to the flight direction (from the right to the left side in the panel). Average wind speed is between 5.5 and 7.1 m s^{-1}. See Table 2 for more information.

and Raasch, 2013). Bange et al. (2006) and Sühring and Raasch (2013) noted that the latent heat flux is more affected by the entrainment of dry air from the free atmosphere than by the surface latent heat flux during LITFASS-2003 experiment, in contrast to the temperature, which is more affected by the sensible heat flux.

3.4 Second-Order Statistics

The smaller variability of the potential temperature over the area of the lake influence is further analysed in Figure 6, where the standard deviation of potential temperature σ_θ is represented along the MT legs. As indicated in Section 3.3, a clear drop in σ_θ is present for the three lowest legs, shifted westward of the lake, following the mean wind direction. Such a horizontal displacement can be an indication for the lake footprint propagation downstream.

At the upper levels, the lack of multiple passes complicates the interpretation of σ_θ with respect to the lake influence. This analysis has to be considered as speculative. At 170 m (MT04), the leg segment with small variances over the lake is extended downstream (X = 3–6 km), while it is much narrower and closer to the lake at 280 m (MT06) between X = 5–6 km. However, σ_θ exhibits lower values also over other regions of theses legs (i.e. the farmland/forest area between km 11 and 14 at leg MT04) or upstream the lake at MT06), leading to an unconfined statistical significance.

The standard deviation of water vapor mixing ratio changes significantly over the different passes at lower heights, including those segments over the lake (Figure 7). These results seem to indicate a rapid change of σ_m over the lake, specially compared to the surrounding area closer to the lake's shorelines. However, no statistically significant minimum is observed over the lake. Sometimes the spatial change of the instantaneous m can

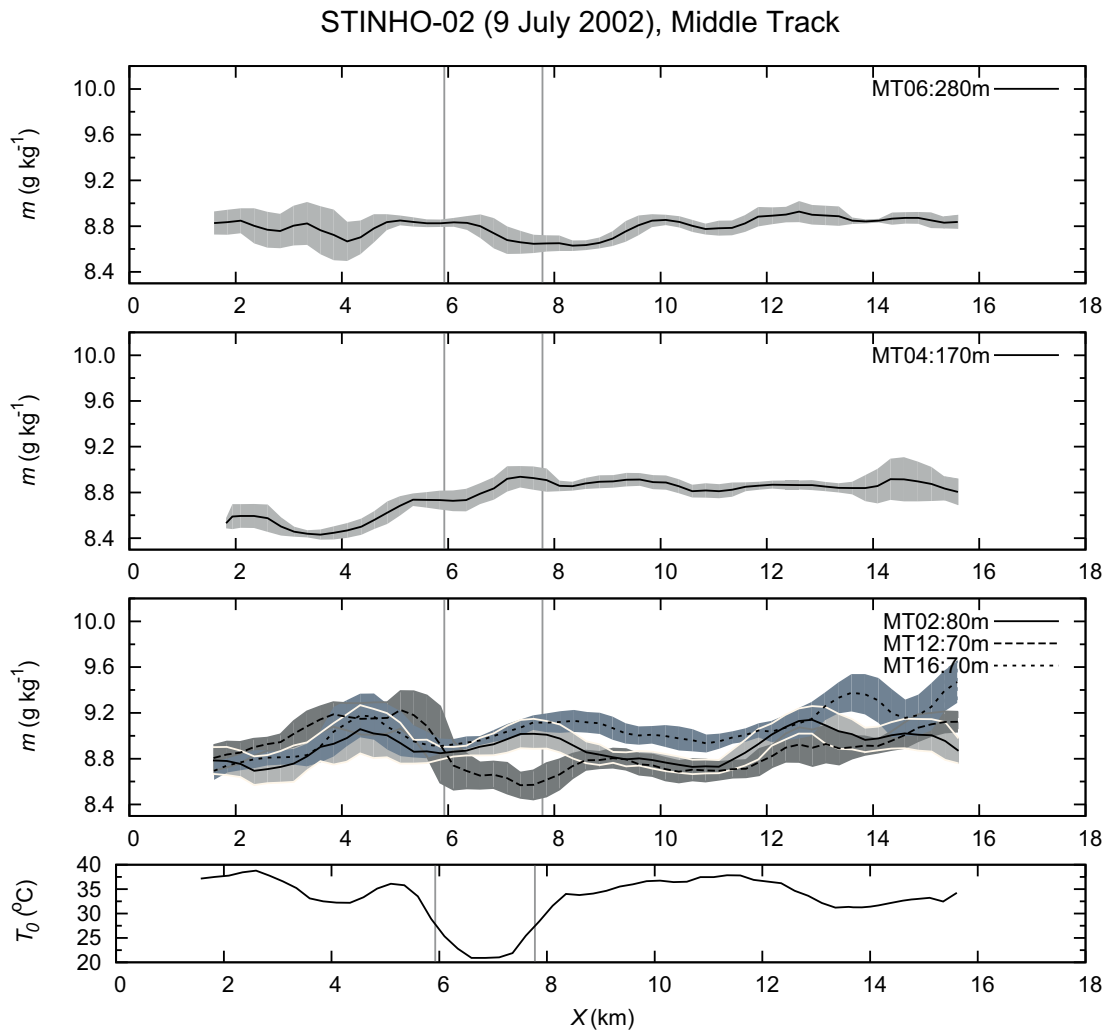

Figure 5: As in Figure 4 but for water vapor mixing ratio.

be very large across the forest-lake discontinuity, especially with the fact of a comparable large window size of 1 km, producing a sudden peak on σ_m (Figure 5). This is the case for the large value detected over the western shoreline in MT12. For the rest of legs, the value of σ_m does not indicate the presence of the lake.

The variance of vertical velocity σ_w for the MT legs increases for higher altitudes (Figure 8) corresponding to CBL theory. At the lowest heights, it does not show any terrain influence. At higher levels, however, its variability increases as the leg-average value also increases. At 280 m, σ_w is smaller at the eastern and western shoreline of the lake.

Another important scaling variable is the surface Reynolds' stress, when turbulence is modulated by wind shear near the ground. This stress is expressed by the vertical flux of horizontal momentum known as the friction velocity u_*, defined according to Stull (1988) as

$$u_* = \left[\overline{u'w'}^2 + \overline{v'w'}^2\right]^{1/4}. \qquad (3.7)$$

The leg-averaged friction velocity u_* does not vary significantly with height for the MT legs (Figure 8), indicating that the variance of vertical wind increases with height due to convection. However, the spatial distribution of u_* and σ_w is very similar along the legs, showing that they are related, following the decomposition from the model of σ_w in Højstrup (1982). Similarly, closer to the surface u_* does not exhibit a clear relationship with the surface pattern.

Since the variance of the vertical wind below 100 m does not reflect any surface influence for MT, the behaviour of the sensible and latent heat fluxes (Figure 9) are very similar to those described for potential temperature and water vapor mixing ratio. Due to a stable stratification over the cold water during the day and its effect on suppressing turbulence (Beyrich et al., 2006), the sensible heat flux presents small or even negative values over the lake along the MT legs for the lowest levels, indicating a negligible or downward heat flux. Higher legs do not show any influence of the lake (not shown).

Similar to σ_m, the spatial distribution of the latent heat flux (Figure 9) changes significantly for the dif-

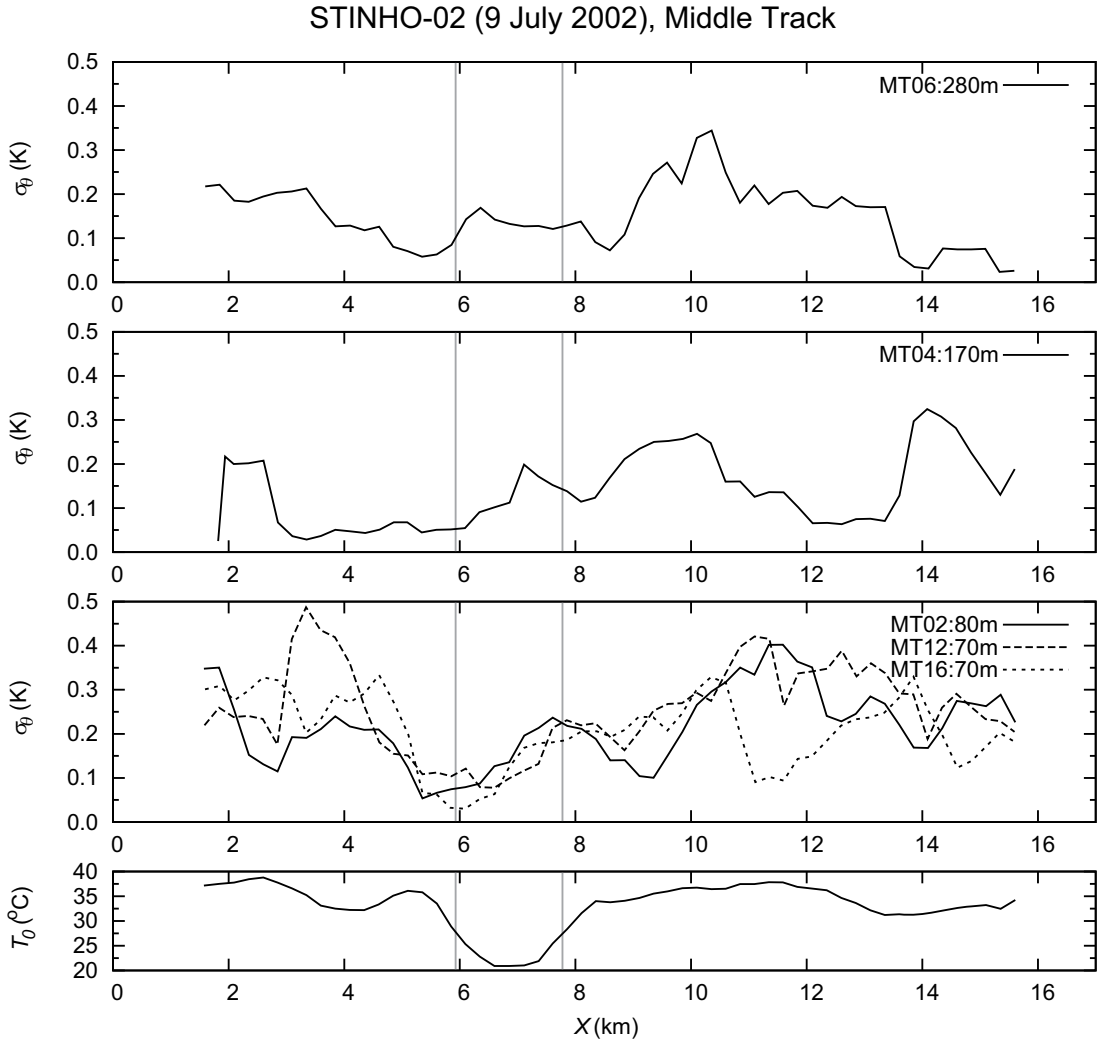

Figure 6: Standard deviation of potential temperature for each middle track (MT) leg at 280 m (MT06), at 170 m (MT04) and below 100 m (MT02, MT12, MT16) of STI09 flight. Data are computed for a window of 1 km width, sequentially marched through the leg by increments of 250 m. Lower panel shows the corresponding distribution of the surface temperature measured during the flight leg (MT02). Wind direction is from the south-east. That means wind is blowing parallel to the flight direction (from the right side to the left side in the panel). Average wind speed is between 5.5 and 7.1 m s^{-1}. See Table 2 for more information.

ferent passes over the lake, precluding the detection of any lake influence in our dataset. Even for the latitudinal north-south legs, performed exclusively over the lake, the latent heat flux presents significant differences (not shown), indicating that the latent heat flux in the surface layer responds to dynamics originating from a larger scale.

3.5 Flights LIT13 and LIT14 (2003) and discussion with STI09 (2002)

In the following, two additional flights (performed during the LITFASS-2003 campaign) are analysed, that were carried out on a flight pattern similar to the STI09 flight (in 2002), see Figure 1a). The LITFASS-2003 campaign took place in June 2003, when the weather was characterized by high insolation and temperatures were mostly above 10 °C at night. However, several rain events modified the day-to-day weather characteristics, providing cases with a large variety of wind and buoyant conditions. They included several straight legs that crossed the lake over the same region as the MT legs described in the previous sections. The flights consisted of five legs at different levels approximately parallel to the mean wind direction which was the Northwest in both cases. LIT13 was performed in the early afternoon of a mostly sunny day but with 5/8 of Cirrus clouds. A storm event took place during the previous morning and early night, leaving a wet land surface with a mean wind speed of 8 m s^{-1}. On the next day, LIT14 was performed in the morning, with the sky partially covered with cirrus and convective clouds and a mean wind speed of 4 m s^{-1}. The effect of the surface humidity was identified on the leg-averaged sensible heat flux at 90 m, with smaller values for LIT13 (110 W m^{-2}) than LIT14 (160 W m^{-2}). Despite of the different surface conditions for both flights, a decrease in both potential temperature mean and variance can be identified over the lake for the

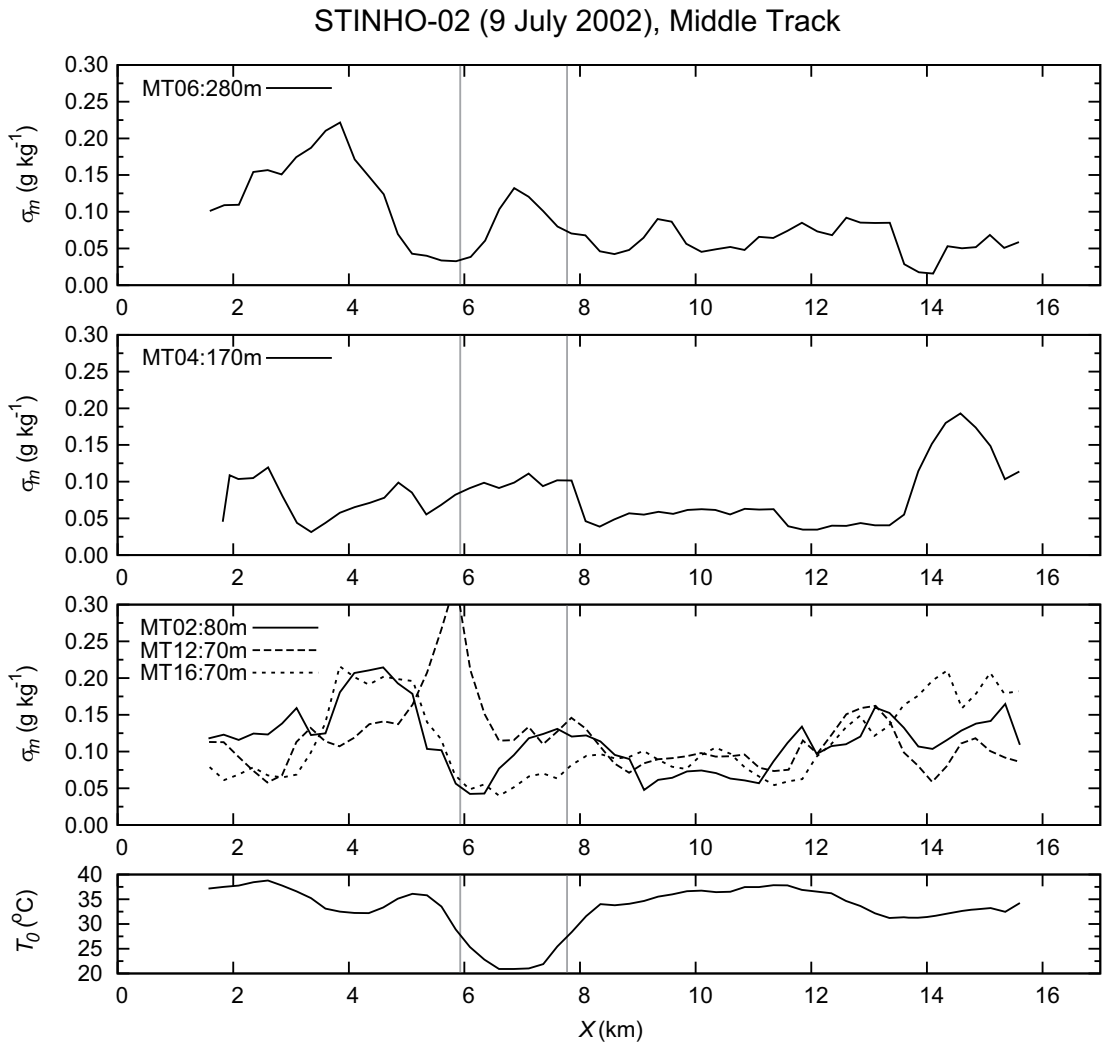

Figure 7: The same as in Figure 6 but for the water vapor mixing ratio.

lowest leg (Figure 10). Although there is less statistical significance by the flights with a single pass, most of them show a drop σ_θ at the vicinity of the lake. This is not significant if each flight is taken individually, but its persistence for most of the flights is a useful information. A clear lake influence on the rest of the variables is difficult to identify since there is only one pass for each level.

In summary, the data analysed for the three flights (STI09, LIT13 and LIT14) indicate similar results, although the lack of several passes per flight along the same path exclude a definitive statement of lake influence. The lake produces a small cooling effect over the first 100 m, which is shifted progressively downstream. However, the decrease of θ is only a few tenths of Kelvin around 80 m. The variance of potential temperature is clearly affected by the presence of the lake by showing a drop of σ_θ (Figure 6 and 10), despite of the mean wind and buoyancy conditions. The variance of m is not so clearly affected by the lake. A decrease is indicated over the lake, but sometimes, the spatial change of the instantaneous m is large across the forest-lake discontinuity, producing a sudden peak on σ_m.

The presence of the lake does not affect the strength of turbulent mixing in the surface layer (either represented by σ_w or u_*, see Figure 8) at observation height. However, the sensible heat flux is very small or even negative over the lake as shown by the small variance of potential temperature. Latent heat flux behaves differently. Moisture distribution responds with a more complex pattern to the surface forcing (due to the presence of forest, agricultural fields and urban areas), and thus the variance of m can be equally large over the lake as over other regions. In general, θ and σ_θ show the strongest and most significant footprint of the lake, with a decrease of values, although this is consistently visible at the lowest flight level of about 80 m only. The results indicate that predictions by LES in former literature e.g Maronga et al. (2014) or Huang and Margulis (2009), where temperature variance is more sensitive to surface heterogeneity than humidity is observed as well in the in-situ data.

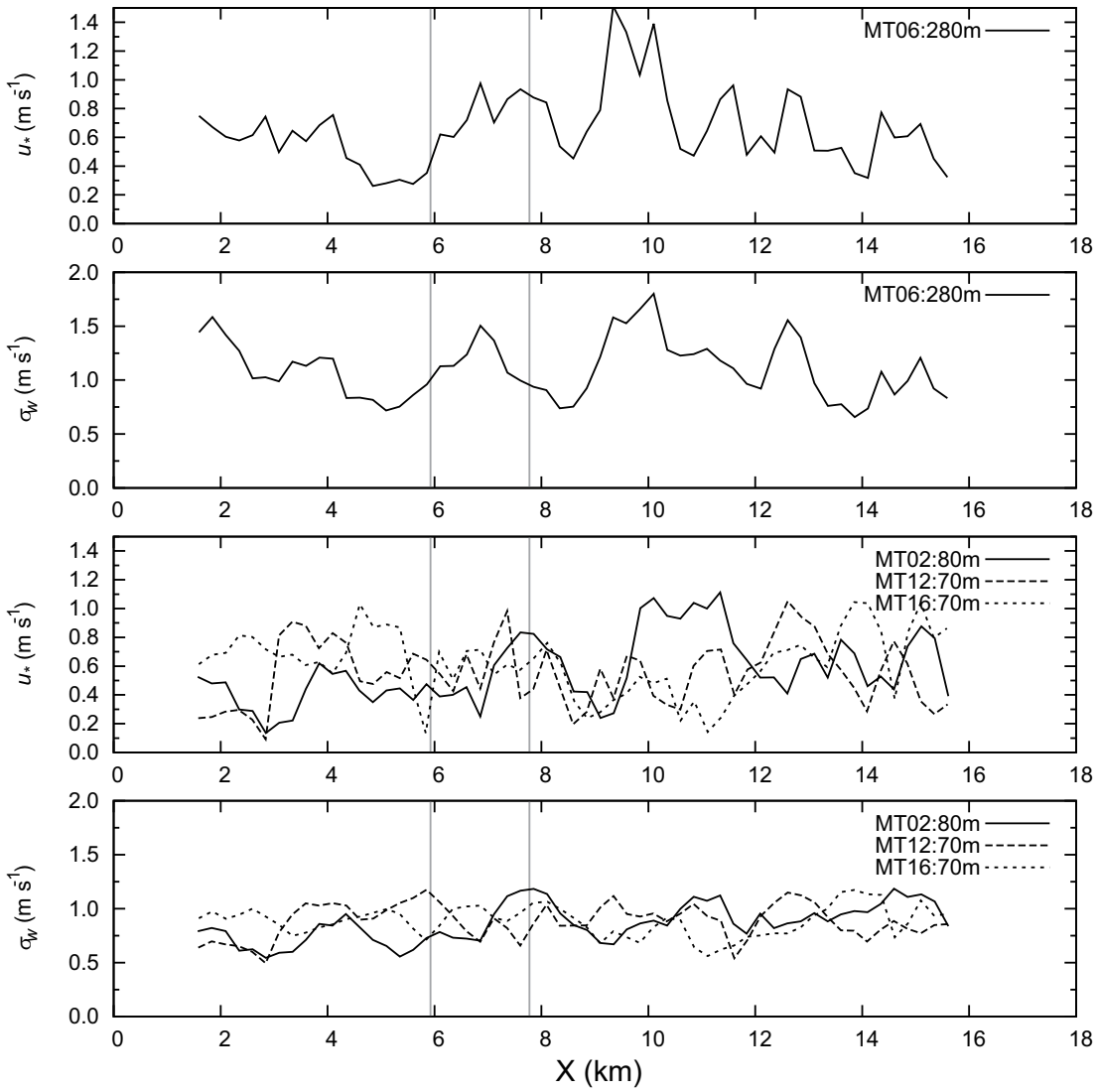

Figure 8: The same as in Figure 6 but for u_* and σ_w for each middle track (MT) leg at 280 m (MT06), and below 100 m (MT02, MT12, MT16) of STI09 flight.

3.6 Lake influence on the rest of flights

An analysis of the rest of LITFASS-2003 campaign flights reveals a similar behaviour in σ_θ. A total of 34 legs crossing over the lake, within the first 100 m, have been analysed. The main difference, with respect to the flights described above (LIT13, LIT14, STI09), which followed the mean wind direction, is that these legs were always oriented in west-east direction, (Figure 1). Flights LIT24, LIT25 and LIT07 applied a vertical matrix at three levels for different days, all characterized by a mean wind direction from the SE but by different speeds. Additionally eight flights were analysed, each one contributing with three legs below 100 m. These flights were performed under different ambient conditions, regarding the mean wind direction, time of the day (either morning or early afternoon) and cloud cover.

In order to detect a systematic influence of the lake on the measurements at the lowest levels, a search for drops in σ_θ has been applied to all LITFASS-2003 flights (including LIT13 and LIT14). For this purpose, it is necessary to define the following parameters as shown in the schematic in Figure 11:

- Leg-average σ_θ(leg): It represents the mean of the σ_θ obtained for each window i of 1 km width sequentially marched through the leg by increments of 250 m, see Eq. 3.5.
- Local-average $\sigma_\theta(A)$: defined as the mean value of σ_θ for three consecutive 1-km windows. This parameter is only evaluated for those 1-km windows that fall within a horizontal distance of ±2 km from the lake boundaries. This restriction in the horizontal distance was applied for preventing those drops in σ_θ whose physical relation with the lake is unlikely in order to avoid other elements that may add more noise to the data. The STI09 flights give us a reasonable justification to relate any significant drop of σ_θ at the vivinity of the lake with the presence of the lake. The

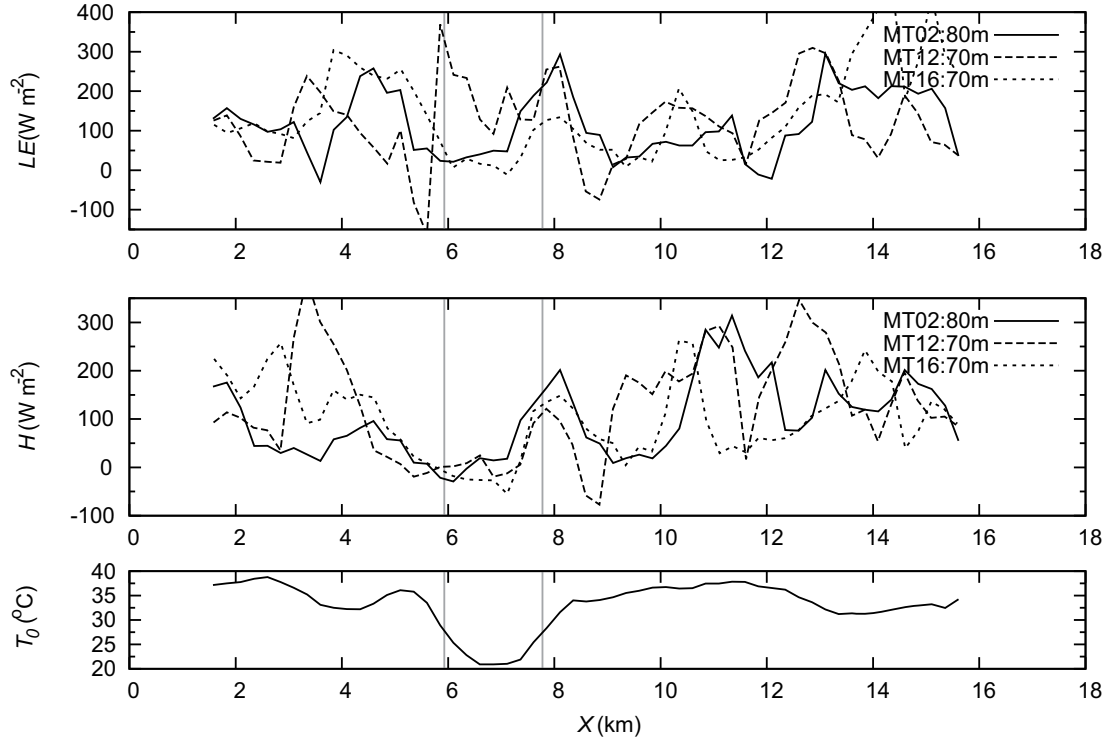

Figure 9: The same as in Fig. 8 but for latent heat flux LE, sensible heat flux H and temperature T_0.

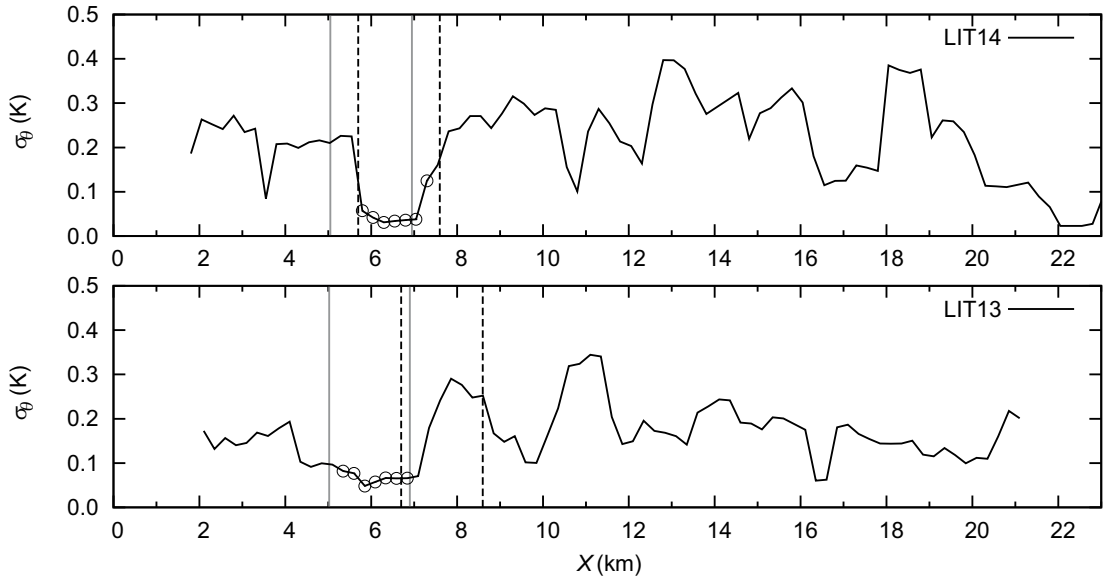

Figure 10: Standard deviation of potential temperature σ_θ for legs LIT14 (top) and LIT13 (bottom). Vertical gray lines indicate the lake boundaries as diagnosed by the surface temperature. Circles indicate the segment of the leg with the lowest values of σ_θ at the vicinity of the lake. This segment has been identified with an automatic algorithm, described at the end of Section 3.6. Black dashed lines indicate the segment of the leg where the lake influence should be detected following the parametrization (δx_{par}) developed in Section 5 (Eq. 5.2). Refer to the text (Section 3.6) for more informations.

value of the threshold (±2 km) was determined after a qualitative revision of the σ_θ evolution for all flights.

- The centre of the segment with the lowest $\sigma_\theta(A)$ or, similarly, with the largest value of $\sigma_\theta(\mathrm{leg}) - \sigma_\theta(A)$ is identified as the central point of the region with the largest influence of the lake, which is assumed to have the same width as the lake. Additionally, the horizontal distance between this point and the centre of the lake is defined as the observed mean propagation distance of the lake influence δx_{obs}, at the leg height $\overline{z}_{\mathrm{obs}}$. This horizontal distance will be used in Section 5.

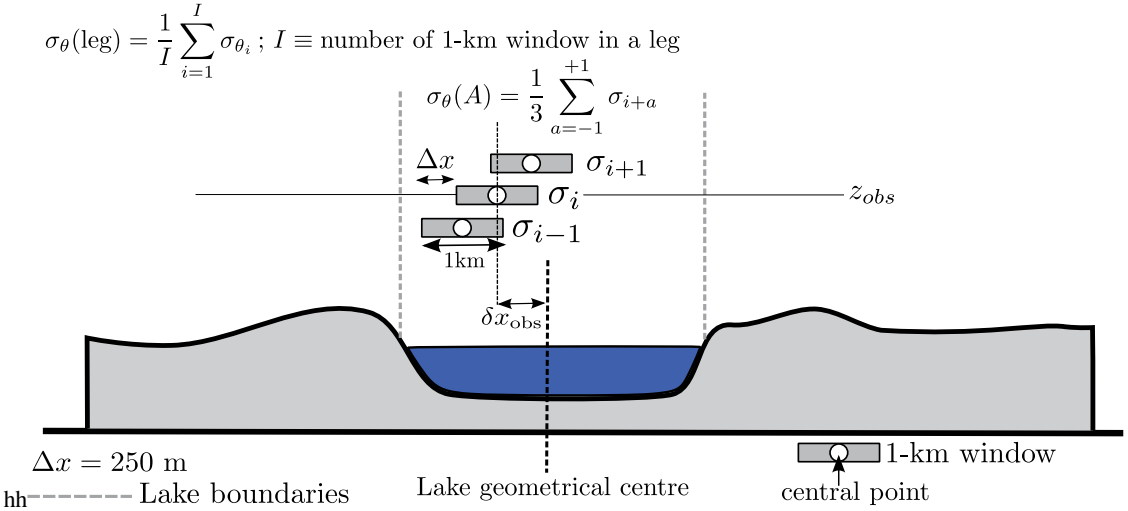

Figure 11: Schematics for the drop search σ_θ in the vicinity of the lake for three consecutive 1-km windows. Note that the sketch is not true to scale.

A clear drop in σ_θ was detected by the computer algorithm search over the lake for all legs except for one case. An example for the flight LIT13 and LIT14 is shown in Figure 10. Circles there mark the segment of the leg where the drop of σ_θ is maximum in the vicinity of the lake. It should be noted that other drops occur as well along the flight leg, as seen for example at $X = 22$ km for LIT14 in Figure 10. In that case this is probably the influence by another lake. However, the programmed algorithm detects only drops in the vicinity of the lake Scharmützelsee. Moreover the decrease in magnitude of this drop exceeds 50 % of the leg-averaged σ_θ for 29 cases. Considering that these results are based on single passes along the given legs, where the random error can play an important role in the determination of the turbulent variances, the drops are significant and confirm previous results in Section 3.5.

4 Vertical propagation of the lake influence

The blending-height theory addresses the decreasing influence of surface heterogeneity with height, identifying a scaling depth where this influence progressively vanishes. Different formulations of the blending height z_{blend} have been discussed in the literature (Mahrt, 2000; Raupach and Finnigan, 1995; Wood and Mason, 1991), depending on which forcing is most relevant. The different blending height formulations are compared and checked with our in-situ data in order to estimate which formulation is the most relevant for our data set. Since 33 out of 34 legs showed an influence of the lake on the measurements of the standard deviation of potential temperature at 100 m, we should find a parametrization which fits to almost all of our cases, indicating a scaling depth larger than our aircraft observation height. All formulations are proportional to the length scale of the surface heterogeneity L_{het}, a stability parameter ψ, which is a measure of the stratification or wind shear production of turbulence, and they are inversely proportional to the wind speed $\overline{u}$ (Mahrt, 2000),

$$z_{\text{blend}} = C_\psi \left(\frac{\psi}{\overline{u}}\right)^p L_{\text{het}} \tag{4.1}$$

where C_ψ and p are non-dimensional coefficients that take a particular value for each formulation. The stability parameter and wind speed are leg averaged. That means each parameter is first calculated within each 1 km window sequentially shifted through the leg by increments of 250 m. Second, all 1 km window parameters of each flight leg (around 54 for a 14 km long flight leg) are then averaged. In this sense, we attempt to receive a parameter which is representative of the whole heterogeneous area. When turbulence is shear-generated, local diffusive mixing dominates and the stability parameter ψ becomes the friction velocity u_*, with $p = 2$ and C_ψ is in the order of 1. With $p = 1$, we obtain the diffusion height z_{diff} (Wood and Mason, 1991), a level at which effects of the surface heterogeneity completely vanish.

When surface heating is important, Wood and Mason (1991) suggested using the spatially-averaged surface heat flux and potential temperature, $\psi = \left(\overline{w'\theta'}\right)_0 / \overline{\theta}_0$, to explicitly account for the influence of buoyancy. For this case, $p = 1$ and C_ψ is of the order of 10^3, as estimated by Mahrt (2000).

Alternatively, Mahrt (1996) suggested considering σ_w as a rough estimation of vertical mixing, without specific attention to whether the origin is due to either wind shear or buoyancy. The variance of vertical velocity can be described in terms of the relationship (Højstrup, 1982),

$$\sigma_w^2 = a u_*^2 + b w_*^2 \tag{4.2}$$

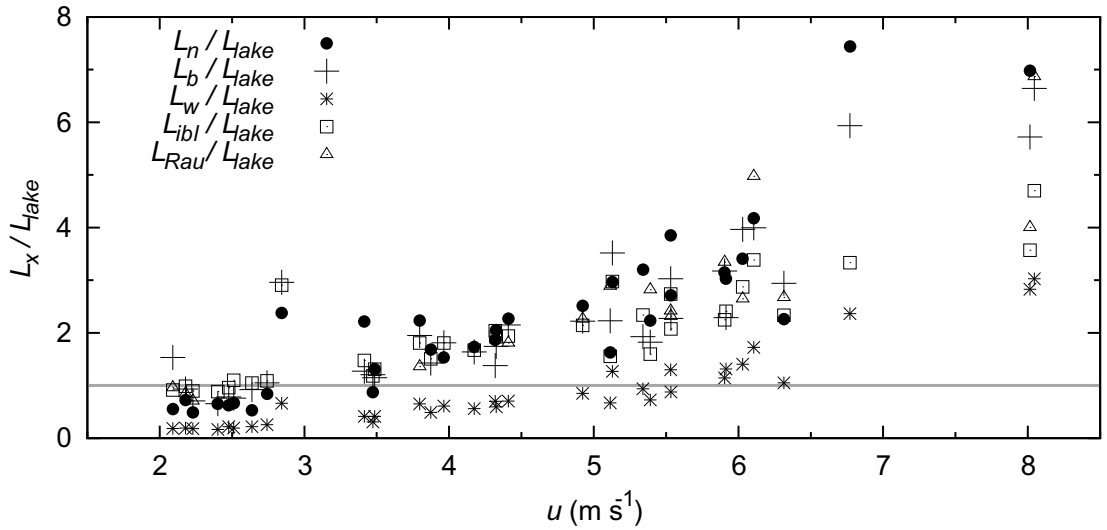

Figure 12: Estimation of the minimum horizontal length scale of the surface heterogeneity that is needed to influence the airborne measurements at the mean observation level for each leg as a function of the leg-averaged wind speed. The x-axis shows the ratio of the particular length scale and the actual geometrical length of the lake, which was crossed by each flight leg. The estimation of the length scale follows the blending-height parameterization for the near-neutral case (L_n/L_{lake}), the modified case after considering the surface heat flux (L_b/L_{lake}) and the generalized case (L_w/L_{lake}). Additionally, boundary-layer convective scaling has been calculated for those cases where the boundary-layer height was available (L_{Rau}/L_{lake}), and minimum length scale for detecting the formation of an IBL (L_{ibl}/L_{lake}). Horizontal straight gray line at $L_x/L_{lake} = 1$ indicates where the geometrical length scale L_{lake} is equal to the minimum length scale L_x.

where w_* is the Deardorff convective velocity scale. Thus, the stability parameter used in this case $\psi = \sigma_w$ (with $p = 2$ and $C_\psi = 2$) generalizes the application of the blending height formulation to shear-driven convective conditions.

Mahrt (2000) uses Eq. (4.1) to estimate the minimum horizontal scale of the surface heterogeneity that would influence the airborne measurements at the mean observation level $\overline{z}_{obs}$,

$$L_{blend} = \frac{1}{C_\psi}\left(\frac{\overline{u}}{\psi}\right)^p \overline{z}_{obs} = L_{het}\frac{\overline{z}_{obs}}{z_{blend}} \qquad (4.3)$$

with L_{blend} taking different values depending on the stability parameter used. If (for our study) $L_{lake} = L_{het} > L_{blend}$, then the lake is expected to exert a heterogeneity signal on the atmosphere at the observation level.

The concept of a blending height is discussed controversially in literature for strong convective conditions since the largest eddies transport the surface properties up to the CBL top. Raupach and Finnigan (1995) proposed a formulation for the maximum horizontal scale of surface heterogeneity L_{Rau}, for which influence in the CBL is confined to depths much smaller than the boundary-layer height z_i,

$$L_{Rau} = C_{Rau}\frac{\overline{u}}{w_*}z_i \qquad (4.4)$$

where C_{Rau} is a non-dimensional coefficient in the order of 1 (Mahrt, 2000). Since the mixing time scale in the CBL is defined as z_i/w_*, L_{Rau} can be interpreted as the horizontal distance covered by the flow during the mixing time scale.

The length scale of the lake L_{lake} is estimated by using the geometrical length of that portion of the leg over the lake surface. This length varies depending on the flight track orientation, since the lake in the east-west direction is five times smaller than in the north-south axis. Hence, the horizontal length scale L_{lake} ranges between 1.5 km and 2 km for all flights. Figure 12 shows the ratio of L_x/L_{lake} versus the leg-averaged wind speed $\overline{u}$ according to Mahrt (2000), where L_x is one of the three possible formulations of L_{blend}:

1. The near-neutral case ($L_{blend} = L_n$),

$$L_n = C_n\left(\frac{\overline{u}}{u_*}\right)^2 \overline{z}_{obs}\,, \qquad (4.5)$$

where C_n is 0.6.

2. The modified case ($L_{blend} = L_b$) after considering the surface heat flux ($\overline{w'\theta'}_{sfc}$) is

$$L_b = C_b\frac{\overline{u}\,\overline{\theta}}{\overline{w'\theta'}_{sfc}}\overline{z}_{obs}\,, \qquad (4.6)$$

where C_b is $3.1 \cdot 10^{-3}$.

3. The generalized case with σ_w and $C_w = 0.5$ ($L_{blend} = L_w$) is

$$L_w = C_w\left(\frac{\overline{u}}{\sigma_w}\right)^2 \overline{z}_{obs}\,. \qquad (4.7)$$

Results for L_{Rau} (Eq. 4.4) for the cases in which the CBL depth z_i was available are also included as is L_{ibl} which is explained later. The CBL depth was measured by a lidar or radiosonde. Further details can be found in Beyrich and Mengelkamp (2006). The horizontal gray line at $L_x/L_{\mathrm{lake}} = 1$ indicates where the geometrical length scale L_{lake} is equal to the minimum length scale L_x. That means, when the ratio L_x/L_{lake} is smaller than one, the geometrical length scale of the lake L_{lake} is larger than the minimum required horizontal length scale of the surface heterogeneity, which is needed to influence the airborne measurements at the mean observation level. All length scales increase for larger wind speeds. Larger wind speeds reduce the Lagrangian time that the flow spends over a particular surface feature. Hence, a longer horizontal length scale of this surface feature is required to achieve a similar depth of influence (Mahrt, 1996). Only for very few cases, $L_{\mathrm{n}}/L_{\mathrm{lake}}$ and $L_{\mathrm{b}}/L_{\mathrm{lake}}$ are less than unity, generally for mean wind speeds $\overline{u} < 3\ \mathrm{m\ s^{-1}}$. Only $L_{\mathrm{w}}/L_{\mathrm{lake}}$ shows values smaller than unity, for almost all the cases (except for those legs with the largest wind speeds).

As mentioned in the introduction, the convective length scale L_{Rau} indicates the size of heterogeneity that are supposed to influence the entire boundary layer. L_{Rau} depends on the intensity of convection (represented by the Deardorff velocity scale w_*), the boundary-layer depth z_i and the mean horizontal wind speed $\overline{u}$ (see Eq. 4.4). The results for L_{Rau} indicate a behaviour similar to L_{n} and L_{b}, with $L_{\mathrm{Rau}} > L_{\mathrm{lake}} \sim 2\,\mathrm{km}$ for larger wind speeds ($\overline{u} > 4\ \mathrm{m\ s^{-1}}$). Under these wind conditions, horizontal convective mixing prevents the lake influence from extending up to the boundary-layer height. However, previous studies over the same area show that the sensible heat flux remains very small throughout the entire CBL over lake Scharmützelsee (Bange et al., 2006), and it only matches with the surrounding area at the upper ABL, where sensible heat flux over land is small (Sühring and Raasch, 2013). Strunin et al. (2004) found that L_{Rau} had to be complemented with a ratio between shear stress and buoyancy flux at 100 m to successfully determine the ability of a CBL for horizontal mixing. In the present study, the lack of iterative passes at higher altitudes precludes a more robust analysis for addressing the vertical extension of the lake.

Flows over surface discontinuities can develop local internal boundary layers (IBL) downstream, when the changes of surface properties are sharp enough or the scale of the surface heterogeneity is large. When a local IBL develops, Mahrt (1996) estimated its maximum depth z_{ibl} with scaling arguments as

$$z_{\mathrm{ibl}} = C_{\mathrm{ibl}} \frac{\sigma_w}{\overline{u}} L_{\mathrm{het}}\,, \tag{4.8}$$

where C_{ibl} was found to be 0.15 (Mahrt, 2000). Similarly to what we have applied for the blending-height parameterizations, it is possible to rewrite (4.8) in order to calculate the minimum length scale that would generate a local IBL with a depth similar to the observation level:

$$L_{\mathrm{ibl}} = \frac{1}{C_{\mathrm{ibl}}} \left(\frac{\overline{u}}{\sigma_w}\right) \overline{z}_{\mathrm{obs}}\,. \tag{4.9}$$

Note that L_{ibl} is very similar to L_{w}, although with a linear dependence on the ratio $\overline{u}/\sigma_w$. Figure 12 shows the values estimated for our dataset, with minimum scales larger than L_{w}. Therefore, larger heterogeneity scales are generally necessary in order to detect the development of an IBL at a given reference level.

In our dataset, we are able to see a slight drop in the potential temperature but none of the legs analysed identify a clear change in the mean variables, as we would expect when entering an IBL. Thus, we can say that a well defined IBL, which is in equilibrium with the underlying surface cannot be clearly identified with our observations according to Eq. 4.9, or alternatively the flow adjusts to the new surface without the formation of an IBL. These observations are in accordance with the LES study from Maronga et al. (2014). They could identify for the LITFASS-2003 case study that blending effects occur above several tens of metres above the ground for temperature fluctuation.

The fact that the IBL top is not well defined in the layer between 60 and 100 m may suggest that the scales estimated for the top of the IBL in (4.8) are valid. As a consequence, between 60 and 100 m, the influence of the underlying surface can only be detected in the second-order moments of the variables. Following this argumentation, we would expect that the lowest flight legs were performed within a layer between the top of the IBL (for those cases where it was generated) and the blending height. In this layer, the surface influence would gradually vanish with altitude. One should keep in mind, that the various scaling derivations were intended more as qualitative arguments based in part on linear theory (Mahrt, 2000). Therefore, quantitative comparisons of the length scales formulations is extremely difficult with more complex atmospheric flow as they occur over heterogeneous terrain.

5 Horizontal propagation of the lake influence

The above scaling estimates neglect important spatial variations of the stability parameters ψ and other variables. Therefore they do not attempt to describe the power-law dependence on the downstream distance that generally applies for the generation of an IBL (Garratt, 1990; Józsa et al., 2007). The current dataset shows that the influence of the lake on the distribution of the standard deviation of potential temperature is commonly shifted downstream. An attempt to characterize this horizontal shift is addressed by analysing the correlation between the atmospheric response (characterized

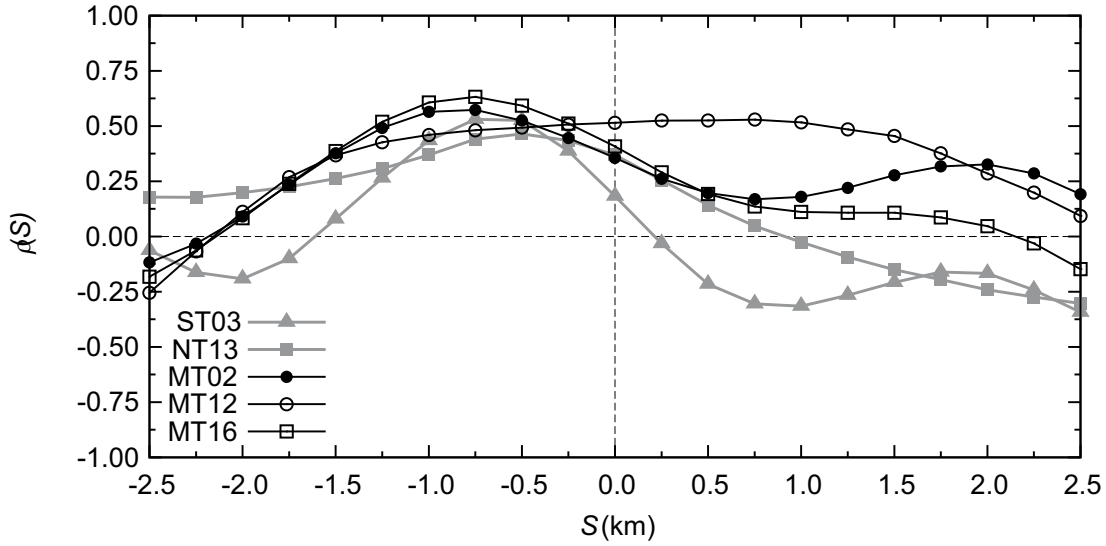

Figure 13: Cross-correlation function $\rho(S)$ between the standard deviation of potential temperature σ_θ and surface radiation temperature T_0 for the five legs of STI09 flight performed below 100 m.

by σ_θ) and the surface radiation temperature T_0. In this case, we have considered the 1-km overlapping windows for each leg below 100 m, as a spatial series of σ_θ and T_0. We then calculated the cross-correlation function,

$$\rho(S) = \frac{\mathrm{cov}\,[\sigma_\theta(x+S), T_0(x)]}{(\mathrm{var}[\sigma_\theta])^{1/2} \cdot (\mathrm{var}[T_0])^{1/2}}, \qquad (5.1)$$

where $S = j \cdot \Delta s$ represents the spatial lag, $\Delta s = 250$ m is the fixed horizontal distance between two consecutive overlapping windows along the leg and $j \in (-10, 10)$. In contrast to the one-point correlation analysis, the cross-correlation function allows us to analyse the spatial displacement of the vertical transport by horizontal advection.

Figure 13 shows the cross-correlation functions for the three legs of STI09 flight performed below 100 m. Further two more legs ST03 and NT13 have been added from STI09 which have not been presented before, but that also cross the lake in a similar way. These two legs have the same track and height than MT02, but are located more to the north (NT13) and to the south (ST03) over the lake. The maximum value of $\rho(S)$ occurs for a spatial lag S between 0.75 and 0.50 km, with the negative sign indicating that the maximum correlation is shifted downstream to the west, since there was predominant easterly wind. The leg MT12 represents one exception to these results, with a function ρ that exhibits a plateau within lags $S = \pm 1.5$ km. A positive correlation is expected since the drop in σ_θ occurs for smaller surface temperatures, as the thermals over these regions are weaker.

The cross-correlation function has been calculated for the rest of cases with a small cross-leg wind component ($u_{\mathrm{cross}}/\overline{u} < 0.5$). A total of 12 legs met this condition, and for 8 of them a maximum correlation of $\rho_{\max} > 0.4$ was obtained. All these cases show the maximum cross-correlation for a corresponding downstream spatial lag.

If we consider $(\sigma_w/\overline{u})$ as a qualitative ratio of the strength of the vertical mixing to the horizontal advective speed, it is possible to relate the spatial lag $S_{\max}$ of the maximum of the correlation function with the leg-averaged wind along the leg direction $\overline{u}_{\|}$, the leg-averaged standard deviation of vertical wind σ_w and the observational height $\overline{z}_{\mathrm{obs}}$. Based on Eq. 4.9, we get:

$$S_{\max} \sim \frac{1}{C_\delta}\left(\frac{\overline{u}_{\|}}{\sigma_w}\right)\overline{z}_{\mathrm{obs}} = \delta x_{\mathrm{par}}, \qquad (5.2)$$

where we call this relation the parameterized distance δx_{par}. C_δ is a non-dimensional coefficient which has to be defined. If this relation (Eq. 5.2) is reasonable $S_{\max}$ and δx_{par} should be equal. Figure 14 shows the absolute difference between δx_{par} and $S_{\max}$ for varying C_δ. In order to obtain C_δ for different conditions, we calculated this difference considering (i) the whole dataset (34 legs), (ii) a subset with only those legs with $\rho_{\max} > 0.4$ (12 legs) and finally (iii) a reduced subset of legs with $\rho_{\max} > 0.4$ and low cross-wind ($u_{\mathrm{cross}}/\overline{u} < 0.5$, 8 legs). The smallest difference is obtained for the latter subset, with a value of $C_\delta \approx 0.4$. The subset of legs with $\rho_{\max} > 0.4$ also show a minimum close to $C_\delta \approx 0.4$, however the absolute difference is higher. A suitable value for parameter C_δ can not be determined when all legs are considered since a minimum value is not found.

For the neutral case, Horst and Weil (1992) found that the level of maximum influence $\overline{z}$ of a given upstream unit surface point source is proportional to the downstream distance δx through the relation

$$\delta x = \frac{\overline{z}}{\kappa\sqrt{C_D}} = \frac{1}{\kappa}\frac{\overline{u}}{u_*}\overline{z}, \qquad (5.3)$$

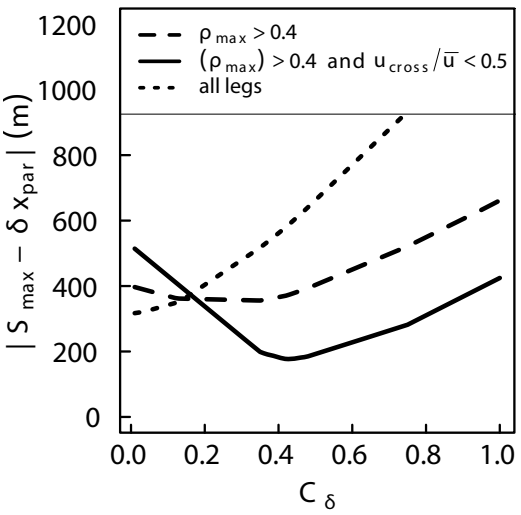

Figure 14: Absolute difference between the parameterized horizontal shift δx_{par} and the spatial lag of the maximum correlation function $S_{\max}$ against C_δ. For all legs (pointed line), legs with $\rho_{\max} > 0.4$ (dashed line) and legs with $\rho_{\max} > 0.4$ and low cross wind $u_{\mathrm{cross}}/\overline{u} < 0.5$ (black line).

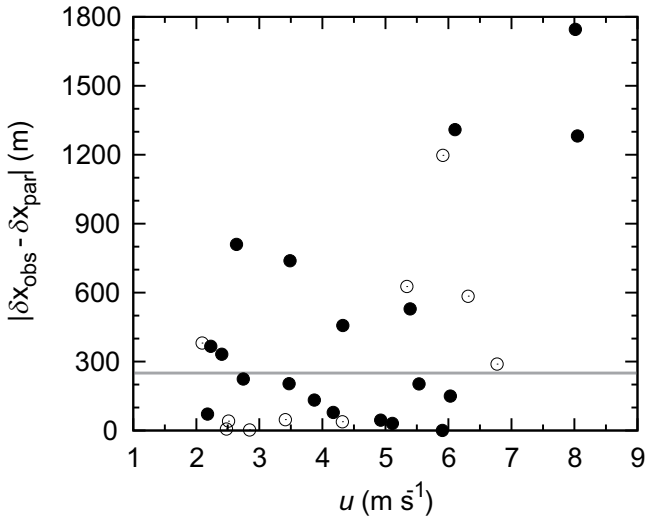

Figure 15: Absolute difference between the parameterized horizontal shift δx_{par} and the observed one δx_{obs} against the mean wind speed $\overline{u}$. A total of 29 legs with a clear drop of σ_θ in the vicinity of the lake could be observed. Open circles indicate those cases with $u_{\mathrm{cross}}/\overline{u} > 0.5$ (large cross-leg winds). Black circle indicate cases with low cross wind $u_{\mathrm{cross}}/\overline{u} < 0.5$. The horizontal grey line indicates the spatial lag between two consecutive overlapping windows (250 m).

where $C_D = (u_*/\overline{u})^2$ is the drag coefficient and $\kappa = 0.40$ is the von-Kármán constant. In our case we have to assume that the lake acts like a unit surface point source. That means we consider the lake as one point with no horizontal extension, from where the spatial distance of a footprint in the boundary layer is calculated. We have seen in previous sections, that for our study, σ_w is a better scaling variable for turbulence compared to u_*. σ_w is needed to calculate the length scale L_w. Only with this length scale L_w, the geometrical length of the lake is large enough in order to show a footprint at the observation height of the lake for the most of our cases, including higher wind speeds (see Figure 12.)

Thus, relation (5.3) with σ_w instead of κ turns into expression (5.2), with a value of C_δ close to κ. The parametrization of (5.2) with $C_\delta = 0.4$ is displayed for the two different legs (LIT13 and LIT14) in Figure 10. The vertical black dashed lines indicate the lake boundaries shifted downstream by the distance δx_{par} following the parameterization. Since the parametrization depends on the horizontal wind speed and on the vertical mixing, the distance of the black dashed lines respect to the lake boundaries is different for both flights (LIT13 and LIT14) as weather conditions were also different. The segment of the lake with the minimum of the σ_θ should be located within the black dashed lines for both cases. For LIT14 the drop of the σ_θ is in between the parametrized distance. LIT13 is a good example for showing that not all cases follow the parametrization. However, it is necessary to use the entire dataset in order to test the validity of the approach given by Eq. 5.2. We have identified the region with a maximum drop in σ_θ over the vicinity of the lake for 29 legs by a computer algorithm detection (as explained in Section 3.6). The detection of a drop in σ_θ is satisfactorily for most cases (indicated by open circles in Figure 10).

In the previous section 3.6, we defined the horizontal distance between the geometrical centre of that region where the drop of σ_θ occurs and the centre of the lake, as the observed mean propagation distance of the lake influence δx_{obs} at the leg height $\overline{z}_{\mathrm{obs}}$.

If expressions of Eq. 5.2 is valid, the parameterized distance δx_{par} should fit to the observed one δx_{obs}. In Figure 15 the difference $|\,\delta x_{\mathrm{obs}} - \delta x_{\mathrm{par}}\,|$ is plotted versus the mean wind speed $\overline{u}$. The discrepancy between the observed and parameterized shifts is smaller than the spatial lag between two consecutive overlapping windows (250 m) for 15 cases. Hence, 55 % of the cases exhibit an observed horizontal shift similar to the parametrized results from Eq. 5.2. However, the parametrization δx_{par} does not hold for all cases. It tends to fail for situations with large wind speeds.

6 Conclusion

The influence of an intermediate-scale lake on airborne measurements taken below 100 m in a CBL has been analysed for 34 flight legs flown during two consecutive field campaigns in the summer of 2002 and 2003. Several first-order and second-order statistics were evaluated in order to check if an lake influence is apparent in the lower CBL in the vicinity of the lake. The spatial variability for mean quantities is not very significant. Although there are some hints that our analysed data indicate a cooling over the lake at 100 m above ground and

that we can distinguish between a drier atmosphere over the lake compared to the moister air over forest.

The second-order moments related to potential temperature (σ_θ) exhibit a clear decrease in the vicinity of the lake at the airborne observation height. Unfortunately, only one flight of the selected dataset contained consecutive passes along the same leg during same environmental conditions and hence a low sampling error. The flight showed that the observed variances of σ_θ are reduced significantly over the lake. But also the remaining flights, each with different environmental conditions, showed reduced σ_θ in 33 out of 34 flight legs. Although due the lack of iterative passes the theoretical sampling error is in the same order as the measurement value, the persistence of a drop in σ_θ for most of the flights in the downstream propagation of the lake is significant. Most likely, the lack of thermals above a cool surface favours such a drop for theses parameters and their random variability. Second-order moments of humidity and vertical wind, however, did not identify the underlying lake, at least in our study.

The fact that, a slight drop is seen in the potential temperature but none of the legs analysed identify a clear change in the mean variables, as we would expect when entering an IBL, suggest that a well defined IBL is not observed in our data set. Therefore, an IBL which should be as well in equilibrium with the underlying surface cannot be clearly identified with our observations according to Eq. 4.9. It seems to be more likely, that the flow adjusts to the new surface, which is indicated by the decrease of variance of temperature over the lake, but without the formation of an IBL.

Several length scales of surface heterogeneity were calculated following previous studies of Mahrt (2000) and Bange et al. (2006). These scales consider different parameters depending on the stability conditions of the flow. Only the scale that considers the variance of vertical velocity or a velocity scale was compatible with our observations. Probably the variety of buoyancy conditions in our dataset (which includes days with a weak surface heat flux and strong winds together with days with strong convection) requires a stability parameter able to describe the vertical mixing induced by both wind shear and thermal heating in order to fit to all conditions during our flight experiment. In addition, the application of a convective scale for those cases where the boundary-layer depth was known, indicates that the 2 km wide lake could affect the lower CBL for wind speeds below 4 m s^{-1}.

Finally, the downstream propagation of the lake influence has been addressed by calculating the cross-correlation function between the surface radiative temperature and the variance of potential temperature for the entire leg. Although a clear relationship between the spatial lag of the maximum correlation and the horizontal advective speed could only be identified for 8 cases, this relation indicates promising results when it is applied solely to the lake influence. After developing a system of that automatically detects the mean horizontal shift of the lake influence, 55 % of the cases exhibit an observed horizontal shift similar to the simple parametrization of Eq. 5.2.

Atmospheric flow is complex. Therefore a quantitative comparison of the various length scales derivations and downstream parametrizations which are based on linear theory is difficult. In future flight experiments, we suggest simultaneous flights with at least three research aircraft, at three different levels above a discontinuity, performing repeated legs. Ideally this could be done using research unmanned air vehicles (UAV) (van den Kroonenberg et al., 2012; Wildmann et al., 2014). By using UAV, also the flight altitude can be maintained with a much higher precision (±1 m) compared to a manned helicopter.

Acknowledgments

The measurements were performed during the LITFASS-2003 experiment, a field experiment within the framework of the EVA_GRIPS project (Evaporation at grid/pixel scale). EVA_GRIPS was funded by the German Federal Ministry of Education and Research (BMBF) as a part of the German climate research program (DEKLIM) under the contract no. 01LD0103. Andreas Lang is acknowledged for its preliminary analysis of the current experimental dataset for his BSc Thesis.

References

Avissar, R., T. Schmidt, 1998: An evaluation of the scale at which ground-surface heat flux patchiness affects the convective boundary layer using large-eddy simulations. – J. Atmos. Sci. **55**, 2666–2689.

Bange, J., R. Roth, 1999: Helicopter-borne flux measurements in the nocturnal boundary layer over land – a case study. – Bound.-Layer Meteor. **92**, 295–325.

Bange, J., F. Beyrich, D.A.M. Engelbart, 2002: Airborne measurements of turbulent fluxes during LITFASS-98: Comparison with ground measurements and remote sensing in a case study. – Theor. Appl. Climatol. **73**, 35–51.

Bange, J., T. Spiess, M. Herold, F. Beyrich, B. Hennemuth, 2006: Turbulent fluxes from helipod flights above quasi-homogeneous patches within the litfass area. – Bound.-Layer Meteor. **121**, 127–151.

Bange, J., M. Esposito, D.H. Lenschow, 2013: Airborne Measurements for Environmental Research – Methods and Instruments, chapter 2: Measurement of Aircraft State, Thermodynamic and Dynamic Variables. – Wiley, 641 pp.

Beyrich, F., H.-T. Mengelkamp, 2006: Evaporation over a heterogeneous land surface: EVA-GRIPS and the LITFASS-2003 experiment – an overview. – Bound.-Layer Meteor. **121**, 5–32.

Beyrich, F., H.-J. Herzog, J. Neisse, 2002: The LITFASS project of DWD and the LITFASS-98 experiment: The project strategy and the experimental setup. – Theor. Appl. Climatol. **1–2**, 3–18.

Beyrich, F., J.-P. Leps, M. Mauder, J. Bange, T. Foken, S. Huneke, H. Lohse, A. Lüdi, W.M. Meijninger, D. Mironov, others, 2006: Area-averaged surface fluxes over the LITFASS region based on eddy-covariance measurements. – Boundary-Layer Meteor. **121**, 33–65.

Garratt, J., 1990: The internal boundary layer – a review. – Bound.-Layer Meteor. **50**, 171–203.

Göckede, M., M. Mauder, T. Foken, 2004: Qualitätsbegutachtung komplexer mikrometeorologischer Messstationen im Rahmen des VERTIKO-Projekts. – Univ. Bayreuth, Abt. Mikrometeorologie.

Grossmann, S., D. Lohse, V. L'vov, I. Procaccia, 1994: Finite size corrections to scaling in high reynolds number turbulence. – Phys. Rev. Lett. **73**, 432.

Hadfield, M., W. Cotton, R. Pielke, 1991: Large-eddy simulations of thermally forced circulations in the convective boundary layer. part i: A small-scale circulation with zero wind. – Boundary-Layer Meteor. **57**, 79–114.

Hadfield, M., W. Cotton, R. Pielke, 1992: Large-eddy simulations of thermally forced circulations in the convective boundary layer. part ii: The effect of changes in wavelength and wind speed. – Boundary-Layer Meteor. **58**, 307–327.

Højstrup, J., 1982: Velocity spectra in the unstable planetary boundary layer.. – J. Atmos. Sci. **39**, 2239–2248.

Horst, T., J. Weil, 1992: Footprint estimation for scalar flux measurements in the atmospheric surface layer. – Boundary-Layer Meteor. **59**, 279–296.

Huang, H.-Y., S.A. Margulis, 2009: On the impact of surface heterogeneity on a realistic convective boundary layer. – Water Resour. Res. **45**, published online. DOI: 10.1029/2008WR007175.

Józsa, J., B. Milici, E. Napoli, 2007: Numerical simulation of internal boundary-layer development and comparison with atmospheric data. – Bound.-Layer Meteor. **123**, 159–175.

Lenschow, D.H., B.B. Stankov, 1986: Length scales in the convective boundary layer. – J. Atmos. Sci. **43**, 1198–1209.

Lenschow, D., J. Mann, L. Kristensen, 1994: How long is long enough when measuring fluxes and other turbulence statistics?. – J. Atmos. Oceanic Technol. **11**, 661–673.

Letzel, M.O., S. Raasch, 2003: Large eddy simulation of thermally induced oscillations in the convective boundary layer. – J. Atmos. Sci. **60**, 2328–2341.

Lumley, L., H. Panofsky, 1964: The Structure of Atmospheric Turbulence. – John Wiley & Sons.

Mahrt, L., 1996: The bulk aerodynamic formulation over heterogeneous surfaces. – Bound.-Layer Meteor. **78**, 87–119.

Mahrt, L., 2000: Surface heterogeneity and vertical structure of the boundary layer. – Bound.-Layer Meteor. **96**, 33–62.

Mann, J., D.H. Lenschow, 1994: Errors in airborne flux measurements. – J. Geophys. Res. Atmos. **99**, 14519–14526.

Maronga, B., S. Raasch, 2013: Large-eddy simulations of surface heterogeneity effects on the convective boundary layer during the LITFASS-2003 experiment. – Bound.-Layer Meteor. **146**, 17–44.

Maronga, B., O.K. Hartogensis, S. Raasch, F. Beyrich, 2014: The effect of surface heterogeneity on the structure parameters of temperature and specific humidity: a large-eddy simulation case study for the litfass-2003 experiment. – Boundary-Layer Meteor. **153**, 441–470.

Mengelkamp, H.-T., F. Beyrich, G. Heinemann, F. Ament, J. Bange, F. Berger, J. Bösenberg, T. Foken, B. Hennemuth, C. Heret, others, 2006: Evaporation over a heterogeneous land surface: the EVA-GRIPS project. – Bull. Amer. Meteor. Soc. **87**, 775–786.

Panofsky, H., D. Larko, R. Lipschutz, G. Stone, E. Bradley, A.J. Bowen, J. Højstrup, 1982: Spectra of velocity components over complex terrain. – Quart. J. Roy. Meteor. Soc. **108**, 215–230.

Raabe, A., K. Arnold, A. Ziemann, F. Beyrich, J.-P. Leps, J. Bange, P. Zittel, T. Spiess, T. Foken, M. Göckede, others, 2005: STINHO – structure of turbulent transport under inhomogeneous surface conditions – part 1: The micro-α scale field experiment. – Meteorol. Z. **14**, 315–327.

Raupach, R.R., J.J. Finnigan, 1995: Scale issues in boundary-layer meteorology: surface energy balances in heterogeneous terrain. – Hydro. Proc. **9**, 589–612.

Sahlée, E., A. Rutgersson, E. Podgrajsek, H. Bergström, 2014: Influence from surrounding land on the turbulence measurements above a lake. – Boundary-Layer Meteor. **150**, 235–258.

Samuelsson, P., E. Kourzeneva, D. Mironov, 2010: The impact of lakes on the european climate as stimulated by a regional climate madel. – Boreal Env. Res. **15**, 113–129.

Shao, Y., J.M. Hacker, 1990: Local similarity relationships in a horizontally inhomogeneous boundary layer. – Boundary-Layer Meteor. **52**, 17–40.

Shao, Y., J.M. Hacker, P. Schwerdtfeger, 1991: The structure of turbulence in a coastal atmospheric boundary layer. – Quart. J. Roy.l Meteor. Soc. **117**, 1299–1324.

Strunin, M.A., T. Hiyama, J. Asanuma, T. Ohata, 2004: Aircraft observations of the development of thermal internal boundary layers and scaling of the convective boundary layer over non-homogeneous land surfaces. – Bound.-Layer Meteor. **111**, 491–522.

Stull, R., 1988: An Introduction to Boundary Layer Meteorology. – Kluwer Academic Publisher, Dordrecht, 666 pp.

Sühring, M., S. Raasch, 2013: Heterogeneity-induced heat-flux patterns in the convective boundary layer: Can they be detected from observations and is there a blending height? – A Large-Eddy Simulation study for the LITFASS-2003 experiment. – Bound.-Layer Meteor. **148**, 309–331.

van den Kroonenberg, A.C., S. Martin, F. Beyrich, J. Bange, 2012: Spatially-averaged temperature structure parameter over a heterogeneous surface measured by an unmanned aerial vehicle. – Bound.-Layer Meteor. **142**, 55–77.

Wildmann, N., M. Hofsäss, F. Weimer, A. Joos, J. Bange, 2014: MASC – a small remotely piloted aircraft (RPA) for wind energy research. – Adv. Sci. Res. **11**, 55–61.

Wood, N., P. Mason, 1991: The influence of stability on effective roughness lengths for momentum and heat transfer. – Quart. J. Roy. Meteor. Soc. **117**, 1025–1056.

A.3 Observations of the temperature and humidity structure parameter over heterogeneous terrain by airborne measurements during the LITFASS 2003 campaign - Publication III

Noname manuscript No.
(will be inserted by the editor)

Observations of the temperature and humidity structure parameter over heterogeneous terrain by airborne measurements during the LITFASS 2003 campaign

Andreas Platis · Daniel Martnez Villagrasa · Frank Beyrich · David Tupman · Jens Bange

Received: date / Accepted: date

Abstract The turbulent structure parameters for temperature (C_T^2) and humidity (C_Q^2), and their cross-structure parameter (C_{QT}), were investigated by using the airborne-measurement platform Helipod during the LITFASS-2003 campaign. The flights were close the ground and obtained data in the surface layer of the convective boundary layer over heterogeneous surface types including forests, lakes and farmland. Variability in C_T^2 along such flight legs was observed. Values of C_T^2 over forested surfaces were one order of magnitude larger than over farmland and two orders of magnitude larger than over the lake. It was not possible to quantify a relationship between variability in C_Q^2 and a surface type. However, the spatially-averaged values of C_Q^2, measured over 8 days, were significantly lower over the lake than the other surfaces. A classification of C_{QT} was only possible between water and land surfaces with lower values over water. We find the correlation coefficient R_{QT} in the range of 0.4-1.0, so less than unity, in contrast with the assumption of unity in Monin-Obukhov similarity theory.

Keywords Helipod · Heterogeneous terrain · Lake · Lower convective boundary layer · Structure parameter

1 Introduction

Long term measurements of turbulent surface fluxes of sensible and latent heat are critical for a better understanding of the regional and global energy and water cycles (Beyrich et al, 2012; Li et al, 2012). Over homogeneous terrain, point measurements (e.g. eddy-covariance) are the most common practice of determining the surface fluxes (Maronga et al, 2014; Braam et al, 2014). However, natural landscapes are usually heterogeneous with different surface types like patches of farmland, water

Andreas Platis
Zentrum für Angewandte Geowissenschaften, Universität Tübingen, Hölderlinstr. 12, 72074 Tübingen
Tel.: +49-7071-2973121
E-mail: andreas.platis@uni-tuebingen.de

and forest. The local surface fluxes of the different surface types may vary considerably (Beyrich et al, 2006; Bange et al, 2006). Compared to local point measurements (Kohsiek et al, 2002; Meijninger et al, 2002), scintillometers have the advantage of being able to measure path-integrated surface fluxes over large-scale heterogeneous surfaces by using electromagnetic waves.

The turbulent refractive index field in the atmosphere affects the scattering of electromagnetic waves, and can be used to characterize the structure of turbulence in the lower atmosphere (Wyngaard and LeMone, 1980). Fluctuations in the refractive index n are primarily caused by fluctuations in temperature T and and the humidity, here expressed by the water vapour mixing ratio Q.

This implies that the refractive index structure parameter C_n^2 can be expressed in terms of the structure parameters of temperature C_T^2 (temperature fluctuation) and humidity C_Q^2 (humidity fluctuation) and the cross structure parameter C_{QT} (Wyngaard et al, 1978; van den Kroonenberg et al, 2012):

$$C_n^2 = a^2 C_T^2 + 2ab\, C_{QT} + b^2 C_Q^2 \,, \tag{1}$$

where a and b depend on the wavelength of the radiation, and on mean atmospheric conditions such as pressure, humidity, and temperature. The temperature fluctuations have the dominant contribution to C_n^2 for electromagnetic radiation at optical wavelengths (i.e. $a^2 C_T^2 \gg b^2 C_Q^2$), while the humidity fluctuations control the microwave part of the spectrum. Hence, using a microwave scintillometer and an near-infrared scintillometer simultaneously, a direct estimation of C_Q^2 and C_T^2, respectively. However, C_{QT} cannot be evaluated with this method (Lüdi et al, 2005).

Fairall et al (1980b) and Wyngaard et al (1978) proposed the following relationship:

$$C_{QT} \approx R_{QT} \sqrt{C_T^2\, C_Q^2}, \tag{2}$$

which allows calculation of C_{QT} with knowledge of the temperature-humidity correlation coefficient R_{QT}. It is often assumed that temperature and humidity fluctuations are perfectly correlated (either positive or negative) which implies that $R_{QT} = \pm\, 1$ (e.g. Andreas, 1989; Hill, 1997; Meijninger et al, 2002; Beyrich et al, 2005). In fact, this assumption is theoretically demanded for a flow that strictly obeys Monin-Obukhov similarity theory (MOST) (Hill, 1989), implying that MOST is valid for C_T^2 and C_Q^2.

However, non-local effects such as advection (Assouline et al, 2008; Maronga, 2014), entrainment at the top of the atmospheric boundary layer (Sempreviva and Hjstrup, 1998; De Bruin et al, 1999; Maronga et al, 2014), differences in sources and sinks (Moene and Schüttemeyer, 2008), and non-stationarity effects (because heat and moisture transport is not similar in heterogeneous terrain (Bertoldi et al, 2013)) are particularly known to result in a breakdown of the similarity between turbulent transports of temperature and humidity (Bertoldi et al, 2013). Upward moving eddies are assumed to carry heterogeneous properties, whereas downward moving eddies carry homogeneous properties. This results in a decorrelation of temperature and humidity as the contrast between the patches increases (Moene and Schüttemeyer,

2008). Thus, the assumption $C_{QT} = \pm\sqrt{C_T^2\, C_Q^2}$ is not always justifiable. In particular over non-homogeneous terrain, the strict validity of MOST and hence the perfect temperature-humidity correlation is questionable (Andreas, 1987; Andreas et al, 1998; de Bruin et al, 1993). R_{QT} and can deviate significantly from, unity, especially under weakly unstable conditions as proposed by Li et al (2012) and Maronga (2014) experimentally and by large eddy simulations (LES) respectively. Fairall et al (1980b) observed a value of $R_{QT} = 0.8$ over the sea. Beyrich et al (2005) and Meijninger et al (2006) found that R_{QT} is smaller than unity, with typical values between 0.7 and 0.9 in a convective boundary layer (CBL).

Besides the behaviour of R_{QT} under surface heterogeneity, our study also investigates the effects on the temperature and humidity structure parameter. Several studies were published in the last recent years, addressing this topic. Beyrich et al (2012) observed during the 'Lindenberg Inhomogeneous Terrain - Fluxes between Atmosphere and Surface: A long-term Study' (LITFASS) 2009 campaign, that near-surface measured C_T^2 differs by an order of magnitude over different types of farmland due to strong surface-flux variability caused by the different type of vegetation (and status of vegetation). Furthermore, the authors presented airborne measurements of C_T^2 using the unmanned mini aerial vehicle M^{2}AV. They found a considerable spatial variability of C_T^2 along the flight path at heights around 100 m. However, it was impossible to directly relate the spatial variability of the structure parameter from a single flight leg to certain characteristics of the underlying surface. Beyrich et al (2012) attributed the spatial variability to single convective plumes. A separation of the effects of the statistical nature of turbulence from those of the heterogeneity of the underlying surface on the spatial variability of structure parameters appears to be a crucial task. Braam et al (2014) noted that variability of structure parameters due to surface heterogeneity has to be constant in time in contrast to temporal fluctuations, e.g. due to larger convective elements. A subsequent study by van den Kroonenberg et al (2012) investigated airborne measurements of the LITFASS-2010 campaign in more detail by averaging the signal of C_T^2 of several flights (made at different times of the day) over the same path. van den Kroonenberg et al (2012) concluded that the spatial series of C_T^2 showed considerable variability along the flight path, caused by surface heterogeneity and temporal variations, however could not relate C_T^2 values directly to certain surface types.

Braam et al (2015) compared C_T^2 airborne measurements by the unmanned mini aerial vehicle M^{2}AV with large-aperture scintillometer (LAS) measurements. They found a discrepancy between LAS data and M^{2}AV data, which could not be fully explained. Other studies investigated C_T^2 over the depth of the CBL (e.g. van den Kroonenberg et al, 2012; Coulman, 1973), in the marine (Fairall et al, 1980a) and nocturnal boundary layers (Cuijpers and Kohsiek, 1989), and proposed a vertical scaling for the structure parameter according to MOST by $z^{-4/3}$. A horizontal variability was not analysed. Studies regarding C_Q^2 and C_{QT} are very rare. Wyngaard and LeMone (1980) and Caughey and Palmer (1979) studied C_Q^2 and C_{QT} with airborne data, but only for the homogeneous marine boundary layer with regard to $z^{-4/3}$ scaling.

In addition, LES has been used for the investigation of heterogeneity effects. Maronga et al (2014) used the LITFASS terrain and ground-based surface fluxes mea-

surements during the LITFASS 2003 campaign as input for their LES. They showed that 50% of the variability of the C_T^2 along a virtual flight path was caused by the remaining noise from random turbulence fluctuations, and could not be related to a surface heterogeneity. In an LES run with a homogeneous surface forcing Maronga et al (2013) and Cheinet and Siebesma (2009) showed a high variability of C_T^2 along a given horizontal path associated with plumes and downdrafts (low C_T^2 outside the plumes alternates with high C_T^2 inside the plumes). Experimental studies by Braam et al (2014) and Petenko and Shurygin (1999) confirmed these findings. The LES results suggest that measured path averages require sufficient temporal averaging and an adequate path length in order to decrease the statistical uncertainty due to randomly distributed convection, especially when regarding airborne measurements (Maronga et al, 2013).

Further, Maronga et al (2014) investigated the vertical propagation of the surface heterogeneity influence on the structure parameter. They showed that local effects of surface heterogeneity remain prominent in the lower ABL. They could not give any proof for a blending height for the structure parameter, but for the LITFASS 2003 case study it seems that blending effects occur above several tens of metres above the ground. The blending height is viewed here as a scaling depth that describes a vertical scale at which the impact of surface heterogeneity decreases to some relatively small value (Mahrt, 2000). The LES results of Maronga et al (2014) and Maronga (2014) suggested that C_T^2 follows MOST, even under heterogeneous surface forcing. Furthermore, they concluded that C_T^2 is highly correlated with the surface sensible heat flux. However, C_Q^2 is decoupled from the latent surface flux even at low levels which is ascribed to the entrainment of dry air at the top of the boundary layer. Cheinet and Cumin (2011) supplemented the previous LES studies by its own LES with data input from daytime observations in summer over the southern Great Plains of the United States, showing also that the distribution of C_Q^2 was determined by entertainment from dry air parcels from the free atmosphere. Therefore C_Q^2 does not follow MOST if entrainment is significant. Li et al (2012) suggested from their experimental data that due to entrainment processes there is a dissimilarity between the turbulent transport of heat and moisture and the corresponding MOST function for the structure parameter.

The aim of this study is to compare previously unpublished airborne in-situ measurements with findings from LES and the previous experimental studies. Therefore the present study uses data from the LITFASS 2003 experiment (Bange et al, 2006; Beyrich and Mengelkamp, 2006), more specifically spatial series of temperature T and water vapour mixing ratio Q over heterogeneous surfaces in order to obtain C_T^2, C_Q^2 and C_{QT}. The spatial series were measured by the helicopter-borne turbulence measurement system Helipod (Bange et al, 2005). The use of in-situ measurements instead of numerical studies has the advantage that they are a direct observation rather than a model simulation obtained during different atmospheric condition, rather than representing a single, ideal situation. In the first part, the study is a repetition and continuation of the analysis of van den Kroonenberg et al (2012) regarding the spatial variability of C_T^2 over heterogeneous terrain, with the addition that we attempt to relate the structure parameters to certain surface types (farmland, water and forest). The contrast (in surface fluxes) between the different land-use types in the current study is

larger than that along the flight legs used in van den Kroonenberg et al (2012), which were different types of crops only. In addition to the spatial series over heterogeneous terrain we use flight data above single surface types, avoiding heterogeneous influences. Further, we introduce measurements of C_Q^2 and C_{QT} and are therefore able to show results of R_{QT}. As far as the authors know, this is the first study of the structure parameter of humidity over heterogeneous terrain using data from airborne sensors.

According to the literature review a heterogeneous surface should induce a variability in structure parameter which is detectable by airborne measurement. The detectability in a CBL of surface-induced variations is favoured by large amplitudes of surface fluxes (e.g water and forest), airborne observations which are below the blending height, and a sufficient repetition of flight legs in order to obtain an adequate temporal averaging. However, detectability might be reduced by factors such as the turbulent variability of the structure parameters due to randomly distributed convection, the role of the window sampling length, and non-local effects (such as advection, entrainment at the top of non-stationarity effects as mentioned above)

The main research questions addressed in this study are:

- Is it possible to determine plausible values of spatially-averaged C_Q^2 and C_{QT} by the Helipod, from its fast-response humidity and temperature measurements along horizontal flights?
- Does heterogeneous terrain affect the spatial variability of C_Q^2, C_T^2 and C_{QT} in the lower CBL? Can we distinguish the variation of the structure parameter due to variations in the characteristics of the underlying surface amidst the noise due to turbulent variations? What factors influence the detectability? Does the variability of C_T^2 induced by surface heterogeneity agree with the results of van den Kroonenberg et al (2012) and previous studies such as Li et al (2012); Maronga (2014); Maronga et al (2014) ?
- Is it possible to relate the dissimilarity ($|R_{QT}| < 1$) between turbulent temperature and moisture transport to certain surface conditions ?

Is there any regularity to be found in the deviations of the correlation coefficient from unity ($|R_{QT}| < 1$) (preferably related to surface conditions).

The paper is organized as follows: In Sect. 2 we explain the method used to calculate the structure parameter. In Sect. 3 we describe the campaign set-up and data which is analysed, the flight experiment and the used foot print model Sect. 5 reports the variability of the observed structure parameters over different surface types and the variability of R_{QT}. Sect. 6 gives a conclusion.

2 Methods

For computing the structure parameter several methods can be used. The 'direct' classical method using the structure function (Tatarskii, 1971; van den Kroonenberg et al, 2012), the wavelet method using the wavelet spectrum as described by Maronga et al (2013) or calculating the structure parameter via the Fourier spectrum as described by Hartogensis et al (2002). Following the study of Braam et al (2015), the most appropriate method is the direct calculation of the structure function for in-situ measurements (both other methods need an infinitely long inertial subrange) Therefore,

for a finite number of observations the structure function $D_S(r)$ for any scalar S is calculated according to:

$$D_S(r) = \frac{1}{N-n} \sum_{i=1}^{N-n} [S(x_i) - S(x_i + r)]^2 \tag{3}$$

for a given data record. N denotes the number of data points in the record, $r = r(n)$ is the spatial displacement (lag), n is the number of data points associated with the lag r, and x_i is the spatial coordinate. The lag r is calculated by

$$r = \frac{n}{f_s} \cdot v_{\mathrm{gs}} \tag{4}$$

where $v_{\mathrm{gs}} \approx 40$ ms^{-1} is the ground speed of the Helipod and f_s the sampling frequency, which was 100 Hz. As shown by Martin and Bange (2014), the influence of airspeed variations and thus the variation of the data point separation length can usually be neglected for second-order turbulence statistics. The methodology of calculating the structure parameter C_T^2, C_Q^2, C_{QT} from the structure function is the same as in van den Kroonenberg et al (2012) and is therefore presented only in the appendix (Sect. 5).

van den Kroonenberg et al (2012) proved that the calculation of C_T^2 from airborne in-situ data by a fast open wire thermometer is possible. A very similar system is used as well in Helipod (as explained in Sect. 3.1). It has to be checked if the Helipod system is able to determine reliable values of the spatially averaged C_Q^2 and C_{QT} by its fast humidity sensor. For that, the statistical errors of the measured structure parameters are investigated. The error calculation is following strictly van den Kroonenberg et al (2012). It is presented in the appendix (Sect. 5) as well. The evaluation reveals that the Helipod is able to determine reliable values of the spatially-averaged C_Q^2 and C_{QT}, from fast-response humidity and temperature measurements along horizontal flights when using at least a window size of $N = 1500$ data points to calculate the spatially resolved structure parameter, which corresponds to a window length of $W = 600$ m.

3 Flight Experiment

3.1 The LITFASS-2003 campaign

The data were collected during the LITFASS-2003 campaign, which was carried out between 19 May and 17 June, 2003 (Beyrich and Mengelkamp, 2006). This field study was embedded in the series of the LITFASS experiments, which were initiated in 1995 in order to develop and test a strategy for the determination of the area-averaged turbulent fluxes over a heterogeneous landscape (see Beyrich et al (2002) for more details).

The campaign was performed around the MOL-RAO (Meteorological Observatory Lindenberg - Richard-Aßmann Observatory) of the German Meteorological Service (*Deutscher Wetterdienst, DWD*) in the area of Brandenburg, Germany, 60 km

south-east from Berlin. The experimental site is a 20 x 20 km^2 area with an absolute altitude variability of less than 100 m. The study area consists of coniferous forest in the western part (43% of the area) and agricultural fields in the eastern part (31%, mainly cereals). The whole area is embedded with lakes and villages that add heterogeneity.

The campaigns were part of the regional 'EVAporation at GRId/Pixel Scale over heterogeneous surfaces' (EVA_GRIPS) and the 'VERTIcal transport of energy and trace gases at anchor stations under Complex natural conditions' (VERTIKO) projects and provided a comprehensive data set on surface-atmosphere interaction processes at the mesoscale level. Measurements included the instrumentation of the Falkenberg boundary-layer field site (GM Falkenberg), a regional network of micro-meteorological stations and airborne measurements by the helicopter-borne turbulence probe Helipod, among other ground-based remote sensing devices (see Raabe et al (2004) and Beyrich and Mengelkamp (2006) for a complete overview).

The Helipod (Bange et al, 2002) is an autonomously operating sensor package attached to a 15 m rope below a helicopter of almost any type. At a mission speed of 40 m/s the Helipod is outside the down-wash area of the rotor blades. The Helipod is equipped with its own power supply, on-board computer, data storage, navigation systems, radar altimeter, and fast responding sensors for wind, temperature, humidity, and surface temperature measurements. The 3-D wind vector is measured with a five-hole probe in combination with GPS and inertial measurement unit (IMU). Temperature is measured with a Pt-100 in a Rosemount housing and a fast open wire thermometer. Humidity is measured by a combination of a dew-point mirror, a humicap and a Lyman-α hygrometer in order to cover the whole range of scales of turbulence (Bange et al, 2005). All these instruments were installed in a container (pod) of 5 m in length and about 0.5 m in diameter. The fast inertial navigation and all meteorological sensors were concentrated in the nose of the pod in order to avoid phase shifting. Due to the small fuselage, and absence of wings and impulse, the influence of the Helipod on the atmospheric flow is small compared to an aircraft. At 40 m/s airspeed and with a sampling rate of 100 Hz, the system resolves turbulent structures down to $\approx$1 m (Bange and Roth, 1999).

Almost 100 flight hours (60 flights) of data were collected during the LITFASS-2003 campaign. The current work focuses on the behaviour of the structure parameters over farmland, forest and lake, so only 15 flights were selected. These flights were performed either in the morning or in the early afternoon during a well developed CBL, with variable wind conditions and consisted of several flight legs. The boundary-layer height varied between 1000 and 2500 m above ground level for all flights and was measured by either a Lidar or radiosondes (Beyrich and Mengelkamp, 2006). All following heights will be given here above ground level. Every leg is a horizontal, straight and level (equal height) flight track. All legs are at around 80 m above ground level, therefore all flight legs presented here are assumed to be inside the surface layer, the lowest 10% of the CBL. An overview of all evaluated flights is listed in Table 1. Two different flight strategies were used for investigation: Flights over a single homogeneous surface only (HOM) and flights covering a heterogeneous terrain (HET) with several mixed surface types (farmland, water, forest).

Table 1 List of selected flights during the LITFASS-2003 campaign. Weather indicates current cloud cover during the flight. Wind speed (WS) was measured at around 80 m above ground by the Helipod. The height of all legs were around 80 m above ground. The CBL height is the maxim measured height during the flight. Local time is UTC + 2 hours.

Flight code	Date	Time (UTC)	Weather (Clouds)	Wind dir (^{o})	WS (m s^{-1})	CBL Height z_i m
single homogeneous surface						
HOM0529_1	29.05.2003	0806–1012	1/8 Ci	95	4.0	1000
HOM0529_2	29.05.2003	1100–1329	6/8 Ci	80	4.0	1200
HOM0530_1	30.05.2003	0806–1012	cloudless	115	3.0	1200
HOM0530_2	30.05.2003	1230–1431	cloudless	160	2.0	1600
HOM0602	02.06.2003	0919–1137	5/8 Cu	125	4.0	2500
HOM0613	13.06.2003	1217–1041	1/8 Cu	300	7.0	1900
HOM0614	14.06.2003	0827–0930	7/8 Ci	300	3.0	1600
heterogeneous terrain						
HET0528	24.05.2003	1053–1308	3-4/8 Cu	52	6.2	1400
HET603	03.06.2003	1020–1225	1/8 Cu	141	5.0	2100
HET0604	04.06.2003	1016–1321	6/8 Cu	145	6.0	1900
HET0606	06.06.2003	1028–12391	2/8 Cu	303	4.8	1200
HET0610	10.06.2003	0758–1010	2/8 Cu	170	3.5	1200
HET0612	12.06.2003	0817–1026	3/8 Cu	305	3.8	2000
HET0613	13.06.2003	0833–1041	2/8 Cu	335	5.0	1400
HET0617	17.06.2003	1132–1333	4/8 Cu	142	2.2	1500

3.2 Homogeneous Flights (HOM)

The flights above homogeneous terrain (*HOM0529_1 - HOM0614*) were carried out on five different days, with a total number of seven flights. The flight pattern (Fig. 1) was designed to measure above single surface types, avoiding heterogeneous influences. The legs were positioned above specific near-homogeneous surfaces types (footprints are shown to be homogeneous in Sect. 3.4) such as forest, lake and farmland. The extent of these forest and farmland patches were around 15-20 kilometres in each direction. The intermediate-scale lake is called Scharmützelsee. This lake has an extent of about 2×10 km^2 mainly oriented in the north-south direction. Each HOM flight covered all three surface types during one flight with each leg flown in two directions (as a reversed track) consecutively. The structure functions $D_T(r)$, $D_Q(r)$ and $D_{QT}(r)$ were calculated over the entire flight leg (window size $W \approx$10 km) for each single homogeneous type in order to derive a mean C_T^2, C_Q^2 and C_{QT} (further abbreviated by $\overline{C_T^2}$, $\overline{C_Q^2}$ and $\overline{C_{QT}}$) for each surface type per leg, as described in Appendix 5. All legs are at around 80 m above ground level. This flight strategy allows us to investigate differences between each surface type for all three structure parameters.

3.3 Heterogeneous Flights

Flights over heterogeneous terrain (HET flights) covered a cross-section of the entire experimental area, with flight legs in west-east direction. The flight track is over a mixed surface and includes different surface types (Fig.1). Eight flights on eight

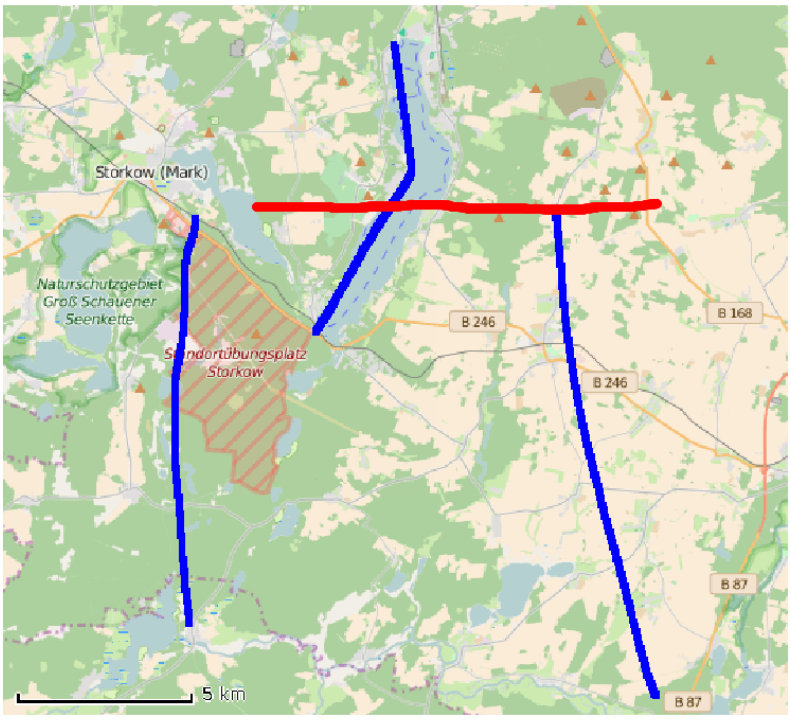

Fig. 1 Flight legs of the HOM flights (blue) and HET flights (red) at LITFASS area. Green colour refers to forest areas, blue to water and beige to farmland. Hatching area is a military zone. Source: Open Street Map.

different days were analysed (Table 1), unfortunately each HET flight leg was only flown in one direction.

The surfaces below HET flights legs are small forest-farmland patches and the intermediate-scale lake Scharmützelsee (Fig. 1). West of the lake a 4 km long forest area is located interrupted by small farmland patches. On the east side of the lake a 3-4 km continuous forest region is followed by a 4 km farmland area containing small forest patches.

According to the method of van den Kroonenberg et al (2012), the spatial series of C_Q^2, C_T^2 and C_{QT} were obtained from calculating $D_Q(r,i)$, $D_T(r,i)$ and $D_{QT}(r,i)$ within a moving window with length $W = 600$ m (window size as estimated in appendix, Sect. 5.2). This window was defined for each data point $i(x_i)$ of the humidity and temperature spatial series, with i as the centre point. By moving this window, the local structure parameters, $C_Q^2(i)$, $C_T^2(i)$ and $C_{QT}(i)$ were calculated. The obtained resolution by moving the window is a structure parameter every 0.4 m (equivalent to a 100 Hz sampling rate at 40 m s^{-1} typical ground speed). The small variations of Helipod's flight speed is typically around 2-3 m s^{-1}. Braam et al (2015) checked the flight speed variation of this order as well in their work. Their result show a variation of the structure parameter with less than 1%.

Braam et al (2014) noted the variability of the structure parameters due to surface heterogeneity is likely to be constant in time in contrast to variations in time and place due to random turbulent fluctuations, e.g. due to larger convection. Thus, the random turbulent fluctuations were reduced by averaging the spatial series of the dimension-less structure parameter over all flights, resulting in the ensemble average

$A_Q(i), A_T(i)$ and $A_{QT}(i)$ for each data point i. Again we follow the method of van den Kroonenberg et al (2012) strictly. The method is shown for any scalar S and can be applied to C_Q^2, C_T^2 and C_{QT}. Each individual spatial series (i.e. one leg) of the structure parameters was normalized with its spatially-averaged value, $\overline{C_{S\,j}^2}$ (mean value of the leg j), so that for each leg we obtain a series that fluctuates around unity and is one in the mean. We define this as a normalized spatial series at each data point i:

$$\widetilde{C_{S\,j}^2}(i) = \frac{C_{S\,j}^2(i)}{\overline{C_{S\,j}^2}} \tag{5}$$

The normalized spatial series of each flight were then averaged over all $f = 8$ flights for each data point i.

$$A_S(i) = \frac{1}{f}\sum_{j=1}^{f} \widetilde{C_{S\,j}^2}(i) \tag{6}$$

With the spatial series of the ensemble average the verification of heterogeneous surface effects is more feasible, as random turbulence influence is diminished. Further, the standard deviation of the averaged A_{S_i} was calculated as well, in order to illustrate the variability over all flights:

$$\sigma_{\widetilde{C_S^2}}(i) = \sqrt{\frac{1}{f}\sum_{j=1}^{f}\left(A_S(i) - \widetilde{C_{S\,j}^2}(i)\right)^2}, \tag{7}$$

With this method we are able to investigate the spatial variability of the structure parameter, in order to address the second and third research questions listed in Section 1.

For the analysis of the structure parameter, the height above the ground is assumed to be 80 m. Although the topography of the LITFASS area is rather flat (Maronga et al, 2014) there is a range of heights of about 60 m in amplitude. The Helipod tried to follow changes in terrain as accurate and fast as possible by using a radar altimeter, which indicates the height above ground by a radar pulse. However, there is still some variability in this height during the flights of about $\pm$30 m. Especially when the Helipod is flying over the lake Scharmützelsee, the lowest elevation in the LITFASS area, the height change is up to 30 m. We studied the correlation between C_T^2 and radar altimeter height for a typical HET flight (Fig. 2). The worst case, when the maximum height variation was encountered, was a rapid height increase by 32 m when the Helipod was approaching the western shore line (longitude 14.03°). Changes in height might affect the structure parameters, because it decreases with height according to $z^{-4/3}$ (Wyngaard and LeMone, 1980; Caughey and Palmer, 1979) under free-convection conditions. It can be expected that, a height increase of 32 m will decrease the magnitude of the structure parameter by 34%. In the lower panel of Fig. 2 the spatial series of C_T^2 is displayed. In addition a corrected C_T^2 (red line) where the structure parameter was normalized to a reference height of 78 m (mean height of the flight leg) assuming a $z^{-4/3}$ dependence. In summary, although we acknowledge that height variation might decrease or increase C_T^2, we demonstrate that for our data

set, the height displacement is negligible compared to other effects, which dominate the variation in structure parameter, such as turbulence (e.g. up- and downdrafts) and surface variability.

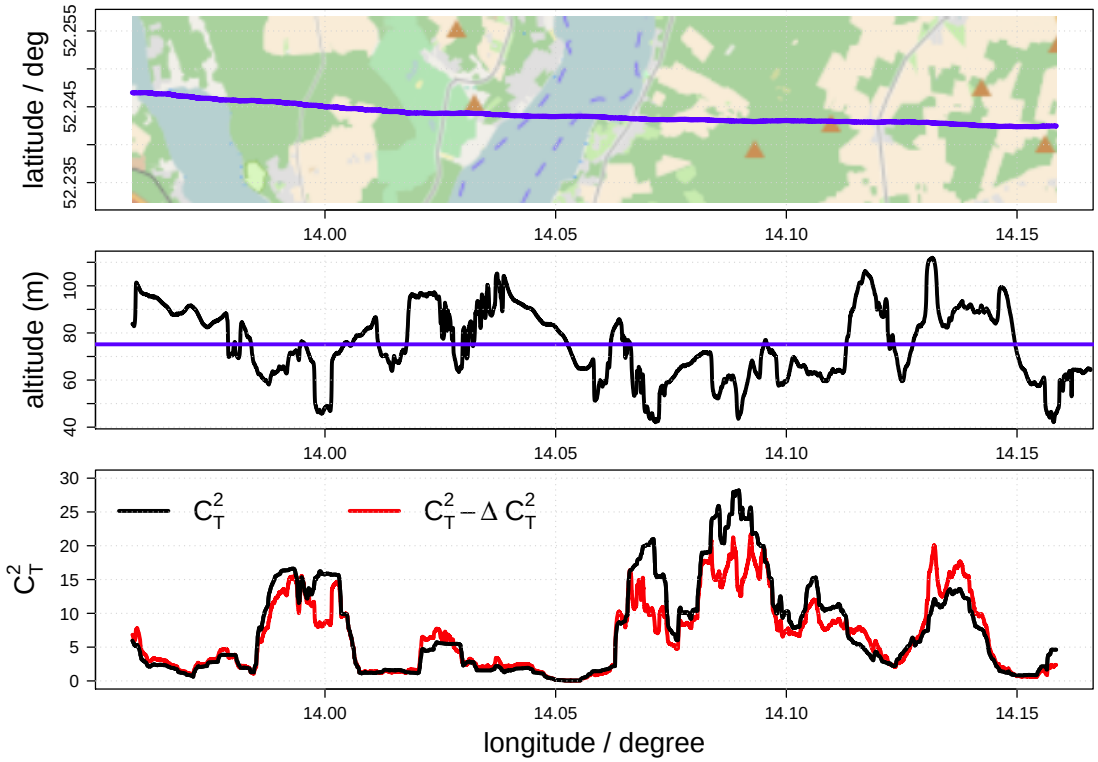

Fig. 2 Flight track of HET0612 (upper panel). Corresponding radar altimeter height (middle panel) and the mean height above ground over the whole flight track (blue line). Spatial series of C_T^2 (black line) with its corrected C_T^2 (red line) by the vertical scaling $z^{-4/3}$-law (Wyngaard and LeMone, 1980; Caughey and Palmer, 1979).

3.4 Footprint Model Analysis

Since the observation height of our measurement is about 80 m above ground level a footprint model is needed to know the source area of the turbulent eddies measured, which defines the area in the landscape the structure parameter corresponds to. The footprint area is calculated according to the model of Kljun et al (2015) which was amongst other things developed for airborne flux data. The footprint model is a two-dimensional parametrization based on the backward Lagrangian stochastic particle dispersion model LPDM-B. Further information are described in Kljun et al (2002). We calculated for all analysed flights the footprint of the flight track. The input parameters are the turbulent wind vector, potential temperature, boundary layer height, flight altitude and surface roughness. The model approximated the distance between the receptor and the maximum contribution to the measurement by the peak location of the crosswind-integrated footprint (Kljun et al, 2015). Hence, the distance from the measurement point is where the maximum source is located.

For the HOM flights the maximum spatial extent and position of the surface area that is contributing to a airborne measurement was 400 m in the upstream direction of the prevailing wind direction. Since the surface patches of forest and farmland, which are below the flight tracks in Fig. 1), have length scales of several kilometres the fetch of HOM flights covered always exclusively the corresponding surface type. However, the lake Scharmützelsee has a longitudinal extent of about 2 km. The flight legs were parallel to the shore line, and close to the downstream shore line (e.g for westerly winds the leg was close the the eastern shore line). However, especially for strong westerly and easterly winds (Flights: HOM0529_1, HOM0529_1, HOM0613) the footprint area still remains very close to the upstream bank.

The footprint of the HET flights is shifted relative to the flight leg, but still covers the same types of surface type as those present below the Helipod. The worst case is shown as an example for the flight HET0528 in Fig. 3. For that case the footprint model calculated the largest spatial extend for the surface area that is contributing to a airborne measurement, due to the highest mean wind speed and a low friction velocity u_* of all HET flights. The displacement between footprint and measurement is up to about 350 m depending on the height above ground of the Helipod. The footprint is shifted to the north-east due to north-easterly wind. Since the main surface element's (forest, farmland, lake) length scales (between 13.99 - 14.12°longitude) are between 2-4 km, hence the footprint still covers the same surface type. In addition the orientation of the surface patches is more aligned in north-south direction. A displacement in that orientation is thus not crucial when flying perpendicular to that main orientation as done for the HET flights, as the fetch remains similar.

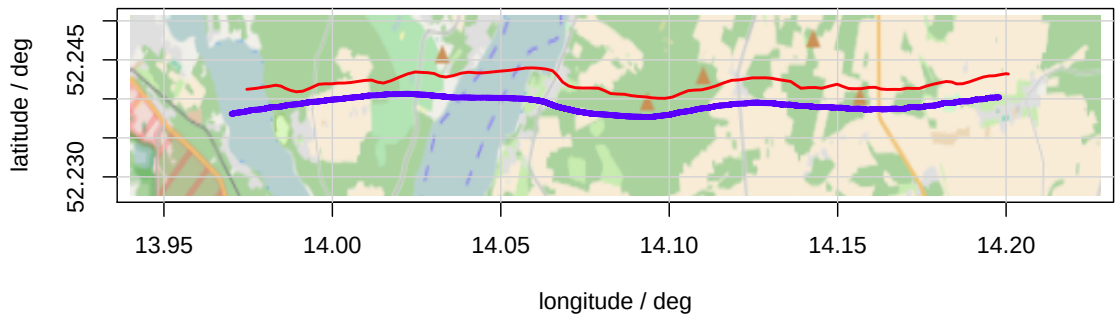

Fig. 3 Footprint (red) calculated by the footprint model from Kljun et al (2015) where the maximum source is located for the flight measurement path (blue) for the flight HET0528 with mean wind speed of 6.2 m s^{-1} and wind direction of 52 °. For reference, the distance between to longitudinal line (e.g 14.00 to 14.10) is 3.4 km.

3.5 Internal Boundary Layer

Beyrich et al (2006) noted that surface flux measurements at that lake were heavily distorted and non-representative due to the close vicinity of the shore and of high trees forming the shoreline. That fact must be considered in the evaluation. Flows over surface discontinuities can develop local internal boundary layers (IBL) down-

stream, when the change of surface properties are sharp enough or the size of the surface heterogeneity patch is large. A simple theoretical method shows that indeed the measurements over the lake could be influenced at 80 m by an IBL. Mahrt et al (1996) estimates the depth of an IBL z_{IBL} as

$$z_{\mathrm{IBL}} = C_{\mathrm{IBL}} \frac{\sigma_w}{\overline{u}} L_{\mathrm{het}} \tag{8}$$

where C_{IBL} was found to be 0.15 (Mahrt, 2000). For the most of HOM flights we found that $\sigma_w \approx 1.5$ m s^{-1} and $\overline{u} \approx 4$ m s^{-1}. L_{het} is the length scale of the new surface type (here it is the lake). The estimation of L_{het} for the lake is not straightforward, and may vary with the direction of the mean flow (Platis et al, 2016). The Lagrangian time of an advected column over the lake surface is less for longitudinally flow than latitudinally flow, because the lake in the east-west direction is five times smaller than in the north-south axis. Hence, the horizontal length scale probably ranges between 2 and 10 km. However, for the dataset of HOM flights, L_{het} is even smaller, because the legs were close to the shore line. For the HOM flights over the lake, the distance between the upstream shore line of the lake and the footprint area (that is actual the distance an air column is advected over the lake before being measured) is only about 1 km. The complete width of the lake does not matter. Therefore we assume L_{het} to be about 1 km. Then, the downwind growth of z_{IBL} is approximately 50 m. That means that the lake flights are probably above the IBL. Hence, we cannot exclude an influence from the surrounding farmland and forest, in particular for HOM flights over the lake. We have to assume that the values of the flights close to the shore line are not representative. A better strategy is to fly perpendicular to the shore line, as done for the HET flights, where L_{het} by the lake is at least 2 km resulting in $z_{\mathrm{IBL}} \geq 112$ m. This implies that measurements at 80 m are influenced by the lake and should be analysed. Likewise this accounts also for all the other surface patches with a dimension at least greater than 2 km.

4 Results

4.1 C_T^2 from Airborne Measurements

The previous analysis from van den Kroonenberg et al (2012) will be extended with the current airborne dataset. In the first part we present results from C_T^2 of the HOM flights and then compare these to the HET flights. Afterwards results of $\overline{C_Q^2}$, and $\overline{C_{QT}}$ are added. In Tab. 2, $\overline{C_T^2}$ of all HOM flights are presented, however there are no data available on 29.05.2003, due to a malfunction of the temperature sensor. Each value represents the measured $\overline{C_T^2}$ over the whole flight leg for one single surface type.

The average over all days of $\overline{C_T^2}$ (the physical unit $10^{-3}\mathrm{K}^2\mathrm{m}^{-2/3}$ is omitted hereafter) over farmland is 3.6 ($\sigma = 1.2$) with minimum and maximum values between $2.6 - 6.2$. The average over forest is 10.4 ($\sigma = 3.6$) with minimum and maximum values between $6.9 - 18.8$. The average over lake is 0.6 ($\sigma = 0.4$). Despite a high variation of $\overline{C_T^2}$, a classification based on different surface types is possible. In general, $\overline{C_T^2}$ over forest is 2-3 times higher than over farmland here. Although the HOM

Table 2 Mean $\overline{C_T^2}$, $\overline{C_Q^2}$, and $\overline{C_{QT}}$ of all analysed legs of the HOM flight pattern. Agriculture and AgricultureR are over farmland and Forest and ForestR are over forest. The R implies this is a reversed leg. That means the same flight track but flown in the opposite direction. Measurements during HET0529_1 and HET0529_2 of $\overline{C_T^2}$ and $\overline{C_{QT}}$ are not available, due to a malfunction of the temperature sensor.

Leg / Name: HOM...	0529_1	0529_2	0530_1	0530_2	0602	0613	0614
$\overline{C_T^2}$ $(10^{-3}\mathrm{K^2 m^{-2/3}})$							
Lake	NA	NA	0.42	0.70	0.53	1.42	0.21
LakeR	NA	NA	0.45	0.40	0.72	1.28	0.20
Agriculture	NA	NA	3.24	3.85	6.22	4.26	2.18
AgricultureR	NA	NA	2.67	4.30	4.28	2.61	2.68
Forest	NA	NA	8.98	18.83	10.65	10.86	6.85
ForestR	NA	NA	7.00	13.68	10.06	9.44	8.15
$\overline{C_Q^2}$ $(10^{-3}\mathrm{g^2 kg^{-2} m^{-2/3}})$							
Lake	0.27	0.48	0.52	2.21	4.05	2.09	0.50
LakeR	0.46	0.84	0.79	0.96	2.18	1.45	0.56
Agriculture	0.43	0.46	0.55	0.66	3.51	1.37	0.50
AgricultureR	0.28	0.54	0.63	0.63	1.58	1.04	0.45
Forest	0.10	0.11	0.66	0.23	2.48	0.87	0.36
ForestR	0.15	0.11	0.43	0.14	1.48	0.61	0.39
$\overline{C_{QT}}$ $(10^{-3}\mathrm{K\ g\ kg^{-1} m^{-2/3}})$							
Lake	NA	NA	0.05	-0.26	-0.23	0.64	0.09
LakeR	NA	NA	0.08	-0.49	-0.29	0.78	0.26
Agriculture	NA	NA	0.83	0.92	2.39	1.745	0.825
AgricultureR	NA	NA	0.94	0.73	0.86	1.35	0.88
Forest	NA	NA	1.01	1.10	1.46	2.57	1.39
ForestR	NA	NA	0.69	0.53	0.42	2.01	1.34

Table 3 Surface sensible heat flux and surface latent heat flux measured during the Helipod HOM flights campaign over agricultural land, lake and forest).

Leg / Name: HOM...	0529_1	0529_2	0530_1	0530_2	0602	0613	0614
Sensible turbulent heat flux in W $\mathrm{m^{-2}}$							
Lake	10.5	-0.8	0.9	-4.0	-3.5	20.4	18.0
Agriculture	150.0	190.9	108.6	175.2	165.2	160.9	107.0
Forest	235.4	362.6	229.7	350.9	388.4	319.8	235.7
Latent turbulent heat flux in $\mathrm{m^{-2}}$							
Lake	126.7	118.0	111.5	90.3	102.7	218.9	117.2
Agriculture	103.3	121.8	112.7	132.73	125.3	239.6	148.4
Forest	72.4	57.4	59.8	79.3	141.9	251.7	134.0

flight data may not be reliable over the lake (Sect. 3.4) due to blending effects from the surrounding forest and farmland these data show significant low values over the lake; $\overline{C_T^2}$ is about 20 times lower than over forest. Separation of the data into surface type classifications of $\overline{C_T^2}$ is valid for each single day, despite the fact that environmental conditions such as cloud cover changed almost every day. The high variation in $\overline{C_T^2}$ is explained by the strong surface fluxes variability caused by the different type of surface vegetation (Tab. 3). The table shows surfaces fluxes measured during the HOM flights over the three surface types. The sensible heat flux over forest is up to 3

times higher than over farmland and up to 2 orders higher than over the lake. Beyrich et al (2006) observed up to four times higher surface sensible heat flux over the forest than over farmland during the LITFASS2003 campaign. Over the water the sensible heat flux is close to zero or negative during the day. The stable stratification over the cold water during the day is suppressing turbulence. The measurement period of LITFASS2003 was in late spring, when the surface temperature of the lake still shows a minimum compared to the surrounding land (see Fig. 4). Similar to our results, Beyrich et al (2012) observed during the LITFASS-2009 campaign, that near-surface measured C_T^2 differs by an order of magnitude between the different types of farmland due to a different surface fluxes, caused by different status of the vegetation. In a subsequent study the direct relation between the airborne structure parameter and surface flux measurements should be analysed in more detail.

The observation of $\overline{C_T^2}$ indicates that local effects of surface heterogeneity remain preserved at the observation heights, which was also shown by Maronga et al (2014) in LES studies. Our in-situ observation agrees with the LES assumptions from Maronga et al (2014) and Maronga (2014), that C_T^2 is highly correlated with the sensible surface flux. For the airborne observations it seems that blending effects reach higher than the Helipod observation height of about 80 m above the ground for the large surface patches with length scales up to 20 km.

Observations also show that solar radiation has a direct influence on C_T^2. For example, we considered the morning flight and noon flight on 30 May, 2003 (HET0530_1 and HET0530_2) on this cloudless day, with low winds of 3 m/s from south-east. The first flight was performed between 1007 and 1219 local time (LOC). The second at 1230 - 1430 LOC. Direct solar irradiance has its maximum during the time period of the second flight. $\overline{C_T^2}$ over forest are about 100%, over farmland 40% higher than measured during morning. This effect is created by stronger solar radiation during noon time that generates strong convective turbulence over forest and farmland, accompanied by a maximum sensible surface flux (Tab 3) at noon during the diurnal cycle, hence the daily variation in the structure parameter is coupled here as well with the surface heat flux. Temperature variance increases with strengthening of convective turbulence, hence also the structure parameter intensifies. These observations confirm the findings of a diurnal cycle by van den Kroonenberg et al (2012). However, measurements above the lake do not show this behaviour because the lake warms more slowly than the ground.

The spatial series of C_T^2 are along the HET flights crossed the whole LITFASS area from west to east, covering mixed heterogeneous surface with individual surface patches not greater than 2-4 km. In Fig. 4 the spatial series of C_T^2 for one single flight (HET0528) was calculated with different window sizes. The same variability in C_T^2 is seen for each window size, but with stronger amplitude for the smallest (330 m) window. Since the surface length scales (which we want to investigate) are of the size of a couple of kilometres (e.g L_{lake}= 2 km), the 600 m window seems to be an adequate compromise between surface length scale and error margin (as shown in Sect. 5) for the study. Likewise as for the HOM flights, low values of C_T^2 are found over the lake and large values over forest and farmland, but a difference between

forest and farmland is not obvious for HET0528. Moreover a drop in C_T^2 is also seen over the forest-farmland area between 14.10 - 14.12 °longitude. For this single flight leg, hence it is not clear if certain structure in the spatial C_T^2 can be related to surface types. As already noted by Beyrich et al (2012) and Braam et al (2014) a separation of the effects of the statistical nature of turbulence like up- and downdrafts from those of the heterogeneity of the surface is necessary by averaging of several flights at the same level and track.

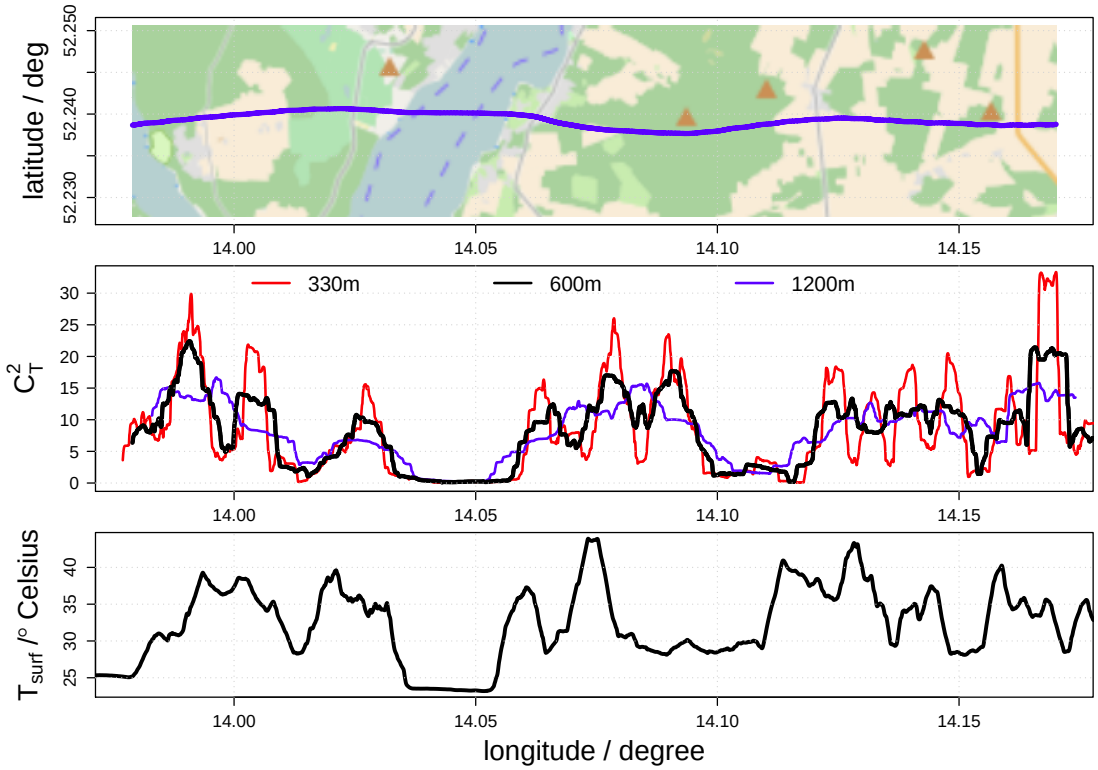

Fig. 4 Flight HET0528 track (upper panel) with mean wind speed of 6.2 m s^{-1} and wind direction of 52 °. Spatial series of C_T^2 of flight HET0528 calculated with three different window sizes (330, 600, 1200 m). Surface temperature measured by Helipod (lower panel). For reference, the distance between to longitudinal line (e.g 14.00 to 14.10) is 3.4 km.

For that, the normalized spatial series of the structure parameter averaged over the 8 flights (A_T), as explained in Sect. 3.3, was calculated according to the methodology of the previous works from van den Kroonenberg et al (2012). It should be noted that the spatial average was calculated from 8 flights and each flight occurred under different environmental conditions. In general, for all 8 flights the weather was a very warm summer-day convective boundary layer with temperatures approximately 30°C at the ground and wind speeds always below 6 ms^{-1}. However, cloud cover, soil moisture, wind magnitude and direction varied each day. A consideration of these forcing was made in by the normalization of the spatial series, but a different propagations of the flow due to changing wind conditions remains. The results are shown in Fig. 5, representing the averaged spatial series of the temperature structure parameter A_T with a black line. The grey area represents the standard deviation of A_T for each data point i, in order to demonstrate the variability over all flights.

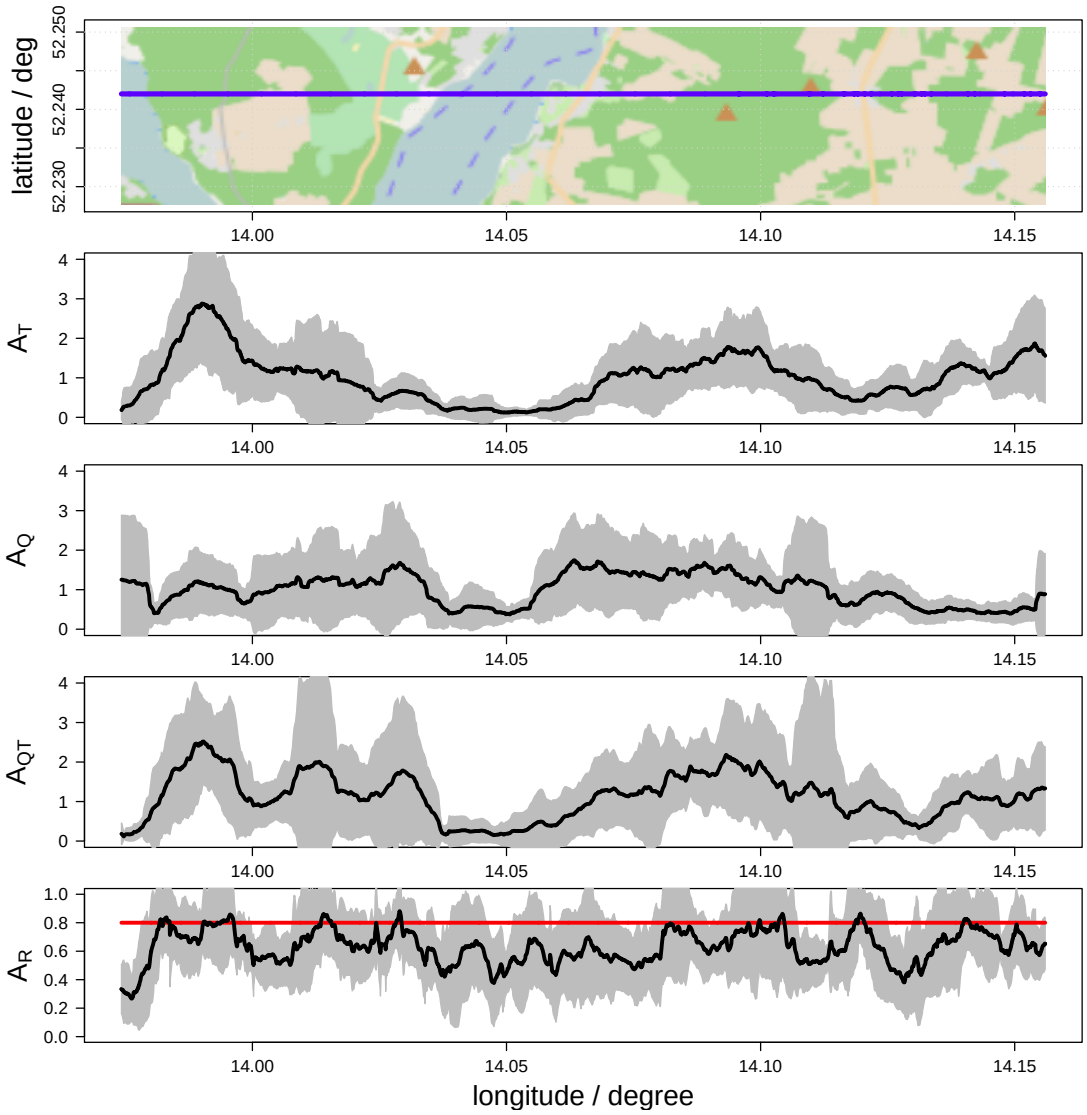

Fig. 5 Spatial Series averaged over 8 flights for leg WE08. At the top the map is plotted with the flight track (blue line) for one of the 8 flights. The coordinates of all other flight tracks differ only marginal. Below is the averaged normalized spatial series A_T , A_Q, A_{QT}, of the structure parameters and A_R. The grey area represents the standard deviation of the averaged normalized structure parameter for each data point i (see Eq. 7). The red line in plot for A_R shows the value 0.8 for R_{QT} proposed by Fairall et al (1980b). For reference, the distance between to longitudinal line (e.g 14.00 to 14.10) is 3.4 km.

A_T demonstrates variability that is readily linked to surface changes. There are consistently higher values over the forest than the farmland, and low values over the lake. The spatial averaged series A_T of 8 legs shows a clear signature of the temperature structure parameter variability along the flight path and is in agreement with the results from HOM flights. It was observed that maxima of A_T occurred at the same position along a flight path during different flights, although still a lot of variability is apparent due to random up- and downdrafts and horizontal displacement caused by wind advection. For example, even if we subtract the maximum standard deviation, about 40% (grey area at 13.98°in Fig. 5), from the averaged $A_T \approx 3$ over forest, the averaged structure parameter over farmland between 14.12 - 14.13 (≈ 0.9) is still lower. Although a single flight is not able to separate random turbulence from

surface heterogeneity, an average of several flights shows promising results that C_T^2 can be linked to different surface fluxes as long as the surface flux variation is large enough (e.g. forest and lake). Nevertheless a determination of exact quantitative C_T^2 values according to a surface type is not possible. Furthermore, it is hard to tell for the HET flights if the underlying surface is farmland or forest, if surface length scales are below 2 km as for the areas between 14.00 - 14.02 and 14.13-14.15°. The strongest variation in C_T^2 is caused by the lake. Since the lake has a low surface temperature ($T_{\mathrm{surf}} < 25°$ Celsius), a correlation between low C_T^2 and low T_{surf} should exist. In Fig. 4 this correlation is verifiable.

To conclude the results from HOM and HET flights, there is a strong indication that C_T^2 measured at about 80 m above ground is influenced by surface heterogeneity even for smaller surface length scales around 2 km, although a clear distinction between the variation of the structure parameter due to variations in the characteristics of the underlying surface amidst the noise due to turbulent variations is not possible. Nevertheless we could classify C_T^2 according to each surface type by using the average over 8 flights combined with the observations of HOM flights. To obtain even more meaningful results by means of an ensemble of aircraft flights, more flights are needed as already proposed by Maronga et al (2014). In contrast to van den Kroonenberg et al (2012) and Beyrich et al (2012) we are able to relate C_T^2 to distinct surface types with low values over the lake, moderate over farmland and high over forest.

4.2 C_Q^2

Table 2 shows the calculated value of $\overline{C_Q^2}$ from HOM flights for each surface type. For clarity, the physical unit $10^{-3}\mathrm{g}^2\mathrm{kg}^{-2}\mathrm{m}^{-2/3}$ of $\overline{C_Q^2}$ will be skipped. The average of $\overline{C_Q^2}$ of all days for farmland is 0.9 with a standard deviation calculated over all legs with σ =0.8 and minimum and maximum values between $0.3-3.5$. The average of forest is 0.6 ($\sigma = 0.6$) with minimum and maximum values between $0.1-2.5$ and lake 1.2 with σ =1.0. We notice that for all flights forest has slightly lower values than farmland, but in general the analysis shows high fluctuations of the humidity structure parameter. A coupling between the underlying surface and $\overline{C_Q^2}$ is vague for the HOM flights. A direct relations to the latent and sensible surface heat flux is not obvious (Tab.3). Similar to $\overline{C_Q^2}$ the latent surface heat fluxes do not show a high variability. The values of $\overline{C_Q^2}$ on the 02.06 (flight HOM0602) are remarkably high. Especially values over forest are ut one order heigher than the days before. An explanation could be increased soil moisture, due to rainfall on the 31 May and 01 June. In addition, on that day the surface sensible heat flux is similar to the other days, but the latent surface heat flux over forest is about two times higher than on the days before. A larger latent high flux will increase the vertical gradient of the water vapour mixing ratio $\frac{dQ}{dz}$ and therefore also fluctuations of Q. It seems that latent heat flux is able to increase the humidity structure parameter for this day.

We extend the analysis of C_Q^2 with the HET flights. A_Q is typically between 0.3-3 and shows less variability than C_T^2 (see Fig 5). The standard deviation σ_Q is large (grey area). This standard deviation is the time variation at a single spatial point,

over all 8 flights, which supports the observations of the HOM flights indicating high fluctuation of C_Q^2. Since each flight shows different values of the local C_Q^2 at each point (due to e.g. different entrainment effects, soil moisture, latent heat flux on each day) along the flight leg, a large scatter causing a large standard deviation σ_Q is the consequence. Hence, the spatial series cannot be related to surface properties.

One exception and contradiction to HOM flights is the sudden drop and broad minimum of A_Q over the lake Scharmützelsee. Although similar low values of A_Q are as well located over farmland in the eastern part of the flight leg, the drop over the lake could be seen in each single HET Flight (not shown). In order to check if C_Q^2 over lake and land are significantly different from each other, a most common statistical two-sample location test (Welch's t-test, Brown and Forsythe (1974)) was used. Two samples were created, one with C_Q^2 of the spatial series of each HET flight over the lake (14.04 - 14.06°longitude) and the second one over land. Applying the test on the two populations, a significant difference between lake and land C_Q^2 is calculated by a 99% significance level, despite the high fluctuation in C_Q^2. A 50% lower mean C_Q^2 is observed over the lake.

To explain the disparity between HOM and HET flights in C_Q^2, we take a closer look to the footprint (-model) of the HOM flights and the ABL dynamics. Apparently, C_Q^2 is not low over the lake for HOM flights. As already suggested in Sect. 3.4 the flight track of HOM flights and its modelled footprint is very close to the shoreline of the lake. C_Q^2 might be distorted and be non-representative here. However, results of C_T^2 show a clear influence by the lake for the same flight track. As supported by many other studies (e.g. Roth and Oke, 1995; Sempreviva and Hjstrup, 1998; Albertson and Parlange, 1999) there is a different behaviour of the passive scalar (water vapour) compared to the active scalar (temperature). Over heterogeneous landscape, water vapour flux and sensible heat flux have different source regions (Kustas and Albertson, 2003). Albertson and Parlange (1999) showed by means of LES that water vapour appeared to be carried more horizontally than sensible heat which was immediately carried upward by plumes under convective conditions. Therefore Kaharabata et al (1999) claimed different footprint estimations for vapour (fluxes) and temperature (fluxes). The footprint model needs to predict differently the source area between the active and passive scalar. As far as to the authors' knowledge, no existing analytic footprint model (also one of the latest and most advanced by Kljun et al (2015) which is used in our study) is able to perform that. Bertoldi et al (2013) could show by LES and aircraft observation that the footprint of water vapour has a larger distance from the flight track than sensible heat. Bertoldi et al (2013) concludes that sensible heat at aircraft altitude appears to be in phase with the surface, whereas latent heat presents a more complicated connection to the surface. This could be an explanation accounting for the difference between C_Q^2 and C_T^2 in our observations, explaining for the discrepancy between our HOM and HET flights. The source area of the HOM flights for water vapour is not over the lake, but over the surrounding farmland and forest. However, one should keep in mind that the land surface coupling is very hard to understand and explain, specially for moisture. Entrainment and soil properties play a crucial role there as well, for example the amount of water in the soil also alters the moisture turbulent flux.

LES results by Maronga et al (2014) and Cheinet and Cumin (2011) suggest that C_Q^2 is decoupled from the surface flux even at low levels which is ascribed to the entrainment of dry air at the top of the boundary layer and is not following MOST. Our airborne observations of C_Q^2 confirm these findings. A proper coupling to surface features as done for C_T^2 is not possible, except for the lake. Maronga et al (2014) did not apply their LES to a sharp land-water discontinuity. Possible this sharp change in surface sensible heat fluxes from positive to negative values over the lake (Beyrich et al, 2006) and the sufficient extent of the lake Scharmützelsee might have caused the reduced values of C_Q^2 at around 80 m height during convective conditions, despite the strong and dominant effect by entrainment. To better distinguish the superimposition of different effects on C_Q^2, we tried to correlate C_Q^2 with the vertical wind speed. Maronga et al (2014) perceived high values of C_T^2 inside updraft plumes ($w \geq 0.3$ m s^{-1}) and low C_T^2 outside. Braam et al (2014) found larger structure parameter values in upward motion and smaller in downward motion. We checked that as well for C_Q^2 and C_T^2 (not shown). For C_Q^2 a weak tendency for updrafts with a larger vertical velocity w is existing, though higher C_T^2 values appear to have a better and stronger correlation to higher positive and negative vertical speed.

In nature, many effects superimpose each other. A distinction of these effects, such as the decoupling from surface and entrainment effects, has to be the challenge in up-following campaigns and studies. In general, we observed no correlation for C_Q^2 to a surface type, independent on the surface length scale, except for the sharp water-land discontinuity. Asignificant C_Q^2 drop is observed there at 80 m observation height. Simultaneous flights at different levels under similar atmospheric conditions and LES are indispensable. A following study will investigate the lake-land discontinuity on active and passive scalars in more detail as well.

4.3 C_{QT} and R_{QT} over heterogeneous surface

The combined structure parameter can be positive or negative. Comparing the mean values of HOM flights $\overline{C_{QT}}$ (Tab. 2), a surface coupling for forest and farmland seems not to be possible, but for the lake. Values are always lower over water than over land. The pattern of $\overline{C_{QT}}$ correlates more with $\overline{C_T^2}$ than with $\overline{C_Q^2}$. The dominating contribution for $\overline{C_{QT}}$ is done by the temperature signal, since $\overline{C_Q^2}$ varies little relative to the noise level. Since the lowest values of $\overline{C_{QT}}$ (HOM flights, see Tab. 2) are reached over the lake, the footprint is located over the water for the HOM flights. The results of A_{QT} (HET flights) of the averaged spatial series of HET flights, see Fig. 5, matches the results of the HOM flights. A significant drop is observable along the flight track (Fig. 5), which corresponds to the lake Scharmützelsee. It was measured for all flights, which is also expressed by its low standard deviation. Two flights (HOM0530_2 and HOM0602) show even negative C_{QT} over the lake, which reassure the lake footprint for C_{QT}. On these two particular days the highest boundary-layer tops during the whole campaign were measured around 2000 m and above. Since the wind speeds were very low, the footprint of the lake was observed clearly even at 80 m. These observations of negative C_{QT} over the lake match to the results from Li

et al (2012). They demonstrated by field experiments, that for negative sensible surface flux forcing C_{QT} is as well negative. This behaviour corresponds to the known characteristics of the turbulent surface fluxes which normally show a downward sensible heat flux over water at day while specific humidity is transported upward in many cases (Beyrich et al, 2006) due to the stable stratification over the cold water as mentioned previously and is seen in Tab. 3 as well. Over land, typically, C_{QT} has a characteristic diurnal cycle: the correlation between humidity and temperature fluctuations is high and positive during day time, and negative during night time (Lüdi et al, 2005).

According to the method of Li et al (2012), we can calculate from Eq. 2 the value of R_{QT} by using the airborne measurements of C_{QT},C_Q^2 and C_T^2 . HOM flights (calculated by the values of Tab. 2) show similar $\overline{R_{QT}}$ over farmland and forest. $\overline{R_{QT}}$ is approximately 0.7 over forest and farmland with a standard deviation of $\sigma_{R_{QT}} = 0.1$. All three measured structure parameters are positive, thus $\overline{R_{QT}}$ is positive. Over lake $\overline{R_{QT}}$ is positive for all used data except for the flights with negative $\overline{C_{QT}}$ as mentioned above. For all positive correlations $\overline{R_{QT}} \approx 0.4$ with $\sigma_{R_{QT}} = 0.2$. The negative correlated flights show the similar absolute value of $|\overline{R_{QT}}| = 0.4$ over the lake.

In Fig. 5, the averaged spatial series of R_{QT} over eight flights is plotted along the corresponding flight legs (black line). It is derived from 2 and defined similar to the average spatial series of the structure parameter at data point i :

$$A_{R_i} = \left| \left\langle \frac{C_{QT\,i}}{\sqrt{C_{T\,i}^2 C_{Q_i}^2}} \right\rangle \right| \tag{9}$$

The brackets $\langle\rangle$ represent the average over the 8 flight legs. Note that the magnitude of the right hand side term is given here, since R_{QT} is negative over lake for 3 flights.

A_{R_i} is in the range of 0.6, hence below the red line (with the common literature value of 0.8 (Fairall et al, 1980b; Beyrich et al, 2005; Meijninger et al, 2006)) for many of the data points. The standard deviation of A_{R_i} (grey area) is around 0.2 throughout most of the flight leg. Strikingly, the maximum value of A_{R_i} is only 0.9 and always less than unity. Over the lake A_{R_i} shows lower values between 0.4 and 0.6 than over land surface. In general, combining results from HOM and HET flights, R_{QT} is in the range between 0.4 and 1.0 along the flight track but it was not possible to assign the variability to surface types, although there is weak indication that values with the underlying lake are lower.

The analysis reveals that R_{QT} is smaller than unity for most of the data, in contrast to the assumptions in Monin-Obukhov similarity theory. Other field experiments confirm our airborne observations results. Fairall et al (1980b) observed a value of $R_{QT} = 0.8$. Beyrich et al (2005); Meijninger et al (2006) found typical values between 0.7 and 0.9 in a convective boundary layer. Li et al (2012) observed in their experimental study a large scatter of R_{QT} and values less than unity. However, violation of MOST is small as long as $|R_{QT}| > 0.7$ (Meijninger et al, 2006). If $|R_{QT}| < 1$, there is a discrepancy between the two similarity functions of C_Q^2 and C_T^2 (Li et al, 2012; Maronga, 2014). Maronga (2014) observed if entrainment is significant, there is a dissimilarity between the transport of heat and moisture, because C_Q^2 does not

follow any more MOST (as already discussed in Sect. 4.2) resulting in R_{QT} lower than unity.

Especially under weakly convective conditions, which is valid over the lake (Beyrich et al, 2005), a reduced surface heat flux narrows the importance of surface forcing/parameters. Our measurements were performed at around 80 m above ground at a height where larger eddies exist than close to the surface. Since the sources of heat and moisture fluxes into the atmosphere at the surface are not identical, these larger eddies may have a different structure for temperature and humidity thus decreasing the correlation between their fluctuations. That allows large-scale processes from an outer layer that produces entrainment and non-local effects like non-stationarity or advection to become more important (Li et al, 2012). Further Moene and Schüttemeyer (2008) expect the strongest decorrelation of temperature and humidity at the transitions between two surface types (where the contrast between the patches increases, e.g. land and lake).

The consequence is an increase in the footprint by the outer layer causing then a decorrelation between temperature and humidity especially for the lake (Li et al, 2012). These findings are consistent and support our airborne observations of disparity in the footprint signals at the lake site between C_Q^2 and C_T^2 as discussed in Sect. 4.2. Further, the results of low R_{QT} over the lake indicate that a violation of MOST is possible.

5 Conclusions

The turbulent structure parameters for temperature C_T^2 and humidity C_Q^2 and their cross-structure parameter C_{QT} were investigated by using Helipod flight data collected in the CBL. The Helipod measured these parameters on flights of up to 20 km length over heterogeneous terrain and close to the ground. This is normally not feasible with a common manned aircraft or unmanned air vehicles due to restrictions on legal permissions. The close-to-ground flights measured data in CBL surface layer over heterogeneous surfaces of different types including forest, lakes and farmland. We showed that the Helipod was able to measure C_Q^2 and C_{QT} in a daytime convective boundary layer, extending measurements of C_T^2, as already done in a previous study by van den Kroonenberg et al (2012). Two types of flight pattern were used to observe the behaviour of the structure parameter over heterogeneous surface.

The homogeneous flights (HOM) were used to calculate the structure parameter over the entire flight leg, in order to derive a structure parameter characterizing one surface type. This method allows a classification of all three structure parameters for each surface type. In order to compute spatially resolved series of the structure parameter, heterogeneous (HET) flights were analysed with a track over a mixed surface and including different surface types.

Variability of C_T^2 was explained by the strong surface fluxes variability caused by the different type of surface vegetation. There is a strong indication that C_T^2 measured at about 80 m above ground is influenced by surface heterogeneity even for smaller surface length scales such as the 2 km wide lake, although C_T^2 variability is as well attributed to random turbulence. A clear distinction between the variation of the

structure parameter due to variations in the characteristics of the underlying surface amidst the noise due to turbulent variations is not possible. Nevertheless we could classify C_T^2 according to each surface type. The highest values of C_T^2 were found over forest patches. Lower values were found over lake and moderate values over farmland. Hence, C_T^2 measured at about 80 m above ground is associated with surface heterogeneity and confirms finding from van den Kroonenberg et al (2012) and LES studies by Li et al (2012); Maronga et al (2014). In general, values over forest were one order larger than over farmland and two orders larger than over lake.

To our knowledge this is the first study investigating a variability of C_{QT} and C_Q^2 over heterogeneous terrain experimentally. The C_Q^2 and C_{QT} behave very similar but behave more complex compared to C_T^2. Our data suggest that C_Q^2 is decoupled from the surface flux even at low levels which is ascribed to the entrainment of dry air at the top of the boundary. A direct relation to latent surface heat fluxes is not possible. These in-situ observation support as well findings from LES studies by Li et al (2012); Maronga et al (2014); Maronga (2014). An exception is the sharp water-land discontinuity. A significant difference between C_Q^2 over lake and land is calculated by the Welch's Test with a 99% significance level, despite the high fluctuation in C_Q^2. A 50% lower mean C_Q^2 is observed over the lake. Possible this sharp change in surface sensible heat fluxes from positive to negative values over the lake might have caused the reduced values of C_Q^2 at around 80 m height during convective conditions In order to investigate a more direct relationship between airborne structure parameter and surface fluxes, the structure parameters should be for example deduced from surface flux measurements for all these surfaces and tried to be up-scaled to flight altitude in a follow-up study.

A disparity is observed between HOM and HET flights for C_Q^2. HOM and HET flights show a clear footprint of the lake in C_T^2, but only HET flights show the lake footprint in C_Q^2. The footprint of water vapour covers a larger distance from the flight track than sensible heat. Hence, C_T^2 at aircraft altitude appears to be in phase with the surface, whereas the footprint of C_Q^2 at the observation height is not any more over the lake but over the surrounding land.

Since the Helipod proved the reliability to measure C_T^2, C_{QT} and C_Q^2, we were able to calculate temperature-humidity correlation coefficient R_{QT}. R_{QT} was in the range between 0.4 and 1.0 along the flight track over heterogeneous terrain similar to findings from Beyrich et al (2005); Fairall et al (1980b). Combining all flights, R_{QT} was on average approximately 0.7. Assigning the R_{QT} variability to underlying surface types was not possible, however there was indication that values with the underlying lake were lower. The results show R_{QT} is much less than unity for most of our measurements, in contrast to the assumption of unity in Monin-Obukhov similarity theory, but violation of MOST is small as long as $R_{QT} > 0.7$ (Meijninger et al, 2006). These observations agree well with LES studies from Li et al (2012); Maronga (2014). A dissimilarity between the transport of heat and moisture ($|R_{QT}| < 1$) might be caused by significant entrainment as reported by Maronga (2014). A new flight strategy with many flight legs over the same track on one day would achieve more statistically significant results.

Acknowledgements The measurements were performed during the LITFASS-2003 experiment, a field experiment within the frame of the EVA_GRIPS project (Evaporation at grid / pixel scale). EVA_GRIPS was funded by the German Federal Ministry of Education and Research (BMBF) as a part of the German climate research program (DEKLIM) under the contract no. 01LD0103.

References

Albertson JD, Parlange MB (1999) Natural integration of scalar fluxes from complex terrain. Advances in Water Resources 23(3):239–252

Andreas E (1987) Spectral measurements in a disturbed boundary layer over snow. J Atmos Sci 44:1912–1939

Andreas EL (1989) Two-wavelength method of measuring path-averaged turbulent surface heat fluxes. Journal of Atmospheric and Oceanic Technology 6(2):280–292

Andreas EL, Hill RJ, Gosz JR, Moore DI, Otto WD, Sarma AD (1998) Statistics of surface-layer turbulence over terrain with metre-scale heterogeneity. Boundary-Layer Meteorology 86(3):379–408

Assouline S, Tyler S, Tanny J, Cohen S, Bou-Zeid E, Parlange M, Katul G (2008) Evaporation from three water bodies of different sizes and climates: measurements and scaling analysis. Advances in Water Resources 31(1):160–172

Bange J, Roth R (1999) Helicopter-borne flux measurements in the nocturnal boundary layer over land - a case study. Boundary-Layer Meteorol 92:295–325

Bange J, Beyrich F, Engelbart DAM (2002) Airborne measurements of turbulent fluxes during LITFASS-98: A case study about method and significance. Theor Appl Climatol 73:35–51

Bange J, Spieß T, Vörsmann P, Nagel D, Maixner U (2005) Helipod measurements of turbulent energy and aerosol transport in the lower atmosphere - benefits for the wind energy use in wind parks. DEWI Magazin 26:26–31

Bange J, Spieß T, Herold M, Beyrich F, Hennemuth B (2006) Turbulent fluxes from helipod flights above quasi-homogeneous patches within the LITFASS area. Bound-Layer Meteor

Bertoldi G, Kustas WP, Albertson JD (2013) Evaluating source area contributions from aircraft flux measurements over heterogeneous land using large-eddy simulation. Boundary-layer meteorology 147(2):261–279

Beyrich F, Mengelkamp HT (2006) Evaporation over a heterogeneous land surface: EVA_GRIPS and the LITFASS-2003 experiment - an overview. Bound-Layer Meteor 121:1–28

Beyrich F, de Bruin HAR, Meijninger WML, Schipper JW, Lohse H (2002) Results from one-year continuous operation of a large aperture scintillometer over a heterogeneous land surface. Bound-Layer Meteor 105:85–97

Beyrich F, Kouznetsov RD, Leps JP, Lüdi A, Meijninger WM, Weisensee U (2005) Structure parameters for temperature and humidity from simultaneous eddy-covariance and scintillometer measurements. Meteorologische Zeitschrift 14(5):641–649

Beyrich F, Leps JP, Mauder M, Bange J, Foken T, Huneke S, Lohse H, Lüdi A, Meijninger WM, Mironov D, et al (2006) Area-averaged surface fluxes over the lit-

fass region based on eddy-covariance measurements. Boundary-layer meteorology 121(1):33–65

Beyrich F, Bange J, Hartogensis OK, Raasch S, Braam M, van Dinther D, Gräf D, van Kesteren B, van den Kroonenberg AC, Maronga B, et al (2012) Towards a validation of scintillometer measurements: the litfass-2009 experiment. Boundary-layer meteorology 144(1):83–112

Braam M, Moene AF, Beyrich F (2014) Variability of the structure parameters of temperature and humidity observed in the atmospheric surface layer under unstable conditions. Boundary-layer meteorology 150(3):399–422

Braam M, Beyrich F, Bange J, Platis A, Martin S, Maronga B, Moene AF (2015) On the discrepancy in simultaneous observations of the structure parameter of temperature using scintillometers and unmanned aircraft. Boundary-Layer Meteorology pp 1–27

Brown MB, Forsythe AB (1974) The small sample behavior of some statistics which test the equality of several means. Technometrics 16(1):129–132

de Bruin HAR, Kohsiek W, van den Hurk BJJM (1993) A verification of some methods to determine the fluxes of momentum, sensible heat and water vapour using standard deviation and structure parameter of scalar meteorological quantities. Bound-Layer Meteor 63:231–257

Caughey S, Palmer S (1979) Some aspects of turbulence structure through the depth of the convective boundary layer. Quarterly Journal of the Royal Meteorological Society 105(446):811–827

Cheinet S, Cumin P (2011) Local structure parameters of temperature and humidity in the entrainment-drying convective boundary layer: a large-eddy simulation analysis. Journal of Applied Meteorology and Climatology 50(2):472–481

Cheinet S, Siebesma AP (2009) Variability of local structure parameters in the convective boundary layer. Journal of the Atmospheric Sciences 66(4):1002–1017

Coulman C (1973) Vertical profiles of small-scale temperature structure in the atmosphere. Boundary-Layer Meteorology 4(1-4):169–177

Cuijpers JWM, Kohsiek W (1989) Vertical profiles of the structure parameter of temperature in the stable, nocturnal boundary layer. Boundary-Layer Meteorol 47:111–129

De Bruin H, Van Den Hurk B, Kroon L (1999) On the temperature-humidity correlation and similarity. Boundary-Layer Meteorology 93(3):453–468

Fairall C, Markson R, Schacher G, Davidson K (1980a) An aircraft study of turbulence dissipation rate and temperature structure function in the unstable marine atmospheric boundary layer. Boundary-Layer Meteorology 19(4):453–469

Fairall C, Schacher G, Davidson K (1980b) Measurements of the humidity structure function parameters, c q 2and c tq, over the ocean. Boundary-Layer Meteorology 19(1):81–92

Hartogensis O, De Bruin H, Van de Wiel B (2002) Displaced-beam small aperture scintillometer test. part ii: Cases-99 stable boundary-layer experiment. Boundary-layer meteorology 105(1):149–176

Hill RJ (1989) Implications of monin-obukhov similarity theory for scalar quantities. Journal of the Atmospheric Sciences 46(14):2236–2244

876 Hill RJ (1997) Algorithms for obtaining atmospheric surface-layer fluxes from scin-
877 tillation measurements. J Atmos Oceanic Technol 14:456–467
878 Kaharabata S, Schuepp P, Fuentes J (1999) Source footprint considerations in the
879 determination of volatile organic compound fluxes from forest canopies. Journal
880 of Applied Meteorology 38(7):878–884
881 Kljun N, Rotach M, Schmid H (2002) A three-dimensional backward lagrangian foot-
882 print model for a wide range of boundary-layer stratifications. Boundary-Layer
883 Meteorology 103(2):205–226
884 Kljun N, Calanca P, Rotach M, Schmid H (2015) A simple two-dimensional param-
885 eterisation for flux footprint prediction (ffp). Geoscientific Model Development
886 8(11):3695–3713
887 Kohsiek W, Meijninger W, Moene A, Heusinkveld B, Hartogensis O, Hillen W,
888 De Bruin H (2002) An extra large aperture scintillometer for long range appli-
889 cations. Boundary-layer meteorology 105(1):119–127
890 Kolmogorov A (1941) Local structure of turbulence in an incompressible fluid for
891 very large Reynolds numbers. Dokl Akad Nauk SSSR 30:299–303
892 van den Kroonenberg A, Martin S, Beyrich F, Bange J (2012) Spatially-averaged
893 temperature structure parameter over a heterogeneous surface measured by an un-
894 manned aerial vehicle. Boundary-layer meteorology pp 1–23
895 Kustas WP, Albertson JD (2003) Effects of surface temperature contrast on land-
896 atmosphere exchange: A case study from monsoon 90. Water Resources Research
897 39(6)
898 Li D, Bou-Zeid E, De Bruin HA (2012) Monin–obukhov similarity functions for the
899 structure parameters of temperature and humidity. Boundary-layer meteorology
900 145(1):45–67
901 Lüdi A, Beyrich F, Mätzler C (2005) Determination of the turbulent temperature–
902 humidity correlation from scintillometric measurements. Boundary-layer meteo-
903 rology 117(3):525–550
904 Lumley L, Panofsky H (1964) The Structure of Atmospheric Turbulence. John Wiley
905 & Sons, 239 pp.
906 Mahrt L (2000) Surface heterogeneity and vertical structure of the boundary layer.
907 Boundary-Layer Meteorology 96(1-2):33–62
908 Mahrt L, Mahrt L, Mahrt L (1996) Observations of fluxes and inland breezes over
909 heterogeneous surfaces. J Atmos Sci 51:2484–2499
910 Maronga B (2014) Monin–obukhov similarity functions for the structure parame-
911 ters of temperature and humidity in the unstable surface layer: Results from high-
912 resolution large-eddy simulations. Journal of the Atmospheric Sciences 71(2):716–
913 733
914 Maronga B, Moene AF, van Dinther D, Raasch S, Bosveld FC, Gioli B (2013) Deriva-
915 tion of structure parameters of temperature and humidity in the convective bound-
916 ary layer from large-eddy simulations and implications for the interpretation of
917 scintillometer observations. Boundary-Layer Meteorology 148(1):1–30
918 Maronga B, Hartogensis OK, Raasch S, Beyrich F (2014) The effect of surface het-
919 erogeneity on the structure parameters of temperature and specific humidity: a
920 large-eddy simulation case study for the litfass-2003 experiment. Boundary-Layer
921 Meteorology 153(3):441–470

Martin S, Bange J (2014) The influence of aircraft speed variations on sensible heat-flux measurements by different airborne systems. Boundary-layer meteorology 150(1):153–166

Meijninger WML, Hartogensis OK, Kohsiek W, Hoedjes JCB, Zuurbier RM, de Bruin HAR (2002) Determination of area-averaged sensible heat fluxes with a large aperture scintillometer over a heterogeneous surface – Flevoland field experiment. Bound-Layer Meteor 105:37–62

Meijninger WML, Beyrich F, Lüdi A, Kohsiek W, de Bruin HAR (2006) Scintillometer-based turbulent fluxes of sensible and latent heat over a heterogeneous land surface – a contribution to LITFASS-2003. Bound-Layer Meteor 121:89–110

Moene AF, Schüttemeyer D (2008) The effect of surface heterogeneity on the temperature–humidity correlation and the relative transport efficiency. Boundary-layer meteorology 129(1):99–113

Petenko I, Shurygin E (1999) A two-regime model for the probability density function of the temperature structure parameter in the convective boundary layer. Boundary-Layer Meteorology 93(3):381–394

Platis A, Altstädter B, Wehner B, Wildmann N, Lampert A, Hermann M, Birmili W, Bange J (2015) An observational case study on the influence of atmospheric boundary-layer dynamics on new particle formation. Boundary-Layer Meteorology pp 1–26

Platis A, Martnez-Villagrasa D, Beyrich F, Bange J (2016) Analysis of the influence of a lake on the lower convective boundary layer from airborne observations. Meteorologische Zeitschrift

Raabe A, Arnold K, Ziemann A, Schröter M, Raasch S, Bange J, Zittel P, Spieß T, Foken T, Göckede M, Beyrich F, Leps JP (2004) STINHO - structure of turbulent transport under inhomogeneous surface conditions - a micro-α scale field experiment and les modelling. Met Zeitschr Submitted

Roth M, Oke TR (1995) Relative efficiencies of turbulent transfer of heat, mass, and momentum over a patchy urban surface. Journal of the Atmospheric Sciences 52(11):1863–1874

Sempreviva AM, Hjstrup J (1998) Transport of temperature and humidity variance and covariance in the marine surface layer. Boundary-Layer Meteorology 87(2):233–253

Tatarskii VI (1971) The effects of the turbulent atmosphere on wave propagation. Israel Program for Scientific Translations

Wyngaard J, LeMone M (1980) Behavior of the refractive index structure parameter in the entraining convective boundary layer. Journal of the Atmospheric Sciences 37(7):1573–1585

Wyngaard JC, Izumi Y, Collins SA (1971) Behavior of the refractive-index-structure parameter near the ground. J Opt Soc Am 61:1646–1650

Wyngaard JC, Pennell WT, Lenschow DH, LeMone MA (1978) The temperature-humidity covariance budget in the convectice boundary layer. J Atmos Sci 35:47–58

Appendix 1

5.1 Calculation of structure parameter

The method follows the 'direct' classical method (Tatarskii (1971); van den Kroonenberg et al (2012)) by using the structure function, with S as generic scalar, which can be replaced by the water vapour mixing ratio Q or temperature T:

$$C_S^2 = \langle D_S(r) r^{-2/3} \rangle_{r_{min}, r_{max}} \tag{10}$$

C_S^2 is a proportionality factor in the 2/3-law expression (Kolmogorov, 1941) for the structure function. Therefore, it is only valid within the inertial subrange of locally isotropic turbulence (Wyngaard et al, 1971). Since $D_S(r)$ can be interpreted as being proportional to the turbulent energy at scale r, the factor C_S^2 is a direct measure for the turbulence energy of the flow over all scales in the inertial subrange. Thus, the inertial subrange is displayed as a horizontal plateau in a plot of $D(S) \cdot r^{-2/3}$ versus r (van den Kroonenberg et al, 2012). The inertial subrange is defined between two boundaries $r_{\min}$ and $r_{\max}$, in between which the the structure function is averaged in order to obtain the structure parameter. The scale of the inertial subrange of quasi-isotropic turbulence is typically from a few millimetres to a few hundred metres (depending on height above the surface, boundary-layer depth etc.). The transition to the dissipation range is presented by the lower limit, below which turbulence is destroyed by dissipation and viscous forces become significant.

For the humidity the Helipod sensors had limited response and could not resolve the smallest scales. We set $r_{\min}$ based on the clear drop off observed in Fig. 6, at scales smaller than 4 m. The scales at which there is transition to the production range is represented by the the upper limit $r_{\max}$. It depends on thermal stratification, boundary-layer height, and on the distance to the ground or the nearest stably stratified layer (Lumley and Panofsky, 1964). However, the prediction of the precise value of the upper limit $r_{\max}$ in a power spectrum or structure function is difficult. We found for all flights, the section between $r_{\min}$ = 4 m and $r_{\max}$ = 30 m to be part of the inertial subrange. In Fig. 6 the limits $r_{\min} = 4$ m and $r_{\max} = 30$ m are plotted for a typical normalized humidity structure function measured by the Helipod (black vertical lines). For C_T^2, the inertial subrange was found to be between $r_{\min}$ = 2.5 m and $r_{\max}$ = 25 m, in agreement with van den Kroonenberg et al (2012), and for C_{QT} betwenn $r_{\min} = 20$ m and $r_{\max} = 40$ m. A very detailed explanation of how to calculate the structure parameter by applying this method can also be found in Platis et al (2015).

To analyse the influence of surface heterogeneity on the structure parameter, a spatially resolved calculation of the structure function is required. Hence, $D_S(r,i)$ is calculated along smaller flight sections (sub-legs) of a window-length W along the whole flight leg at every data point i. In general three steps are needed to obtain the local structure parameter:

- We take a sub-sample of length W with N data points along the whole flight leg at every data point i.
- $D_S(r,i)$ is calculated for this sub-leg of length W (Eq. 3) at each data point i.

– $C_S^2(i)$ is obtained by averaging over the inertial sub-range of $D_S(r,i)$ in between the boundaries $r_{\min}$ and $r_{\max}$.

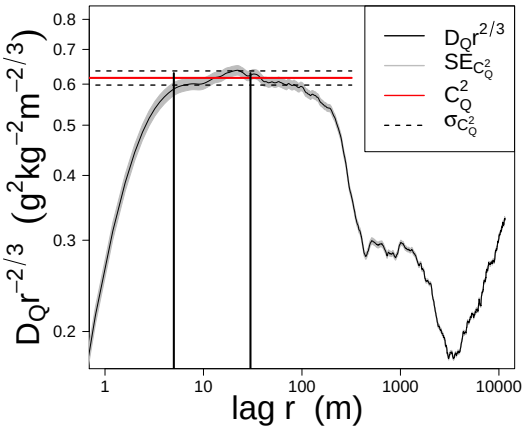

Fig. 6 Normalized structure function of the water vapour mixing ratio and the standard error (grey area). The red line represents the mean value in the section between $r_{\min}$ = 4 m and $r_{\max}$=30 m which is C_Q^2. The black dashed lines are $\pm\sigma_{C_Q^2}$.

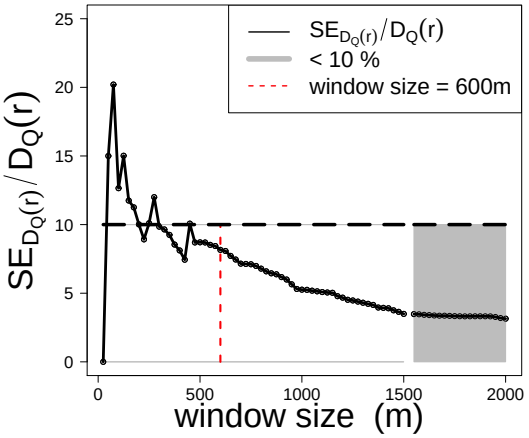

Fig. 7 Relative standard error $SE_{D_Q(r)}/D_Q(r)$ in % for$r = r_{\max}$. The window size of 600 m is marked with a red line. The error is below 10% for a 600 m window size.

5.2 Standard Error

In order to define a minimum length of the sub-legs W, the statistical error is calculated (Eq. 4) as a function of the W, i.e. the number N of data points measured along the sub-leg:

$$N = \frac{W}{v_{\text{gs}}} \cdot f_s \ , \tag{11}$$

where $v_{\text{gs}} \approx 40$ m/s is the ground speed of the Helipod and f_s the sampling frequency, which was 100 Hz. With the method proposed by van den Kroonenberg et al (2012), for a fixed lag $r(n)$ the statistical standard error of the average of the structure parameter $SE_{D_S(r)}$ calculated along W is estimated by

$$SE_{\overline{d(n)}}(r) = \frac{\sigma_{d(n)}}{\sqrt{N-n}} =: SE_{D_S(r)} \tag{12}$$

where n is the number of data points included by certain lag r and $\sigma_{d(r)}$ is the standard deviation of Eq. 14. $D_S(r)$ can be estimated by

$$\overline{d(r)} = \frac{1}{N-n} \sum_{i=1}^{N-n} d(i,r) =: D_Q(r) \quad , \tag{13}$$

with

$$d(i,r) = \left[S(x_i) - S\left(x_i + r(n)\right)\right]^2 \quad . \tag{14}$$

In Fig. 6 the normalized structure function for the humidity $D_Q(r)$ is plotted including the standard error $SE_{D_Q(r)}$ (grey area) for a sub-leg length of window size $W = 2000$ m ($N = 5000$ data points). The error increases in the inertial sub range with increasing r. Since we are only considering data for C_Q^2 between $r_{\min}$ and $r_{\max}$, the maximum error occurs at $r_{\max}$ =30 m with a relative standard error $SE_{D_Q(r_{\max})}/D_Q(r_{\max})$ of 5% at lag $r_{\max}$.

The standard error (12) is a function of the data record length N of the sub-leg, the lag $r(n)$, and the standard deviation $\sigma_{d(n)}$ of the data series $d_i(n)$ in (14).

Fig. 7 displays the decrease in the relative standard error with increasing window size W (increasing N) for a representative case on 30 May, 2003 at 11:00 UTC Flight HET0530_2). Due to restrictions on computational time, only window sizes W from 0 to 2000 m were calculated with an interval of 25 m. The error $SE_{D_Q(r)}$ should be below a certain threshold (e.g 10 %) marked here with a grey area. For a window size greater than $W \approx 500$ m this criterion is fulfilled. Furthermore for W greater than 500 m the record size N is large enough to ensure that $\sigma_{d(n)}$ decreases for increasing N. The window length also takes into account the sizes of the turbulent eddies. In order to measure all relevant scales of the inertial subrange, the length $W(N)$ of sub-legs (with record size N) should be larger than the integral length scale I. To gain better statistics for these scales, W should be at least twice the integral length scale, $W \approx 2 \cdot I$. The largest integral length scale I from all selected flights was calculated to be about 300 m (not shown). Thus, for this study, a window size of $N = 1500$ data points was selected to calculate the spatially resolved structure parameter, which corresponds to a window size of $W = 600$ m.

5.3 Standard Deviation of C_S^2 in the inertial sub-range

When calculating C_S^2 from the structure function, there is an additional source of uncertainty. The structure parameter is calculated by the mean value $\langle D_S(r) r^{-2/3} \rangle_{r_{\min}, r_{\max}}$ (plateau value, see e.g Fig. 6) of the normalized structure function between $r_{\min}$ and $r_{\max}$, here done for the humidity Q. This average value has a standard deviation $\sigma_{C_S^2}$, displayed in Fig. 6. The red line represents the average value and the black dashed lines mean $\pm\sigma_{C_S^2}$. The relative error of C_S^2 is defined as

$$\mathrm{RE}_{C_Q^2} = \frac{\sigma_{C_Q^2}}{\langle D_Q(r) r^{-2/3} \rangle_{r_{min}, r_{max}}} = \frac{\sigma_{C_Q^2}}{C_Q^2} \tag{15}$$

It describes the uncertainty in C_Q^2, since the plateau is not flat. $\mathrm{RE}_{C_Q^2}$ decreases with increasing window size W and is about 10 % for $W = 600$ m and below 1% for $W > 2000$ m (not shown). Since $\mathrm{RE}_{C_Q^2}$ and $SE_{D_Q(r)}$ are on the same order of about 10 % of $D_Q(r)$ (the width of they grey band in Fig. 6 is in the same order as $\mathrm{RE}_{C_Q^2}$), the error does not play a role. $\mathrm{RE}_{C_Q^2}$. For C_T^2 and C_{QT} we obtain the same order of error (not shown). Therefore, we will always accept an error in C_S^2 of 10% for a $W = 600$m window for the Helipod measurement. In the analysis in Sect. 4 we can neglect both errors since variability due to random turbulence and surface influence a much larger.